Universidade do Porto

Faculdade de Engenharia

FEUP

Use of Pd-Ag Membrane Reactors in the Water-Gas Shift Reaction for Producing Ultra-Pure Hydrogen

Dissertation

Presented to the Faculty of Engineering – University of Porto, for the degree of

Doctor of Philosophy (PhD) in Chemical and Biological Engineering

by

Diogo Manuel Pereira Mendes

Supervisors: Prof. Luis Miguel Palma Madeira

Prof. Adélio Magalhães Mendes

July, 2010

LEPAE - Laboratory for Process, Environmental and Energy Engineering
Chemical Engineering Department
Faculty of Engineering – University of Porto

Abstract

The main objective of this work was the development of an efficient unit integrating the water-gas shift (WGS) reaction with hydrogen removal in a single piece of equipment, using a Pd-based membrane reactor (MR). The removal of H_2 from the reaction zone is expected to enhance the reaction conversion over the equilibrium limitations based on feed conditions, producing simultaneously highly pure hydrogen.

A lab set-up was built to perform the experimental work. The unit was designed to measure the activity of low-temperature WGS catalysts, to determine the reaction kinetics, to characterize the separation ability towards hydrogen of the Pd-Ag membrane and to study the application of the MR for the WGS reaction.

The catalytic activity for the low-temperature WGS reaction of three commercial samples (Au/TiO_2, CuO/Al_2O_3 and $CuO/ZnO/Al_2O_3$) was evaluated and compared with a lab-prepared catalyst (Au/CeO_2, synthesized at ITQ – Valencia, Spain). It was observed that the nanosized Au/CeO_2 material reveals the highest CO conversion at the lowest temperature investigated (150 ºC). However, while in the deactivation tests performed the $CuO/ZnO/Al_2O_3$ catalyst showed a good stability for the entire range of temperatures considered $(150-300\ ºC)$, the Au/CeO_2 sample clearly showed two distinct behaviors: a progressive deactivation at lower temperatures and a good stability at higher ones, above 250 °C.

After the catalysts screening, the kinetics of the WGS reaction was determined over the material showing the best compromise between activity and stability. The $CuO/ZnO/Al_2O_3$ catalyst was then tested in a wide range of temperatures $(180-300\ ºC)$ as well as space times, using a simulated reformate gas mixture in the feed; an integral reactor under the conditions of no mass and heat transfer limitations was used. Several kinetic models were proposed, which were subjected to a rigorous parameter estimation and model discrimination in order to obtain the most appropriate one. For temperatures from $180-200\ ºC$, the best fitting model was the one based on an associative (Langmuir-Hinshelwood) mechanism while the redox pathway showed the best fit for the range $230-300\ ºC$. It was then proposed a composed kinetic model that comprehends the first one for $180-200\ ºC$ and the second one for $230-300\ ºC$, revealing distinct rate-controlled steps for each range. The validity of this composed model was assessed experimentally and a satisfactory agreement was obtained.

A dense metallic permeator tube was prepared at ENEA (Frascati, Italy) by an innovative annealing and diffusion welding technique starting from a commercial flat sheet membrane of Pd-Ag. A “finger-like” assembly of the self-supported membrane has been built, its

permeance and selectivity towards hydrogen determined and used as a packed-bed membrane reactor (PBMR) for producing ultra-pure hydrogen via WGS reaction. The commercial $CuO/ZnO/Al_2O_3$ catalyst was used for packing the membrane reactor. The performance of the reactor was evaluated in terms of CO conversion and H_2 recovery in a wide range of conditions. Carbon monoxide conversions remained in most cases above the thermodynamic equilibrium based on feed conditions; in particular, it is worth mentioning that around 100 % of CO conversion and almost complete H_2 recovery was achieved at 300 ºC with a feed space velocity of $1200\ L_N \cdot kg_{cat}^{-1} \cdot h^{-1}$, a feed pressure of 4 bar, a permeate pressure of 3 bar and using $1\ L_N \cdot min^{-1}$ of sweep gas.

A phenomenological model was then proposed to describe the membrane reactor performance. It takes into account the expression obtained for H_2 permeation rate through the Pd-Ag membrane and the combined kinetic model for the WGS reaction on the copper-based catalyst. In general, the simulation results showed a good adherence to the experimental data, taken for a wide range of operating conditions, either in terms of CO conversion, H_2 recovery or outlet streams compositions.

Finally, it was investigated the performance and energy efficiency achieved by an integrated system based on two different ethanol fuel processor configurations: a Conventional Reactor- and a Membrane Reactor-based one. The analysis showed that the MR-based process configuration is simpler although with a minor advantage in terms of energy efficiency (30 %) compared with the conventional system (27 %). The importance of optimizing the integrated systems that comprehend synergistic effects was evidenced.

The Pd-Ag membrane reactor designed proved to produce efficiently an ultra-pure hydrogen stream based on the WGS reaction compatible with low-temperature polymer electrolyte membrane fuel cell (PEMFC) requirements.

Resumo

O objectivo principal deste trabalho foi o desenvolvimento de uma unidade eficiente que integra a reacção de gás-de-água (*water-gas shift*, WGS) com a remoção de hidrogénio numa única peça de equipamento, utilizando um reactor de membrana à base de Pd. Espera-se que a remoção do hidrogénio do meio reaccional aumente a conversão da reacção acima das limitações impostas pelo equilíbrio baseado nas condições de alimentação, produzindo simultaneamente hidrogénio de elevada pureza.

Foi montada uma instalação laboratorial para realizar o trabalho experimental. A unidade foi projectada para nela se medir a actividade dos catalisadores de WGS a baixa temperatura, determinar a cinética da reacção, caracterizar a capacidade de separação ao hidrogénio da membrana de Pd-Ag e estudar a aplicação do reactor de membrana na reacção de WGS.

Foi avaliada a actividade catalítica, na reacção de WGS a baixa temperatura, de três amostras comerciais (Au/TiO_2, CuO/Al_2O_3 e $CuO/ZnO/Al_2O_3$) e comparou-se com a de um catalisador preparado em laboratório (Au/CeO_2, sintetizada no ITQ – Valência, Espanha). Observou-se que o material nanométrico Au/CeO_2 revela a maior conversão de CO à temperatura mais baixa investigada (150 ºC). No entanto, embora nos testes de desactivação realizados o catalisador $CuO/ZnO/Al_2O_3$ tenha mostrado uma boa estabilidade em toda a gama de temperaturas considerada $(150-300\ ºC)$, a amostra Au/CeO_2 mostrou claramente dois comportamentos distintos: uma desactivação progressiva a temperaturas mais baixas e uma boa estabilidade nas mais elevadas, acima de 250 °C.

Após a selecção do catalisador, foi determinada a cinética da reacção de WGS sobre o material que mostrou o melhor compromisso entre actividade e estabilidade. O catalisador de $CuO/ZnO/Al_2O_3$ foi então testado num amplo intervalo de temperaturas $(180-300\ ºC)$, bem como de tempos espaciais, usando-se uma alimentação constituída por uma mistura gasosa que simula a composição de uma corrente de reformação; foi utilizado um reactor integral em condições de ausência de limitações à transferência de massa e calor. Propuseram-se vários modelos cinéticos, os quais foram submetidos a uma rigorosa estimativa de parâmetros e discriminação dos modelos a fim de encontrar-se o mais apropriado. Para temperaturas no intervalo $180-200\ ºC$, o modelo com o melhor ajuste foi o baseado num mecanismo associativo (Langmuir-Hinshelwood), enquanto o modelo redox mostrou o melhor ajuste no intervalo $230-300\ ºC$, revelando a existência de passos controlantes distintos em cada intervalo. Foi então proposto um modelo cinético composto que responde de acordo com a temperatura de reacção segundo um ou o outro modelo. A validade deste modelo composto

foi avaliada experimentalmente tendo-se registado um ajuste satisfatório aos dados experimentais.

Nas instalações do ENEA (Frascati, Itália), foi sintetizado um tubo metálico denso e permeável por uma técnica inovadora de recozimento e soldadura por difusão a partir de uma membrana comercial de folha plana de Pd-Ag. O dispositivo, baseado nesta membrana auto-suportada, foi construído numa configuração "tipo-dedo", tendo-se determinado a sua permeância e selectividade ao hidrogénio e sido posteriormente utilizado como um reactor de membrana de leito fixo para produzir hidrogénio ultra-puro através da reacção de WGS. Utilizou-se o catalisador comercial de $CuO/ZnO/Al_2O_3$ no empacotamento do reactor de membrana. O desempenho do reactor foi avaliado em termos de conversão de CO e recuperação de H_2 num vasto intervalo de condições. As conversões de monóxido de carbono permaneceram na maioria dos casos acima do equilíbrio termodinâmico baseado nas condições de alimentação; em especial, importa realçar que se atingiu uma conversão de CO de cerca de 100 % e uma recuperação de H_2 quase completa a 300 ºC, com uma velocidade espacial de $1200\ L_N \cdot kg_{cat}^{-1} \cdot h^{-1}$, uma pressão na alimentação de 4 bar, uma pressão no permeado de 3 bar e utilizando $1\ L_N \cdot min^{-1}$ de gás de arrasto.

Propôs-se então um modelo fenomenológico para descrever o desempenho do reactor de membrana. O modelo tem em conta a expressão obtida da permeação do H_2 através da membrana de Pd-Ag e o modelo cinético composto no catalisador à base de cobre. Em geral, os resultados da simulação mostraram uma boa aderência aos dados experimentais obtidos num amplo intervalo de condições experimentais, quer em termos de conversão de CO, recuperação de H_2 ou composições das correntes de saída.

Finalmente, investigou-se o desempenho e a eficiência energética obtidos por um sistema integrado baseado em duas configurações diferentes de um processador de combustível alimentado a etanol: um baseado num reactor convencional e outro num reactor de membrana. A análise mostrou que o processo cuja configuração se baseia no uso de um reactor de membrana é mais simples, embora com uma vantagem reduzida em termos de eficiência energética (30 %) comparativamente ao o sistema convencional (27 %). Foi ainda evidenciada a importância da optimização dos sistemas integrados que compreendem efeitos sinergéticos.

O reactor de membrana de Pd-Ag construído mostrou ser capaz de produzir de forma eficiente uma corrente de hidrogénio ultra-puro, baseado na reacção de WGS, compatível com os requisitos das células de combustível de membrana electrolítica polimérica de baixa temperatura.

Sommaire

L´objectif principal de cette thèse été le développement d´une unité efficiente qu´intègre la réaction du gaz-à-l'eau (*water-gas shift*, WGS) avec le remuement de l´hydrogène dans une unique pièce d équipement, utilisant un réacteur de membrane à la base Pd. On espère que le remuement de l´hydrogène du milieu réactionnaire augmente la convertion de la réaction au dessus des limitations imposées par l´équilibre basé sur des conditions d´alimentation, produisant simultanément l´hydrogène de pure élevé.

On a monté une installation de laboratoire pour réaliser les travaux expérimentaux. L´unité a été projectée pour mésurer l´activité des catalyseur de WGS à baisse température, déterminer la cinétique de réaction, caractériser la capacité de séparation de l´hydrogène de la membrane de Pd-Ag et étudier l´application du réacteur de la membrane pour la réaction de WGS.

On a évalué l'activité catalytique, dans la réaction WGS à baisse température, des trois échantillons commercials (Au/TiO_2, CuO/Al_2O_3 e $CuO/ZnO/Al_2O_3$) et on a comparé avec cel d´un catalyseur préparé en laboratoire (Au/CeO_2, sinthétisé dans le ITQ – Valence, Espagne). On a observé que le matériel nanométrique Au/CeO_2 révèle la plus grande convertion de CO à la plus baisse des températures enquêtée (150 ºC). Mais, même si les tests de désactivation réalisés au catalyseur $CuO/ZnO/Al_2O_3$ a montré une bonne stabilité dans toute gamme de températures considerées $(150-300\ ºC)$, l´échantillon Au/CeO_2 a montré clairement deux comportements distintifs : une désactivation progressive aux tempéatures plus baisses et une bonne stabilité dans les plus élevées, au dessus de 250 °C.

Après la séléction du catalyseur, on a determiné la cinétique de la réaction de WGS sur le matériel qui a montré le meilleur compromis entre l´activité et la stabilité. Le catalyseur de $CuO/ZnO/Al_2O_3$ a été testé dans une intervalle ample de températures $(180-300\ ºC)$, bien comme de temps spacials, en usant une alimentation constituée par un mélange du gaz qui simule la composition d´un courant de réformation; on a utilisé un réacteur intégral dans des conditions d´absence de limitations à la transférence de masse et de chaleur. On a proposé plusieurs modèles cinétiques, lesquelles ont été soumis a un rigoureux aperçu des paramètres et d´absolution de modèles a fin de trouver le plus convenat. Pour des températures dans l´intervalle $180-200\ ºC$, le modele avec le meilleur réglage a été basé sur un mécanisme associatif (Langmuir-Hinshelwood), lorsque le modèle redox a montré le meilleur réglage dans l´intervalle $230-300\ ºC$, révélant l´éxistance de pas controlés distintifd dans chaque intervalle. C´est alors qu´on a proposé un modèle cinétique composé qui répond en accord

avec la température de la réaction selon un ou autre modèle. La validité de ce modèle composé a été évalué expérimentalement, ayant été enregistré un réglage satisfatoire aux données expérimentales.

Dans les intallations du ENEA (Frascati, Italie), on a synthétisé un tube métallique dense et perméable pour une technique innovatrice de recuisson et de soudure pour difution a partir d´une membrane commerciales de feuille plate de Pd-Ag. Le dispositif, basé sur cette membrane auto-supporter, a été construit dans une configuration "type-doigt", ayant été determiné sa perméance et séléctivité à l´hydrogène et ayant été après utilisé comme réacteur de membrane de lit fixe pour produire l´hydrogène ulta-pure atravers la réaction de WGS. On a utilisé le catalyseur commercial $CuO/ZnO/Al_2O_3$ dans l´empaquetage du réacteur de membrane. Le dégagement du réacteur a été évalué aux termes de convertions de CO et récupération de H_2 dans un vaste intervalle de conditions. Les convertions de monoxyde de carbone sont restées dans la plupart des cas au dessus de l´équilibre thermodynamique basé sur des conditions d´alimentation; en spécial, il faut mettre en valeur qu´on a atteint une convertion de CO d´environ 100 % et une récupération de H_2 presque complète à 300 ºC, avec une vitesse spaciale de 1200 $L_N \cdot kg_{cat}^{-1} \cdot h^{-1}$, une pression dans l´alimentation de 4 bar, une pression dans la perméant de 3 bar et utilisant 1 $L_N \cdot min^{-1}$ de gaz de traîne.

Alors, on a proposé un modèle phénoménolgique por décrire le dégagement du réacteur de membrane. Le modèle a fait cas de l´expression obtenu par la perméation du H_2 atravers la membrane de Pd-Ag et le modèle cinétique composé de la réaction de WGS dans le catalyseur à base de cuivre. En général, les résultts des simulations ont montré une adhérece aux données expérimentales obtenues dans un ample intervalle de conditions expérimentales, soit en termes de convertion de CO, de récupération de H_2 ou de composition des courants de sortis.

Finalement, on a enquêté le dégagement et l´efficience énergétique obtenus par un système intégré et basé sur deux configurations distintives d´un processeur de combustible alimenté par l´éthanol: basé sur un réacteur conventionnel et un autre sur un réacteur de membrane. L´analyse a montré que le proccès qui a la configuration basée sur l´usage d´un réacteur de membrane est plus simple, quoique avec un avantage réduit en termes d´efficience énergétique (30 %) comparativement au système conventionnel (27 %). On a aussi rendu évident l´importance de l´optimisation des systèmes intégrés qui comprennent des effets synergétiques.

Le réacteur de membrane de Pd-Ag construit, nous a montré d´être capable de produire de façon efficiente un courant d´hydrogène ultra-pure, basé sur la réaction de WGS, compatible

avec les requisits des piles de combustibles de membrane à electrolyte polymère qui opère à baisse température.

Acknowledgments

I would like to express my sincere gratitude to both of my supervisors, Professor Miguel Madeira and Professor Adélio Mendes, for his friendship, support, encouragement, expert advice and patience. Many thanks, to both, for providing me the opportunity to work in a field of research that I have found extremely interesting and for always challenging me to reach higher goals within my work. I would like also to thank to another member of the LEPAE staff, Professor José Sousa, who always provided me with valuable support.

To Ing. Silvano Tosti and his team for receiving me during my stay at ENEA – Frascati (Italy), and for their collaboration in the synthesis of Pd-Ag membranes. Thanks to the fantastic people that I meet during my stay in Rome. I really enjoyed the time I spent there.

To Professor Hermenegildo García, from the Instituto de Tecnologia Química – UPV (Spain), for their collaboration in the synthesis and characterization of catalyst samples.

I also thank my colleagues, for their friendship, for all of their generous help and stimulating discussions. A special thank goes to Sandra Sá for her help and support in the simulation work. I would also like to thank my lab mates for their support and valuable suggestions during my thesis work. Thanks to the graduate students with whom I have worked most closely and from whom I have consistently received support and encouragement.

I am also grateful to the Portuguese Foundation for Science and Technology (FCT) for my doctoral grant (ref. SFRH/BD/22463/2005), and for the financial support through the projects PTDC/EQU-ERQ/2006 and POCTI/EQU/59345/2004.

I cannot end up without deeply thank my father, Manuel Mendes, and my mother, Joaquina Mendes, for their unflagging care, love and support throughout my life. I would also like to acknowledge my friends for their constant encouragement and love that I have relied throughout my life.

Table of Contents

Chapter 1

General Introduction

This chapter describes the motivation behind this research and provides a basic introduction to the study.

At the end, the objectives for the PhD work are established and a description of the structure of the thesis is presented.

1.1 Relevance and Motivation

1.1.1 Hydrogen as a future energy carrier

For many decades, the global economy was effectively built on the notion that cheap and abundant fossil fuel energy sources will be always available. The recent financial crises, characterized by a greater volatility in the fossil fuels prices, have shown, once again, the unsustainable foundations of today's economy. Continued reliance on fossil fuels and vehicle technologies will bring significant economical and social challenges. This will not only be due to the local depletion and global misdistribution of high quality fossil fuels, but also to the expected increase of the energy demands as well as the carbon taxes that result from the

conversion of the fossil fuels. We must, therefore, rapidly develop sustainable energy sources, which, in addition, do not produce net emissions of carbon dioxide.

Recently, hydrogen has received increased attention worldwide because of its potential as an energy carrier. It can be made from widely available primary energy sources including fossil sources and renewables (e.g. biomass, wastes, solar, wind, hydro or geothermal), enabling a more diverse primary supply for fuels (Kothari et al., 2008; Pena et al., 1996; Turner, 1999). Additionally, if H_2 is produced from fossil sources with carbon capture and sequestration, it would be possible to produce and use fuels with near-zero full fuel cycle emissions of greenhouse gases, with large reductions in emissions of air pollutants, and essentially zero oil use. The only by-product of hydrogen combustion is water or water vapor; if air is used for combustion, small amounts of NO_x can however also be produced (Züttel et al., 2008).

Today, world production of hydrogen is of the order of 50 million tons per year (Sigfusson, 2007), where basic chemical manufacturing (e.g. ammonia and methanol) and petroleum refining processes (hydrotreating and hydrocracking) represent the larger market shares – Figure 1.1. However, 95 % of the hydrogen produced is used to supply the demand of existing industries. Even if all this hydrogen was used to replace fossil fuels, it only would account for 2 % of the global primary energy use (Raman, 2004).

Hydrogen demand is expected to increase in the coming years due to the treatment of heavier oil and tar sands and to the proliferation in the market of fuel cells fed with hydrogen and air. Additionally, the growing environmental concerns and stringent emission norms are also contributing to the soaring demand for hydrogen, which can no longer be sustained by traditional hydrogen production methods. To accomplish an increase in hydrogen production capacity in a clean, sustainable, and cost-competitive way, new and more efficient technologies should be implemented.

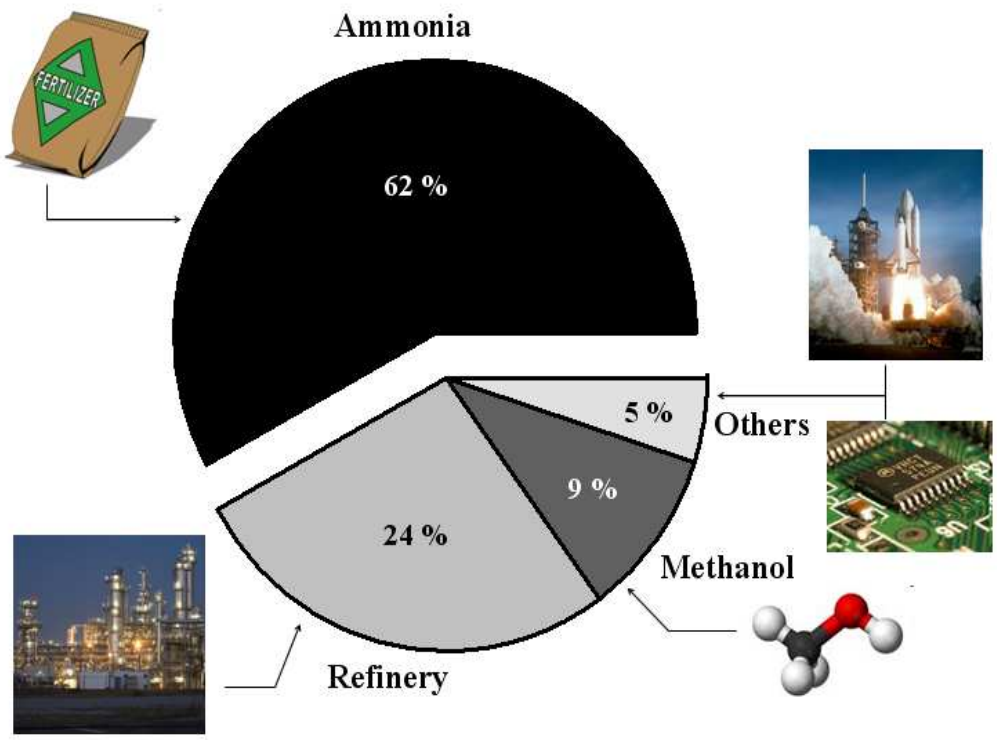

Figure 1.1 – Market share of the currently produced hydrogen (Suresh et al., October 2007).

1.1.2 Routes for hydrogen production

Today, nearly all hydrogen production is based on fossil raw materials. Hydrogen production technologies fall into four general categories: thermochemical, electrochemical, photobiological and photochemical (Haryanto et al., 2005). Thermochemical processes are the most used technologies for producing hydrogen from feedstocks such as natural gas, coal, or biomass (Holladay et al., 2009). Among the current technologies, steam methane reforming (SMR) is the most energy-efficient and commercialized process for the production of hydrogen, accounting for 48 % of the total H_2 produced, while the reforming of naphtha/oil accounts 30 % and gasification of coal 18 % (Wawrzinek and Keller, 2007). A traditional reforming process scheme for such a hydrogen plant is shown below:

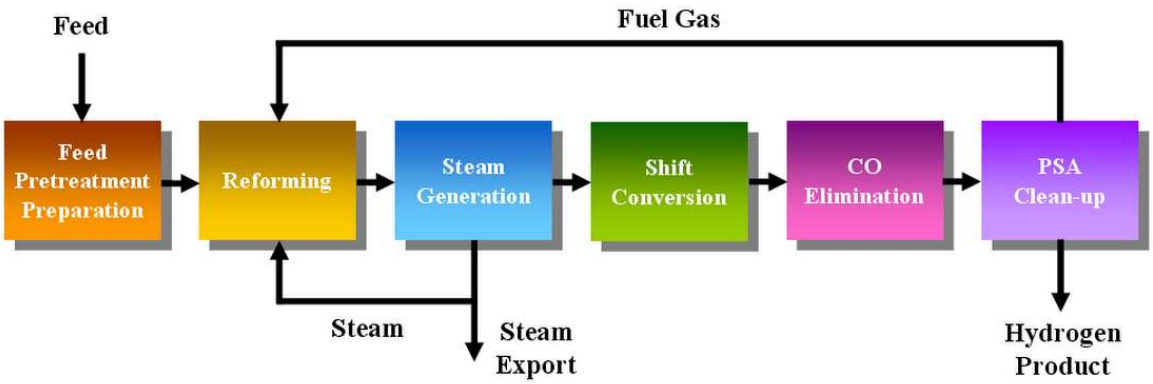

Figure 1.2 – Typical block diagram of a fuel processor operating in the steam reforming mode.

The traditional reforming process consists primarily on a treatment section to remove the impurities (cf. Figure 1.2), which are poisonous to reforming and shift catalysts. The key process step is the reforming section where the carbonaceous species react with steam over an appropriated catalyst to produce an H_2 rich-mixture. Because almost all catalysts used for the steam reforming of gases or liquid hydrocarbons produce CO, the water-gas shift (WGS) reaction is an important step in the reforming process; it reduces the CO content simultaneously producing more H_2, as shown in equation 1.1:

$$CO + H_2O \leftrightarrow CO_2 + H_2 \qquad (\Delta H_r^{298\,K} = -41.1\ kJ \cdot mol^{-1}) \qquad (1.1)$$

Further reduction in the amount of CO can be achieved by catalytic methanation (CO elimination stage in Figure 1.2). In addition to methanation, other methods could be used to purify H_2, such as pressure swing adsorption (PSA), cryogenic distillation, or membrane technology (Mendes et al., 2010). An example of an industrial steam methane reformer can be seen in Figure 1.3.

Steam methane reforming, although based on non-renewable sources, is the best option available at the moment to produce H_2 in large quantities while other technologies do not achieve the required maturity. However, in the future, the steam reforming of liquid fuels (e.g. methanol and ethanol obtained from biomass) are expected to be a promising choice in H_2-based energy systems (Haryanto et al., 2005; Olah et al., 2006).

Figure 1.3 – A steam methane reforming (SMR) process for the hydrogen production ($800\ m_N^3 \cdot h^{-1}$) (Allam, 2004).

1.1.3 Small scale power generation

Fuel cells are an important technology for the hydrogen economy and have the potential to revolutionize the power generation scenario, offering cleaner and more-efficient alternatives to the combustion of gasoline and other fossil fuels. Polymer electrolyte membrane fuel cell (PEMFC) can generate electric power and deliver it from micro to mega-watt applications making them applicable for wide use, i.e. from all sizes down to mobile phones and electronic gadgets to transportation or stationary power stations – Figure 1.4 (Gencoglu and Ural, 2009; Larminie and Dicks, 2003). Moreover, they offer compactness, modularity, low operating temperature $(80-110\ ^{o}C)$, high power density, fast start–up and response time and no shielding requirement for personnel safety (Barbir, 2005; Song, 2002).

Figure 1.4 – Collage of fuel cell applications and demonstrations.*

Rapid developments of the PEMFC technology in recent years have foster research in all areas of fuel processor for hydrogen generation. However, PEMFC, in particular for road vehicles applications, still have a few technological problems associated with water management and CO sensitivity of anode catalyst. The main targets are to develop active, selective, and stable catalytic systems for reducing the CO concentration in the H_2 stream fed to fuel cells to less than 0.2 ppm (ISO, 2008); this avoids CO poisoning of the anode, reduces the size and increases the efficiency of the fuel processor. In conclusion, the challenges associated to the smaller scale hydrogen generation units for PEMFC applications has been motivating the interest of many scientists and engineers on the WGS reaction technology as a process to reduce the CO content on the H_2 fuel streams.

* These figures were taken from websites: http://www.garmanage.com (accessed June 2010); http://bobpotchen.com (accessed June 2010); http://www.eco-trees.org (accessed June 2010); http://i.treehugger.com (accessed June 2010); http://www.techgadgets.in (accessed June 2010); http://www.hydrogencarsnow.com (accessed June 2010); http://www.ballard.com (accessed June 2010).

1.2 Objectives and Outline

The conventional processes for hydrogen manufacture that are commercially mature and are energy efficient at large scale operation (such as SMR) can not be economically down-scaled for small scale applications. For instance, the use of cryogenic distillation for hydrogen separation is prohibitively cost intensive at small scales. Moreover, conventional routes are designed and optimized for long runs and continuous operation and are not designed to meet the varying power demands and frequent shut-offs and restarts, which might be often encountered in small stationary systems and vehicular power applications (Krumpelt et al., 2002). The large number of process units and the use of superheated steam also make these technologies more difficult to implement at smaller scales. There is therefore the need for development of alternative compact reactor technology that can be compatible and energy efficient at small scales.

To develop a novel reactor technology for small scale applications, it is first essential to understand the chemistry of the reaction system and the design and operating issues related to it. As referred previously, the WGS process is designed to remove the bulk of carbon monoxide of a synthesis gas stream while also generating hydrogen. The extension of the WGS reaction is limited by the thermodynamic equilibrium (Moe, 1962) and due to its exothermicity, the equilibrium constant decreases increasing the temperature. However, the reaction has favorable kinetics at high temperatures. To improve the CO conversion, a promising approach considers the use of Membrane Reactors (MRs), combining the reaction and the separation of a reaction product through a selective membrane. In this way, according to *Le Chatelier's* principle, the equilibrium can be shifted and an increase in CO conversion above the equilibrium values is possible. In the present case, if hydrogen is removed selectively using a permselective membrane, it is possible to achieve two main objectives at the same time in a compact single unit:

- maximize the CO conversion thereby maximizing hydrogen product yield, and

- produce hydrogen in ultra-pure form that can be directly used in downstream low-temperature PEMFCs (e.g. in vehicle applications).

Permselective hydrogen membranes based on Pd are considered the most suitable for hydrogen extraction because of their very high perm-selectivity (Mendes et al., 2010).

Then, the main objectives of this thesis are:

1) to evaluate the most suitable catalytic systems to carry out the WGS reaction at low temperatures;

2) to design and build a lab scale Pd-Ag membrane reactor (MR);

3) to give an experimental proof-of-principle of the developed reactor concept.

The outline of this thesis is as follows:

Chapter 2 addresses a comprehensive literature review of WGS catalysis and kinetics. Additionally, an overview on the most used membranes for H_2 separation with special focus on Pd-based materials is provided. This chapter also includes a description on the effects of the most relevant parameters affecting the WGS reaction in membrane reactors.

In ***Chapter 3***, the catalytic performance for the low-temperature WGS reaction of a prepared gold-based catalyst is compared with that of commercial samples; the Au/CeO_2 catalyst was prepared at ITQ, in Valencia, in the framework of a collaboration with Prof. Hermenegildo García. The catalytic activities of the selected samples were evaluated in a wide range of operating conditions in a packed-bed reactor. The samples were also characterized in order to obtain additional information on the redox properties, textural and morphological structure of the catalytic materials. After this preliminary screening, a commercial Cu-based sample was selected for the subsequent studies.

In ***Chapter 4***, the kinetics of the WGS reaction using a copper-based catalyst is addressed. Several kinetic models were tested in a wide range of temperatures and contact times, aiming to find a robust one for modeling studies of WGS reactors (conventional or

not). A composed kinetic model was proposed and used to simulate the WGS packed-bed reactor, as well as the MR in chapter 6.

In ***Chapter 5***, the preparation of Pd-Ag tubular membranes and the MR design in a non-conventional configuration is described; the "finger-like" MR was conceived in the framework of another collaboration, with Ing. Silvano Tosti, from ENEA, at Frascati (Rome). Further, the experimental tests performed to evaluate the perm-selectivity and the permeability of hydrogen at different temperatures and hydrogen partial pressures is presented. The experimental measurements and data analysis of the Pd-Ag membrane reactor carrying out the WGS reaction for a wide range of experimental conditions is finally shown.

In ***Chapter 6,*** a phenomenological model is proposed to describe the performance of a Pd-Ag membrane reactor. The model was formulated taking into account the composed WGS reaction kinetic model previously developed (chapter 4) and the membrane properties determined in chapter 5. The adherence of the theoretical results to the experimental data is presented and analyzed.

In ***Chapter 7,*** the performance and the energy efficiency achieved by an integrated system based on two different ethanol fuel processor configurations is theoretically studied. A MR-based plant is then described and compared with a conventional process configuration. A commercial process simulation software, HYSYS, was used to solve the mass and energy balances, and to compute the operating conditions for each process unit. The importance of optimizing integrated systems and the improvements achieved by a MR-based configuration when compared with a conventional one are illustrated.

Finally, in ***Chapter 8,*** the general conclusions drawn from this work and the suggestions for future work are summarized.

1.3 References

Allam, R., 2004. Hydrogen: The fuel of the future, Presented at the London City Hall, 19 November, London, UK, Available on the Air Products web site (Accessed July 2010), http://www.airproducts.com.

Barbir, F., *PEM fuel cells: theory and practice*. Elsevier: Burlington, MA, 2005.

Gencoglu, M.T., Ural, Z., Design of a PEM fuel cell system for residential application. *Int. J. Hydrogen Energy* **2009**, 34 (12), 5242-5248.

Haryanto, A., Fernando, S., Murali, N., Adhikari, S., Current status of hydrogen production techniques by steam reforming of ethanol: A review. *Energy & Fuels* **2005**, 19 (5), 2098-2106.

Holladay, J.D., Hu, J., King, D.L., Wang, Y., An overview of hydrogen production technologies. *Catal. Today* **2009**, 139 (4), 244-260.

ISO, 2008. Hydrogen fuel - product specification - Part 2: proton exchange membrane (PEM) fuel cell applications for road vehicles, ISO/TS 14687-2. International organization for standardization.

Kothari, R., Buddhi, D., Sawhney, R.L., Comparison of environmental and economic aspects of various hydrogen production methods. *Renewable Sustainable Energy Rev.* **2008**, 12 (2), 553-563.

Krumpelt, M., Krause, T.R., Carter, J.D., Kopasz, J.P., Ahmed, S., Fuel processing for fuel cell systems in transportation and portable power applications. *Catal. Today* **2002**, 77 (1-2), 3-16.

Larminie, J., Dicks, A., *Fuel cell systems explained*. 2nd ed.; John Wiley & Sons: Chichester, 2003.

Mendes, D., Mendes, A., Madeira, L.M., Iulianelli, A., Sousa, J.M., Basile, A., The water-gas shift reaction: from conventional catalytic systems to Pd-based membrane reactors - A review. *Asia-Pac. J. Chem. Eng.* **2010**, 5 (1), 111-137.

Moe, J.M., Design of water-gas shift reactors. *Chem. Eng. Prog.* **1962**, 58 (3), 33-36.

Olah, G.A., Goeppert, A., Prakash, G.K.S., *Beyond oil and gas: The methanol economy*. Wiley-VCH: Weinheim, Germany, 2006.

Pena, M.A., Gomez, J.P., Fierro, J.L.G., New catalytic routes for syngas and hydrogen production. *Appl. Catal., A* **1996**, 144 (1-2), 7-57.

Raman, V., 2004. Hydrogen production and distribution, Presented at the SAE Toptec symposium: Facets of implementing a hydrogen economy, 19 February, Sacramento, CA, Available on the Air Products web site (Accessed July 2010), http://www.airproducts.com.

Sigfusson, T.I., Pathways to hydrogen as an energy carrier. *Philos. Trans. R. Soc. London, Ser. A* **2007**, 365 (1853), 1025-1042.

Song, C.S., Fuel processing for low-temperature and high-temperature fuel cells - Challenges, and opportunities for sustainable development in the 21st century. *Catal. Today* **2002**, 77 (1-2), 17-49.

Suresh, B., Yoneyama, M., Schlag, S., October 2007. Hydrogen, Chemical Industries Newsletter. SRI Consulting, Available on the SRI Consulting web site (Accessed July 2010), www.sriconsulting.com.

Turner, J.A., A realizable renewable energy future. *Science* **1999**, 285 (5428), 687-689.

Wawrzinek, K., Keller, C., 2007. Industrial hydrogen production & technology, 2nd International workshop on functional materials for mobile hydrogen storage, Karlsruhe research center.

Züttel, A., Borgschulte, A., Schlapbach, L., *Hydrogen as a future energy carrier*. Wiley-VCH: Weinheim, Germany, 2008.

Chapter 2

Water-Gas Shift Reaction – State of the Art

The water-gas shift reaction (WGS) is a well-known step for upgrading carbon monoxide to hydrogen from synthesis gas. For more than 90 years after its first industrial application, many issues in respect of the catalyst, process configuration, reactor design, reaction mechanisms and kinetics have been investigated. More recently, a renewed interest in the WGS reaction carried out in hydrogen perm-selective membrane reactors (MRs) has been observed because of the growing use of polymeric electrolyte membrane fuel cells that operate using high-pure hydrogen. Moreover, membrane reactors are viewed as an interesting technology in order to overcome the equilibrium conversion limitations in traditional reactors.

This chapter reviews the most relevant topics of WGS MRs technology – catalysis and membrane science. The most used catalysts and relevant progress achieved so far are described and critically reviewed. The effects of the most important parameters affecting the water-gas shift reaction in membrane reactors are detailed. In addition an overview on the most used membranes in membrane reactors is also presented and discussed.

The contents of this chapter were adapted from: Mendes, D., Mendes, A., Madeira, L.M., Iulianelli, A., Sousa, J.M., Basile, A., The water-gas shift reaction: from conventional catalytic systems to Pd-based membrane reactors - A review. *Asia-Pac. J. Chem. Eng.* **2010**, 5, 111-137.

2.1 Introduction: Historical Background Regarding the WGS reaction

The blossoming of the water-gas shift (WGS) reaction is related to the production of a combustible gas (water-gas = CO + H_2) when steam is passed through a bed of incandescent coke, first observed by Felice Fontana in 1780, as described in literature (Burns et al., 2008; Häring, 2008). The following century was marked by notorious discoveries and developments related to alkali chemical manufacture and gas production by gasification (Häring, 2008; Ihde, 1984). Ludwig Mond, one of the greatest chemist-industrialists of all time, focused part of his industrial chemical technology developments on the synthesis of ammonia from coal and coke. Mond developed the process for producing the so called "Mond gas" (the product of the reaction of air and steam passed through coal/coke – CO_2, CO, H_2, N_2, etc.), which became the basis for future coal gasification processes. Mond and his assistant Carl Langer were the first to use the term "fuel cells" while performing experiments with the world's first working fuel cell using coal-derived "Mond-gas" (Chen, 2002). One of the hardest tasks was to feed pure hydrogen to the "Mond battery" due to the large quantities of carbon monoxide present in "Mond Gas", which poisoned the Pt electrode. Therefore, Mond solved this problem by passing the "Mond Gas" mixture and steam over finely divided nickel at 400 ºC, reacting the carbon monoxide and steam to give carbon dioxide and more hydrogen. After CO_2 removal by a simple alkaline wash, the H_2-rich stream obtained could be successfully fed to the hydrogen cell (Weintraub, 2003).

The WGS reaction (equation 1.1) was discovered and for the first time reported in the literature by the end of the 19th century (Mond and Langer, 1888). Years later, in 1913, the WGS reaction found industrial application in the production of synthesis gas (or water-gas), as a part of the Haber-Bosch process of ammonia manufacture – cf. Figure 2.1 (Bosch and Wild, 1914).

Since the Fe-based catalyst for ammonia synthesis is deactivated by carbon oxides, the WGS reaction became an important step toward CO upgrade to H_2. In terms of process

(Figure 2.1), coal/coke was first blasted with air in a water-gas generator, exothermically producing carbon dioxide and carbon monoxide, thereby maintaining the high-temperature (HT) of the coal (around 1000 ºC) and raising it into an incandescent form. The water-gas ($CO + H_2$) was then produced via an endothermic reaction ($C + H_2O \rightarrow CO + H_2$), by passing steam through the fuel bed. After the removal of dust particles, the mixed gas was added to steam and CO was catalytically shifted in a converter to produce more hydrogen and carbon dioxide. Then, the gas was dried, compressed and passed through caustic scrubbers for CO_2 removal. By passing the gas mixture counter-currently over an ammoniacal cuprous solution, the CO was posteriorly eliminated by absorption (Quirk, 1963).

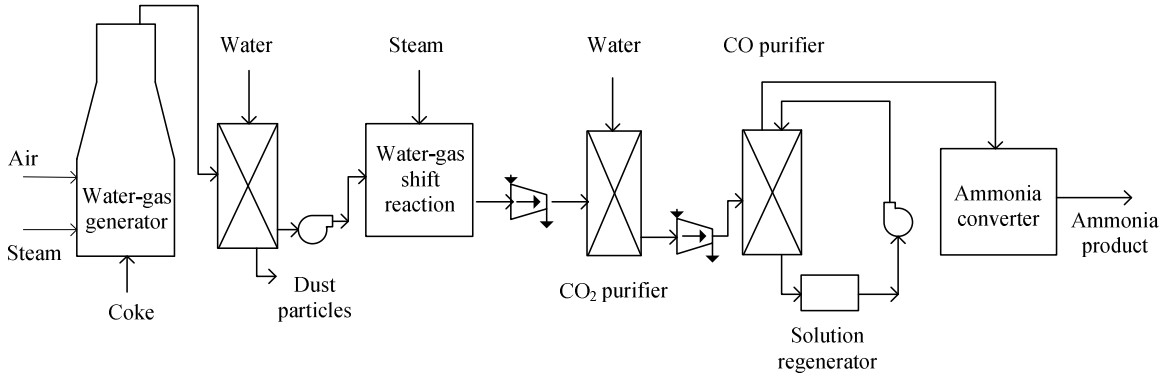

Figure 2.1 – Summarized sketch of the Haber-Bosh process (Quirk, 1963).

Industrially, the process integration of the WGS reaction is dependent upon the origin of the synthesis gas. By the beginning of the 20th century, and because the major source of synthesis gas production was coal and coke, the WGS reaction was used as a standalone process. By that time, the most common and economical design was to conduct the reaction in a single stage, at temperatures around $450-600$ ºC, and employing as catalyst Fe oxide stabilized in Cr oxide (Quirk, 1963). The next evolution of the process was the introduction of a second-stage converter at temperatures around $320-360$ ºC using the same catalyst. The two-stage converter systems reduced the CO level to $3000-4000$ ppm compared to the

single-stage converters that could not reduce the CO content to much less than 10 000 ppm (1 %) (Ladebeck and Wang, 2003). With the discovery in the 1960s of Cu-based low-temperature (LT) shift catalyst and improvements in HT Fe-based shift catalysts, a CO content < 0.5 % in the reformate stream was achieved (Ruettinger and Ilinich, 2006).

From the beginning of the 20th century until today, the use of the WGS reaction followed the increased industrial demand for hydrogen production. This has been accomplished using natural gas as feedstock instead of only coal, and employing better catalysts that improve the yields and permit the adjustment of the H_2-to-CO ratio of the product, mainly for ammonia and methanol synthesis, but also for the Fisher-Tropsch process and in refining operations (desulfuration, hydrogenation processes, etc.). With growing concerns about environmental issues, H_2 production from synthesis gas for fuel cell applications has become a huge focus of attention. In this context, new catalysts were developed in order to obey rigid safety requirements (in addition to fuel cell requirements) such as lower operation temperature, use of non-pyrophoric materials and with high attrition resistance, improving simultaneously the WGS activity for on-board hydrogen processing. To obtain high-purity hydrogen from either synthesis gas or from the products of the WGS reaction, competitive separation processes were investigated with the aim of overcoming the performance limitations and costs of traditional methods. It is the goal of this chapter to review some of the important developments in the combination of WGS reaction and hydrogen purification.

2.1.1 Thermodynamic considerations - parameters influencing the process

The WGS reaction is an equilibrium-limited reaction, and CO conversion is favored at lower temperatures due to its exothermicity (equation 1.1). Equation 1.2 is widely seen in the literature to describe the equilibrium constant (K_p) as a function of temperature (T) (Moe, 1962):

$$K_p = exp\left(\frac{4577.8}{T} - 4.33\right) \tag{1.2}$$

As the temperature increases, the equilibrium constant and the equilibrium CO conversion (X_{CO}^{eq}) inherently decrease (Figure 2.2). Hence, H_2 production and CO consumption are in principle favored at lower reaction temperatures. Also, lower temperatures are favorable from the point of view of steam economy. However, the WGS reaction is controlled by the kinetics at these conditions, making highly active and stable WGS catalysts necessary.

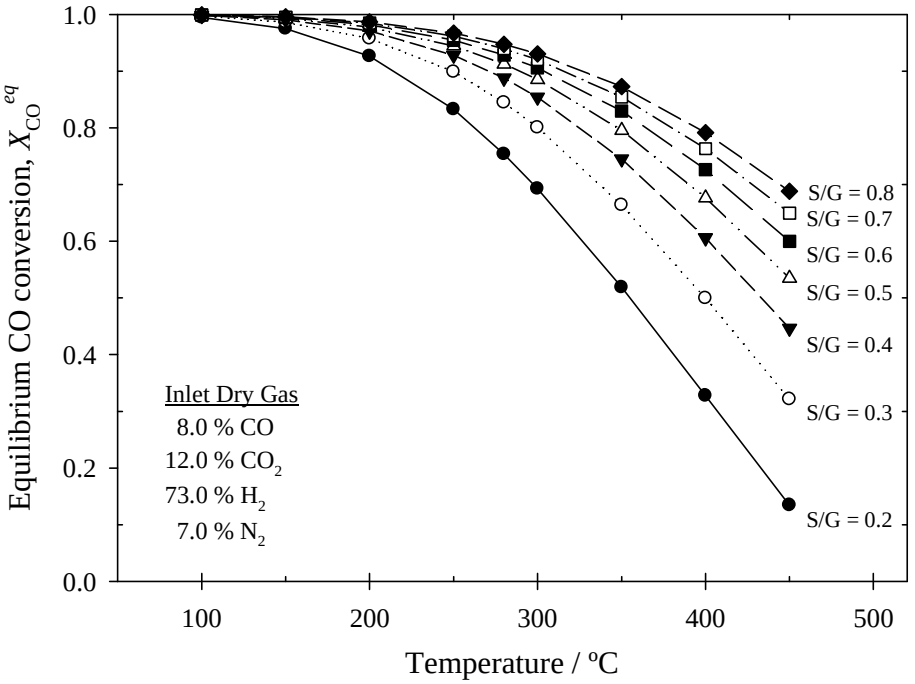

Figure 2.2 – CO equilibrium conversion of a typical reformate stream from a methane steam reforming process at various steam-to-dry gas (S/G) ratios.

Considering the range of pressures used for H_2 production, it is worth mentioning the reaction pressure does not affect the equilibrium of the WGS reaction because there is no variation in the number of moles during the course of the reaction (Ladebeck and Wang, 2003). Nevertheless, up to that point (i.e. up to the equilibrium), total pressure positively affects the CO conversion because it increases the reaction rate.

The WGS reaction is traditionally conducted in two- or three-stage catalytic converters instead of one. This allows a smaller adiabatic temperature rise and a better steam management, thereby making the process more economical (Thomas and Thomas, 1997). The first stage is characterized by working at higher temperatures, favoring fast CO consumption and minimizing catalyst bed volume. In the following stages, the reaction takes place at progressively lower temperatures for obtaining higher conversions, which are limited by the reaction equilibrium. Inter-stage cooling systems are used to conduct the next WGS reaction at a lower temperature, favoring the approach to higher equilibrium conversions.

The synthesis gas composition influences the CO conversion at equilibrium in the WGS reaction, obtained by solving equation 1.3, where K_p is expressed based on the basis of the feed composition (y_i^{in} refers to the molar fraction of species *i* at the reactor inlet) and assuming ideal gas behavior:

$$K_p = \frac{\left(y_{CO_2}^{in} + y_{CO}^{in} X_{CO}^{eq}\right)\left(y_{H_2}^{in} + y_{CO}^{in} X_{CO}^{eq}\right)}{\left(y_{CO}^{in} - y_{CO}^{in} X_{CO}^{eq}\right)\left(y_{H_2O}^{in} - y_{CO}^{in} X_{CO}^{eq}\right)} \qquad (1.3)$$

Typically, most of the synthesis gas produced worldwide comes from the steam reforming (SR) of natural gas, naphtha, or heavy hydrocarbon feedstocks. The CO, H_2 and CO_2 contents in the reformate stream will change depending on the process and reformate operation (cf. Table 2.1), thereby affecting maximum (equilibrium) CO conversions.

The water content in the WGS reactor will also play an important role in obtaining higher or lower CO equilibrium conversions. The effect of temperature and water concentration on the CO equilibrium conversion for the WGS reaction is shown in Figure 2.2 for a typical dry reformate gas used in a large-scale hydrogen or syngas production plant, excluding any residual hydrocarbons. It is clear from Figure 2.2, that an increase in the molar steam-to-dry gas (S/G) ratio improves the CO equilibrium conversion, especially above 150 ºC. However, the amount of water added to the reformer or between the WGS stages must be balanced

taking into account the desired CO composition at the end of the process, the available steam, the catalyst capacity for H_2O activation, and the operating conditions.

Table 2.1 – Typical dry exit gas (molar compositions) of methane steam reforming, methane auto-thermal reforming and coal gasification processes for H_2 production.

Component	Feedstock		
	CH_4 [a]	CH_4 [b]	Coal [c]
CO	0.08	0.128	0.570
CO_2	0.12	0.080	0.049
H_2	0.73	0.578	0.381
CH_4	0.04	0.004	–
N_2	0.03	0.211	–

[a] $830-850\ ^oC$, $25-50$ atm, Ni-based catalyst, S/C = 3.0;

[b] $830-850\ ^oC$, $25-50$ atm, Ni-based catalyst, O_2/C = 0.30, S/C = 3.0;

[c] $1100-1400\ ^oC$, $75-85$ atm, O_2/coal (kg/kg) = 0.899, H_2O/coal (kg/kg) = 0.318.

2.2 Description of the WGS Reaction in Traditional Reactors

The CO-shift process facilities are economically dependent on the feedstock used for synthesis gas generation, both in terms of equipment and catalysts. Methane (via SR) is actually the preferred raw material, with naphtha being preferentially used in areas where natural gas is not available. However, coal, the most abundant fossil fuel on the planet, is being looked as the possible future major source of H_2, due to the development of integrated gasification combined cycle (IGCC) and integrated gasification fuel cell (IGFC) technologies (Shoko et al., 2006).

Taking into account the exothermic nature of the WGS reaction, higher CO conversions are favored at lower temperatures. But kinetics are almost instantaneous at very high temperatures. Because of the inherent temperature increase during the reaction, synthesis gas generation is typically conducted in adiabatic CO-shift reactors to avoid catalyst overheating and improve the reaction conversion (Figure 2.3). As mentioned previously, even though the

reaction is thermodynamically favored at lower temperatures, the reaction kinetics are penalized and a large volume of catalyst is needed to approach high CO equilibrium conversions. The process is characterized by low space velocities, < 20 000 h^{-1}, currently representing the largest reactor in a fuel processor (Ruettinger and Ilinich, 2006).

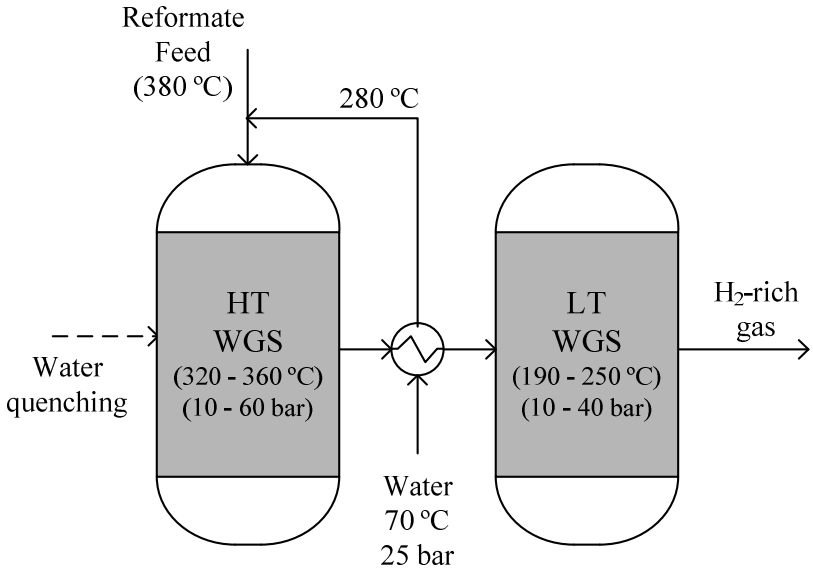

Figure 2.3 – Conventional two-stages process diagram of the WGS reaction unit.

In a typical industrial operation, Ni-based catalysts are primarily used for the SR of natural gas at high temperatures (> 700 ºC) using high H_2O/CO ratios (at least $3-5$). Then, the cooled gas from the reformer (at about $350-450$ ºC) is driven into a HT CO-shift converter (cf. Figure 2.3), commonly in the temperature range of $320-360$ ºC and at a total pressure between 10 bar and 60 bar, containing a Fe-based oxide catalyst (Newsome, 1980). Depending on the feedstock and the performance of the HT CO-shift reactor, an outlet stream with a CO concentration between 1 % and 5 % is typically obtained at a temperature around $400-450$ ºC. This stream is then cooled to about 200 ºC (by thermal quenching with water or by an inter-cooler system between stages) (Ladebeck and Wang, 2003). To avoid water condensation in the catalyst pores, and its subsequent deactivation, the inlet temperature is usually kept at least about 20 ºC above the dew point of the feed gas (Ruettinger and Ilinich, 2006). In some operations, water is injected between the stages to

adjust the S/G ratio before entering into an LT CO-shift reactor, operating in the range of $190-250\ ^{o}C$ and $10-40$ bar. Typical temperature gradients of $20-30\ ^{o}C$ in the catalyst bed are observed, and an outlet stream with a CO concentration less than 0.5 % is obtained (Ruettinger and Ilinich, 2006). Further reduction of CO and CO_2 to acceptable limits for proton exchange membrane fuel cell (PEMFC) applications and for ammonia synthesis involves other H_2 clean-up systems discussed below. In particular, CO concentration higher than 0.2 ppm for on-board vehicle applications (ISO, 2008) poisons the Pt catalyst of the PEMFC.

2.2.1 The most used catalysts - operating conditions and catalytic properties

Many efforts in recent years have attempted to find the best heterogeneous catalysts to carry out the WGS reaction. The catalysts used in this process might be distinct, depending on the reaction temperature. On the other hand, in a staged WGS process the reaction temperature depends on the stage. At the moment, there are two main classes of materials being used in industry as CO-shift catalysts: Fe-based and Cu-based catalysts. Since their first industrial application, numerous developments have been taken place in catalyst compositions and manufacturing procedures, attempting to improve their activity, stability, and selectivity.

Fe-based catalysts

The Fe-based catalysts are some of the earliest heterogeneous catalysts used industrially in the WGS reaction and are commonly called HT shift catalysts, operating in the temperature range of around $320-450\ ^{o}C$, because of improved catalytic performance and selectivity. Most industrial HT shift catalysts contain Cr oxide (Cr_2O_3) as well as Fe oxide, and it has been generally believed that Cr_2O_3 is a structural promoter, retarding sintering and loss of surface area of the Fe oxide, thus enhancing the activity and stability of Fe catalysts

(Rase, 2000). However, its replacement should be envisaged in view of health and environmental problems associated with hexavalent Cr.

The Fe-Cr catalyst activity is not seriously affected by poisoning, even though sulfur and chlorine compounds are potential sources of poisoning when present at high levels in the reaction medium (Newsome, 1980).

To improve the catalytic activity of Fe-Cr, a reduction treatment is typically performed during HT WGS reactor start-up between 250 and 400 ºC (Ruettinger and Ilinich, 2006). The active phase, Fe_3O_4 (magnetite), is obtained by partially reducing α-Fe_2O_3 (hematite) using the process gas mixture with a relatively low concentration of the reductants in the presence of steam. CrO_3 is also reduced to Cr_2O_3, creating a solid crystalline solution (Newsome, 1980). During and after the reduction process, the temperature should be carefully controlled because of the exothermic nature of the reactions involved and the inherent heat release, which may lead to catalyst sintering and loss in activity/surface area. It is also crucial to avoid converting the magnetite active phase into lower oxides, carbides, or metallic Fe species since they catalyze undesired side reactions (i.e. methanation and Fisher-Tropsch processes), reducing selectivity and promoting extra hydrogen consumption (Rhodes et al., 1995).

Due to these reasons, the type of pretreatment to be applied to these Fe-Cr catalysts has been the focus of extensive research work. For instance, Gonzalez et al. (Gonzalez et al., 1986) studied the influence of thermal treatments and reduction processes on WGS activity. They concluded that reduction by H_2/N_2 or by the process stream ($CO + H_2O$) should be performed at a temperature below 500 ºC to obtain higher activity without over-reduction of Fe_2O_3. In fact, water vapor acts as a mild oxidant compared to the high reducing capacity of CO. However, liquid water condensation should be avoided since it can originate chromate leaching.

The addition of structural and chemical promoters has also been an interesting method to improve catalyst activity. Topsøe and Boudart (Topsøe and Boudart, 1973) and Natesakhawat et al. (Natesakhawat et al., 2006), among other authors, suggested that the addition of other cations (metal promoters) into the metal lattice might change the electronic properties, improving the catalyst activity. The Fe-chrome catalyst was promoted by adding Cu to increase the catalytic activity and selectivity, even at lower H_2O/C ratios where secondary reactions might happen, leading to energy reduction costs. On the other hand, Andreev et al. (Andreev et al., 1986) studied the effect of adding CuO, CoO, MnO, and ZnO on the activity of Fe-Cr catalysts, where Cu- and Co- oxides proved to be catalytic promoters of interesting relevance. More recently, Rhodes et al. (Rhodes et al., 2002) studied the promotion of Fe-Cr catalysts with B, Cu, Ba, Pb, Hg and Ag. In this case, by adding Hg, Ag, or Ba and then Cu, higher catalytic activity was observed for temperatures between 350 and 440 ºC. The authors attributed this fact to the different ionic sizes compared to that of Fe^{2+}, influencing the covalency of the Fe^{2+}/Fe^{3+} system and enhancing the conductance of the magnetite solid.

Efforts are also being made in the development of Cr-free catalytic systems due to the problems mentioned above. In this regard, Natesakhawat et al. (Natesakhawat et al., 2006) selected three metals, Al, Mn and Ga, to be incorporated in the hematite lattice and compared the activity of each formulation with Fe-Cr. The Fe-Al catalyst presented high activity, albeit lower than the Fe-Cr sample. Ionic radius similarities with Fe^{3+} did not revealed to be the crucial issue for the replacement of Cr. Instead, it is plausible that Cr acts as an active site and/or promotes some electronic structural change in the lattice. The impregnation of the Cr-free catalyst with Cu and Co revealed an enhancement in catalyst activity. Rangel Costa et al. (Rangel Costa et al., 2002) used Th instead of Cr in a Cu-doped Fe-based catalysts for the HT WGS reactor. Its high activity was assigned to an increase in surface area by thorium, potentially a promising catalyst to replace the conventional Fe-Cr.

Cu-based catalysts

The industrial WGS process was revolutionized by the use of Cu-based catalysts because the enhancement obtained in the process allows higher CO conversions and yields in the production of H_2. Since their first usage, several Cu formulations have been employed in the LT WGS stage (Lloyd et al., 1989). Improvements in the catalyst activity, stability, and resistance to poisoning and sintering were based on such developments. However, the thermal stability of the LT WGS catalysts is still inferior to the HT catalyst. In fact, Cu crystallites are very susceptible to thermal sintering via surface migration, reducing the fully active catalyst life. One of the major advances in achieving enhanced stability in Cu catalysts was the introduction of additional components, acting as structural spacers that decrease the aggregation of Cu crystallites during operation. Nevertheless, operating temperatures should be restricted, usually to below 300 ºC (Twigg and Spencer, 2001).

The most used LT WGS catalyst is a mixture of Cu, Zn, and Al oxides. Besides their role as structural promoters, zinc and aluminum oxides also seem to function as chemical promoters, although this point remains controversial. Several authors observed an enhancement in the catalytic activity of Cu supported on ZnO due to synergetic effects responsible for improved covalency between the different oxidation states of Cu in the metal lattice (Kanai et al., 1994; Yurieva and Minyukova, 1985). In the work by Ginés et al. (Ginés et al., 1995), the improvement in WGS activity over binary Cu/ZnO by ternary $Cu/ZnO/Al_2O_3$ catalysts revealed the effect of adding alumina as a factor responsible to contributing to the formation of hydrotalcite phase, leading to an improvement in catalyst performance. Structure sensitivity is an important concept which reveals the complexity of these catalytic systems. The dependence of the specific activity on some catalyst characteristics (e.g. Cu metal surface area, Cu loading, metallic Cu dispersion/dimension, and calcination temperature) are of great interest in order to optimize catalyst synthesis. There is also little consensus on this issue. For instance, according to Lloyd et al. (Lloyd et

al., 1989), the specific activity (or turnover frequency - TOF) increases with the dispersion of metallic Cu on the catalyst surface, supporting the idea that Cu-based systems are structurally sensitive. In contrast, structural insensitivity was observed by Ginés et al. (Ginés et al., 1995). These authors observed that the TOF is essentially constant over a certain range of metallic Cu dispersions, CuO loading, calcination temperature, and Al/Zn atomic ratio. Yeragi et al. (Yeragi et al., 2006) also inferred that the dispersion of the catalytically active Cu metal has no significant effect on the CO conversion in Mn-promoted Cu/Al_2O_3 catalysts for the LT WGS reaction.

One of the most critical aspects that opened the way to the general use of Cu-based catalysts to conduct the WGS reaction at LT was the change of feedstock from coal to naphtha or natural gas and the improved feedstock desulphurization units. In this way, a reduction in the amount of chlorine and sulfur compounds was obtained, substances for which Cu's high affinity is well known. Consequently Cu-based catalysts were able to work for long periods without deactivation ($2-4$ years depending on the operating conditions) (Lloyd et al., 1989; Twigg and Spencer, 2001). Moreover, ZnO also serves to somewhat protect the Cu from sulfur poisoning in the case of inefficient removal in the upstream units.

As happens with Fe-Cr catalysts, to improve the activity of Cu-based formulations a reduction treatment at temperatures between 180 and 260 ºC is typically performed during LT WGS reactor startup (Ruettinger and Ilinich, 2006). The operation is typically carried out by adding small amounts of H_2 and/or CO to an inert gas (nitrogen or natural gas), reducing CuO, and dispersing it into a large surface area. During the reduction process, the catalyst bed temperature should be carefully controlled because of the highly exothermic nature of the reaction(s) involved and the possibility of catalyst sintering.

The addition of structural and chemical promoters has also been made in this case to enhance the activity and temperature stability of Cu-based catalysts. Several researchers have been focusing their attention on Cu-Mn oxide catalysts because they exhibit good activity

and heat stability compared to the conventional Cu-based materials (Gottschalk and Hutchings, 1989; Tanaka et al., 2003; Yeragi et al., 2006). The electron accepting potential of the catalyst and the facilitated covalency between the Cu oxidation states are possible reasons given for the activity enhancement.

2.2.2 WGS catalysts developments

Until recently, shift reactors in fuel cell systems at the kilowatt scale have been utilizing the above mentioned industrial Fe and Cu-based catalysts (Deshpande and Krause, 2007). Despite the fact that Fe-Cr formulations have the advantages of being cheap and stable, a major limitation of this catalyst is the need for temperatures above 350 ºC for acceptable activity, a described previously. The Cu-based formulations have good activity even below 200 ºC, but are susceptible to poisoning and operate in a limited temperature range because of problems with Cu sintering (Twigg and Spencer, 2001). Disadvantages of Cu-based catalysts materials include the need for activation before operation by a slow and controlled reduction process; upon shutdown the catalyst must be purged with an inert gas to prevent condensation and re-oxidation. Moreover, repeated start-up/shutdown cycles may well result in water condensation and subsequent catalyst deactivation. Therefore, besides higher activity at lower temperatures and improved stability, new WGS catalysts should possess other important characteristics: absence of pyrophoricity, stability towards condensation and poisoning, fast start-up and no requirement for exceptional pretreatments (Ghenciu, 2002). Certainly, if the reaction bed containing conventional/commercial WGS catalysts is pyrophoric during operation, then these catalytic materials should not be used in portable applications.

Co-based catalysts

In recent years, and as mentioned above, there has been a renewed interest in the WGS reaction because of its potential application to high-purity hydrogen for PEM fuel cells. In

this case, hydrogen should contain very low concentrations of CO (≤ 0.2 ppm for on-board vehicle applications (ISO, 2008)) in order to avoid poisoning of the Pt electrodes. Therefore, extensive research efforts are underway to design active and stable catalysts to obtain a more efficient WGS step in fuel process. The reduced tolerance of both Fe-Cr oxide and, in particular, the Cu-based catalysts to sulfur compounds, concentrated the efforts to find a promising catalytic system able to withstand these impurities. As referred above, coal-derived synthesis gas was initially used to produce chemicals or fuels in industry. Currently, coal is gathering increased interest, particularly in countries with richer coal resources. Therefore, as in the past, nowadays (even with the change of primary feedstock to natural gas) sulfur removal units and/or a guard bed catalyst have proven to be necessary to protect various catalysts from H_2S and COS (carbonyl sulfide) present in feed streams. In this sense, sulfur-tolerant Co-based catalysts have found a strong interest by the catalysis community (Farrauto et al., 2003; Hutchings et al., 1992; Lund, 1996; Mellor et al., 1997; Newsome, 1980). Actually, Co-based systems have the advantage of being even more sulfur tolerant, preserving their catalytic activity for the WGS reaction either in the presence or in the absence of sulfur, when compared with conventional HT and LT WGS catalyst systems. The low activity at temperatures between 200 and 300 ºC make them less useful for LT applications (Farrauto et al., 2003). Nevertheless, cobalt catalysts show higher catalytic activity than the standard commercial Fe-Cr-oxide HT WGS catalyst (Hutchings et al., 1992). However, the introduction of Co as a catalytic promoter causes an increase in the production of methane as by-product, thereby decreasing the H_2 yield of the process. Another disadvantage is the temperature rise due to exothermic CO hydrogenation, which can result in loss of surface area by sintering, reducing the catalytic activity. The addition of potassium carbonate promoter to Co catalysts seems to overcome the problem of methane formation and also enhances the catalytic activity (Hutchings et al., 1992).

Au-based catalysts

In recent years, essentially two new materials have gained much attention to overcome the described limitations: Au- and Pt-based catalysts. Reducible oxide-supported nano-size Au- and Pt-based catalysts seem to be promising candidates for fuel processing, mainly due to their high activity at LTs and potential stability in oxidizing atmospheres (Bunluesin et al., 1998; Cameron et al., 2003; Mendes et al., 2009; Swartz et al., 2001). In this regard, Burch (Burch, 2006) pointed out that a well prepared, carefully activated Au catalyst can be at least as active as an equivalent Pt catalyst, and if the best available samples are considered, then Au is apparently significantly more active than Pt. Selection between both catalysts is, however difficult, because most available data are presented for very specific experimental conditions, not only in what concerns catalyst preparation and pre-treatment, but also with respect to the operating conditions used in activity tests.

For many years, Au was mainly regarded as a commodity and as a precious substance. Its catalytic behavior was not really recognized due to its poor chemisorption ability toward reactant molecules, such as O_2 and H_2, compared with Pt group metals (PGM), for example. However, due to the work of Haruta and coworkers, there has been renewed interest in using Au as catalyst. These authors observed a high catalytic activity for the CO oxidation reaction using catalysts containing Au particles smaller than 5 nm, deposited on a selected metal oxide (e.g. TiO_2, α-Fe_2O_3 and Co_3O_4) (Haruta, 2002; Haruta et al., 1993; Haruta et al., 1989). The size of the Au particles is, indeed, essential to obtain an active catalyst because at small sizes the metallic character of Au is reduced, the mobility of surface atoms on small particles is accelerated and more atoms come into contact with the support (Bond and Thompson, 1999). The major factor determining the catalytic performance and selectivity is the contact of Au with the support. The preparation method and pre-treatment of oxide-supported Au catalysts are extremely important in order to obtain a high dispersion of small Au particles

and strong interaction with the support. These issues have been widely reported to affect the activity of Au reducible oxide systems (Andreeva et al., 1998; Tabakova et al., 2004).

Several authors report the predominant oxidation state and the nature of active Au catalysts as being the zero-valent metallic state (Burch, 2006; Haruta et al., 1989; Tabakova et al., 2006a). However, evidence exists that under WGS conditions the active form of Au is a nano-sized metallic Au cluster in intimate contact with the surface vacancies of the oxide support (Boccuzzi et al., 1999; Chen and Goodman, 2004; Tabakova et al., 2003). The reducible oxygen vacancies existent in the metal oxides are useful for interacting and anchoring Au atoms, changing the electronic structure by partial electron donation to the Au cluster (Campbell, 2004; Fu et al., 2003). Therefore, very active reaction sites are reported to be formed at the perimeter of the metal-support interface. Moreover, different supports induce Au particles with shapes having a varying amount of edge, corner, or step surface defects. This fact favors the increase of the perimeter interfaces around Au particles and reducible-oxide surfaces, described as special sites for catalyzing the reaction (Mavrikakis et al., 2000). High catalytic activity for the WGS reaction using Au-based catalysts operating at LT was reported for the first time using nano-sized Au/Fe_2O_3 (Andreeva et al., 1996a; Andreeva et al., 1996b). In 1997, Sakuray et al. (Sakurai et al., 1997) reported the use of Au/TiO_2 catalyst for both forward and reverse WGS reactions presenting high activities, comparable to the conventional commercial catalyst $CuO/ZnO/Al_2O_3$. Since then, many authors have been reporting studies over highly dispersed Au on different metal oxide supports, e.g. Al_2O_3 (Andreeva et al., 1996a), ThO_2 (Tabakova et al., 2006b), ZrO_2 (Idakiev et al., 2006), CeO_2 (Andreeva et al., 2002; Mendes et al., 2009; Yuan et al., 2008), TiO_2 (Chen and Goodman, 2004; Idakiev et al., 2004; Mendes et al., 2009), mixed oxides of CeO_2-TiO_2 (Idakiev et al., 2007), Fe_2O_3-ZnO and Fe_2O_3-ZrO_2 (Tabakova et al., 2000), as well as over supports of a different crystalline state (Tabakova et al., 2000).

Among the oxide supports, ceria has been the subject of increased attention due to their better apparent specific interaction with Au. Ceria found enormous application as an oxygen storage component in automobile three-way catalysts, releasing/accepting oxygen in the exhaust stream of a combustion engine. Therefore, when associated with other catalysts, ceria can effectively convert harmful carbon monoxide to less harmful carbon dioxide. Not only because of the high oxygen storage capacity and reducibility, ceria has found innumerous other applications due to its high thermal stability, electric conductivity, good diffusivity, and optical properties (Trovarelli, 1996). Au-supported ceria has also been reported as a very good catalyst system for CO oxidation (Deng et al., 2005; Panzera et al., 2004), alcohol oxidation (Abad et al., 2008), and NO_x reduction (Ilieva et al., 2006). For the practical application of ceria catalyst it should be nanocrystalline, with high surface area and demonstrable thermal stability (Trovarelli, 1996).

Among other techniques, temperature-programmed reduction (TPR) has been widely used to characterize the reducibility of ceria-based materials. In Figure 2.4, the existence of two peaks centered at 473 ºC and 756 ºC for ceria is evident, showing the reduction of the surface capping oxygen and of the bulk oxygen. The oxygen storage capacity and reducibility is greatly enhanced by the addition of noble or transition metals, favoring the generation of very active sites at the border between the metal and the support (Bunluesin et al., 1998; Hilaire et al., 2001). An example is shown in Figure 2.4, for nano-sized Au deposited on ceria support. The peak corresponding to the reduction of surface oxygen on CeO_2 is shifted to a much lower temperature (95 ºC), although the reduction of the bulk oxygen remains almost unaffected. This behavior is similar to the case of PGM supported on ceria (Trovarelli, 1996). The peak on the TPR profile at 63 ºC for Au/CeO_2 (cf. Figure 2.4) is most probably related to the reduction of oxygen species on some nano-Au particles smaller than 2 nm absorbed during calcination in air in accordance with Boccuzzi et al. (Boccuzzi et al., 2001).

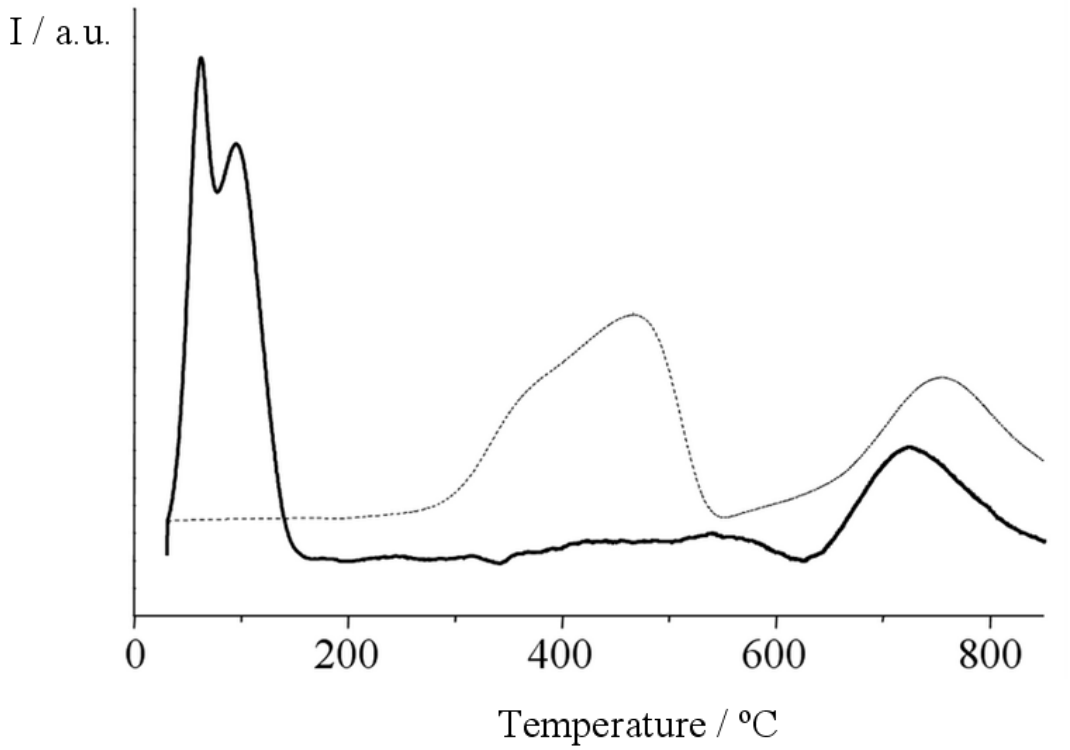

Figure 2.4 – Typical thermoprogrammed reduction by hydrogen gas of CeO_2 (dotted line) and Au/CeO_2 (continuous line) samples.

Even though the high catalytic activity associated with Au-ceria catalysts is well recognized, a major problem hindering their commercialization is related to their stability under WGS reaction conditions. Generally, the following explanations are used to describe the reason(s) for catalyst deactivation: (1) sintering of the metal particles (Luengnaruemitchai et al., 2003), (2) "irreversible" over-reduction of the ceria support (Zalc et al., 2002), (3) loss of ceria surface area (Fu et al., 2005) and (4) blocking of the ceria surface by formation of surface carbonates and/or formates (Deng and Flytzani-Stephanopoulos, 2006; Karpenko et al., 2007; Kim and Thompson, 2005). However, a totally coherent explanation is still not available due to the wide variety of catalyst morphologies and surface compositions. Moreover, a correlation between the change in surface properties of the catalyst and the decay in catalytic activity during the WGS reaction is needed (Karpenko et al., 2007), despite the existing studies that address this issue.

In the work by Fu et al. (Fu et al., 2005), the stability of a Au/La_2O_3 doped CeO_2 catalyst, prepared by different methods, was tested for the WGS reaction. During 120 h at 300 ºC and with a typical reformate feed, no significant deactivation was detected for the sample synthesized by the deposition-precipitation method, although the Au and ceria crystallite size and total surface area slightly changed. Long term experiments at 250 ºC revealed a higher decay rate in activity during CO conversion, explained by surface area loss of ceria and the inherently weak Au/ceria interaction when exposed to the WGS reaction mixture. Karpenko and co-authors (Karpenko et al., 2007) justified the deactivation behavior at 180 ºC as being due to the formation of carbonate reaction intermediate absorbed on the ceria support, blocking the active sites. Therefore, the rate of carbonate decomposition rate is too low at such a low temperature to keep the steady-state carbonate coverage at a low enough level, leading to catalyst deactivation. The authors confirmed the carbonate formation by obtaining complete catalyst activity regeneration with an oxidation treatment. Contrary to the work of Fu et al. (Fu et al., 2005), no sintering of ceria particles was detected during the WGS reaction. Nevertheless, it must be noted that this study was performed at a lower temperature. At an intermediate temperature (240 ºC), Kim and Thomson (Kim and Thompson, 2005) observed a fast and considerable (~ 50 %) loss of activity during 12 hours on-stream, attributed to the formation of carbonates and/or formates on the catalyst surface. Another interesting observation made by these authors is the rate of deactivation of the catalyst caused by an increase in the gas hourly space velocity (GHSV). This deactivation might be related to the increasing concentration of intermediate species in the reactor because of the smaller contact time. Along this line, Mendes et al. (Mendes et al., 2009) studied the influence of Au content on the rate of deactivation decay. In spite of the initial higher activity of the Au (2.5 wt.%)/CeO_2 catalyst, after almost 20 h of operation this sample presented a lower performance than another one with a smaller Au content (1.5 wt.%). Even though it is difficult to establish which of the above-mentioned deactivation mechanisms

predominates at particular reaction conditions, it is possible to infer that the observed decay in the rate of CO conversion is strongly dependent on temperature (Karpenko et al., 2007; Mendes et al., 2009). However, it seems reasonable to assume that higher reaction temperatures promote carbonate and/or formate decomposition (decreasing the fouling deactivation); nevertheless, particle sintering effects are more favorable to exist under these conditions.

Pt-based catalysts

The same deactivation pathways described previously for Au-based catalysts have also been observed for Pt/CeO_2 catalysts under synthetic and real reformate conditions. Indeed, Jacobs et al. (Jacobs et al., 2003) concluded that formates are reaction intermediate species and that at higher temperatures their concentration is limited by the WGS reaction rate, while formate surface concentration remains close to the adsorption/desorption equilibrium at lower temperatures. Platinum group metals (PGM) formulations have been developed by Johnson-Matthey in order to overcome the performance limitations of traditional Pt/CeO_2 catalysts, namely trying to achieve higher catalytic activity, durability and absence of methanation activity over a large range of temperatures ($200-500\ ^{o}C$). In Figure 2.5, the performance of several new Pt-based catalysts coated on monolithic supports is presented. Subsequent experiments revealed no activity decay for more than 800 h over a wide range of temperatures and at high space velocities (Ghenciu, 2003). PGM catalysts were used in a Johnson-Matthey fuel processor for stationary applications at a $2-10\ kW$ load (electric), allowing conduction of the WGS reaction in a single stage. Besides a higher CO conversion, as reported in Figure 2.5, a significant reduction in reactor volume was possible compared to using a traditional Cu-based catalyst (Ghenciu, 2003).

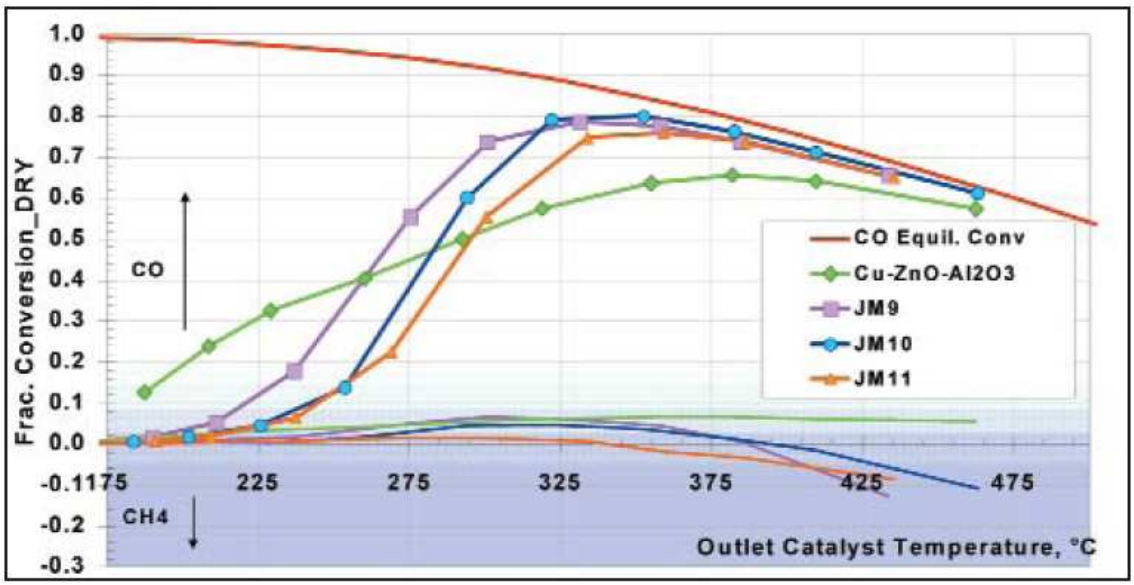

Figure 2.5 – Performance of Johnson-Matthey PGM WGS catalysts at high space velocity vs. $Cu/ZnO/Al_2O_3$ sample. Synthetic reformate containing 11.4 % CO and 1.4 % CH_4 (mol dry gas). Weight hourly space velocity (WHSV) = $202500\ cm^3 \cdot g_{cat}^{-1} \cdot h^{-1}$ (Ghenciu, 2003).

2.2.3 Selection of WGS catalysts for membrane reactor applications

It is known that the WGS reaction products (CO_2 + H_2) inhibit the reaction and lower the reaction rate over WGS catalysts. This inhibition is dependent on the nature of the catalyst and temperature range and, therefore, the reaction is clearly more effective in membrane reactors (MRs). Depending on the properties of the membrane there are two possible outcomes. In the case of a CO_2-selective membrane, the concentration of H_2 along the catalyst bed will attain high levels. As referred to above, an excess of H_2 is negative for a traditional Fe-based catalyst due to over-reduction of the magnetite active phase. The other case is the use of an H_2-selective membrane, so CO_2 will be present at a higher concentration in the reaction medium, affecting the reaction rate. Therefore, a new challenge is presented in making highly effective conventional HT catalysts used in traditional WGS processes, suitable for MR applications. Generally, for large stationary fuel processing plants, Lund et al. (Lund, 2002) proposed that weakening the surface oxygen bond strength would lead to higher catalytic activity as well as to a reduction of the inhibition by CO_2. Experimental

evidence showed that the Cu-promoted Fe-Cr HT shift catalyst is less resistant to rate inhibition by high levels of CO_2 than the Cu-ceria one. On the other hand, Qi and Flytzani-Stephanopoulos (Qi and Flytzani-Stephanopoulos, 2004) identified Cu-Ce(La-doped)O_x catalyst as the best composition for MR applications in the temperature range $300-600$ ºC using simulated coal gas. The WGS reaction was also conducted with artificially high CO_2 concentrations at 450 ºC, showing stability during 10 h of operation.

Generally, Cu-ceria catalysts are very promising to conduct the WGS reaction, requiring no activation and possessing high catalytic activity at high space velocities, selectivity (no methanation until at least 600 ºC), thermal stability; interestingly some compositions are non-pyrophoric (Kusar et al., 2006). However, these properties are very dependent on the synthesis method and mixed oxide compositions, which influence the chemical and electronic interactions between both oxides (Zheng et al., 2007). Other promising catalysts for WGS MR applications are the Pt-based catalysts, which generally reveal a lower inhibition effect by the forward WGS reaction products over a wide temperature range, i.e. relatively low partial orders with respect to both CO_2 and H_2, as discussed below (cf. Table 2.2).

Even though there is not much data available in the literature for Au-based catalysts catalyzing the WGS reaction using a real reformate feed composition, they are very promising when compared to the traditional Cu-based catalysts because their performance is less affected by the presence of reaction products (although they exhibit higher inhibition by CO_2 and H_2 than Pt-based catalysts (see Table 2.2)). Compared with the research focused on Pt-based catalysts, the science of Au catalysis is still quite new and major developments are expected in the near future (Cameron et al., 2003).

Table 2.2 – Comparison of apparent activation energies and reaction orders for the forward reaction over different WGS catalysts.

Catalyst	Operating conditions *	Ea ($kJ \cdot mol^{-1}$)	Reaction Orders **				Reference
			CO	H_2O	CO_2	H_2	
40 wt.% $Cu/ZnO/Al_2O_3$	1 bar, 190 ºC	79	0.8 (5 – 25 %)	0.8 (10 – 46 %)	-0.9 (5 – 30 %)	-0.9 (25 – 60 %)	(Koryabkina et al., 2003)
8 % Cu/Al_2O_3	1 bar, 200 ºC	62	0.9 (5 – 25 %)	0.8 (10 – 46 %)	-0.7 (5 – 30 %)	-0.8 (25 – 60 %)	
8 % Cu/CeO_2	1 bar, 240 ºC	56	0.9 (5 – 25 %)	0.4 (10 – 46 %)	-0.6 (5 – 30 %)	-0.6 (25 – 60 %)	
10 atom% $Cu/Ce(30\ atom\%\ La)O_x$	1 bar, 450 ºC	70.4	0.8 (1 – 10 %)	0.2 (11 – 50 %)	-0.3 (5 – 35 %)	-0.3 (5 – 40 %)	(Qi and Flytzani-Stephanopoulos, 2004)
Fe_2O_3/Cr_2O_3	1 bar, 450 ºC	118	1 (20 – 75 %)	0 (10 – 40 %)	–	–	(Rhodes and Hutchings, 2003)
Pd/CeO_2	1 atm, 200 – 240 ºC	38	0	0.5	-0.5	-1	(Hilaire et al., 2001)
1 % Pt/Al_2O_3	1 atm, 285 ºC	68	0.06 (5 – 25 %)	1.0 (10 – 46 %)	-0.09 (5 – 30 %)	-0.44 (25 – 60 %)	
1 % Pt/Al_2O_3	1 atm, 315 ºC	84	0.1 (5 – 25 %)	1.1 (10 – 46 %)	-0.07 (5 – 30 %)	-0.44 (25 – 60 %)	(Phatak et al., 2007)
1 % Pt/CeO_2	1 atm, 200 ºC	75	-0.03 (5 – 25 %)	0.44 (10 – 46 %)	-0.09 (5 – 30 %)	-0.38 (25 – 60 %)	

1.4 %Pt-8.3 % CeO_2/Al_2O_3	1 bar, 200 – 260 ºC	86	0.13	0.49	-0.12	-0.45	(Germani and Schuurman, 2006)
2 % Pt /CeO_2-ZrO_2	1.3 bar, 200 – 240 ºC	71	0.07	0.67	-0.16	-0.57	(Radhakrishnan et al., 2006)
2 % Pt-1 % Re/CeO_2-ZrO_2	1.3 bar, 210 – 240 ºC	71	-0.05	0.85	-0.05	-0.32	
2 wt.% Au/$CeZrO_4$	170 ºC	-	0.7	0.6	-0.3	-0.9	(Burch, 2006)
4.5 wt.% Au/CeO_2	1 bar, 180 ºC	-	1	1	-0.5	-0.7	(Denkwitz et al., 2007)
2.6 wt.% Au/CeO_2 ***	1 bar, 180 ºC	40	0.5 (0.2 – 2 kPa)	0.5 (0.7 – 10 kPa)	-0.5 (1.2 – 3.4 kPa)	-0.5 (3.2 – 75 kPa)	(Leppelt et al., 2006)

* – Total pressure and temperature at which the reaction order measurements were carried out.

** – Values between brackets represent the ranges of concentrations for each species in the feed, or their partial pressures.

*** – Partial orders for water and carbon monoxide were obtained without reaction products in the feed.

2.2.4. Mechanisms and kinetics

Although the WGS reaction involves only four species, there is still no full agreement in the literature concerning the reaction mechanism. In this section, an overview will be given of the reaction kinetics, which is crucial for reactor/membrane reactor modeling and design, and the most accepted reaction mechanisms are then presented.

The WGS reaction rate equations are generally written as follows (Qi and Flytzani-Stephanopoulos, 2004):

$$r = R_f (1-\beta) \tag{1.4}$$

$$R_f = R_f^0 \exp\left(-\frac{E_a}{\Re T}\right) \tag{1.5}$$

$$\beta = \frac{p_{CO_2}\, p_{H_2}}{K_{eq}\, p_{CO}\, p_{H_2O}} \tag{1.6}$$

where r is the experimental reaction rate, β is the approach to equilibrium, R_f is the forward reaction rate, K_{eq} is the WGS reaction equilibrium constant, p_i is the partial pressure for component *i*, E_a is the apparent activation energy, $\Re$ is the gas constant, and T is the absolute temperature.

Comparison of activation energies reported in literature is generally difficult since most studies omit the inhibitory effects from H_2 and CO_2, or are performed at very specific conditions that vary substantially from study to study. Some literature values of kinetic parameters are reported in Table 2.2 for the most relevant catalysts. In particular, Table 2.2 presents results for two catalysts operated at 450 °C and one at 315 °C whose kinetic data can be compared; even without the presence of CO_2 and H_2 in the feed stream, higher apparent activation energy was observed for the Fe-based catalyst (Fe_2O_3/Cr_2O_3) when compared with the 10 atom.% Cu/Ce(30 atom.% La)O_x and Pt/Al_2O_3 catalysts. It is possible that the reaction mechanism or the rate-determining step for that catalyst is distinct from the

other catalysts (see below). Concerning the effect of the support, the difference between the ceria-based and alumina-based catalysts (with lower apparent activation energy for the ceria-based) might be the result of modification of the ceria surface by the addition of Cu. This addition increases the reducibility of the surface oxygen in the ceria support.

Over the lower range of temperatures, the Au/CeO_2 catalyst reported by Lepplet et al. (Leppelt et al., 2006) presents one of the lowest apparent activation energies. Although the tests were conducted using an idealized reformate feed, this system is considered to be very promising to conduct the WGS reaction, at least in the LT range.

Typically, the reaction rate data are fitted to a power-law equation of the form:

$$r = k_f \, p_{CO}^{a} \, p_{H_2O}^{b} \, p_{CO_2}^{c} \, p_{H_2}^{d} \left(1-\beta\right) \tag{1.7}$$

where k_f is the forward reaction rate constant; *a-d* are the forward reaction orders. From Table 2.2, it is important to note that the apparent reaction orders and activation energy values on Pt samples are very similar, with the exception of the apparent reaction order for water. The apparent forward reaction order for H_2O is close to 1 for most of the alumina-supported Pt-based catalysts and close to 0.5 for the ceria-supported catalysts. Considering these two materials, Al_2O_3 supports are revealed to be less promising in terms of their capacity for H_2O activation. Indeed, in all cases, the difference in H_2O reaction order on alumina- and ceria-supported catalysts suggests that different reaction mechanisms and/or distinct sites for H_2O activation may exist in these materials.

To the best of author's knowledge, only one work describes the measurement of WGS reaction orders on Au-ceria catalyst with a realistic reformate feed, a 4.5 wt.% Au/CeO_2 catalyst – Table 2.2 (Denkwitz et al., 2007). Compared to runs performed with the 2.6 wt.% Au/CeO_2 catalyst in which an idealized reformate (only CO and H_2O in N_2) was used (Leppelt et al., 2006), a higher apparent reaction order for H_2O was obtained. This can be explained by water dissociation on the catalyst surface, where OH groups react with

hydrogen to produce water (reverse reaction). Therefore, the WGS reaction is sensitive towards the partial pressure of water in the feed. Also, competitive adsorption between H_2O and H_2 on the same adsorption sites is considered (Denkwitz et al., 2007).

Concerning CO, the apparent reaction order of the forward reaction for all Pt-based catalysts changes from slightly positive (Pt/Al_2O_3) to slightly negative (Pt/CeO_2 or $Pt\text{-}Re/CeO_2\text{-}ZrO_2$). As suggested by Phatak et al. (Phatak et al., 2007), the nearly zero order with respect to CO can be explained by the decrease in CO binding strength as surface coverage increases. In other words, due to the strong adsorption of CO over the Pt surface, CO coverage is close to saturation so that further increase in CO partial pressure has no effect or reduces the reaction rate slightly by surface blocking, even at high pressures or low temperatures. On the other hand, CO adsorption on Au nanoparticles is very weak, resulting in a low CO coverage over the surface. Therefore, an increase in CO partial pressure favors CO concentration at the metal surface, enhancing the reaction rate; this is corroborated by the high reaction order for $Au/CeZrO_4$ and Au/CeO_2 catalysts – Table 2.2. For a realistic reformate feed, a higher apparent reaction order for CO is expected due to the co-adsorption of hydrogen on Au (Bus et al., 2005).

For Pt catalysts, the forward reaction order with respect to CO_2 is slightly negative and close to zero, which can be explained by the weak interaction of CO_2 with Pt. A more significant inhibition effect by CO_2 over Au-based catalysts is observed. This can be explained by the blocking of ceria surface sites and/or increase of the reverse WGS reaction by a higher amount of carbonate species adsorbed on the active sites.

The high adsorption capacity of H_2 on Pt results in the observed inhibition of the WGS reaction (partial orders in the range of -0.32 to -0.57). In fact, Phatak et al. (Phatak et al., 2007) suggested that after CO attains its saturation coverage, the available free Pt sites required for the activation of water might be occupied by atomic hydrogen, inhibiting the forward reaction rate. For Au-based catalysts the same analysis is valid.

Generally, a clear difference is noticeable in the reaction orders obtained for Cu-based, Au-based and Pt-based catalysts under the same reaction conditions. Even though Cu-based and Au-based catalysts have similar reaction order values, the spread of values for Pt-based catalysts suggest that the reaction mechanism or rate determining steps on this material is distinct from the other types.

Among numerous studies, two main distinct reaction mechanisms for the WGS reaction have been proposed. A regenerative (oxidation-reduction cycle) mechanism of Rideal-Eley type, first proposed by Kulkova and Temkin in 1949, as mentioned by Newsome (Newsome, 1980), describes the dissociation of water on the catalyst surface producing H_2 and the inherent oxidation of the vacant site (*). To complete the catalytic cycle, a CO molecule promotes the reduction of an oxidized site (O), yielding CO_2 (Ruettinger and Ilinich, 2006), as described by the following reaction scheme:

$$H_2O + (*) \leftrightarrow H_2 + (O) \tag{1.8}$$

$$CO + (O) \leftrightarrow CO_2 + (*) \tag{1.9}$$

One of the earliest kinetic expressions for the WGS reaction over Fe-based catalysts was then proposed, assuming equation 1.9 as the rate-controlling step:

$$r = k^{+} p_{CO} \left(\frac{p_{H_2O}}{p_{H_2}} \right)^{\frac{1}{2}} - k^{-} p_{CO_2} \left(\frac{p_{H_2}}{p_{H_2O}} \right)^{\frac{1}{2}} \tag{1.10}$$

where k^{+} and k^{-} are rate constants for the forward and reverse reactions, respectively, and p_i is the partial pressure of a given reaction species. Since 1949, numerous equations have been proposed by different authors, as can be seen in the work by Newsome, dated from 1980 (Newsome, 1980).

The other mechanism normally considered is the associative mechanism of the Langmuir-Hinshelwood (LH) type, which involves the dissociative adsorption of water to form reactive hydroxyl groups that when combined with adsorbed CO produces a surface intermediate structure (formate and/or carbonate) that subsequently decomposes into CO_2

and H_2 (Ladebeck and Wang, 2003) [cf. equations 1.11-1.16]. Infrared spectroscopy has been used by many authors to validate this associative mechanism, namely for observing the presence of characteristic bound vibrations of formate or carbonate-like species (reaction intermediates). However, some precautions in analyzing these data should been taken, as mentioned by Rhodes et al. (Rhodes et al., 1995).

$$H_2O + 2(*) \leftrightarrow H^* + OH^* \quad (1.11)$$

$$CO + (*) \leftrightarrow CO^* \quad (1.12)$$

$$OH^* + CO^* \leftrightarrow HCOO^* + (*) \quad (1.13)$$

$$HCOO^* + (*) \leftrightarrow CO_2(*) + H(*) \quad (1.14)$$

$$CO_2^* \leftrightarrow CO_2 + (*) \quad (1.15)$$

$$2H^* \leftrightarrow H_2 + 2(*) \quad (1.16)$$

Recently, Ayastuy et al. (Ayastuy et al., 2005) derived the kinetic expression for the WGS reaction over a commercial Cu-based catalyst in the LT range. The authors proposed a mechanism of LH type, which describes their experimental results fairly well, with a surface reaction between molecularly adsorbed reactants to give a formate intermediate and atomically adsorbed hydrogen as the rate-determining step. This mechanism yielded the following rate equation:

$$r = \frac{k_f \left(p_{CO} p_{H_2O} - \frac{p_{CO_2} p_{H_2}}{K_{eq}} \right)}{\left(1 + K_{CO} p_{CO} + K_{H_2O} p_{H_2O} + K_{H_2}^{0.5} p_{H_2}^{0.5} + K_{CO_2} p_{CO_2} p_{H_2}^{0.5} \right)} \quad (1.17)$$

where K_i is the equilibrium adsorption constant of species *i*.

Diagne et al. (Diagne et al., 1990) studied the WGS reaction mechanism, between $250-400\ ^{o}C$, over a commercial Fe oxide catalyst. They found that as the temperature increased, there was a decrease in the formate coverage. Moreover, they suggested that at the upper temperature limit there is the possibility of a transition state from the associative (LH) to the regenerative mechanism. The dissociation of water on the catalyst surface is the key

difference between both mechanisms. In the redox mechanism, reoxidation of the vacant site by the oxygen species dissociated from the water molecule must occur so that the WGS reaction proceeds. In fact, the discussion around the predominant mechanism in Fe-based catalysts seems to be less controversial, where the regenerative (redox) mechanism is generally accepted (Kochloefel, 1997; Lloyd et al., 1989; Rhodes et al., 1995). It is possible that the WGS reaction mechanism over magnetite differs from that over other metallic catalysts because during the reaction Fe is not reduced to the metallic state, in contrast to what happens with other metals (e.g. Cu, Au, Pt, and Pd). Nevertheless, an interesting point referred to by Rhodes et al. (Rhodes et al., 1995), Grenoble et al. (Grenoble et al., 1981), and Hutchings et al. (Hutchings et al., 1992) is that although cobalt-based catalysts are stable oxides during the reaction, as Fe-based ones, the predominant attributed mechanism seems to be the associative one (LH). Rhodes et al. (Rhodes et al., 1995) suggested that oxidation of divalent to trivalent cobalt by hydroxyl groups from dissociated water is difficult when compared to divalent Fe.

The question of the dominant reaction mechanism in the LT WGS reaction over Cu-based catalysts has provoked more discussion than the Fe-based system for the HT reaction. Even though literature seems to support both theories, the formate-based mechanism has fewer controversial aspects than the redox one. For Cu-based catalysts, re-oxidation occurs (Rhodes et al., 1995) but at a lower rate than observed, clearly supporting that redox is not the predominant mechanism over such materials (Campbell and Daube, 1987).

Grenoble et al. (Grenoble et al., 1981) proposed a bifunctional associative mechanism to describe the WGS reaction pathway over Cu/Al_2O_3 catalysts. The major difference between this mechanism and the conventional one is that instead of both reagents being activated on the same site, hydroxyl groups are produced due to water adsorption on the catalyst support, while carbon monoxide is adsorbed on metal vacancy sites. To validate the predominance of

the associative mechanism, the decomposition of the formate intermediate into CO_2 and H_2 should be detected. Even though the exact nature of the intermediate species remains unclear, experiments conducted with the probe species formic acid have been used successfully to support the generation of formate group intermediates (Grenoble et al., 1981; Rhodes et al., 1995).

Rodriguez et al. (Rodriguez et al., 2007) analyzed the Cu (100) surface after the WGS reaction, in the temperature range of around $300-380\ ^{o}C$. Their measurements revealed a surface predominantly free of formate or carbonate species and therefore a predominance of the redox mechanism. However, XPS (X-ray photoelectron spectroscopy) analysis over the metal/oxide surfaces of a Cu/ZnO catalyst after the WGS reaction gave typical peaks of adsorbed formate or carbonate species, opening up the possibility of an associative mechanism or simply spectator species bounded to the oxide.

Between the two reactant species, water is more difficult to activate on Pt or Au metal surfaces because of its thermodynamic stability and high activation energy (Henderson, 2002; Liu and Rodriguez, 2007). Therefore, a hydrophilic oxide support is needed to adsorb and activate water. As suggested by Grenoble et al. (Grenoble et al., 1981) for Cu/Al_2O_3 catalyst, Pt- and Au-based supported catalysts are denoted bifunctional catalytic systems too, where the metal activates the CO and the support the H_2O. However, it is also still unclear for these systems which is the predominant reaction mechanism. Bunluesin et al. (Bunluesin et al., 1998), for example, proposed a redox reaction mechanism in which the CO molecule adsorbed on the metal (Pt, Pd, Rh) reacts with oxygen, which is supplied by the metal-ceria interface; water dissociation takes place on an oxygen vacancy site of ceria to form hydrogen and atomic oxygen that reoxidize the ceria support. In contrast, Shido and Iwasawa (Shido and Iwasawa, 1993), Tabakova et al. (Tabakova et al., 2003), Jacobs et al. (Jacobs et al., 2003), and Azam et al. (Azzam et al., 2007), among other authors, observed the formation of intermediate species produced by the reaction of CO with the terminal hydroxyl groups of

ceria. The decomposition of intermediate species is suggested to be facilitated by the presence of water (oxidant) in the gas phase and is rate determining.

Generally, the discrepancy in conclusions about the rate-controlling mechanism in the LT WGS reaction is attributed to differences in the experimental conditions used. Jacobs et al. (Jacobs et al., 2005; Jacobs et al., 2003) suggested that temperature and gas composition might be relevant to the predominant reaction pathway. However, the catalyst structure, e.g. catalyst composition, nature of catalyst support, size distribution of metal crystallites, and catalyst preparation procedure, also seem to be of reasonable influence on the reaction mechanism to occur by either associative or redox mechanisms.

2.2.5 Hydrogen purification

As mentioned above, since the economic boom of the 1990s, the inherently increased energy demand coupled with growing concerns about environmental issues led to renewed emphasis on the so-called hydrogen economy (Bockris, 2002). Fuel cell technology is presently viewed as a key to the implementation. They are unique since they convert chemical energy directly into electric energy at moderate temperatures and can also work as stored energy in batteries (Steele and Heinzel, 2001). Besides, they offer several other advantages such as high efficiency compared to traditional internal combustion systems, low pollutant emissions, high energy density, quiet operation and easy monitoring. When hydrogen from reformed fuel is used in downstream catalytic processes (PEMFC), the final CO concentration is well above the allowable levels (CO concentration ≤ 0.2 ppm for on-board vehicle applications (ISO, 2008)) due to the equilibrium-limited shift reaction. However, methanation and preferential oxidation (PROX) can be used to remove CO (cf. Figure 2.6, where two process plants used for on-site H_2 generation are shown). Also, most of the refineries worldwide are being forced to decrease the sulfur content of their products (e.g. gasoline and diesel fuels) due to new environmental legislation. Therefore,

improvements on the hydrodesulfurization (HDS) units are required where additional hydrogen is used (Figure 2.6). As referred previously, the main industrial process used to produce H_2 is steam methane reforming (SMR), using off-gas and natural gas; in any case, hydrogen needs to be purified after being processed to meet the required grades.

A) Traditional process

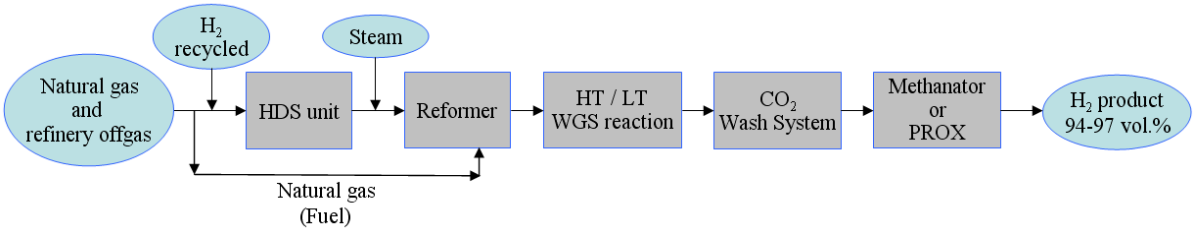

B) PSA-based process

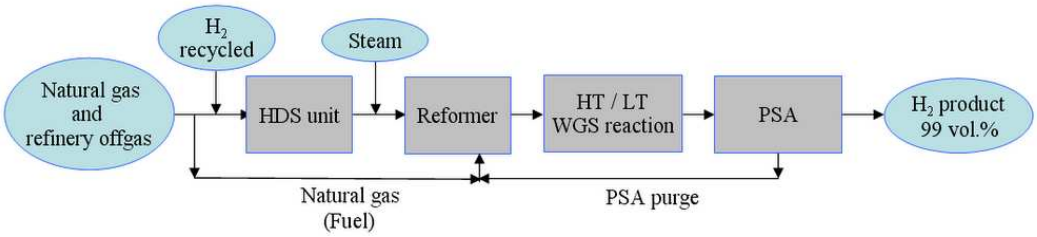

Figure 2.6 – Hydrogen production and purification process schemes; a) traditional process using an absorption and catalytic approach for hydrogen purification b) PSA-based hydrogen purification.

Hydrogen can be purified using several different processes, such as pressure swing adsorption (PSA), cryogenic distillation (CD), or membrane separation. However, in many existing hydrogen plants, the conventional process, as shown in Figure 2.6-A is used, producing a stream of medium-purity (94 – 97 %) hydrogen. The conventional process accomplishes carbon dioxide removal by absorption followed by methanation or oxidation of remaining carbon oxides (in addition to the WGS reaction). Since the 1980s, most hydrogen plants use PSA technology to recover and purify hydrogen to levels above 99.9 % (cf. Figure 2.6) (Stöcker et al., 1998). PSA-based hydrogen plants have many technical advantages compared to traditional SMR technology:

- The reformer can be operated at higher pressures/temperatures (despite the increase on the manufacture cost of the reformer reactor);
- Lower steam to carbon ratios are used;
- No LT shift unit is necessary;
- Higher H_2 purity is obtained;
- No methane is present in the H_2 stream;
- Less complex operation as a result of the reduced number of unit operations in series.

A commercial PSA unit typically consists of a multi-column system formed by $4-12$ adsorbent beds. More beds are used to provide higher hydrogen recovery and/or higher capacity (Miller and Stöcker, 1999). Alternatively, one may consider the use of a membrane separation process. Actually, membrane-based processes are considered to be the most promising technologies for the production of high-purity hydrogen (Cheng et al., 2002). The membrane separation process is based on the selective permeation of hydrogen through the membrane. Table 2.3 summarizes the comparative characteristics and performance of three technologies for purifying hydrogen: PSA, CD and membrane separation.

Table 2.3 – Comparison of hydrogen purification technologies.

Characteristic	**PSA**	**CD**	**Membranes** [a]
H_2 purity / vol.%	≥ 99.9	$95-99$	< 95
H_2 recovery / vol.%	$75-90$	$90-98$	< 90
H_2 product pressure	Feed Pressure	Variable	<< Feed pressure
By-products available	No	Yes	No
Feed Pressure / bar	$10-50$	$15-35$	$15-125$
Capital Cost	High	Very High	Low
Energy Consumption	Intensive	Very Intensive	Low
Flexibility to expansion	Very Good	Good	Limited
Reliability	High	Moderate	High

[a] – Values based on the systems typically used in refineries (Patel et al., 2005).

The combination of low cost and long-lasting hydrogen separation membranes and the WGS reaction (cf. Figure 2.7) has been the focus of attention of several R&D programs.

Membranes and a WGS reactor can be combined in a MR unit with synergistic benefits. For equilibrium-limited reactions, the continuous removal of a product from the reaction medium shifts the reaction toward the formation of products, thereby giving a higher conversion. Depending on the type of membrane, either hydrogen or carbon dioxide can be selectively removed in principle, having both strategic advantages and disadvantages.

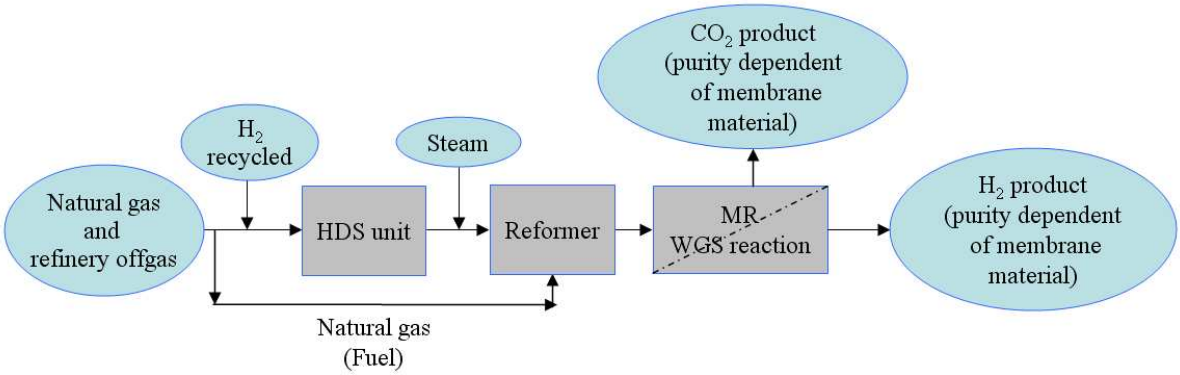

Figure 2.7 – Hydrogen production and purification based on the WGS MR unit.

2.3 Membrane Reactors

In the last three decades or so, an intense worldwide effort on membrane catalysis has been carried out, which is summarized in several review articles (Armor, 1998; Lin, 2001; Lu et al., 2007; Marcano and Tsotsis, 2002; McLeary et al., 2006; Saracco and Specchia, 1994; Shu et al., 1991). A brief history on MRs is reported elsewhere (Basile et al., 2008d). According to the International Union of Pure and Applied Chemistry (IUPAC) definition (Koros et al., 1996), a MR is a device for simultaneously carrying out a reaction (SR, dry reforming, ATR, etc.) and membrane-based separation in the same physical device. Therefore, the membrane not only plays the role of a separator but also might take part in the reaction itself. For example, a MR is an engineering apparatus that selectively removes a product from or introduces a reactant into the reaction system, giving the possibility of better performance than a traditional reactor (TR). For example, this improvement in performance

due to the membrane effect could be achieved, for example, by shifting the conversion of an equilibrium-limited reaction toward the reaction products by selectively removing a reaction product from the reaction side to the permeate side. Some of the significant advantages of using MRs with respect to TRs can be summarized as follows:

- Conversion enhancement of equilibrium-limited reactions;
- Enhancement of the hydrogen yield and hydrogen selectivity (in the field of MRs used for hydrogen production);
- Achievement of the same performance attained in the TR at milder operating conditions or, instead, achievement of better performance at the same operating conditions as in the TR;
- Reduced capital costs due to the combination of reaction and separation in only one system.

The membranes can be classified into organic, inorganic, and organic/inorganic hybrids. In particular, inorganic membranes can be subdivided into two classes:

1. Dense metallic membranes (pure metal or metal alloys);

2. Porous membranes.

In this chapter, the first type will be particularly addressed.

The choice of membrane type to be used in MRs depends on parameters such as the productivity, separation selectivity, membrane life time, mechanical and chemical integrity at the operating conditions and, particularly, the cost. Generally, inorganic membranes offer several advantages over organic ones, due to their stability and good chemical and mechanical resistance in processes operating at temperatures above 100 °C. Most of the progress in the areas of membrane separation and MRs has been mainly related to the development of new membrane materials that are able to resist HTs and with good mechanical strength, for example. This significant progress is reflected in an increasing number of scientific publications, which have grown exponentially over the last few years, as recently shown by McLeary et al. (McLeary et al., 2006). The synthesis of stable microporous or dense inorganic membrane materials is probably the key factor for increasing

the application of MRs in the catalysis field. A list of several types of reactions that can be carried out in inorganic MRs was presented by Drioli et al. (Drioli et al., 2000). The authors pointed out the advantages of using MRs in reactions for which a low thermodynamic equilibrium conversion imposes a limit on the conversion for the traditional systems. In these cases, higher conversions can be achieved by using a MR working at the same operating conditions. In fact, thermodynamics is a rigid limit for TRs, which may be overcome using innovative systems such as MRs. On the other hand, MRs are well integrated in the optic of the process intensification strategy. For these two reasons, it is expected that the interest in MRs is going to grow quickly in the near future. In fact, many scientists are working in the field, and the results obtained up to now reveal that this technology could have some commercial applications in the near future. From an engineering point of view, its success depends on several different key factors which need to be further evaluated, including the following:

1. The exact role of the membranes and their characteristics/properties;
2. The appropriate chemical processes able to couple with the MRs;
3. The operating conditions to better utilize MRs.

In particular, Armor (Armor, 1998) presented a discussion in 1998 on the critical issues that need to be solved in order to validate the use of MRs. The author highlighted the fact that without an acceptable and targeted utility of inorganic MRs, it will be difficult to use them in real applications. Saracco et al. (Saracco and Specchia, 1994) stated that, although important progress has been made in the field, their large-scale application is still far from being achieved. The same conclusion was presented by Dixon (Dixon, 2003), who pointed out that more than 500 publications appeared on MRs from 1998 to 2002, but only a few cases focused on possible industrial applications. For example, an application of a pilot-scale MR for direct ultra-pure hydrogen production has been commercialized by the largest gas company in Tokyo (Tokyo Gas Company, Ltd.). This MR is able to produce pure hydrogen

(purity > 99.999 %) working at $500-550\ ^{o}C$ (Mori, 2005). This example, along with interesting research results described below, points out the potential of MRs in hydrogen production and related areas.

2.3.1 Dense and composite metallic membranes

Dense metal membranes have attracted the interest of many researchers due to their permselective characteristics that permit complete separation of product from gaseous mixtures without requiring a further separation/purification unit. In particular, there are a few types of dense hydrogen permselective metal membranes: Pd, Pd-alloy, Ti, V, etc (Basile et al., 2008d).

Problems such as the embrittlement, deposition of carbonaceous impurities and poisoning by CO and H_2S may occur with Pd-based membranes. The embrittlement phenomenon affects pure Pd membranes due to exposure to hydrogen at lower temperatures. Such a phenomenon may produce pinholes on the membrane, which will negatively affect the hydrogen permselectivity of the membrane. This problem can be avoided by using Pd-alloy membranes, obtained by alloying the Pd with Ni, Cu, and, in particular, Ag. In fact, Pd-Ag membranes show good stability, relatively lower material costs and better mechanical properties than pure Pd membranes. Although Pd-Ag membranes show lower hydrogen diffusivity, they exhibit higher hydrogen solubility with respect to pure Pd membranes. Moreover, their hydrogen permeability increases with the percentage of Ag in the alloy up to a maximum, which occurs at around 23 wt.% Ag (Shu et al., 1991). One of the most relevant problems that Pd and Pd-alloy membranes suffer from is CO poisoning, which can be avoided by operating at temperatures above 250 °C. Pd-Ag membranes are most commonly used in MRs in order to carry out reforming reactions for producing pure hydrogen (Basile et al., 2008a; Basile et al., 2008c; Criscuoli et al., 2001; Kikuchi et al., 1991; Lin et al., 1998; Shu et al., 1994; Tosti et al., 2003; Tosti et al., 2000a).

There are, in the literature, some discrepancies concerning the industrial feasibility of Pd and Pd-alloy MRs as a more competitive alternative to TRs. Lu et al. (Lu et al., 2007) and Armor (Armor, 1998) have pointed out that the cost of Pd and the limited membrane life are the most relevant commercial limitations for using dense Pd and Pd-alloy membranes. On contrary, Criscuoli et al. (Criscuoli et al., 2001) reported that, even though both MR capital and operating costs are higher than for TRs, it is possible to determine a range in which they might be cost effective by reducing the Pd thickness. In fact, MRs could represent a possible alternative to TRs at a Pd thickness below 20 μm. Tosti et al. (Tosti et al., 2006) illustrated that Pd-Ag MRs (consisting of thin-walled permeator tubes produced by diffusion welding of Pd-Ag foils) present reduced costs on account of their reduced metal thickness. Moreover, Tosti verified the long life of a Pd-Ag MR operating continuously over 12 months, subjected to thermal and hydrogenation cycle tests. For Shu et al. (Shu et al., 1991), the Pd cost is not the limiting step for the application of Pd-based MRs in several small and medium processes, but considering large plants and the hydrogen economy, the cost of Pd could be a key factor in the development of Pd-based MRs.

Although there are a large number of scientific studies on catalytic MRs, to the best of the author's knowledge only a very small number of them focused on the analysis of the costs (Criscuoli, 2006). Taking into account the fact that the MRs are not yet a well established technology and that different problems have to be overcome before industrial scale implementation, a realistic analysis must still be made.

From the viewpoint of cost reduction and in order to carry out reforming reactions for producing hydrogen in low cost MRs, there is a strong need to develop non-Pd membranes (or, at least membranes with low Pd content), for example, Ti-, Ni-, Nb-, or V-based membranes (Phair and Donelson, 2006) and low cost, hydrogen permeable alloys (Adams and Mickalonis, 2007; Basile et al., 2008b; Criscuoli, 2006; Hara et al., 2002; Luo et al., 2006; Nishimura et al., 2002; Tereschenko et al., 2007). Alternative research in this field is

also focused on the preparation of thin Pd-based films deposited onto porous (metallic or ceramic) supports, although the formation of uniform thin metallic films on the supports is one of the most important problems that arise when using the Pd-based composite membranes in MRs. In fact, depending on the film thickness, the hydrogen permeation through the Pd or its alloys could be relatively low. Therefore, taking into account the fact that the separation characteristics of a Pd-based membrane are dominated by the nature of the thin metallic film instead of the support, reduced Pd film thicknesses are required in order to have both higher hydrogen fluxes and better MR economy.

The main techniques for coating metallic thin films onto supports can be summarized as follows:

1. Electroless plating (EP).
2. Chemical vapor deposition (CVD).

Normally, EP produces Pd particles by reduction of a plating solution containing Pd-amine complexes. Due to impurities in the plating solution, the Pd layer deposited on the support may have defects. However, the EP technique shows such advantages as high coating adhesion, low equipment cost and operation simplicity.

The CVD method is used because of the simplicity to deposit a metal film onto the support. For both techniques (EP and CVD), a disadvantage can be the difficult to control the metal alloy composition of the deposit.

Pd or Pd-alloy membranes show very high hydrogen selectivities. Theoretically, a defect-free Pd membrane should show infinite selectivity toward hydrogen over other species. In some cases, the hydrogen selectivity is found to have a finite value, due to pinhole formation. The hydrogen flux through Pd and Pd-alloy membranes can be illustrated by the following equation:

$$J_{H_2} = \frac{L_{H_2}}{\delta}\left(\left(p_{H_2}^{R}\right)^{n} - \left(p_{H_2}^{P}\right)^{n}\right) \tag{1.18}$$

$$L_{H_2} = L^0_{H_2} \exp\left(-\frac{E_a}{\Re T}\right) \tag{1.19}$$

where J_{H_2} is the hydrogen flux, L_{H_2} is the hydrogen permeability, $0.5 < n < 1$, $L^0_{H_2}$ is the pre-exponential factor, E_a is the apparent activation energy, $\Re$ the ideal constant, T is the absolute temperature, $p^R_{H_2}$ and $p^P_{H_2}$ are the hydrogen partial pressure on the retentate and permeate sides, respectively, and δ is the membrane thickness. When the hydrogen diffusion through the metal film is the rate-limiting step and hydrogen atoms form an ideal solution in the metal, equation 1.18 becomes *Sieverts' law*, with $n = 0.5$. From a panoramic view, Table 2.4 comprises a list of permeation/separation data for different Pd-based membranes prepared through different techniques. In the table, parameters such as membrane type, membrane thickness, temperature and pressure of the permeation tests, hydrogen flux, hydrogen permeance, *ideal* separation factor, apparent activation energy, preparation method, and reference to the works are reported. The membrane effect on the separation of a gas mixture is only determined by two parameters: the permeability and the separation factor. Due to a lack of information in the papers considered, only the *ideal* separation factor (the so-called permselectivity or, in short, selectivity) is reported, defined as the ratio between a target pure gas flux (generally hydrogen) to the flux of another pure gas (e.g. nitrogen) at the same operating conditions.

2.4 The Water-Gas Shift Reaction in Membrane Reactors

Conventionally, the WGS reaction is limited by thermodynamic constrains, as previously mentioned: its conversion may be closer to the thermodynamic predictions, depending on the suitable choice of catalyst. In other words, the laws of thermodynamics set a rigid limit for the conversion achievable in TRs in which this reaction proceeds only to partial completion.

Table 2.4 – Permeation data of different Pd-based membranes from literature.

Membrane type	T (°C)	ΔP (kPa)	Active layer (μm)	$Flux_{H_2}$ ($mol \cdot m^{-2} \cdot s^{-1}$)	L_{H_2} ($mol \cdot m^{-2} \cdot s^{-1} \cdot Pa^{-1}$)	α_{H_2/N_2}	E_{a,H_2} ($kJ \cdot mol^{-1}$)	Preparation method [b]	Reference
Ti-Ni-Pd	450	300	45	$\sim 3.3\times10^{-3}$	–	∞	42.2	Cold rolling	(Tereschenko et al., 2007)
Pd/α-Al_2O_3	370	400	1	4.0×10^{-1}	–	3000 – 8000	–	ELP	(Nair and Harold, 2007)
Pd-Ag/Ni	400	–	1.2 – 3	–	2.0×10^{-5}	–	–	MEMS	(Zhang et al., 2007)
Pd/$BaZrO_3$	600	–	41	–	1.2×10^{-9}	5.7	–	CVD	(Okada et al., 2007)
Pd-Ag	300	30	1.3 – 5	$1.0 - 5.0\times10^{-1}$	2.1×10^{-8}	> 500	–	MS	(Mejdell et al., 2008)
Pd-Ag/α-Al_2O_3	550	400	11	7.0×10^{-2}	5.0×10^{-4}	~ 1000	21.0	ELP	(Nair et al., 2007)
Pd/ZrO_2/PSS	500	100	10	8.3×10^{-2}	8.3×10^{-7} [a]	–	7.1	ELP	(Wang et al., 2004)
Pd/α-Al_2O_3	300	290	1	2.1	3.8×10^{-3} [a]	–	–	MCVD	(Sato et al., 2005)
Pd/Al_2O_3	450	–	4.8	–	3.0×10^{-6}	60	–	ELP	(van Dyk et al., 2003)
Pd-Ag/Al_2O_3	–	142	10	1.0×10^{-1}	1.0×10^{-6} [a]	1500	–	ELP	(Liang and Hughes, 2005a)
Pd-PSS	320 – 500	–	20	–	–	–	12.5	ELP	(Lin et al., 2003)
Pd/Al_2O_3	300	30	2 – 4	$1.0 - 2.0\times10^{-1}$	6.7×10^{-6} [a]	5000	–	CVD	(Itoh et al., 2005)
Pd/Al_2O_3	528	–	2 – 3	–	1.2×10^{-6}	< 18	–	ELP	(Kleinert et al., 2005)
Pd-Ag	400 – 500	162	50	–	–	∞	33.3	LT	(Basile et al., 2005)
Pd/PNS	500	358	–	8.3×10^{-2}	–	3.7	–	MS	(Ryi et al., 2006)
Pd-Cu alloy	452	–	0.75	1.6	–	$500_{(H_2/He)}$	–	DST	(Hoang et al., 2004)
Pd/Ni	400	20	2.5	3.1×10^{-1}	1.2×10^{-5} [a]	–	–	DC-SP	(Zhang et al., 2006)

Pd-Ag	347	400	5.5	–	1.0×10^{-6}	> 4500	9.8	SELP	(Hou and Hughes, 2003)
Pd-Ag/PSS	400 – 500	100	2 – 3	3.0×10^{-1}	3.0×10^{-6} [a]	–	25.7	ELP	(Tong et al., 2005a)
Pd_{84}-Cu_{16}/ZrO_2-PSS	480	250	5	6.0×10^{-1}	5.3×10^{-4} [a]	∞	14.5	ELP	(Gao et al., 2005)
Pd_{90}-Ag_{10}/α-Al_2O_3	200 – 343	80 – 250	20	1.4×10^{-1}	1.3×10^{-6} [a]	30 – 178	–	ELP	(Huang et al., 2003)
Pd/MPSS	500	100	6	3.0×10^{-1}	3.0×10^{-6} [a]	–	16.7	ELP	(Tong et al., 2005b)
Pd-Ag/α-Fe_2O_3/PSS	500	100 – 500	16 – 20	–	4.9×10^{-4}	3500 – 5000	–	SELP	(Yepes et al., 2006)
Pd-Cu/α-Al_2O_3	450	345	11	8.0×10^{-1}	2.3×10^{-6} [a]	1150	–	ELP	(Roa et al., 2003)
Pd/TiO_2	500	45	0.3 – 0.4	2.8×10^{-1}[a]	6.3×10^{-6} [a]	1140	–	ELP UV	(Wu et al., 2000)
Pd-Ni/SS	350 – 550	68	0.8	1.4×10^{-1}–1.3	$2.0-1.9\times10^{-5}$ [a]	300 – 4700	–	VED	(Nam et al., 1999)
Pd/α-Al_2O_3	300 – 500	100	2.0	1.0×10^{-1}	–	> 1000	–	MCVD	(Yan et al., 1994)
Pd/PSS	520	150	10	1.8×10^{-1}	1.2×10^{-6} [a]	–	–	ELP	(Liang and Hughes, 2005b)

[a] Calculated value

[b] CVD – chemical vapor deposition; DC-SP – DC sputtering; DST – dual sputtering technique; ELP – electroless plating; ELP UV – electroless plating under irradiation by UV; LT – lamination technique; MCVD – metallorganic chemical vapor deposition; MEMS – micro-electro-mechanical-systems; MPSS – macroporous stainless steel; MS – magnetron sputtering; PSS – porous stainless steel; SELP – sequential electroless plating; SS – stainless steel; VED – vacuum electrodeposition.

As a consequence, the interest of scientists seems quite justified in searching for alternatives to TRs. Among different technologies, the membrane one seems to be promising. In particular, due to the attractive possibility of realizing both reaction and gas separation/purification in the same device, MRs are currently considered as good candidates for replacing TRs. With respect to a classic configuration of a TR consisting of a reactor unit in series with a separation unit, a MR represents a modern solution having many potential advantages: reduced capital and downstream separation costs, as well as enhanced yields and selectivities. From the viewpoint of the WGS process in a MR, a reaction product (e.g. hydrogen, in the case of Pd membranes) moves to the permeate side, enabling the WGS reaction to proceed toward completion and so making it possible to achieve the following: (1) higher conversion than a TR working under the same operating conditions, or (2) the same conversion as a TR, but working under milder operative conditions. In fact, great interest toward the WGS reaction assisted by MRs has been evidenced in the literature, and many studies are focused on hydrogen recovery from a catalytic shift MR, either using Pd-based (Basile et al., 2001; Basile et al., 1996a; Basile et al., 1996b; Basile et al., 1995; Demange et al., 2007; Hsu and Buxbaum, 1986; Iyoha et al., 2007; Kikuchi et al., 1989; Tosti et al., 2000b; Uemiya et al., 1991; Violante et al., 1993) or silica membranes (Battersby et al., 2008; Brunetti et al., 2007; Giessler et al., 2003).

Obviously, CO_2-selective membranes also allow shifting the WGS reaction, although they fall out of the scope of this review. In this sense, one can mention the use of CO_2-selective polymeric membranes containing amino groups, the works by Ho et al. (Ho, 2006; Huang et al., 2005) being of relevance. The main advantage of the use of such membranes is that a high-purity H_2 product is recovered at high pressure (H_2 is recovered in the retentate stream, not in the permeate one). Besides, polymeric membranes are also cheaper, but their operation is limited by reaction temperature.

2.4.1 Effects of temperature

In different scientific works, the WGS reaction carried out in MRs has been analyzed while paying attention to the influence of temperature on CO conversion. Generally, two opposite effects on the MR system occur by increasing the temperature. On one hand, a temperature increase induces a positive effect in terms of higher hydrogen permeability through the membrane. In fact, higher temperatures enhance the hydrogen permeating flux from the reaction side to the permeate side, resulting in a shift toward the reaction products, which allows one to obtain higher CO conversion. On the other hand, since the WGS reaction is exothermic, a temperature increase will result in a detrimental effect on the equilibrium CO conversion.

Figure 2.8 sketches the CO conversions obtained with different MRs reported in literature in the temperature range of $50-400$ ºC. The performance of a few TRs (Daniells et al., 2005; Goerke et al., 2004; Sakurai et al., 2005; Venugopal and Scurrell, 2003; Zerva and Philippopoulos, 2006), expressed in terms of CO conversion, is also included. The dependence of the WGS thermodynamic equilibrium conversion (based on a simulated reformate feed gas mixture with composition 5 % CO, 13.8 % H_2O, 3.1 % CO_2, 28.1 % H_2 and 50 % N_2 (Utaka et al., 2003)) with temperature is also presented. Unfortunately, it is not possible to directly compare the results proposed in Figure 2.8 due to the different operating conditions (pressure, catalyst type, H_2O/CO feed molar ratio, etc.) used for the experimental tests. In particular, Uemiya et al. (Uemiya et al., 1991) carried out the WGS reaction in a composite MR packed with almost 12 g of a commercial Fe-Cr oxide catalyst at 400 °C, 1.0 bar of reaction pressure, different H_2O/CO feed molar ratios (in Figure 2.8: H_2O/CO = 3/1), and using argon as sweep gas in a co-current flow configuration. The composite membrane consisted of a thin Pd film (thickness 20 μm) supported on a porous-glass cylinder (mean pore size, 300 nm). The best performance of this reactor was a CO conversion of around 95.0 % at 400 ºC.

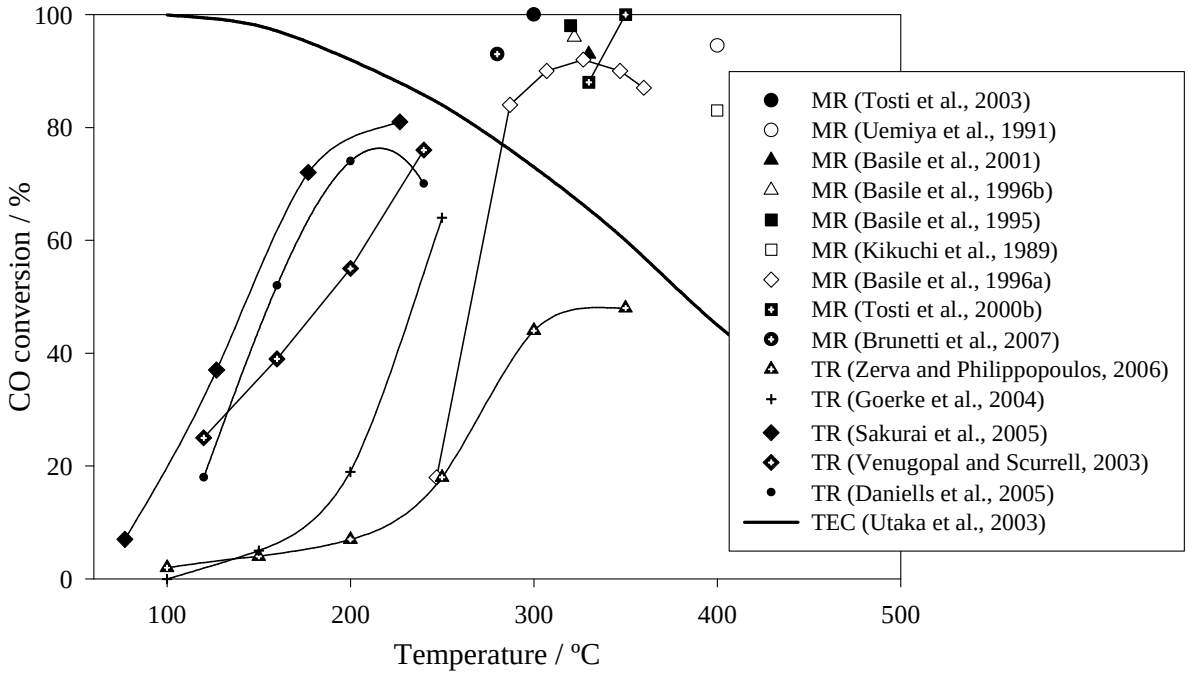

Figure 2.8 – CO conversion *versus* reaction temperature of different MRs and TRs from literature.

Basile et al. (Basile et al., 2001) used a Pd-Ag based rolled membrane (thickness 50 μm) for carrying out the WGS reaction at 1.0 bar, $H_2O/CO = 1/1$ and nitrogen as sweep gas in co-current mode. As shown in Figure 2.8, a CO conversion of 93.0 % was achieved at around 330 °C. These authors also studied this reaction using a MR in which the composite membrane was an ultra-thin Pd film (~ 0.1 μm) coated on the inner surface of a porous ceramic support (γ-Al_2O_3) by the co-condensation technique (Basile et al., 1996b). A CO conversion of around 96.0 % with the MR working at 1.1 bar and $H_2O/CO = 2/1$ was obtained. In another work, Basile et al. (Basile et al., 1995) illustrated that a CO conversion of around 98.0 % could be reached, by using a MR working at around 320 °C and utilizing a composite membrane with a 10 μm Pd film coated on a ceramic support. Furthermore, Basile et al. (Basile et al., 1996a) used a composite MR in which the membrane, produced by the co-condensation technique, consisted of an ultra-thin Pd film (~ 0.2 μm) coated on a ceramic support (α-Al_2O_3/γ-Al_2O_3). The authors carried out the tests at a H_2O/CO molar feed ratio < 1/1 (0.98/1) in order to reduce the energy consumption due to the excess of water vapor at

ratios > 1/1. In this case, as shown in Figure 2.8, the CO conversion increases by increasing the temperature up to a maximum around 92.0% at 327 °C, representing a compromise between the kinetic rate of the reaction, hydrogen permeation through the membrane, and the thermodynamic considerations of the WGS reaction. On the contrary, the thermodynamic equilibrium shows a continuously decreasing trend by increasing the temperature. Kikuchi et al. (Kikuchi et al., 1989) demonstrated that a thin Pd-based composite MR, packed with 3.0 g of a commercial Fe_2O_3-Cr_2O_3 catalyst and using argon in co-current flow configuration on the permeate side, is able to overcome the thermodynamic equilibrium, reaching a CO conversion of around 83.0 % at 400 °C, when H_2/CO = 1/1 and W/F = 1300 $g_{cat} \cdot min \cdot mol_{CO}^{-1}$.

Brunetti et al. (Brunetti et al., 2007) carried out the WGS reaction in a supported silica MR, packed with 3.4 g of a CuO/CeO_2 catalyst and working between $220-290$ ºC and $2.0-6.0$ bar. The membrane had a porous stainless steel disk as the support. The macropores of the support were modified by packing with silica xerogel (500 nm) under a pressure of 10 MPa and by coating with an intermediate layer of γ-alumina. The mesoporous γ-alumina layer was coated on the support disk from a boehmite sol (γ-AlOOH) by a soaking-rolling procedure. The thickness of the γ-alumina layer was about 5 μm and the top surface was smooth and defect free. A CO conversion close to 95.0 % was obtained at 280 °C, 4.0 bar and H_2O/CO = 1/1.

Iyoha et al. (Iyoha et al., 2007) carried out the HT WGS reaction in 100 wt.% Pd and 80 wt.% Pd-20 wt.% Cu shell-and-tube MRs at 900 °C and at around 2.4 bar of transmembrane pressure difference. The tube bundle consisted of four parallel Pd-based tubes (15.25 cm length, 3.175 mm o.d.) with a wall thickness of 125 μm. The modest catalytic activity of the Pd-based membrane surface for the forward WGS reaction, the high rate of hydrogen extraction through the Pd membrane and the long residence times $(1-5$ s) resulted in a consistent shift in CO conversion, achieving 93.0 % at 900 °C and H_2O/CO =

1.5/1. Carbon monoxide conversion decreased from 93.0 % to 66.0 % when the Pd-based MR was replaced with another MR containing a Pd_{80}-Cu_{20} membrane, due to the lower hydrogen permeance of the Pd/Cu membrane.

An important application of the WGS reaction carried out in MRs is represented by the hydrogen isotope recovery from the breeder blanket in fusion reactor systems. In fact, the tritium produced in the breeder needs a proper extraction process to reach the required purity level. In particular, an innovative and complex design of finger-type palladium-silver membrane was developed in order to work under hydrogen atmosphere by Demange et al (Demange et al., 2007). Hsu and Buxbaum (Hsu and Buxbaum, 1986) studied Pd-catalyzed oxidative diffusion to extract hydrogen from a metal solution at very low partial pressures.

Concerning the tritium recovery from tritiated water, a conceptually modified version of the tritium recovery plant for ceramic breeder in the fusion fuel cycle, working with two membrane reaction/separation units, was studied by Violante et al. (Violante et al., 1993). In this work, a Pd-Ag membrane was used for recovering tritiated molecular hydrogen from tritiated water via the WGS reaction.

Tosti et al. (Tosti et al., 2000b) used a Pd-ceramic membrane in order to manufacture a Pd-based MR for recovering hydrogen and its isotopes in a closed-loop process with particular reference to the design of the international thermonuclear experimental reactor (ITER) blanket tritium recovery system. In particular, a thin Pd-Ag layer (50 μm) supported on a ceramic tube (pore size 12 μm), obtained by means of a rolling technique, was used in a MR for recovering tritium from tritiated water by WGS reaction. As shown in Figure 2.8, the CO conversion reached in the MR was around 88.0 % at 330 °C and 100 % at 350 °C, with a co-current nitrogen sweep. In an continuation of this study, Tosti et al. (Tosti et al., 2003) proposed a Pd-Ag thin-wall permeator as a MR. The membrane was obtained by coating porous ceramic tubes with thin Pd-Ag metal foils (50 μm). The metal foils were prepared by a cold-rolling and annealing procedure. The experimental tests on the MR were carried out in

the temperature range of $300-330$ ºC with a feed pressure of 1.0 bar. As shown in Figure 2.8, a CO conversion close to 100 % was attained at around 300 °C, $H_2O/CO = 1/1$ and using N_2 as sweep gas. Therefore, with reference to a closed-loop process, Tosti et al. demonstrated that by utilizing low H_2O/CO ratios the WGS reaction carried out in a Pd-based MR involves higher conversions than a TR, constituting an interesting result in fusion nuclear applications, where the tritium inventory can be reduced.

2.4.2 Effects of sweep gas

A sweep gas stream can be used on the permeate side of MRs for improving the hydrogen permeation driving force. In fact, referring to Pd-based membranes only selective to hydrogen, the effect of a sweep gas acts positively on the hydrogen permeation through the membrane by decreasing the hydrogen partial pressure on the permeate side (increasing the driving force), thus allowing higher hydrogen permeation flux through the membrane. As a result, the WGS reaction is shifted toward the products, resulting in higher CO conversion. In the meanwhile, the operating costs increase with increasing the mass flow rate of the sweep gas, causing the need to increase the plant size in order to avoid pressure drops into permeate side of the MR. Moreover, when an inert gas (nitrogen, helium, argon, etc.) is used as sweep gas, the operating costs increase, too, due to the hydrogen separation process for recovering the ultra-pure hydrogen stream. On the contrary, using steam as sweep gas, the separation process can be carried out through the condensation process, obtaining directly pure hydrogen with a partial recovery of heat due to steam condensation. However, the adequate use of a sweep gas involves choosing an inert gas or steam for this role and its molar flow rate, taking into account the consequent costs. Obviously, a balance between the advantages, in terms of higher CO conversion, hydrogen yield and recovery, and the costs determines the optimal choice of the sweep gas and its molar flow rate to be used.

In order to make a realistic comparison between different experimental results, and to the best of the author's knowledge, the CO conversion of different MRs working at almost the same operating conditions (reaction pressure, H_2O/CO feed ratio, and reaction temperature) and at different sweep gas flow rates is presented in Table 2.5. Moreover, nitrogen was used as sweep gas in all cases. In the case of membranes that are not entirely permselective for hydrogen, a higher sweep gas flow rate does not significantly improve CO conversion. In fact, Giessler et al. (Giessler et al., 2003) demonstrated that the conversion of CO was not increased in a MR when the sweep gas flow rate was increased from 50 to 300 $mL \cdot min^{-1}$ (cf. Table 2.5), using a molecular sieve silica membrane at 250 °C, reaction pressure of 1.0 bar and H_2O/CO = 1/1. By using a Pd-based composite MR (a Pd layer supported on two layers of γ-Al_2O_3 and α-Al_2O_3) at 322 °C, reaction pressure of 1.1 bar, and H_2O/CO = 0.96/1, Basile et al. (Basile et al., 1996b) obtained a CO conversion enhancement from 92.0 % to only 94.0 % by going from no sweep to around 30 $mL \cdot min^{-1}$ of sweep gas. Furthermore, no significant variation in terms of CO conversion was registered by Basile et al. (Basile et al., 2001) when the sweep gas flow rate was changed from 250 $mL \cdot min^{-1}$ (CO conversion = 94.0 %) to 515 $mL \cdot min^{-1}$ (CO conversion = 98.5 %) in a Pd-Ag composite MR working at 330 °C, reaction pressure of 1.0 bar, and H_2O/CO = 1/1. On the contrary, by using a MR containing a membrane selective only to hydrogen (60 μm Pd layer on a ceramic support), Tosti et al. (Tosti et al., 2000b) showed that the CO conversion is enhanced from 84.0 % to 100 % when the sweep gas flow rate is increased from 230 to 470 $mL \cdot min^{-1}$. Hence, it is possible to highlight that the use of a sweep gas plays a more important role in the improvement of the CO conversion when the MR utilizes a membrane only selective toward hydrogen. This is because there is some permeation of the reactants through the membrane when it is not permselective only to hydrogen, so that the conversion of the reactants never reaches 100 %.

2.4.3 H_2O/CO molar ratio effect

Table 2.6 illustrates the influence of H_2O/CO molar ratio on the CO conversion reported in different experimental studies conducted on MRs from the literature. As shown in Table 2.6, CO conversion was improved from 65.0 % to 92.0 % in the study of Battersby et al. (Battersby et al., 2008), by increasing the H_2O/CO molar ratio from 1/1 to 3/1. This interesting result was achieved by carrying out the WGS reaction in a silica MR working at 250 °C, reaction pressure of 1.0 bar, and without sweep gas. Uemiya et al. (Uemiya et al., 1991) improved CO conversion from 94.0 % to 98.0 % by increasing the ratio H_2O/CO from 1/1 to 5/1 by using a MR using a composite membrane consisting of a Pd layer (20 μm) supported on a porous glass support and working at 400 °C and 300 $mL \cdot min^{-1}$ of argon as sweep gas. Basile et al. (Basile et al., 1996b) also obtained a CO conversion enhancement from around 94.0 % to 98.0 % at a H_2O/CO ratio higher than 1/1 (up to 3/1) by using a Pd-composite (Pd/γ-Al_2O_3/α-Al_2O_3) MR, working at 322 °C, 1.1 bar of reaction pressure, and 7.1 $mL \cdot min^{-1}$ of nitrogen as sweep gas. Although Table 2.6 shows that a higher H_2O/CO ratio generally favors an increase in CO conversion, Giessler et al. (Giessler et al., 2003) found that a high H_2O/CO ratio negatively affected the membrane structure in terms of pore widening and/or pore closure in a silica MR. In general, in different cases a H_2O/CO molar ratio > 1/1 positively affects the CO conversion (limiting reactant), since the excess water shifts the WGS reaction toward the products; however, the advantage in terms of higher CO conversions by using H_2O/CO > 1/1 is not consistent enough to compensate for the economical disadvantage due to the excess water. Hence, from an economical point of view, the optimum could be represented by a MR able to achieve high CO conversions working at stoichiometric or a H_2O/CO slightly < 1/1, ambient pressure, relatively low temperature and without using sweep gas (Basile et al., 1996b).

Table 2.5 - Influence of the sweep gas flow rate on the CO conversion in MRs from literature.

Membrane type	***T*** **(°C)**	$P_{reaction}$ **(bar)**	**CO conversion (%)**	**Sweep gas flow rate (mL·min^{-1})**	**H_2O/CO**	**Reference**
Silica supported on α-Al_2O_3	250	1.0	99.5 99.1	50.0 (N_2) 300.0	1.00	(Giessler et al., 2003)
Pd/γ-Al_2O_3/-αAl_2O_3	322	1.1	94.0 92.0	28.2 (N_2) –	0.96	(Basile et al., 1996a)
Pd/Ag-ceramic support	330	1.0	98.5 94.0	515.0 (N_2) 250.0 (N_2)	1.00	(Basile et al., 2001)
Pd-ceramic support	350	1.1	~ 100 ~ 100 84.0	470.0 (N_2) 340.0 230.0	1.00	(Tosti et al., 2000b)

Table 2.6 - Influence of the H_2O/CO molar ratio on the CO conversion in MRs from literature.

Membrane type	***T*** **(°C)**	$P_{reaction}$ **(bar)**	**CO conversion (%)**	**H_2O/CO**	**Sweep gas flow rate ($mL \cdot min^{-1}$)**	**Reference**
Pd(20μm) on porous glass support	400	0.48 – 2.9	94.0 97.0 98.0	1.00 2.00 5.00	300.0 (Ar)	(Uemiya et al., 1991)
Hydrophobic silica membrane	250	1	85.0 95.0 98.0	0.90 1.50 2.50	20.0 – 60.0 (N_2)	(Giessler et al., 2003)
Pd/γ-Al_2O_3/α-Al_2O_3	322	1.14 1.1	94.3 97.2 98.0	0.96 2.10 3.00	7.1 (N_2)	(Basile et al., 1996a)
Silica membrane	250	1	65.0 88.0 92.0	1.00 2.00 3.00	–	(Battersby et al., 2008)

2.4.4 The effect of pressure

When using membranes only permeable to hydrogen in MRs, a total pressure increase of the reaction medium acts positively on the reactor performance in terms of conversion. In fact, the hydrogen permeating flux through dense Pd or Pd-alloy membranes follows equation 1.18 and, therefore, the higher the driving force (higher retentate partial pressure, for the same permeate partial pressure), the higher the permeation of hydrogen across the membrane. As a result, the WGS reaction is shifted toward the reaction products, thereby favoring CO consumption. Besides, before reaching equilibrium conditions, reaction kinetics is also favored by increasing the system total pressure. In terms of the thermodynamics of the WGS reaction, it is not affected by the pressure since the reaction proceeds with no variation in the total number of moles.

At industrial scale, a balance between the positive effects due to a pressure increase on the MR performances (higher CO conversion, hydrogen yield and recovery) and the consequent disadvantages, in terms of higher operating costs (for realizing MRs mechanically resistant, pumping and reactants compression), should be evaluated. To the best of the author's knowledge, only few experimental results concern the reaction pressure influence on the WGS reaction carried out in MRs as shown in Table 2.7. Basile et al. (Basile et al., 2001) improved the CO conversion from 93.5 % to 97.0 % by increasing the reaction pressure from 1.0 to 1.75 bar, using a MR with a Pd-Ag rolled membrane working at 330 °C, H_2O/CO molar ratio = 1/1, and 440 mL·min^{-1} of nitrogen as sweep gas. In another work, Basile et al. (Basile et al., 1996a) improved the CO conversion from 99.2 % to 99.9 % in the pressure range of $1.1-1.2$ bar, using a Pd-composite MR at 322 °C, H_2O/CO molar ratio = 1/1, and 28 mL·min^{-1} of nitrogen as sweep gas. Brunetti et al. (Brunetti et al., 2007) used a silica MR at 280 °C, stoichiometric H_2O/CO ratio, reaction pressure range of $3.2-6.0$ bar, and no sweep gas. They found that CO conversion increased

Table 2.7 – Influence of the total pressure on the CO conversion in MRs from literature.

Membrane type	***T*** **(°C)**	$P_{reaction}$ **(bar)**	**CO conversion (%)**	**H_2O/CO**	**Sweep gas flow rate (mL·min^{-1})**	**Reference**
Pd/Ag rolled membrane	331	1.00	93.5	1.0	440.0	(Basile et al., 2001)
		1.50	95.0			
		1.75	97.0			
Pd/γ-Al_2O_3/α-Al2O3	322	1.10	99.2	1.0	28.2	(Basile et al., 1996a)
		1.15	99.6			
		1.20	99.9			
			99.7		–	
Silica supported on PSS [a]	280	3.20	91.0	1.0	–	(Brunetti et al., 2007)
		4.00	95.5			
		6.00	92.5			

[a] PSS – porous stainless steel

up to a maximum of 95.5 % at 4.0 bar. At higher pressures, the permeation of the products is enhanced, but so is the permeation of the reactants through the membrane with imperfect permselectivity toward hydrogen. The decreasing trend of CO conversion at pressures higher than 4.0 bar may be due to the loss of reactants, which has a detrimental effect on CO conversion.

2.5 Conclusions

The potential of hydrogen as an energy carrier will certainly play a very important role in future energy systems. Therefore, many companies, academic institutions and government laboratories are focusing their efforts in trying to produce hydrogen in a more technically, environmentally and economically attractive way, based on the idea of sustainable development.

From a techno-economic viewpoint, SR of natural gas is currently the most favorable hydrogen production method, mainly for applications such as ammonia synthesis and methanol production. The process involves a reformer unit, where a H_2-rich stream containing CO and CO_2, among other species, is obtained. CO is undesirable since it leads to the deactivation of fuel cell catalysts, so it should be removed. HT and LT WGS reactions became an important step toward upgrading CO to H_2. After almost a century since its first industrial application, HT and LT WGS are carried out in adiabatic reactors using Fe- and Cu-based catalysts. However, such catalysts need to be carefully activated, may deactivate easily in an oxidizing environment and are pyrophoric if exposed to air. Au- and Pt-based catalysts appear to be highly promising for fuel processing. However, their performance, particularly in the case of Au-based catalysts, is highly dependent on the catalyst preparation method, on the size of the metal particles and on the intimate contact with the surface vacancies of the oxide support. Reaction temperature is also a very important factor with respect to the activity and deactivation of such catalysts.

The WGS reaction is an equilibrium-limited reaction where MRs can have an important role in enhancing the performance. However, a new challenge is presented in making highly effective conventional catalysts used in traditional WGS processes suitable for MR applications (due to the inhibitory effect of reaction products). Pt-based catalysts appear to be very promising for WGS MR applications due to their smaller inhibiting effect by the forward WGS reaction products. Also, Cu-ceria and Au-based catalysts are very interesting compared to the traditional ones. However, much work should be done in the future to further study their resistance to poisoning and sintering.

Despite the fact the WGS reaction involves only four species, a wholly satisfactory and universally accepted reaction mechanism fails to exist. For Fe-based WGS catalysts, a regenerative mechanism is generally accepted. However, much more discussion exists for the Cu-based catalysts, where evidence supporting both reaction pathways (regenerative and associative) exists. Up to now, precious-metal-based catalysts have gained a general consensus on the predominance of the associative mechanism.

Hydrogen upgrading in refinery applications can be achieved by using PSA, membrane, or cryogenic separation processes. Membranes are excellent candidates for hydrogen purification, especially when incorporated into a MR, combining the reaction/separation process in a single unit. Despite difficulties in the formation of a uniform metallic thin film, Pd-based membranes show very high hydrogen selectivity, being described in many works as a promising candidate for WGS MR technology.

In this chapter, an extensive overview was presented concerning the WGS reaction carried out in Pd-based MRs, paying particular attention to the effect of the membrane in shifting the reaction toward the products, yielding this way conversions above those based on thermodynamic equilibrium determined from feed composition.

2.6 References

Abad, A., Corma, A., Garcia, H., Catalyst parameters determining activity and selectivity of supported gold nanoparticles for the aerobic oxidation of alcohols: The molecular reaction mechanism. *Chem. Eur. J.* **2008**, 14 (1), 212-222.

Adams, T.M., Mickalonis, J., Hydrogen permeability of multiphase V-Ti-Ni metallic membranes. *Mater. Lett.* **2007**, 61 (3), 817-820.

Amandusson, H., Ekedahl, L.G., Dannetun, H., Hydrogen permeation through surface modified Pd and Pd-Ag membranes. *J. Memb. Sci.* **2001**, 193 (1), 35-47.

Andreev, A., Idakiev, V., Mihajlova, D., Shopov, D., Iron-based catalysts for the water gas shift reaction promoted by first-row transition metal oxides. *Appl. Catal.* **1986**, 22 (2), 385-387.

Andreeva, D., Idakiev, V., Tabakova, T., Andreev, A., Low-temperature water-gas shift reaction over Au/α-Fe_2O_3. *J. Catal.* **1996a**, 158 (1), 354-355.

Andreeva, D., Idakiev, V., Tabakova, T., Andreev, A., Giovanoli, R., Low-temperature water-gas shift reaction on Au/α-Fe_2O_3 catalyst. *Appl. Catal., A* **1996b**, 134 (2), 275-283.

Andreeva, D., Idakiev, V., Tabakova, T., Ilieva, L., Falaras, P., Bourlinos, A., Travlos, A., Low-temperature water-gas shift reaction over Au/CeO_2 catalysts. *Catal. Today* **2002**, 72 (1-2), 51-57.

Andreeva, D., Tabakova, T., Idakiev, V., Christov, P., Giovanoli, R., Au/α-Fe_2O_3 catalyst for water-gas shift reaction prepared by deposition-precipitation. *Appl. Catal., A* **1998**, 169 (1), 9-14.

Armor, J.N., Applications of catalytic inorganic membrane reactors to refinery products. *J. Membrane Sci.* **1998**, 147 (2), 217-233.

Ayastuy, J.L., Gutierrez-Ortiz, M.A., Gonzalez-Marcos, J.A., Aranzabal, A., Gonzalez-Velasco, J.R., Kinetics of the low-temperature WGS reaction over a CuO/ZnO/Al_2O_3 catalyst. *Ind. Eng. Chem. Res.* **2005**, 44 (1), 41-50.

Azzam, K.G., Babich, I.V., Seshan, K., Lefferts, L., Bifunctional catalysts for single-stage water-gas shift reaction in fuel cell applications. Part 1. Effect of the support on the reaction sequence. *J. Catal.* **2007**, 251 (1), 153-162.

Basile, A., Chiappetta, G., Tosti, S., Violante, V., Experimental and simulation of both Pd and Pd/Ag for a water gas shift membrane reactor. *Sep. Purif. Technol.* **2001**, 25 (1-3), 549-571.

Basile, A., Criscuoli, A., Santella, F., Drioli, E., Membrane reactor for water gas shift reaction. *Gas Sep. Purif.* **1996a**, 10 (4), 243-254.

Basile, A., Drioli, E., Santella, F., Violante, V., Capannelli, G., Vitulli, G., A study on catalytic membrane reactors for water gas shift reaction. *Gas Sep. Purif.* **1996b**, 10 (1), 53-61.

Basile, A., Gallucci, F., Iulianelli, A., De Falco, M., Liguori, S., Hydrogen production by ethanol steam reforming: Experimental study of a Pd-Ag membrane reactor and traditional reactor behaviour. *Int. J. Chem. Reactor Eng.* **2008a**, 6, A30.

Basile, A., Gallucci, F., Iulianelli, A., Tereschenko, G.F., Ermilova, M.M., Orekhova, N.V., Ti-Ni-Pd dense membranes - The effect of the gas mixtures on the hydrogen permeation. *J. Memb. Sci.* **2008b**, 310 (1-2), 44-50.

Basile, A., Gallucci, F., Iulianelli, A., Tosti, S., CO-free hydrogen production by ethanol steam reforming in a Pd-Ag membrane reactor. *Fuel Cells* **2008c**, 8 (1), 62-68.

Basile, A., Gallucci, F., Paturzo, L., Hydrogen production from methanol by oxidative steam reforming carried out in a membrane reactor. *Catal. Today* **2005**, 104 (2-4), 251-259.

Basile, A., Tosti, S., Gallucci, F., Synthesis, characterization and applications of palladium membranes. In *Membrane Science and Technology - Inorganic membranes: synthesis, characterization and applications*, Mallada, R., Menéndez, M., Eds. Elsevier: Amsterdam, 2008d.

Basile, A., Violante, V., Santella, F., Drioli, E., Membrane integrated system in the fusion reactor fuel cycle. *Catal. Today* **1995**, 25 (3-4), 321-326.

Battersby, S., Duke, M.C., Liu, S.M., Rudolph, V., da Costa, J.C.D., Metal doped silica membrane reactor: Operational effects of reaction and permeation for the water gas shift reaction. *J. Memb. Sci.* **2008**, 316 (1-2), 46-52.

Boccuzzi, F., Chiorino, A., Manzoli, M., Andreeva, D., Tabakova, T., FTIR study of the low-temperature water-gas shift reaction on Au/Fe_2O_3 and Au/TiO_2 catalysts. *J. Catal.* **1999**, 188 (1), 176-185.

Boccuzzi, F., Chiorino, A., Manzoli, M., Lu, P., Akita, T., Ichikawa, S., Haruta, M., Au/TiO_2 nanosized samples: A catalytic, TEM, and FTIR study of the effect of calcination temperature on the CO oxidation. *J. Catal.* **2001**, 202 (2), 256-267.

Bockris, J.O.M., The origin of ideas on a hydrogen economy and its solution to the decay of the environment. *Int. J. Hydrogen. Energ.* **2002**, 27 (7-8), 731-740.

Bond, G.C., Thompson, D.T., Catalysis by gold. *Cat. Rev.- Sci. Eng.* **1999**, 41 (3-4), 319-388.

Bosch, C., Wild, W., 1914. Hydrogen production. Canadian patent 153379.

Brunetti, A., Barbieri, G., Drioli, E., Lee, K.H., Sea, B., Lee, D.W., WGS reaction in a membrane reactor using a porous stainless steel supported silica membrane. *Chem. Eng. Process.* **2007**, 46 (2), 119-126.

Bunluesin, T., Gorte, R.J., Graham, G.W., Studies of the water-gas-shift reaction on ceria-supported Pt, Pd, and Rh: implications for oxygen-storage properties. *Appl. Catal., B* **1998**, 15 (1-2), 107-114.

Burch, R., Gold catalysts for pure hydrogen production in the water-gas shift reaction: activity, structure and reaction mechanism. *Phys. Chem. Chem. Phys.* **2006**, 8 (47), 5483-5500.

Burns, D.T., Piccardi, G., Sabbatini, L., Some people and places important in the history of analytical chemistry in Italy. *Microchim. Acta* **2008**, 160 (1-2), 57-87.

Bus, E., Miller, J.T., van Bokhoven, J.A., Hydrogen chemisorption on Al_2O_3-supported gold catalysts. *J. Phys. Chem. B* **2005**, 109 (30), 14581-14587.

Cameron, D., Holliday, R., Thompson, D., Gold's future role in fuel cell systems. *J. Power Sources* **2003**, 118 (1-2), 298-303.

Campbell, C.T., The active site in nanoparticle gold catalysis. *Science* **2004**, 306 (5694), 234-235.

Campbell, C.T., Daube, K.A., A surface science investigation of the water-gas shift reaction on Cu(111). *J. Catal.* **1987**, 104 (1), 109-119.

Chen, E.L., History. In *Fuel Cell Technology Handbook*, Hoogers, G., Ed. CRC Press: Boca Raton, Florida, 2002.

Chen, M.S., Goodman, D.W., The structure of catalytically active gold on titania. *Science* **2004**, 306 (5694), 252-255.

Cheng, Y.S., Pena, M.A., Fierro, J.L., Hui, D.C.W., Yeung, K.L., Performance of alumina, zeolite, palladium, Pd-Ag alloy membranes for hydrogen separation from Towngas mixture. *J. Membr. Sci.* **2002**, 204 (1-2), 329-340.

Criscuoli, A., Economics associated with implementation of membrane reactors. In *Nonporous inorganic membranes: for chemical processing*, Sammels, A.F., Mundschau, M.V., Eds. Wiley-VCH: Weinheim, Germany, 2006.

Criscuoli, A., Basile, A., Drioli, E., Loiacono, O., An economic feasibility study for water gas shift membrane reactor. *J. Memb. Sci.* **2001**, 181 (1), 21-27.

Daniells, S.T., Makkee, M., Moulijn, J.A., The effect of high-temperature pre-treatment and water on the low temperature CO oxidation with Au/Fe_2O_3 catalysts. *Catal. Lett.* **2005**, 100 (1-2), 39-47.

Demange, D., Welte, S., Glugla, M., Experimental validation of upgraded designs for PERMCAT reactors considering mechanical behaviour of Pd/Ag membranes under H_2 atmosphere. *Fusion Eng. Des.* **2007**, 82 (15-24), 2383-2389.

Deng, W.L., De Jesus, J., Saltsburg, H., Flytzani-Stephanopoulos, M., Low-content gold-ceria catalysts for the water-gas shift and preferential CO oxidation reactions. *Appl. Catal., A* **2005**, 291 (1-2), 126-135.

Deng, W.L., Flytzani-Stephanopoulos, M., On the issue of the deactivation of Au-ceria and Pt-ceria water-gas shift catalysts in practical fuel-cell applications. *Angew. Chem. Int. Ed.* **2006**, 45 (14), 2285-2289.

Denkwitz, Y., Karpenko, A., Plzak, V., Leppelt, R., Schumacher, B., Behm, R.J., Influence of CO_2 and H_2 on the low-temperature water-gas shift reaction on Au/CeO_2 catalysts in idealized and realistic reformate. *J. Catal.* **2007**, 246 (1), 74-90.

Deshpande, V.A., Krause, C., 2007. Fuel processor for producing a hydrogen rich gas. Texaco, USA.

Diagne, C., Vos, P.J., Kiennemann, A., Perrez, M.J., Portela, M.F., Water-gas shift reaction over chromia-promoted magnetite - Use of temperature-programmed desorption and chemical trapping in the study of the reaction mechanism. *React. Kinet. Catal. Lett.* **1990**, 42 (1), 25-31.

Dixon, A.G., Recent research in catalytic inorganic membrane reactors. *Int. J. Chem. Reactor Eng.* **2003**, 1, R6.

Drioli, E., Basile, A., Criscuoli, A., High temperature membrane reactors for clean productions. *Clean Prod. Process* **2000**, 2 (3), 179-186.

Farrauto, R., Hwang, S., Shore, L., Ruettinger, W., Lampert, J., Giroux, T., Liu, Y., Ilinich, O., New material needs for hydrocarbon fuel processing: Generating hydrogen for the PEM fuel cell. *Annu. Rev. Mater. Res.* **2003**, 33, 1-27.

Fu, Q., Deng, W.L., Saltsburg, H., Flytzani-Stephanopoulos, M., Activity and stability of low-content gold-cerium oxide catalysts for the water-gas shift reaction. *Appl. Catal., B* **2005**, 56 (1-2), 57-68.

Fu, Q., Saltsburg, H., Flytzani-Stephanopoulos, M., Active nonmetallic Au and Pt species on ceria-based water-gas shift catalysts. *Science* **2003**, 301 (5635), 935-938.

Gao, H.Y., Lin, J.Y.S., Li, Y.D., Zhang, B.Q., Electroless plating synthesis, characterization and permeation properties of Pd-Cu membranes supported on ZrO_2 modified porous stainless steel. *J. Memb. Sci.* **2005**, 265 (1-2), 142-152.

Germani, G., Schuurman, Y., Water-gas shift reaction kinetics over mu-structured $Pt/CeO_2/Al_2O_3$ catalysts. *AlChE J.* **2006**, 52 (5), 1806-1813.

Ghenciu, A.F., Review of fuel processing catalysts for hydrogen production in PEM fuel cell systems. *Curr. Opin. Solid State Mater. Sci.* **2002**, 6 (5), 389-399.

Ghenciu, A.F., Fuel Processing Catalysts for Hydrogen Reformate Generation for PEM Fuel Cells. *FuelCell Magazine* **2003**, April/ May.

Giessler, S., Jordan, L., da Costa, J.C.D., Lu, G.Q., Performance of hydrophobic and hydrophilic silica membrane reactors for the water gas shift reaction. *Sep. Purif. Technol.* **2003**, 32 (1-3), 255-264.

Ginés, M.L., Amadeo, N., Laborde, M., Apesteguía, C.R., Activity and structure-sensitivity of the Water-Gas shift reaction over Cu-Zn-Al mixed-oxide catalysts. *Appl. Catal., A* **1995**, 131 (2), 283-296.

Goerke, O., Pfeifer, P., Schubert, K., Water gas shift reaction and selective oxidation of CO in microreactors. *Appl. Catal., A* **2004**, 263 (1), 11-18.

Gonzalez, J.C., Gonzalez, M.G., Laborde, M.A., Moreno, N., Effect of temperature and reduction on the activity of high-temperature Water Gas Shift catalysts. *Appl. Catal.* **1986**, 20 (1-2), 3-13.

Gottschalk, F.M., Hutchings, G.J., Manganese oxide Water Gas shift catalysts - Initial optimization studies. *Appl. Catal.* **1989**, 51 (1), 127-139.

Grenoble, D.C., Estadt, M.M., Ollis, D.F., The chemistry and catalysis of the water gas shift reaction - 1. The kinetics over supported metal-catalysts. *J. Catal.* **1981**, 67 (1), 90-102.

Hara, S., Hatakeyama, N., Itoh, N., Kimura, H.M., Inoue, A., Hydrogen permeation through palladium-coated amorphous Zr-M-Ni (M = Ti, Hf) alloy membranes. *Desalination* **2002**, 144 (1-3), 115-120.

Häring, H.W., *Industrial Gases Processing* Wiley-VCH: Weinheim, Germany, 2008.

Haruta, M., Catalysis of gold nanoparticles deposited on metal oxides. *Cattech* **2002**, 6 (3), 102-115.

Haruta, M., Tsubota, S., Kobayashi, T., Kageyama, H., Genet, M.J., Delmon, B., Low-temperature oxidation of Co over gold supported on TiO_2, α-Fe_2O_3, and Co_3O_4. *J. Catal.* **1993**, 144 (1), 175-192.

Haruta, M., Yamada, N., Kobayashi, T., Iijima, S., Gold catalysts prepared by coprecipitation for low-temperature oxidation of hydrogen and of carbon monoxide. *J. Catal.* **1989**, 115 (2), 301-309.

Henderson, M.A., The interaction of water with solid surfaces: fundamental aspects revisited. *Surf. Sci. Rep.* **2002**, 46 (1-8), 5-308.

Hilaire, S., Wang, X., Luo, T., Gorte, R.J., Wagner, J., A comparative study of water-gas-shift reaction over ceria supported metallic catalysts. *Appl. Catal., A* **2001**, 215 (1-2), 271-278.

Ho, W.W.S., 2006. CO_2-selective membranes containing amino groups. US Patent No. 10145297, University of Kentucky Research Foundation, USA.

Hoang, H.T., Tong, H.D., Gielens, F.C., Jansen, H.V., Elwenspoek, M.C., Fabrication and characterization of dual sputtered Pd-Cu alloy films for hydrogen separation membranes. *Mater. Lett.* **2004**, 58 (3-4), 525-528.

Hou, K., Hughes, R., Preparation of thin and highly stable Pd/Ag composite membranes and simulative analysis of transfer resistance for hydrogen separation. *J. Memb. Sci.* **2003**, 214 (1), 43-55.

Hsu, C., Buxbaum, R.E., Palladium-catalyzed oxidative diffusion for tritium extraction from breeder-blanket fluids at low concentrations. *J. Nucl. Mater.* **1986**, 141, 238-243.

Huang, J., El-Azzami, L., Ho, W.S.W., Modeling of CO_2-selective water gas shift membrane reactor for fuel cell. *J. Memb. Sci.* **2005**, 261 (1-2), 67-75.

Huang, T.C., Wei, M.C., Chen, H.I., Preparation of hydrogen-permselective palladium-silver alloy composite membranes by electroless co-deposition. *Sep. Purif. Technol.* **2003**, 32 (1-3), 239-245.

Hutchings, G.J., Copperthwaite, R.G., Gottschalk, F.M., Hunter, R., Mellor, J., Orchard, S.W., Sangiorgio, T., A comparative evaluation of cobalt chromium oxide, cobalt manganese oxide, and copper manganese oxide as catalysts for the water-gas shift reaction. *J. Catal.* **1992**, 137 (2), 408-422.

Idakiev, V., Tabakova, T., Naydenov, A., Yuan, Z.Y., Su, B.L., Gold catalysts supported on mesoporous zirconia for low-temperature water-gas shift reaction. *Appl. Catal., B* **2006**, 63 (3-4), 178-186.

Idakiev, V., Tabakova, T., Tenchev, K., Yuan, Z.Y., Ren, T.Z., Su, B.L., Gold nanoparticles supported on ceria-modified mesoporous titania as highly active catalysts for low-temperature water-gas shift reaction. *Catal. Today* **2007**, 128 (3-4), 223-229.

Idakiev, V., Tabakova, T., Yuan, Z.Y., Su, B.L., Gold catalysts supported on mesoporous titania for low-temperature water-gas shift reaction. *Appl. Catal., A* **2004**, 270 (1-2), 135-141.

Ihde, A.J., *The Development of Modern Chemistry*. Dover Publications: Mineola, NY, 1984.

Ilieva, L., Pantaleo, G., Ivanov, I., Venezia, A.M., Andreeva, D., Gold catalysts supported on CeO_2 and CeO_2-Al_2O_3 for NO_x reduction by CO. *Appl. Catal., B* **2006**, 65 (1-2), 101-109.

ISO, 2008. Hydrogen fuel - product specification - Part 2: proton exchange membrane (PEM) fuel cell applications for road vehicles, ISO/TS 14687-2. International organization for standardization.

Itoh, N., Akiha, T., Sato, T., Preparation of thin palladium composite membrane tube by a CVD technique and its hydrogen permselectivity. *Catal. Today* **2005**, 104 (2-4), 231-237.

Iyoha, O., Enick, R., Killmeyer, R., Howard, B., Morreale, B., Ciocco, M., Wall-catalyzed water-gas shift reaction in multi-tubular Pd and 80 wt%Pd-20 wt%Cu membrane reactors at 1173 K. *J. Memb. Sci.* **2007**, 298 (1-2), 14-23.

Jacobs, G., Crawford, A.C., Davis, B.H., Water-gas shift: steady state isotope switching study of the water-gas shift reaction over Pt/ceria using in-situ DRIFTS. *Catal. Lett.* **2005**, 100 (3-4), 147-152.

Jacobs, G., Williams, L., Graham, U., Thomas, G.A., Sparks, D.E., Davis, B.H., Low temperature water-gas shift: in situ DRIFTS-reaction study of ceria surface area on the evolution of formates on Pt/CeO_2 fuel processing catalysts for fuel cell applications. *Appl. Catal., A* **2003**, 252 (1), 107-118.

Kanai, Y., Watanabe, T., Fujitani, T., Saito, M., Nakamura, J., Uchijima, T., Evidence for the migration of ZnO_x in a Cu/ZnO methanol synthesis catalyst. *Catal. Lett.* **1994**, 27 (1-2), 67-78.

Karpenko, A., Leppelt, R., Cai, J., Plzak, V., Chuvilin, A., Kaiser, U., Behm, R.J., Deactivation of a Au/CeO_2 catalyst during the low-temperature water-gas shift reaction and its reactivation: A combined TEM, XRD, XPS, DRIFTS, and activity study. *J. Catal.* **2007**, 250 (1), 139-150.

Kikuchi, E., Uemiya, S., Matsuda, T., Hydrogen-production from methane steam reforming assisted by use of membrane reactor. *Stud. Surf. Sci. Catal.* **1991**, 61, 509-515.

Kikuchi, E., Uemiya, S., Sato, N., Inoue, H., Ando, H., Matsuda, T., Membrane reactor using microporous glass-supported thin-film of palladium - 1. Application to the water gas shift reaction. *Chem. Lett.* **1989**, 3, 489-492.

Kim, C.H., Thompson, L.T., Deactivation of Au/CeO_x water gas shift catalysts. *J. Catal.* **2005**, 230 (1), 66-74.

Kleinert, A., Grubert, G., Pan, X.L., Hamel, C., Seidel-Morgenstern, A., Caro, J., Compatibility of hydrogen transfer via Pd-membranes with the rates of heterogeneously catalysed steam reforming. *Catal. Today* **2005**, 104 (2-4), 267-273.

Kochloefel, K., Water gas shift and COS removal. In *Handbook of heterogenous catalysis*, Ertl, G., Knözinger, H., Weitkamp, J., Eds. Weinheim: VCH Verlagsgesellschaft mbH, 1997; Vol. 4.

Koros, W.J., Ma, Y.H., Shimidzu, T., Terminology for membranes and membrane processes. *Pure Appl. Chem.* **1996**, 68 (7), 1479-1489.

Koryabkina, N.A., Phatak, A.A., Ruettinger, W.F., Farrauto, R.J., Ribeiro, F.H., Determination of kinetic parameters for the water-gas shift reaction on copper catalysts under realistic conditions for fuel cell applications. *J. Catal.* **2003**, 217 (1), 233-239.

Kusar, H., Hocevar, S., Levec, J., Kinetics of the water-gas shift reaction over nanostructured copper-ceria catalysts. *Appl. Catal., B* **2006**, 63 (3-4), 194-200.

Ladebeck, J.R., Wang, J.P., Catalyst development for water-gas shift. In *Handbook of fuel cells, fuel cell technology and applications*, John Wiley & Sons, England, 2003; Vol. 3, pp. 190-201.

Leppelt, R., Schumacher, B., Plzak, V., Kinne, M., Behm, R.J., Kinetics and mechanism of the low-temperature water-gas shift reaction on Au/CeO_2 catalysts in an idealized reaction atmosphere. *J. Catal.* **2006**, 244 (2), 137-152.

Liang, W.Q., Hughes, R., The catalytic dehydrogenation of isobutane to isobutene in a palladium/silver composite membrane reactor. *Catal. Today* **2005a**, 104 (2-4), 238-243.

Liang, W.Q., Hughes, R., The effect of diffusion direction on the permeation rate of hydrogen in palladium composite membranes. *Chem. Eng. J.* **2005b**, 112 (1-3), 81-86.

Lin, Y.M., Lee, G.L., Rei, M.H., An integrated purification and production of hydrogen with a palladium membrane-catalytic reactor. *Catal. Today* **1998**, 44 (1-4), 343-349.

Lin, Y.M., Liu, S.L., Chuang, C.H., Chu, Y.T., Effect of incipient removal of hydrogen through palladium membrane on the conversion of methane steam reforming: Experimental and modeling. *Catal. Today* **2003**, 82 (1-4), 127-139.

Lin, Y.S., Microporous and dense inorganic membranes: current status and prospective. *Sep. Purif. Technol.* **2001**, 25 (1-3), 39-55.

Liu, P., Rodriguez, J.A., Water-gas-shift reaction on metal nanoparticles and surfaces. *J. Chem. Phys.* **2007**, 126, 164705.

Lloyd, L., Ridler, D.E., Twigg, M.V., The Water-gas shift reaction. In *Catalyst handbook*, 2nd ed.; Twigg, M.V., Ed. Wolfe Publishing Ltd., London, 1989.

Lu, G.Q., da Costa, J.C.D., Duke, M., Giessler, S., Socolow, R., Williams, R.H., Kreutz, T., Inorganic membranes for hydrogen production and purification: A critical review and perspective. *J. Colloid Interface Sci.* **2007**, 314 (2), 589-603.

Luengnaruemitchai, A., Osuwan, S., Gulari, E., Comparative studies of low-temperature water-gas shift reaction over Pt/CeO_2, Au/CeO_2, and Au/Fe_2O_3 catalysts. *Catal. Commun.* **2003**, 4 (5), 215-221.

Lund, C.R.F., Effect of adding Co to MoS_2/Al_2O_3 upon the kinetics of the water-gas shift. *Ind. Eng. Chem. Res.* **1996**, 35 (9), 3067-3073.

Lund, C.R.F., 2002. Water-Gas shift kinetics over iron oxide catalysts at membrane reactor conditions, Grant DE-FG26-99FT40590. Final Report to the U.S. Department of Energy.

Luo, W., Ishikawa, K., Aoki, K., High hydrogen permeability in the Nb-rich Nb-Ti-Ni alloy. *J. Alloys Compd.* **2006**, 407 (1-2), 115-117.

Marcano, J.G.S., Tsotsis, T.T., *Catalytic membranes and membrane reactors*. 1 ed.; Wiley-VCH: Weinheim, Germany, 2002.

Mavrikakis, M., Stoltze, P., Norskov, J.K., Making gold less noble. *Catal. Lett.* **2000**, 64 (2-4), 101-106.

McLeary, E.E., Jansen, J.C., Kapteijn, F., Zeolite based films, membranes and membrane reactors: Progress and prospects. *Microporous and Mesoporous Materials* **2006**, 90 (1-3), 198-220.

Mejdell, A.L., Klette, H., Ramachandran, A., Borg, A., Bredesen, R., Hydrogen permeation of thin, free-standing Pd/Ag23% membranes before and after heat treatment in air. *J. Memb. Sci.* **2008**, 307 (1), 96-104.

Mellor, J.R., Copperthwaite, R.G., Coville, N.J., The selective influence of sulfur on the performance of novel cobalt-based water-gas shift catalysts. *Appl. Catal., A* **1997**, 164 (1-2), 69-79.

Mendes, D., Garcia, H., Silva, V.B., Mendes, A., Madeira, L.M., Comparison of nanosized gold-based and copper-based catalysts for the low-temperature water-gas shift reaction. *Ind. Eng. Chem. Res.* **2009**, 48 (1), 430-439.

Miller, J.Q., Stöcker, J., 1999. Selection of a hydrogen separation process. UOP LLC, Des Plaines, IL.

Moe, J.M., Design of water-gas shift reactors. *Chem. Eng. Prog.* **1962**, 58 (3), 33-36.

Mond, L., Langer, C., 1888. Improvements in obtaining hydrogen. British Patent No. 12608.

Mori, T., 2005. RD&D for launching the initial market by hydrogen from natural gas, Proceedings of the International Hydrogen Energy Congress and Exhibition (IHEC) Istanbul, Turkey.

Nair, B.K.R., Choi, J., Harold, M.P., Electroless plating and permeation features of Pd and Pd/Ag hollow fiber composite membranes. *J. Memb. Sci.* **2007**, 288 (1-2), 67-84.

Nair, B.K.R., Harold, M.P., Pd encapsulated and nanopore hollow fiber membranes: Synthesis and permeation studies. *J. Memb. Sci.* **2007**, 290 (1-2), 182-195.

Nam, S.E., Lee, S.H., Lee, K.H., Preparation of a palladium alloy composite membrane supported in a porous stainless steel by vacuum electrodeposition. *J. Memb. Sci.* **1999**, 153 (2), 163-173.

Natesakhawat, S., Wang, X.Q., Zhang, L.Z., Ozkan, U.S., Development of chromium-free iron-based catalysts for high-temperature water-gas shift reaction. *J. Mol. Catal. A: Chem.* **2006**, 260 (1-2), 82-94.

Newsome, D.S., The Water-Gas shift reaction. *Catal. Rev.-Sci. Eng* **1980**, 21 (2), 275-318.

Nishimura, C., Komaki, M., Hwang, S., Amano, M., V-Ni alloy membranes for hydrogen purification. *J. Alloys Compd.* **2002**, 330, 902-906.

Okada, S., Mineshige, A., Kikuchi, T., Kobune, M., Yazawa, T., Cermet-type hydrogen separation membrane obtained from fine particles of high temperature proton-conductive oxide and palladium. *Thin Solid Films* **2007**, 515 (18), 7342-7346.

Panzera, G., Modafferi, V., Candamano, S., Donato, A., Frusteri, F., Antonucci, P.L., CO selective oxidation on ceria-supported Au catalysts for fuel cell application. *J. Power Sources* **2004**, 135 (1-2), 177-183.

Patel, N., Ludwig, K., Morris, P., Insert flexibility into your hydrogen network - Part 1. *Hydrocarbon Process., Int. Ed.* **2005**, 75-84.

Phair, J.W., Donelson, R., Developments and design of novel (non-palladium-based) metal membranes for hydrogen separation. *Ind. Eng. Chem. Res.* **2006**, 45 (16), 5657-5674.

Phatak, A.A., Koryabkina, N., Rai, S., Ratts, J.L., Ruettinger, W., Farrauto, R.J., Blau, G.E., Delgass, W.N., Ribeiro, F.H., Kinetics of the water-gas shift reaction on Pt catalysts supported on alumina and ceria. *Catal. Today* **2007**, 123 (1-4), 224-234.

Qi, X.M., Flytzani-Stephanopoulos, M., Activity and stability of Cu-CeO_2 catalysts in high-temperature water-gas shift for fuel-cell applications. *Ind. Eng. Chem. Res.* **2004**, 43 (12), 3055-3062.

Quirk, R.P., Ammonia. In *Kirk-Othmer Encyclopedia of Chemical Engineering Technology*, 1963; Vol. 2.

Radhakrishnan, R., Willigan, R.R., Dardas, Z., Vanderspurt, T.H., Water gas shift activity and kinetics of Pt/Re catalysts supported on ceria-zirconia oxides. *Appl. Catal., B* **2006**, 66 (1-2), 23-28.

Rangel Costa, J.L., Marchetti, G.S., Rangel, M.C., A thorium-doped catalyst for the high temperature shift reaction. *Catal. Today* **2002**, 77 (3), 205-213.

Rase, H.F., *Handbook of commercial catalysts: Heterogeneous catalysts*. CRC Press: Boca Raton, FL, 2000.

Rhodes, C., Hutchings, G.J., Studies of the role of the copper promoter in the iron oxide/chromia high temperature water gas shift catalyst. *Phys. Chem. Chem. Phys.* **2003**, 5 (12), 2719-2723.

Rhodes, C., Hutchings, G.J., Ward, A.M., Water-Gas Shift reaction - Finding the mechanistic boundary. *Catal. Today* **1995**, 23 (1), 43-58.

Rhodes, C., Williams, B.P., King, F., Hutchings, G.J., Promotion of Fe_3O_4/Cr_2O_3 high temperature water gas shift catalyst. *Catal. Commun.* **2002**, 3 (8), 381-384.

Roa, F., Way, J.D., McCormick, R.L., Paglieri, S.N., Preparation and characterization of Pd-Cu composite membranes for hydrogen separation. *Chem. Eng. J.* **2003**, 93 (1), 11-22.

Rodriguez, J.A., Liu, P., Hrbek, J., Evans, J., Perez, M., Water gas shift reaction on Cu and Au nanoparticles supported on $CeO_2(111)$ and $ZnO(000_1)$: Intrinsic activity and importance of support interactions. *Angew. Chem.-Int. Edit.* **2007**, 46 (8), 1329-1332.

Ruettinger, W.F., Ilinich, O., Water Gas shift reaction (WGSR) In *Encyclopedia of chemical processing* Lee, S., Ed. Taylor & Francis: 2006; pp. 3205-3215.

Ryi, S.K., Park, J.S., Kim, S.H., Cho, S.H., Park, J.S., Kim, D.W., Development of a new porous metal support of metallic dense membrane for hydrogen separation. *J. Memb. Sci.* **2006**, 279 (1-2), 439-445.

Sakurai, H., Akita, T., Tsubota, S., Kiuchi, M., Haruta, M., Low-temperature activity of Au/CeO_2 for water gas shift reaction, and characterization by ADF-STEM, temperature-programmed reaction, and pulse reaction. *Appl. Catal., A* **2005**, 291 (1-2), 179-187.

Sakurai, H., Ueda, A., Kobayashi, T., Haruta, M., Low-temperature water-gas shift reaction over gold deposited on TiO_2. *Chem. Commun.* **1997**, (3), 271-272.

Saracco, G., Specchia, V., Catalytic inorganic-membrane reactors: Present experience and future opportunities. *Cat. Rev.- Sci. Eng.* **1994**, 36 (2), 305-384.

Sato, K., Hanaoka, T.A., Niwa, S., Stefan, C., Namba, T., Mizukami, F., Direct hydroxylation of aromatic compounds by a palladium membrane reactor. *Catal. Today* **2005**, 104 (2-4), 260-266.

Shido, T., Iwasawa, Y., Reactant-promoted reaction-mechanism for water gas shift reaction on Rh-doped CeO_2. *J. Catal.* **1993**, 141 (1), 71-81.

Shoko, E., McLellan, B., Dicks, A.L., da Costa, J.C.D., Hydrogen from coal: Production and utilisation technologies. *Int. J. Coal Geol.* **2006**, 65 (3-4), 213-222.

Shu, J., Grandjean, B.P.A., Kaliaguine, S., Methane steam reforming in asymmetric Pd-Ag and Pd-Ag/porous SS membrane reactors. *Appl. Catal., A* **1994**, 119 (2), 305-325.

Shu, J., Grandjean, B.P.A., Vanneste, A., Kaliaguine, S., Catalytic palladium-based membrane reactors: A review. *Can. J. Chem. Eng.* **1991**, 69 (5), 1036-1060.

Steele, B.C.H., Heinzel, A., Materials for fuel-cell technologies. *Nature* **2001**, 414 (6861), 345-352.

Stöcker, J., Whysall, M., Miller, G.Q., 1998. 30 years of PSA technology for hydrogen purification. UOP LLC, Des Plaines, IL.

Swartz, S.L., Seabaugh, M.M., Holt, C.T., Dawson, W.J., Fuel processing catalysts based on nanoscale ceria. *Fuel Cell Bull.* **2001**, 4 (30), 7-10.

Tabakova, T., Boccuzzi, F., Manzoli, M., Sobczak, J.W., Idakiev, V., Andreeva, D., Effect of synthesis procedure on the low-temperature WGS activity of Au/ceria catalysts. *Appl. Catal., B* **2004**, 49 (2), 73-81.

Tabakova, T., Boccuzzi, F., Manzoli, M., Sobczak, J.W., Idakiev, V., Andreeva, D., A comparative study of nanosized IB/ceria catalysts for low-temperature water-gas shift reaction. *Appl. Catal., A* **2006a**, 298, 127-143.

Tabakova, T., Boccuzzi, F.B., Manzoli, M., Andreeva, D., FTIR study of low-temperature water-gas shift reaction on gold/ceria catalyst. *Appl. Catal., A* **2003**, 252 (2), 385-397.

Tabakova, T., Idakiev, V., Andreeva, D., Mitov, I., Influence of the microscopic properties of the support on the catalytic activity of Au/ZnO, Au/ZrO_2, Au/Fe_2O_3, Au/Fe_2O_3-ZnO, Au/Fe_2O_3-ZrO_2 catalysts for the WGS reaction. *Appl. Catal., A* **2000**, 202 (1), 91-97.

Tabakova, T., Idakiev, V., Tenchev, K., Boccuzzi, F., Manzoli, M., Chiorino, A., Pure hydrogen production on a new gold-thoria catalyst for fuel cell applications. *Appl. Catal., B* **2006b**, 63 (1-2), 94-103.

Tanaka, Y., Utaka, T., Kikuchi, R., Sasaki, K., Eguchi, K., Water gas shift reaction over Cu-based mixed oxides for CO removal from the reformed fuels. *Appl. Catal., A* **2003**, 242 (2), 287-295.

Tereschenko, G.F., Ermilova, M.M., Mordovin, V., Orekhova, N.V., Gryaznov, V.M., Iulianelli, A., Gallucci, F., Basile, A., New Ti-Ni dense membranes with low palladium content. *Int. J. Hydrogen Energy* **2007**, 32 (16), 4016-4022.

Thomas, J.M., Thomas, W.J., *Principles and practice of heterogeneous catalysis*. Wiley - VCH: Weinheim, Germany, 1997.

Tong, J.H., Shirai, R., Kashima, Y., Matsumura, Y., Preparation of a pinhole-free Pd-Ag membrane on a porous metal support for pure hydrogen separation. *J. Memb. Sci.* **2005a**, 260 (1-2), 84-89.

Tong, J.H., Suda, H., Haraya, K., Matsumura, Y., A novel method for the preparation of thin dense Pd membrane on macroporous stainless steel tube filter. *J. Memb. Sci.* **2005b**, 260 (1-2), 10-18.

Topsøe, H., Boudart, M., Mössbauer spectroscopy of CO shift catalysts promoted with lead. *J. Catal.* **1973**, 31 (3), 346-359.

Tosti, S., Basile, A., Bettinali, L., Borgognoni, F., Chiaravalloti, F., Gallucci, F., Long-term tests of Pd-Ag thin wall permeator tube. *J. Memb. Sci.* **2006**, 284 (1-2), 393-397.

Tosti, S., Basile, A., Chiappetta, G., Rizzello, C., Violante, V., Pd-Ag membrane reactors for water gas shift reaction. *Chem. Eng. J.* **2003**, 93 (1), 23-30.

Tosti, S., Bettinali, L., Violante, V., Rolled thin Pd and Pd-Ag membranes for hydrogen separation and production. *Int. J. Hydrogen Energy* **2000a**, 25 (4), 319-325.

Tosti, S., Violante, V., Basile, A., Chiappetta, G., Castelli, S., De Francesco, M., Scaglione, S., Sarto, F., Catalytic membrane reactors for tritium recovery from tritiated water in the ITER fuel cycle. *Fusion Eng. Des.* **2000b**, 49, 953-958.

Trovarelli, A., Catalytic properties of ceria and CeO_2-containing materials. *Cat. Rev.- Sci. Eng.* **1996**, 38 (4), 439-520.

Twigg, M.V., Spencer, M.S., Deactivation of supported copper metal catalysts for hydrogenation reactions. *Appl. Catal., A* **2001**, 212 (1-2), 161-174.

Uemiya, S., Sato, N., Ando, H., Kikuchi, E., The water gas shift reaction assisted by a palladium membrane reactor. *Ind. Eng. Chem. Res.* **1991**, 30 (3), 585-589.

Utaka, T., Okanishi, T., Takeguchi, T., Kikuchi, R., Eguchi, K., Water gas shift reaction of reformed fuel over supported Ru catalysts. *Appl. Catal., A* **2003**, 245 (2), 343-351.

van Dyk, L., Miachon, S., Lorenzen, L., Torres, M., Fiaty, K., Dalmon, J.A., Comparison of microporous MFI and dense Pd membrane performances in an extractor-type CMR. *Catal. Today* **2003**, 82 (1-4), 167-177.

Venugopal, A., Scurrell, M.S., Hydroxyapatite as a novel support for gold and ruthenium catalysts: Behaviour in the water gas shift reaction. *Appl. Catal., A* **2003**, 245 (1), 137-147.

Violante, V., Basile, A., Drioli, E., Membrane separation technologies - Their application to the fusion reactor fuel cycle. *Fusion Eng. Des.* **1993**, 22 (3), 257-263.

Wang, D., Tong, H.H., Xu, H.Y., Matsumura, Y., Preparation of palladium membrane over porous stainless steel tube modified with zirconium oxide. *Catal. Today* **2004**, 93-95, 689-693.

Weintraub, B., Ludwig Mond: Great Chemist-Industrialist; Alfred Mond (Lord Melchett): Great Zionist Leader. *Bulletin of the Israel Chemical Society* **2003**, 14, 26-31.

Wu, L.Q., Xu, N.P., Shi, J., Preparation of a palladium composite membrane by an improved electroless plating technique. *Ind. Eng. Chem. Res.* **2000**, 39 (2), 342-348.

Xue, E., OKeeffe, M., Ross, J.R.H., Water-gas shift conversion using a feed with a low steam to carbon monoxide ratio and containing sulphur. *Catal. Today* **1996**, 30 (1-3), 107-118.

Yan, S.C., Maeda, H., Kusakabe, K., Morooka, S., Thin palladium membrane formed in support pores by metalorganic chemical vapor deposition method and application to hydrogen separation. *Ind. Eng. Chem. Res.* **1994**, 33 (3), 616-622.

Yepes, D., Cornaglia, L.M., Irusta, S., Lombardo, E.A., Different oxides used as diffusion barriers in composite hydrogen permeable membranes. *J. Memb. Sci.* **2006**, 274 (1-2), 92-101.

Yeragi, D.C., Pradhan, N.C., Dalai, A.K., Low-temperature water-gas shift reaction over Mn-promoted Cu/Al_2O_3 catalysts. *Catal. Lett.* **2006**, 112 (3-4), 139-148.

Yuan, Z.Y., Idakiev, V., Vantomme, A., Tabakova, T., Ren, T.Z., Su, B.L., Mesoporous and nanostructured CeO_2 as supports of nano-sized gold catalysts for low-temperature water-gas shift reaction. *Catal. Today* **2008**, 131 (1-4), 203-210.

Yurieva, T.M., Minyukova, T.P., State of copper in Cu-Zn-Al oxide catalysts for methanol synthesis. *React. Kinet. Catal. Lett.* **1985**, 29 (1), 55-61.

Zalc, J.M., Sokolovskii, V., Loffler, D.G., Are noble metal-based water-gas shift catalysts practical for automotive fuel processing? *J. Catal.* **2002**, 206 (1), 169-171.

Zerva, C., Philippopoulos, C.J., Ceria catalysts for water gas shift reaction: Influence of preparation method on their activity. *Appl. Catal., B* **2006**, 67 (1-2), 105-112.

Zhang, Y., Gwak, J., Murakoshi, Y., Ikehara, T., Maeda, R., Nishimura, C., Hydrogen permeation characteristics of thin Pd membrane prepared by microfabrication technology. *J. Memb. Sci.* **2006**, 277 (1-2), 203-209.

Zhang, Y., Lu, J., Maeda, R., Nishimura, C., Microfabricated pd and Pd-25Ag alloy membranes. *J. Alloys Compd.* **2007**, 446, 579-582.

Zheng, X.C., Zhang, X.L., Wang, X.Y., Wu, S.H., Influence of ceria preparation method on the performance of CuO/CeO_2 catalysts. *React. Kinet. Catal. Lett.* **2007**, 92 (2), 195-203.

Chapter 3

Comparison of Nanosized Gold-Based and Copper-Based Catalysts for the Low-Temperature WGS Reaction

In this chapter, the catalytic performances for the low-temperature water-gas shift reaction of different catalysts – Au/TiO_2 type A (from World Gold Council), Au/CeO_2 (developed at UPV-CSIC), CuO/Al_2O_3 (from BASF) and $CuO/ZnO/Al_2O_3$ (from REB Research & Consulting) – have been compared. The catalysts were characterized by different techniques such as Raman spectroscopy, BET surface area measurements, temperature-programmed reduction, and high-resolution transmission electron microscopy, which gave additional information on the redox properties, textural and morphological structure of the investigated samples. The performances of these catalysts were evaluated in a wide range of operating conditions in a packed-bed reactor. It was observed that the presence of reaction products in the feed (CO_2 and H_2), as well as CO and H_2O feed concentrations, have significant effects on the catalytic performances. With a simulated reformate feed the Au/CeO_2 catalyst reveals the highest CO conversion at the lowest temperature investigated (150 °C). However, while in the deactivation tests performed the $CuO/ZnO/Al_2O_3$ catalyst showed a good stability for the entire range of temperatures tested ($150-300$ ºC), the Au/CeO_2 sample clearly showed two distinct behaviors: a progressive deactivation at lower temperatures and a good stability at higher ones. The selection of the best catalytic system is therefore clearly dependent upon the range of temperatures used.

The contents of this chapter were adapted from: Mendes, D., Garcia, H., Silva, V.B., Mendes, A., Madeira, L.M., Comparison of nanosized gold-based and copper-based catalysts for the low-temperature water-gas shift reaction. *Ind. Eng. Chem. Res.* **2009**, 48 (1), 430-439.

3.1 Introduction

The WGS (equation 1.1) is a moderate exothermic reaction where high conversions can only be achieved operating at low temperatures. On the other hand, under such conditions the reaction is controlled by the kinetics, so highly active and stable low-temperature WGS catalysts are needed.

Due to the lack of a systematic study in which the most promising catalytic systems are tested under similar conditions, in this work the catalytic performances of various commercially available catalysts, namely, Au/TiO_2 type A (World Gold Council), CuO/Al_2O_3 (BASF), $CuO/ZnO/Al_2O_3$ (REB Research & Consulting), and a laboratory-made one, Au/CeO_2, for conducting the WGS reaction at temperatures ranging from 150 ºC to 300 °C are compared. The experimental tests were carried out in a fixed-bed reactor where criteria parameters such as the CO conversion level and stability were used to perform catalyst evaluation and selection. The runs were done in a wide range of operating conditions (steam/gas ratio and temperature) under a simulated reforming feed composition. Several characterization techniques have also been employed to provide insight into the properties of the investigated samples.

3.2 Experimental Section

3.2.1 Catalyst preparation

Nanoparticulated ceria ($npCeO_2$) was firstly prepared adding under stirring, at ambient temperature, an ammonia aqueous solution (1.12 L, 0.8 M) over 375 mL of $Ce(NO_3)_4$ (0.8 M). The colloidal dispersion of CeO_2 nanoparticles was heated in a poly(ethylene terephthalate) (PET) vessel at 100 ºC during 24 h. The resulting yellow precipitate was filtered using a membrane of 3 kDa, washed with deionized water and dried under vacuum overnight. The cerium oxide synthesized, which was prepared following a procedure

previously described (Chane-Ching, 1987), showed a very high surface area (S_{BET} = 180 $m^2 \cdot g^{-1}$, measured by adsorption of N_2), owing to the small size of the nanoparticles (~ 5 nm).

The gold/ceria sample was then prepared by the deposition-precipitation method. Therefore, gold was deposited on the nanoparticulated ceria using the following procedure: a solution of $HAuCl_4.3H_2O$ (270 mg) in 160 mL of deionized water was brought to pH 10 by addition of a 0.2 M NaOH solution. Once the pH value was stable, the solution was added to a gel containing colloidal CeO_2 (4.01 g) in H_2O (50 mL). After adjusting the pH of the slurry to a value of 10 by adding a 0.2 M solution of NaOH, the slurry was maintained at room temperature under vigorous stirring for 18 h. The Au/npCeO_2 solid was then filtered and exhaustively washed with several liters of distilled water until no traces of chlorides were detected by the $AgNO_3$ test. This step has the goal to avoid the presence of Cl^- which can strongly adsorb on the cationic sites of the catalyst. The sample was dried under vacuum at room temperature for 1 h. Then, the supported catalyst was added over 1-phenylethanol at 160 ºC and the mixture was allowed to react for 20 minutes (this ensures complete reduction of gold nanoparticles). Finally, the catalyst was filtered, washed with acetone and water, and dried under vacuum at room temperature. The total Au content of the final Au/npCeO_2 catalyst was 1.5 wt.%, as determined by chemical analysis (atomic absorption spectroscopy).

The Au/TiO_2 catalyst was bought from the World Gold Council (U.K.) and is referred to as a reference Au catalyst (type A). The CuO/Al_2O_3 sample (CU-1271, Selectra Shift) was supplied by BASF (Germany), and the CuO/ZnO/Al_2O_3 commercial catalyst (~ 50 wt.% CuO and 40 wt.% ZnO) was acquired from REB Research and Consulting, Ferndale, MI. Both Cu-based catalysts were crushed and sieved to give a particle size of < 180 μm (similar to that of the powdered gold solids).

3.2.2 Techniques used for catalysts characterization

3.2.2.1 Adsorption of nitrogen (measurement of the superficial area)

The N_2 adsorption/desorption isotherms were used to determine the superficial specific area of the catalytic materials. The measurements were performed using a Micromeritics 2000 ASAP automated gas sorption analyzer at the temperature of liquid nitrogen (77 K). The samples were exhaustively outgassed at 450 ºC under vacuum (10^{-4} Torr) before area measurements.

The superficial specific area of the materials was calculated by using the BET (Brunauer-Emmett-Teller) equation (Brunauer et al., 1938), as follows:

$$\frac{P}{V\left(P_o - P\right)} = \frac{1}{V_m \cdot c} + \frac{c-1}{V_m \cdot c} \times \frac{P}{P_o} \qquad (2.1)$$

where V is the volume of adsorbed gas at pressure P, V_m is the volume of gas required for monolayer coverage, P_o is the gas pressure required for saturation at the temperature of the experiment, and c is a constant related to the heat of adsorption and liquefaction (BET constant). Once the value V_m is determined, the specific surface area (S_{BET}) can be calculated by the following equation:

$$S_{BET} = N_a \cdot \sigma \cdot V_m / V_o \qquad (2.2)$$

where N_a is the Avogadro's number (6.02×10^{23} molecules·mol^{-1}), σ is the cross-sectional area of the adsorbate, and V_o is the molar volume.

3.2.2.2 High-resolution transmission electron microscopy

Samples for transmission electron microscopy (TEM) were prepared by suspending the catalyst powders by ultrasonication in isopropyl alcohol and depositing a drop of the suspension on a metallic (copper in case of Au-based catalysts and gold in case of Cu-based

samples) grid, coated with a porous carbon film. The grid was finally air-dried for 15 minutes.

For crystal analysis and indexation, Au/npCeO_2 samples were examined by bright- and dark-field electron microscopy in a JEOL 2200 FS equipped with a field emission gun, operating at 200 kV and with a point resolution of 0.23 nm. For the other catalysts, the electronic microscopy images were obtained by bright-field electron microscopy in a Philips-CM10 at 100 kV. Moreover, in order to be representative and statistically meaningful, many images from several regions of various samples were recorded and the most characteristic results are here presented.

3.2.2.3 Chemical analysis

Chemical analysis of Au in Au/CeO_2 sample was carried out using a Philips MiniPal 25 fm analytic X-ray apparatus and the corresponding calibration plot.

3.2.2.4 Raman spectroscopy

Raman spectra were collected with a Renishaw inVia Raman spectrometer equipped with a Leica DMLM microscope and a diode laser (785 nm) as excitation source. A ×50 objective of 8 mm optical length was used to focus the depolarized laser beam on a spot of about 2 μm in diameter, and the laser power at the sample was 16.0 mW. Raman scattering was measured with a CCD array detector in the $100-2000$ cm^{-1} spectral region with a resolution of 2 cm^{-1}. Each reported spectrum is the average of 10 scans of different areas of the solid, each with an exposure time of 10 seconds.

3.2.2.5 H_2-Temperature programmed reduction

Temperature programmed reduction (TPR) experiments were carried out with a Micromeritics Autochem 2910 apparatus equipped with a thermal conductivity detector

(TCD). The reactor consisted of a quartz U-shaped tube where the sample (100 mg), diluted with inert SiC to avoid thermal gradients, was introduced. A thermocouple in contact with the catalytic bed allowed the control of the temperature inside the catalyst. Before the TPR was started, the samples were pretreated in argon at room temperature for 30 min with a flow rate of 15 $mL_N \cdot min^{-1}$. The samples were subsequently contacted with a H_2/Ar mixture (H_2/Ar molar ratio of 0.10 and a total flow of 50 $mL_N \cdot min^{-1}$) and heated, at a rate of 10 $K \cdot min^{-1}$, up to a final temperature of 1100 K.

3.2.3 Experimental reaction apparatus, procedures, and analysis

The catalytic activity determined for the WGS reaction is expressed as the degree of CO conversion. The experiments were carried out using a conventional packed-bed reactor operating isothermally and at atmospheric pressure. The 6 mm i.d. stainless steel reactor was encased in an electric oven (Memmert, Type UNE200), controlled by a programmable temperature controller (cf. Figure 3.1). The reactor was typically loaded with 250 mg of the catalyst, supported by two fritted Teflon disks (PTFE 25 μm, Omnifit) to avoid the catalyst powder dispersion over the pipes. In the stability tests, the reactor was loaded with 150 mg of catalyst. A thermocouple was introduced from the top of the reactor, and it was placed at the center of the catalyst bed, which was shown to operate under isothermal conditions (within ± 2 °C).

All the WGS catalysts were activated *in situ* with a mixed gas flow of H_2/N_2 measured by means of mass flow controllers. The reduction protocols applied were based on literature information to ensure complete metal oxide reduction, without sintering (Ginés et al., 1995; Leppelt et al., 2006). For Cu-based catalysts the reduction protocol considers heating the catalyst, in nitrogen, from room temperature to 80 °C; then the reduction mixture (5 vol.% H_2/N_2, total flow rate of 30 $mL_N \cdot min^{-1}$) is admitted, and the samples are heated at 5 $°C \cdot min^{-1}$ from 80 ºC to 230 °C and maintained at this temperature for 4 h. Nevertheless, the

terminology used when referring to these samples is the commercial one, which makes reference to the copper oxide state. For Au-based catalysts the reduction protocol considers heating to 200 °C in a N_2 stream and keeping the solids at this temperature for 30 min. Subsequently, reduction is performed for 45 min in a 10 vol.% H_2/N_2 stream (at a total flow rate of 30 $mL_N \cdot min^{-1}$), followed by 30 min in a N_2 flow, both at 200 °C. In all cases, after reduction, the catalysts were cooled or heated to the reaction temperature and the reactor was flushed with N_2 prior to the introduction of the reaction mixture. To avoid overheating of the catalyst bed and subsequent metal particle sintering, strict temperature and hydrogen flow rate controls were performed.

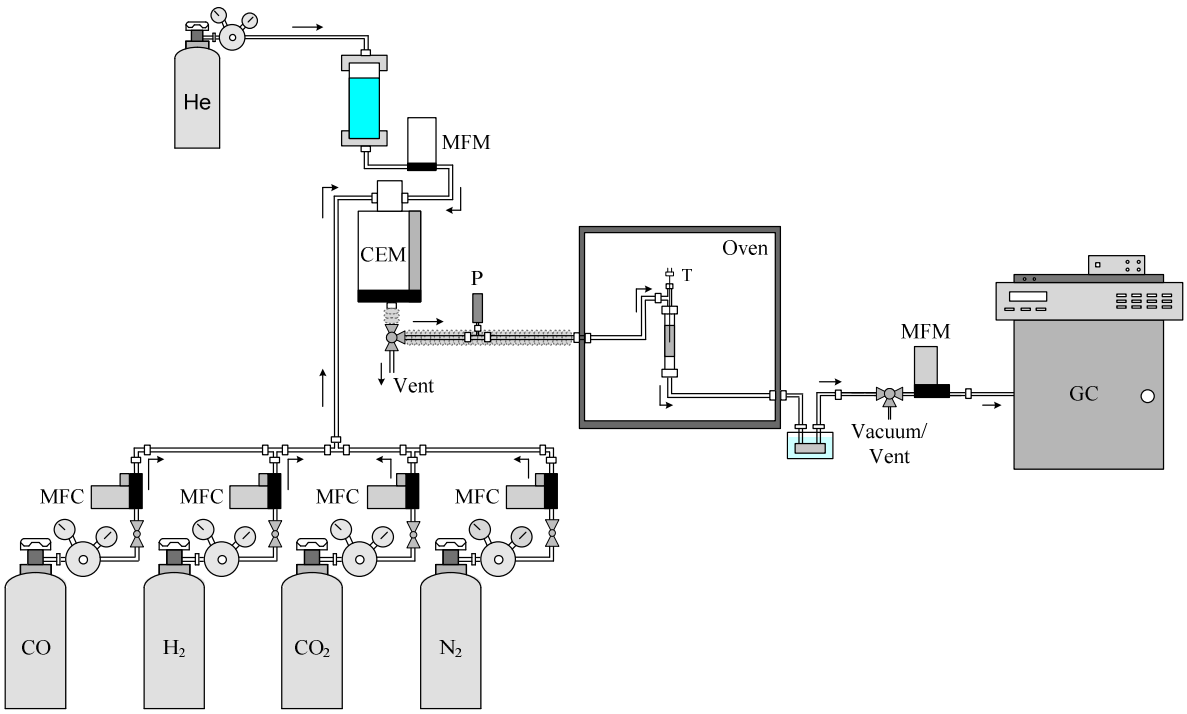

Figure 3.1 – Scheme of the experimental set-up (CEM: controller-evaporator-mixer; GC: gas chromatograph; MFC: mass flow controller; MFM: mass flow meter; P: pressure gauge; T: thermocouple).

The reaction was started by introducing, for instance, a typical reforming gas mixture of 4.70 % CO, 34.78 % H_2O, 28.70 % H_2, 10.16 % CO_2, and 21.66 % N_2 (vol.%) in the reactor feed, using four mass flow controllers (Bronkhorst Hi-Tec, model F201) – cf. Figure 3.1.

Deionized water was metered, vaporized, and mixed in a controller evaporator mixer (CEM, Bronkhorst) system with the other gases before entering the reactor. The GHSV (gas hourly space velocity) was fixed at 4800 $mL_N \cdot g_{cat}^{-1} \cdot h^{-1}$ and the reaction temperature varied between 150 °C and 300 °C. The pressure was measured using a pressure transducer (Druck, ref. 4010, 7 bar). The reactor outlet stream was passed through a condenser at ≈ 10 °C to remove water before further analysis. The gas-phase products were then analyzed in an online gas chromatograph (Dani 1000 GC). A chromatographic column (Supelco Carboxen 1010 plot, from Sigma-Aldrich, 30 m × 0.32 mm i.d.), with He as the carrier gas (1 $mL_N \cdot min^{-1}$) and a TCD (Valco thermal conductivity detector), was used to analyze N_2, CO, and CO_2 (more details regarding the GC operating conditions and the calibration method can be found in Appendix A). The carbon and the nitrogen molar balance relative errors were typically lower than 10 %. Regarding hydrogen, it is well-known that it is difficult to measure its composition by GC with the used detector since its thermal conductivity is close to that of helium, the carrier gas. Therefore, the H_2 composition in the gas streams was calculated from the mass balance (difference from 100 %, dry basis), which is required for mass flow rate corrections. During the analysis, a temperature program was used as follows: (i) isothermal operation at 35 °C for 7.5 min; (ii) heating from 35 ºC to 80 °C with a rate of 10 $°C \cdot min^{-1}$; (iii) keeping the sample at 80 °C for 8 min. All the pipes and valves along the water feed stream and in the reactor exit were heated to 130 °C to prevent the condensation of water.

3.3 Results and Discussion

3.3.1 Characterization of the samples

The structural and morphological properties of the samples used in this work were first investigated. The metal loading (in the case of copper samples, this refers to the oxide form),

the surface areas of the formulations, and the average size of the metal particles, as estimated by the HRTEM technique, are given in Table 3.1.

As illustrated in Figure 3.2, spherical copper particles homogeneously distributed on the respective surface were obtained for the CuO/Al_2O_3 sample, for which HRTEM results indicate an average size of around 9.2 nm (cf. Table 3.1). The low copper content in this catalyst is evident in the picture since only a little aggregation is seen. For the $CuO/ZnO/Al_2O_3$ solid the smaller particle size and the higher copper loading are perceptively presented in the picture since a higher density of CuO particles (aggregation) is seen (Figure 3.2). This also occurs for the Au-based catalysts, in which the particle size is even smaller, being particularly noticed for the Au/TiO_2 sample. HRTEM was used to report the size of gold nanoparticles. Therefore, the gold nanoparticles have been identified by the fringe distance shown in Figure 3.3 that corresponds to the gold interatomic distance.

Table 3.1 – Physical properties of the studied samples.

Sample	**Active metal loading (wt.%)**	**S_{BET} (m^2/g)**	**Average metal particle size (nm)**
CuO/Al_2O_3	5–20 [a]	110	9.2
$CuO/ZnO/Al_2O_3$	~ 50 [a]	9.0	6.9
Au/TiO_2	1.5 [a]	37	4.0
Au/CeO_2	1.5	180	4.4 [b]

[a] Data given by the manufacturer.

[b] 200 particles were counted, due to the poor contrast between gold and ceria.

The catalysts were also studied by Raman spectroscopy (Figure 3.4). In the case of CuO/Al_2O_3 no peaks were recorded, probably due to the strong fluorescence of the material. In contrast, for $CuO/ZnO/Al_2O_3$ and Au/CeO_2 the peaks characteristic of ZnO (380 cm^{-1}) and CeO_2 (475 cm^{-1}) were observed. In the latter sample, the observed peak corresponds to the Ce-O vibration bond. The Au-Au vibration appears below 200 cm^{-1} and is not visible due to

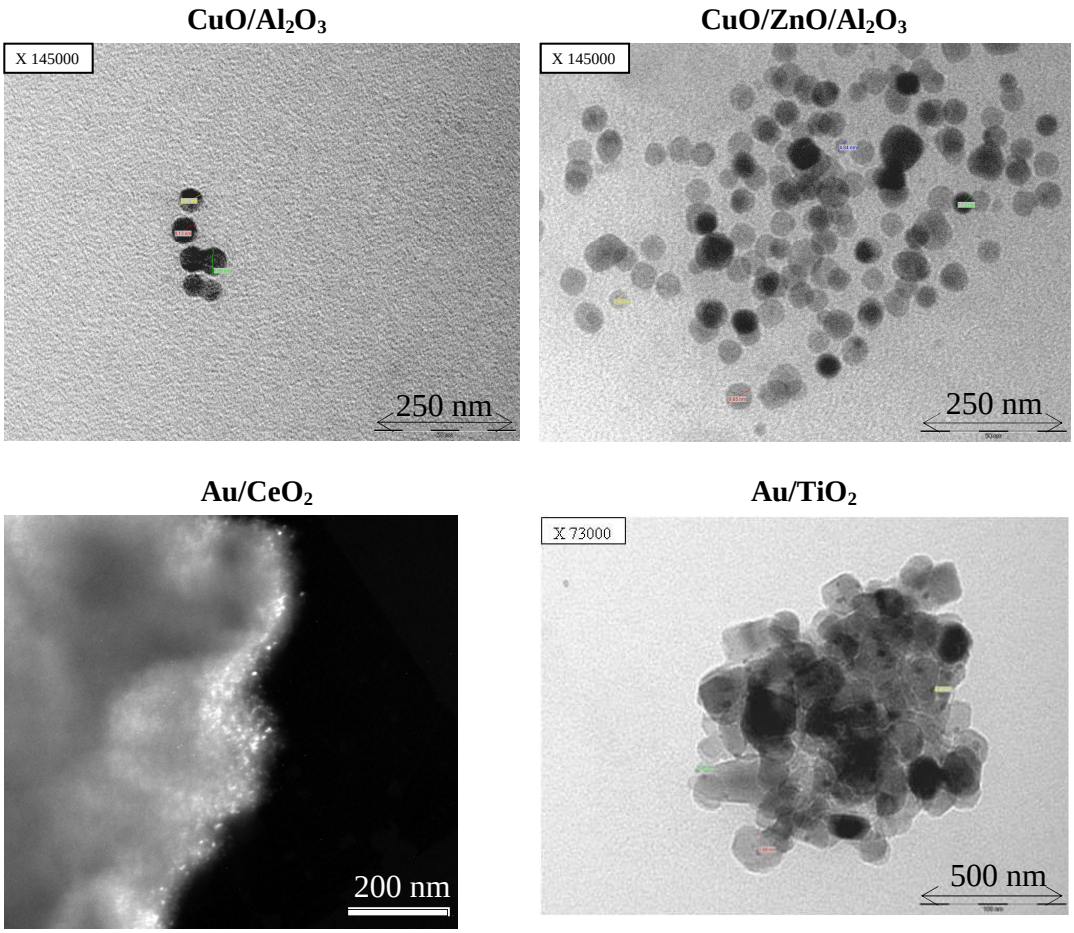

Figure 3.2 – TEM pictures of the catalyst samples studied.

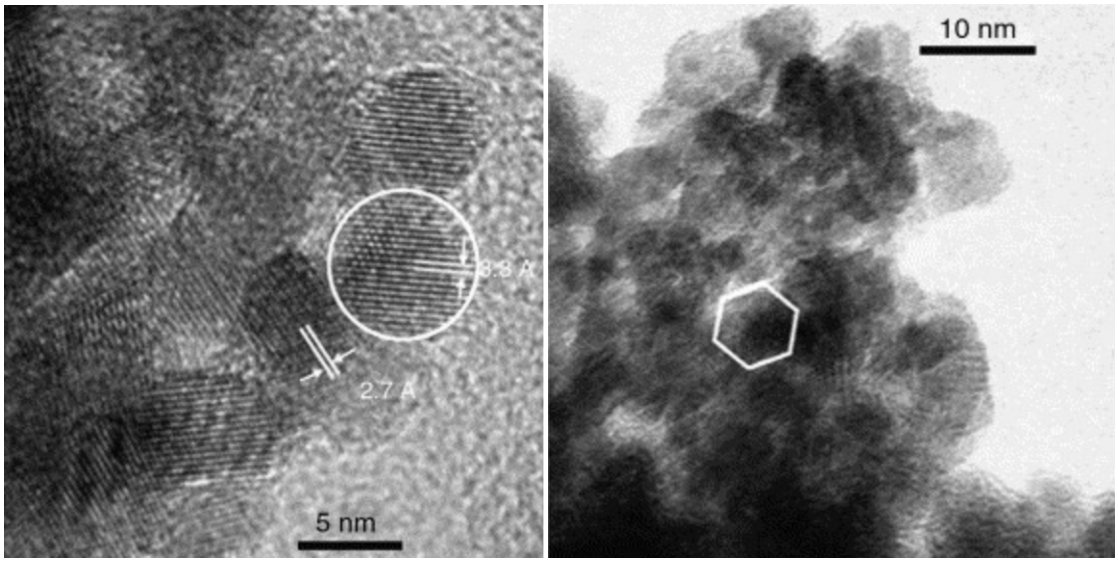

Figure 3.3 – Left: High resolution TEM of the Au/CeO_2 sample, the white lines correspond to the (202) (3.3 Å) Ce_6O_{11} and the (200) CeO_2 (2.7 Å) lattice spacing. Right: A hexagonal faceted (111) Au crystal is circled.

the low loading of the materials and the low intensity of the peak. From the Au/TiO_2 Raman spectrum it can also be concluded that titanium dioxide is predominantly constituted by the anatase phase (due to the well-known TiO_2 anatase bands at 398, 516, and 640 cm^{-1}).

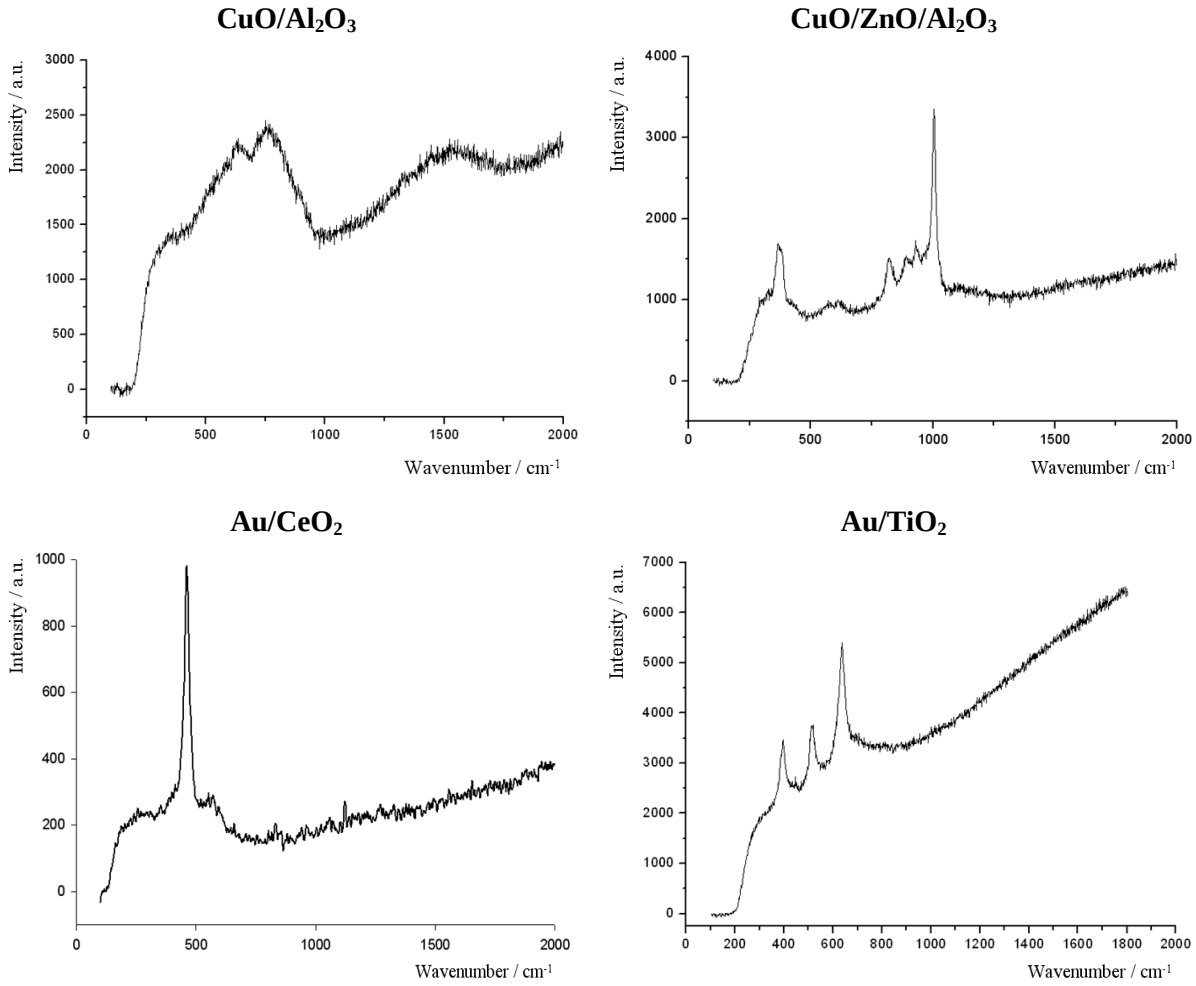

Figure 3.4 – Raman spectra of the catalysts studied in this work.

The TPR technique was used to evaluate the reducibility of the synthesized sample, before and after Au addition to the ceria support. The redox characteristics of this type of catalyst are known to be relevant for their performance in the WGS reaction. Comparison of the TPR profiles of CeO_2 and Au/CeO_2 clearly reveals that the presence of gold nanoparticles on the surface of the ceria support exerts a remarkable influence, favoring the reducibility of this metal oxide (Figure 3.5). Thus, the reduction peak that appears at about

470 °C in CeO_2 becomes considerably shifted to much lower temperatures (about 95 °C) when gold nanoparticles are present in the solid. The peak in the TPR profile at 63 °C is most probably related to the reduction of oxygen species, adsorbed during calcination in air, on some nanogold particles smaller than 2 nm, in accordance with Boccuzzi et al. (Boccuzzi et al., 2001). In conclusion, Figure 3.5 shows the reducibility increase of the Au/CeO_2 sample with the TPR promotional effect of gold on the surface reduction of ceria, leading to the creation of oxygen vacancies. Therefore, the gold particles located in close contact with these oxygen-vacancy defects of ceria may be very active sites for WGS reaction.

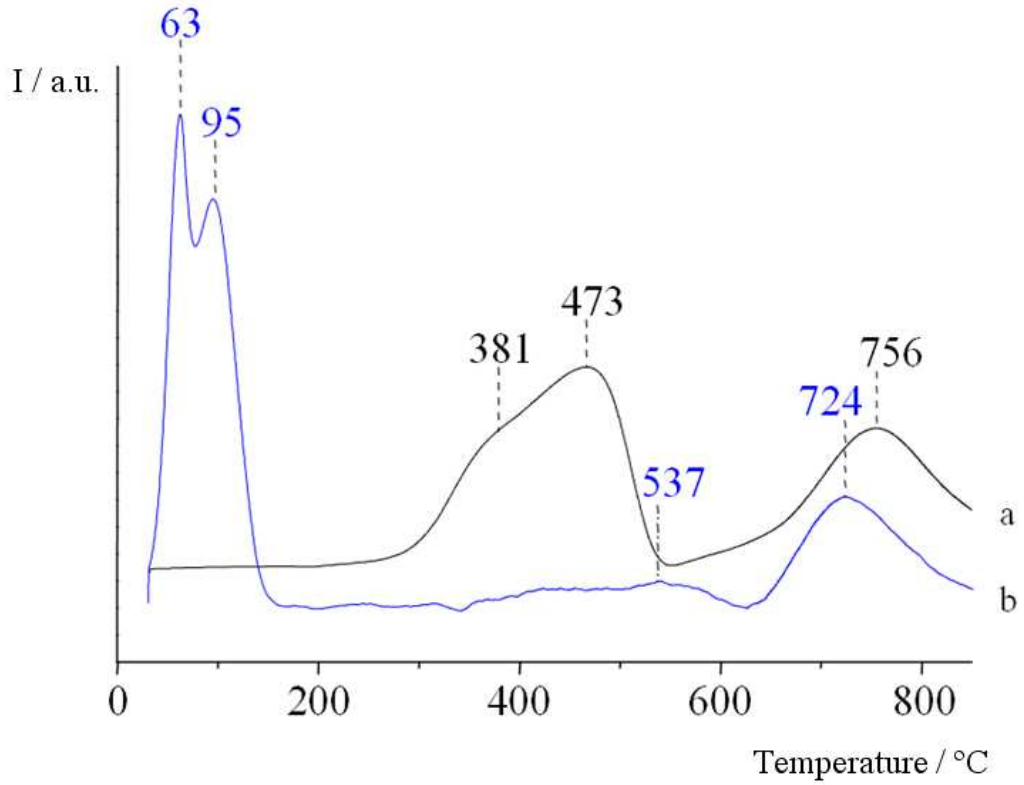

Figure 3.5 – Thermoprogrammed reduction by hydrogen gas of CeO_2 (a) and Au/CeO_2 (b).

3.3.2 Catalytic tests

In this section the catalytic performance of Au/CeO_2 toward the WGS reaction is compared with that of three commercial catalysts: (i) Au/TiO_2, purchased from the World Gold Council and which has the same Au content and a similar average particle size (cf.

Table 3.1); (ii) the commercial CuO/Al_2O_3 (CU-1271, Selectra shift) received from BASF; (iii) the commercial $CuO/ZnO/Al_2O_3$ purchased from REB Research & Consulting. The catalytic tests started by performing experiments using two different feeds: one with just CO and H_2O (diluted in He) and the other with a typical reformate composition (4.70 % CO, 34.78 % H_2O, 28.70 % H_2, and 10.16 % CO_2 balanced in N_2). The effects of H_2O and CO concentration in the feed are also important to analyze, and this was therefore done for each catalyst, at different temperatures. Data presented below concern the steady state (each data point in the graphs results from the average of at least three analyses; the maximum standard deviation obtained was 1.5 %) with the exception of the Au/CeO_2 sample, because in this case some catalyst deactivation was observed (see section 3.3.2.4 regarding stability tests). For this reason the activity measurements for this sample began at high temperatures (in which deactivation is negligible) and ended at low temperatures, the CO conversion being measured in the first 10 000 s until a relative error below ca. 5 % was obtained, in three consecutive analyses. During the night, the catalysts being tested were under a N_2 atmosphere to avoid reoxidation.

3.3.2.1 Effect of reaction products in the feed composition

Figure 3.6 illustrates the effect of the reaction products (H_2 and CO_2) on the performance attained by each catalytic system at different temperatures. As expected, the CO conversion increases with the reaction temperature due to the kinetic constraints, in some cases approaching the thermodynamic equilibrium conversion (dashed lines in the figures). After this point, the conversion decreases due to the exothermic nature of the reaction. The equilibrium conversion (X_{CO}^{eq}) values were calculated on the basis of the equilibrium constant (equation 1.2) obtained by Moe (Moe, 1962). Assuming ideal gas behavior, the equilibrium conversion was then obtained by solving equation 1.3.

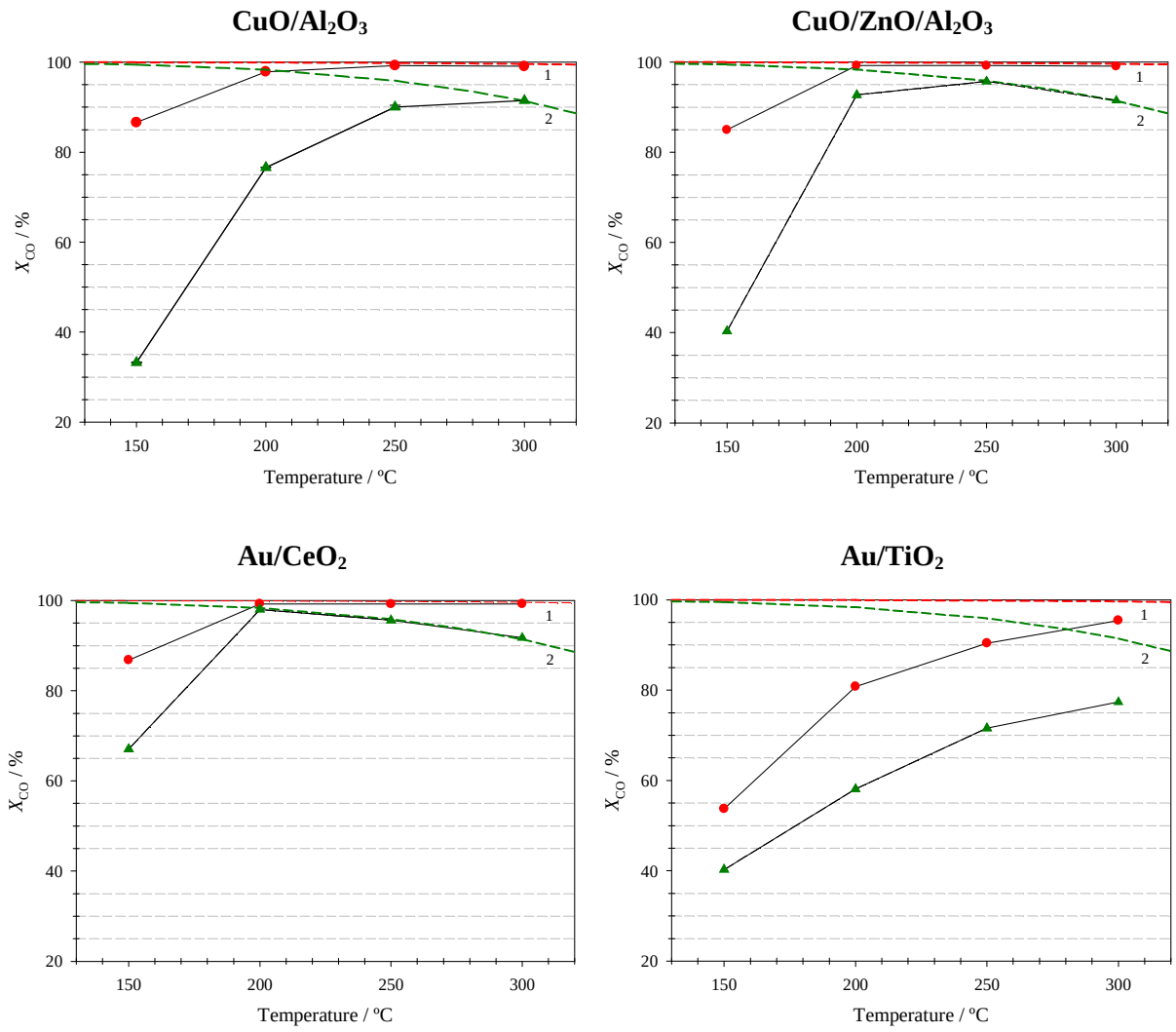

Figure 3.6 - The effect of reaction products in the feed stream over the CO conversion for each catalyst, at different temperatures. The lines represent the thermodynamic conversion. Feed composition: (●, 1) 4.74 % CO + 35.39 % H_2O and 59.87 % He, (▲, 2) 4.74 % CO + 35.39 % H_2O + 28.46 % H_2 + 10.06 % CO_2 and 21.35 % N_2.

Under only CO and water in helium, catalysts CuO/Al_2O_3, $CuO/ZnO/Al_2O_3$, and Au/CeO_2 reveal a similar CO conversion that is higher than that reached by the Au/TiO_2 sample in the entire range of temperature tested (Figure 3.6). At 150 °C and for the first group of catalysts, the CO conversion reached is similar and approximately 86 %, although for the Au/CeO_2 formulation this value is already affected by some deactivation noticed at low temperatures (cf. section 3.3.2.4 about stability tests). At higher temperatures the CO

conversions tend to that predicted by the thermodynamics, but are always higher than that exhibited by the Au/TiO_2 catalyst.

The detrimental effect of H_2 and CO_2 in the feed stream is clearly noted in all the catalysts tested, in agreement with *Le Chatelier's* principle (reaction equilibrium shifts in the opposite direction, toward reactant formation, decreasing CO conversion). Several authors use empirical power law models to fit the kinetic data. Most of them show the negative effect of the presence of one or both reaction products (Amadeo and Laborde, 1995; Ayastuy et al., 2005; Ovesen et al., 1992). In our case, the major difference was obtained for the CuO/Al_2O_3 sample at 150 °C, reaching a CO conversion of only 33 % when the reaction products are present in the reactor feed, compared with 87 % in their absence. At 150 °C both Cu-based catalysts are shown to be strongly affected by the presence of CO_2 and H_2. However, this drawback seems to be attenuated with the temperature increase. The presence of ZnO seems to be important in terms of the performance reached, i.e. in terms of tolerance to the presence of hydrogen and carbon dioxide. It is worth noting that the role of ZnO and Al_2O_3 regarding the WGS activity and the nature of the active sites for copper-based catalysts is still controversial. Besides their role as structural promoters (Campbell and Daube, 1987; Fujitani et al., 1994; Koryabkina et al., 2003; Yurieva et al., 1993), both oxides gathered some literature support working also as chemical promoters. In fact, several authors observed an enhancement in the catalytic activity of Cu supported on ZnO due to synergetic effects responsible for improved covalency between the different oxidation states of copper in the metal lattice (Ghiotti and Boccuzzi, 1987; Ginés et al., 1995; Shido and Iwasawa, 1991; Shishido et al., 2006). Moreover, the catalytic performance improvement from binary CuO/ZnO to ternary $CuO/ZnO/Al_2O_3$ catalysts reveals the effect of adding alumina; alumina is reported to form a hydrotalcite phase that improves the catalyst performance (Ginés et al., 1995). On the other hand, the lower copper loading in the CuO/Al_2O_3 catalyst (see Table 3.1) might influence the lower CO conversion obtained with this sample.

Under the operating conditions of Figure 3.6, the Au/CeO_2 sample shows the best performance. It is known that, for Au-based catalysts, the synthesis method (which was the same for both samples – deposition/precipitation) and corresponding conditions affect their WGS performance. Nevertheless, the influence of the gold support (ceria or titania) may have a major role in terms of their activity. As succeeds with Cu-based catalysts, many authors believe that the WGS reaction on supported noble materials, namely, on reducible metal oxides (CeO_2, TiO_2, ZrO_2 ...), is a bifunctional system too. The reaction mechanism is assumed to be conducted in two different sites: the dispersed metallic phase, which is mainly responsible for adsorption/activation of CO, and the metal oxide support, which is hydrophilic in nature and is mainly responsible for adsorption/activation of H_2O (Grenoble et al., 1981; Jacobs et al., 2005; Panagiotopoulou et al., 2006). Both ceria and titania have the capacity to be reduced under the WGS reaction conditions. Several authors refer to the reducibility of the support as being an important key to a higher catalyst activity due to the formation of either oxygen vacancies within the support or partially reduced sites at the metal-support interface (Frost, 1988; Fu et al., 2003; Golunski et al., 2002; Jacobs et al., 2005; Panagiotopoulou et al., 2006). Thus, the higher WGS activity obtained with the ceria-supported catalyst can be due to its higher redox capacity and mobility of the surface oxygen/hydroxyl group when compared with the titania-supported catalyst. Indeed, Idakiev et al. (Idakiev et al., 2004) also found a shift of the TPR peak to low temperatures after incorporation of Au in TiO_2 (from 400 ºC to 100 °C), but the intensity of such a low-temperature peak is almost negligible compared to that of the original support, in opposition to what happens for the Au/CeO_2 sample (see section 3.3.1). Finally, the higher surface area of the ceria support, also responsible for a better metal dispersion, is certainly an important parameter for the activity enhancement attained.

3.3.2.2 Effect of the CO content in the feed

The effect of the CO content in the feed stream is also important to analyze due to the inherent implications on the thermodynamic equilibrium. In addition, this also allows to study the performance of WGS catalysts under different feed compositions as happens when the WGS feed proceeds from different steam reforming processes and hydrocarbon feedstocks. The effect of the CO concentration on the conversion is illustrated in Figure 3.7.

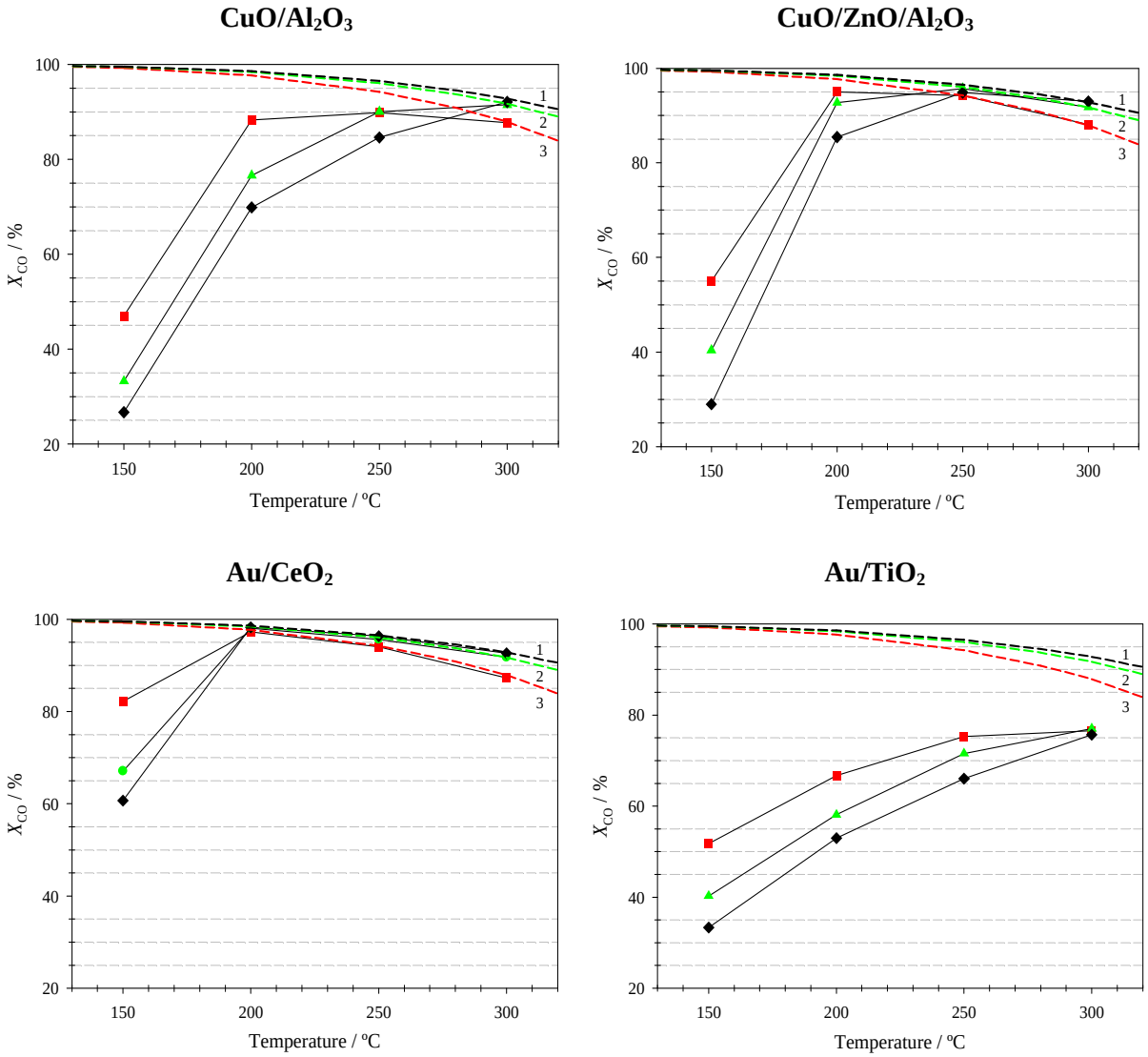

Figure 3.7 – The effect of CO content in the feed stream composition over the CO conversion for each catalyst, at different temperatures. The lines represent the thermodynamic conversion. Feed composition: (◆, 1) 9.42 % CO, (▲, 2) 4.74 % CO, (■, 3) 2.38 % CO. In all cases the rest of the feed is 35.39 % H_2O, 28.46 % H_2, 10.06 % CO_2 and balance in N_2.

The CO concentration decrease in the gas feed produces an increase in the performance of all catalysts, at least at 150 °C. This behavior seems to be not consistent with that predicted by *Le Chatelier's* principle, but is also observed in other works (Amadeo and Laborde, 1995; Luengnaruemitchai et al., 2003). Amadeo and Laborde (Amadeo and Laborde, 1995) studied the influence of the partial pressure of the WGS reactants and products on the CO conversion over a copper-based commercial catalyst at 503 K. The authors justified the observed negative effect by the proportional formation of CO_2 when the feed CO partial pressure increases. In the work by Luengnaruemitchai et al. (Luengnaruemitchai et al., 2003), the effect of CO and H_2O concentrations over the catalytic performance of Au/CeO_2 was studied, with an idealized feed consisting of $0.5-2$ % CO and 2.6 % H_2O in helium. However, no explanation was given for the negative effect of the increasing CO concentration for this catalytic system. Nevertheless, as the temperature increases the catalytic systems tested in this work tend to create a "zone" where the effect of the CO concentration on the catalytic performance is less significant, revealing that its effect on the conversion can change with the reaction temperature (Figure 3.7). However, this zone is located at different temperatures, according to the higher or lower catalyst activity. Beyond that region, the data tend to follow the equilibrium conversion lines, as predicted by *Le Chatelier's* principle (the conversion is higher for higher CO contents in the reactant feed, because this shifts the equilibrium).

For Cu-based WGS catalysts different reaction orders regarding CO concentration have been reported. For instance, Ayastuy et al. (Ayastuy et al., 2005) and Ovesen et al. (Ovesen et al., 1992) reported a unity order of reaction with respect to CO over ternary Cu-based catalysts. On the other hand, Salmi and Hakkarainen (Salmi and Hakkarainen, 1989) reported variable CO reaction orders as a function of temperature, ranging from 1 to 0.45. For Au/CeO_2 catalysts Leppelt et al. (Leppelt et al., 2006) reported a CO reaction order of 0.5 (see Table 2.2). In fact, for all WGS catalysts studied the CO positive reaction order is

verified only above a certain temperature. The negative (retardation) effect observed in this work for both Cu and Au catalysts at lower temperatures can be explained on the basis of the associative mechanism, namely, on the intermediate species (formates and/or carbonates) formed during the reaction. Once the CO concentration increases, the formation of intermediate species also increases. At lower temperatures, the coverage of this species over the catalyst surface increases for both copper-based (Rhodes et al., 1995) and gold-based (Karpenko et al., 2007) catalysts due to a slower decomposition of these intermediates into the final reaction products. Therefore, a blocking effect of the active sites by the reaction intermediates, which is more severe at lower temperatures, should happen, decreasing the overall CO conversion; this is also behind the deactivation observed for the Au/CeO_2 catalyst at lower temperatures (section 3.3.2.4). The decomposition of formates and/or carbonates is favored by the temperature increase, the CO conversion being no longer negatively affected by the CO partial pressure (in most cases it is inclusively positively affected). The temperature range of this transition clearly depends on the performance of each catalytic system. It is therefore important that the usage of empirical power rate laws available in the literature takes into account the temperature range (and other operating conditions) in which the experiments are performed.

The Cu-based catalysts used in this study presented a similar behavior, where the apparent negative order dependence on CO happens in the same temperature range. However, for the Au-based catalysts this does not happen. From Figure 3.7 it is clear that, for the Au/TiO_2 sample, no positive order dependence on CO was attained in the used range of temperatures. On the other hand, for the Au/CeO_2 sample the positive effect was reached at around 200 °C. Assuming the above-mentioned catalyst's bifunctionality, it is found that the supports responsible for the H_2O activation can be responsible for this difference. As referred to above, the synergistic effects between gold (where CO is adsorbed) and titania are lower

than with ceria; therefore, in the latter the formation of intermediate hydroxyl groups (via adsorbed water) is not limiting, so higher CO contents are favorable for a higher activity.

The ceria-supported gold catalyst is, once again, the one that seems to be more promising because it is considerably active and less affected by the CO concentration, at least at low temperatures $(150-200\ ^{o}C)$. At high temperatures $(250-300\ ^{o}C)$ $CuO/ZnO/Al_2O_3$ exhibits a similar performance. Au/TiO_2 is the worst sample, also in agreement with the data of Figure 3.6.

3.3.2.3 Effect of the H_2O content in the feed

The dependence of the catalysts' performances on the water vapor concentration in the feed stream was also analyzed. It is clearly seen from Figure 3.8 that, in general, the water vapor content enhances the catalysts' performance in the temperature range $150-300\ ^{o}C$, in agreement with the thermodynamic prediction. This fact is also in agreement with the positive reaction order with respect to water obtained in power law rates (Amadeo and Laborde, 1995; Ayastuy et al., 2005; Leppelt et al., 2006; Ovesen et al., 1992; Salmi and Hakkarainen, 1989) – see also Table 2.2.

For the Au/TiO_2 sample the activity results in the temperature range $150-200\ ^{o}C$ are not influenced by the water vapor content. For higher temperatures the increase in the water vapor content above 35.39 % (v/v) does not bring any change in the CO conversion, clearly opposed to what happens with the other catalysts. Once again the influence of the support is clearly noticed. The Au/CeO_2 catalyst revealed to be, in terms of catalytic performance, the most promising one since no significant changes were detected with the water vapor concentration, and above 200 °C the conversion reaches the thermodynamic one. It seems therefore that the interaction between gold and ceria, which was highlighted by TPR, results in an activity enhancement. Actually, Rodriguez et al. (Rodriguez et al., 2007) pointed out

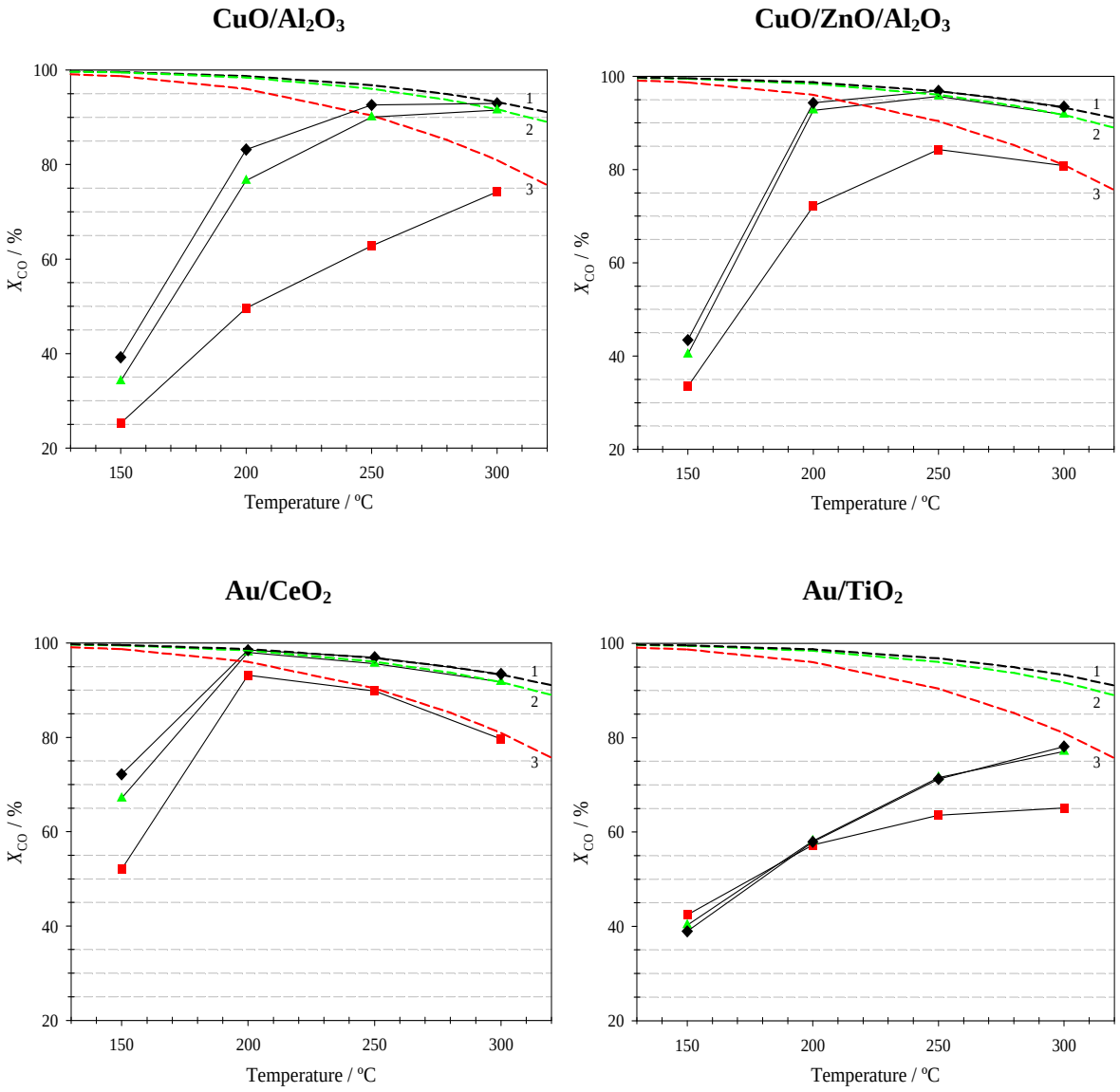

Figure 3.8 – The effect of H_2O content in the feed stream composition over the CO conversion for each catalyst, at different temperatures. The lines represent the thermodynamic conversion. Feed composition: (◆, 1) 43.74 % H_2O, (▲, 2) 35.39 % H_2O, (■, 3) 16.90 % H_2O. In all cases the rest of the feed is 4.74 % CO, 28.46 % H_2, 10.06 % CO_2 and balance in N_2.

recently that the noble metal nanoparticles promote the partial reduction of the ceria support by CO or CO/H_2O mixtures, creating in ceria surface oxygen vacancies where the H_2O activation takes place. This evidence corroborates the preview studies by Tabakova et al. (Tabakova et al., 2003), who have used FTIR spectroscopy to find experimental evidence for modification of ceria in the presence of gold and the appearance of oxygen vacancies at the ceria surface after reduction with hydrogen. The authors stressed the importance of oxygen

vacancies and showed that the WGS reaction proceeds at the boundary between small metallic gold particles and ceria, where CO adsorption on gold and H_2O dissociation on ceria defects take place. The difference in the support reducibility, as well as its capacity to allow the formation of OH groups, might be the responsible for the distinct behavior observed in the WGS activity of the two Au-based catalysts, when the water vapor concentration is changed.

In the literature it is reported that the water content is crucial for the CO conversion performance of a commercial CuO/ZnO catalyst (Ginés et al., 1995), in agreement with our results (Figure 3.8). Comparing both Cu-based catalysts, it can be seen that the $CuO/ZnO/Al_2O_3$ catalyst is less influenced by the H_2O concentration. This fact can be connected with the different structures of the Cu particles in each catalyst, described as a possible site for H_2O activation (Rodriguez et al., 2007). However, taking into account the catalyst bifunctionality suggested by Grenoble et al. (Grenoble et al., 1981), we may conclude that the support oxide sites are close to the maximum capacity to activate the water vapor. The $CuO/ZnO/Al_2O_3$ sample exhibits, once again, higher CO conversion than the CuO/Al_2O_3 sample.

3.3.2.4 Deactivation tests

An important issue to take into account for the industrial application of any catalyst in hydrogen fuel processing is its stability under WGS conditions. WGS copper-based catalysts are known to be highly stable; however, the gold-based ones, particularly when supported in ceria, have been subjected to extensive work to understand and overcome this problem. Generally, four issues have been widely discussed: (1) the sintering of the metal particles (Luengnaruemitchai et al., 2003; Wang et al., 2002), (2) the “irreversible” over-reduction of the ceria support (Ghenciu, 2002), (3) the loss of surface area of ceria (Burch, 2006; Fu et al., 2005), and (4) the blocking of the ceria surface by formation of surface carbonates and/or

formates (Deng and Flytzani-Stephanopoulos, 2006; Karpenko et al., 2007; Kim and Thompson, 2005).

The two most promising catalysts of this study were then evaluated in terms of their stability. The CO conversion levels were measured at different temperatures after reduction of the samples, and the results are shown in Figure 3.9. It can be seen that the $CuO/ZnO/Al_2O_3$ catalyst showed a better stability than Au/CeO_2 under the WGS reaction conditions. CuO/ZnO formulations are known to be deactivated by thermal sintering and/or poisoning of the catalyst surface at temperatures above 300 °C (Twigg and Spencer, 2001). In this case, under our experimental conditions, no signs of deactivation were detected, even at 300 °C, which is reported in the literature as being the maximum temperature to avoid the surface migration of the metal particles over the catalyst support. On the other hand, the catalytic activity of Au/CeO_2 decreased progressively at temperatures of 150 ºC and 200 °C, remaining stable at higher temperatures (see Figure 3.9).

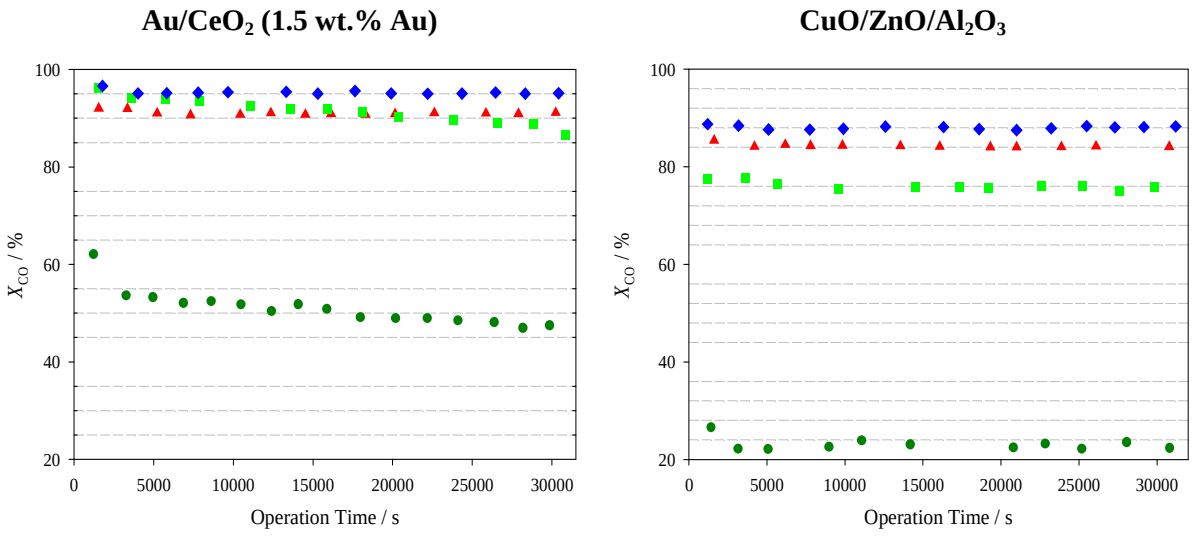

Figure 3.9 – The effect of the time on stream in the WGS activity, at different temperatures. Feed composition: 4.74 % CO, 35.39 % H_2O, 28.46 % H_2, 10.06 % CO_2 and 21.35 % N_2. Temperature: (◆) 300 ºC, (▲) 250 ºC, (■) 200 ºC, (●) 150 ºC.

It is therefore clear that the deactivation of the gold-based catalyst is strongly dependent on the temperature. Such deactivation of Au/CeO_2 seems to be not consistent with literature references about sintering of the gold particles, because when temperature increases, changes in conversion with time are not detectable. It is not possible to establish which deactivation(s) mechanism(s) is/are present; however, a surface fouling might occur since, at lower temperatures, where the intermediates decomposition is slower, reaction species might block the catalyst sites and consequently decrease the CO conversion. With the temperature increase, the intermediates decomposition is accelerated and no deactivation happens. This idea is in line with the work by Jacobs et al. (Jacobs et al., 2003), where it was concluded that formates are reaction intermediate species and that at higher temperatures their concentration is limited by the WGS reaction rate, while at lower temperatures the formate surface concentration remains close to the adsorption/desorption equilibrium. Karpenko and coauthors (Karpenko et al., 2007) also justified the deactivation behavior at lower temperatures, now due to the formation of carbonates adsorbed on the ceria support, blocking the sites. Therefore, the carbonate decomposition rate is too low to keep the steady-state carbonate coverage at a low level, promoting the catalyst deactivation. The authors confirmed the carbonate formation, obtaining complete catalyst activity regeneration with an oxidation treatment.

A comparison test in terms of CO conversion obtained for gold/ceria catalysts with different Au loadings (~ 1.5 wt.% and 2.5 wt.%) was then performed at 150 °C. The results are presented in Figure 3.10.

For the catalyst with higher Au loading a higher CO conversion was obtained during the first 30 000 s (~ 8.3 h). It is reported in the literature that the reaction rate of Au/CeO_2 catalysts varies as a volcano-type curve as a function of the gold metal loading. Maxima at 5 wt.% (Leppelt et al., 2006) and 3 wt.% (Andreeva et al., 2002) were reported. Nevertheless, Figure 3.10 shows also that the deactivation rate of this catalyst is higher than

for the 1.5 wt.% Au/ceria catalyst. The activity of the lower Au loading catalyst seems to remain nearly constant, after ca. 20 000 s (~ 5.6 h), a fact that can be explained by the adsorption/desorption equilibrium of carbonates and/or formates at the catalyst surface. The higher deactivation observed in the 2.5 wt.% Au/ceria catalyst might be due to the higher carbonate and/or formate concentration at the catalyst surface, formed at the beginning of the reaction as a consequence of its higher catalytic performance, leading thus to a higher surface coverage and promoting a stronger blocking effect.

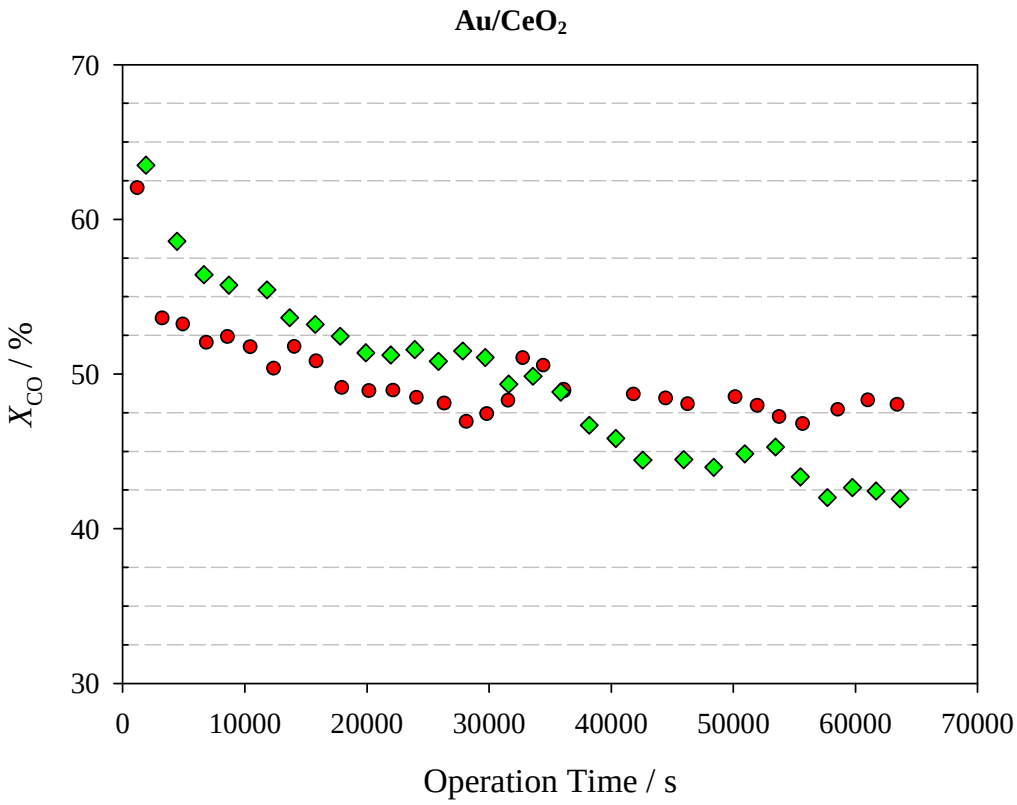

Figure 3.10 – The effect of the operation time in the WGS activity, at 150 ºC, for Au/CeO_2 catalysts with different Au loadings. Feed composition: 4.74 % CO, 35.39 % H_2O, 28.46 % H_2, 10.06 % CO_2 and 21.35 % N_2. Au loading: (♦) 2.5 wt.%, (●) 1.5 wt.%.

3.4 Conclusions

The catalytic performance of Au/TiO_2, Au/CeO_2, CuO/Al_2O_3, and $CuO/ZnO/Al_2O_3$ catalysts has been investigated for WGS reaction in the low temperature range. It was found

that the presence of reaction products in the feed stream has a higher negative effect on CO conversion for Cu-based catalysts when compared with the gold-based ones, namely, at 150 °C. Under the reformate conditions (4.74 % CO, 35.39 % H_2O, 28.46 % H_2, 10.06 % CO_2, balance N_2), the Au/CeO_2 sample is shown to be the most active (particularly at low temperatures, i.e. $150-200$ ºC). The activity of gold/ceria indicates that the support plays an important role in this reaction catalysis. The commercial $CuO/ZnO/Al_2O_3$ catalyst showed the best relation of activity/stability. In addition, it was found that the CO concentration present in the reactor feed greatly affects the activity of all catalysts tested. Depending on the reaction temperature, this effect is negative or positive in terms of the catalyst's performance. We also observed that water had a positive effect on CO conversion for all the catalysts, except for the Au/TiO_2 catalyst.

The results of this study indicate that the catalyst selection has to take into account the operation reaction temperature range. At temperatures ≥ 250 °C Au/CeO_2 is clearly a better option since it seems not to be affected by the deactivation mechanism and shows a higher CO conversion than $CuO/ZnO/Al_2O_3$. However, at lower temperatures, the stability is a negative factor for its selection and the latter seems to be a better option.

3.5 References

Amadeo, N.E., Laborde, M.A., Hydrogen production from the low-temperature water-gas shift reaction: kinetics and simulation of the industrial reactor. *Int. J. Hydrogen Energy* **1995**, 20 (12), 949-956.

Andreeva, D., Idakiev, V., Tabakova, T., Ilieva, L., Falaras, P., Bourlinos, A., Travlos, A., Low-temperature water-gas shift reaction over Au/CeO_2 catalysts. *Catal. Today* **2002**, 72 (1-2), 51-57.

Ayastuy, J.L., Gutierrez-Ortiz, M.A., Gonzalez-Marcos, J.A., Aranzabal, A., Gonzalez-Velasco, J.R., Kinetics of the low-temperature WGS reaction over a $CuO/ZnO/Al_2O_3$ catalyst. *Ind. Eng. Chem. Res.* **2005**, 44 (1), 41-50.

Boccuzzi, F., Chiorino, A., Manzoli, M., Lu, P., Akita, T., Ichikawa, S., Haruta, M., Au/TiO_2 nanosized samples: A catalytic, TEM, and FTIR study of the effect of calcination temperature on the CO oxidation. *J. Catal.* **2001**, 202 (2), 256-267.

Brunauer, S., Emmett, P.H., Teller, E., Adsorption of gases in multimolecular layers. *J. Am. Chem. Soc.* **1938**, 60, 309-319.

Burch, R., Gold catalysts for pure hydrogen production in the water-gas shift reaction: activity, structure and reaction mechanism. *Phys. Chem. Chem. Phys.* **2006**, 8 (47), 5483-5500.

Campbell, C.T., Daube, K.A., A surface science investigation of the water-gas shift reaction on Cu(111). *J. Catal.* **1987**, 104 (1), 109-119.

Chane-Ching, J.Y., 1987. Nouveau composé de cérium IV et son procédé de préparation, EP 0208580 A1.

Deng, W.L., Flytzani-Stephanopoulos, M., On the issue of the deactivation of Au-ceria and Pt-ceria water-gas shift catalysts in practical fuel-cell applications. *Angew. Chem. Int. Ed.* **2006**, 45 (14), 2285-2289.

Frost, J.C., Junction effect interactions in methanol synthesis catalysts. *Nature* **1988**, 334 (6183), 577-580.

Fu, Q., Deng, W.L., Saltsburg, H., Flytzani-Stephanopoulos, M., Activity and stability of low-content gold-cerium oxide catalysts for the water-gas shift reaction. *Appl. Catal., B* **2005**, 56 (1-2), 57-68.

Fu, Q., Saltsburg, H., Flytzani-Stephanopoulos, M., Active nonmetallic Au and Pt species on ceria-based water-gas shift catalysts. *Science* **2003**, 301 (5635), 935-938.

Fujitani, T., Saito, M., Kanai, Y., Kakumoto, T., Watanabe, T., Nakamura, J., Uchijima, T., The role of metal-oxides in promoting a copper catalyst for methanol synthesis. *Catal. Lett.* **1994**, 25 (3-4), 271-276.

Ghenciu, A.F., Review of fuel processing catalysts for hydrogen production in PEM fuel cell systems. *Curr. Opin. Solid State Mater. Sci.* **2002**, 6 (5), 389-399.

Ghiotti, G., Boccuzzi, F., Chemical and physical properties of copper-based catalysts for CO shift reaction and methanol synthesis. *Catal. Rev.-Sci. Eng* **1987**, 29 (2-3), 151-182.

Ginés, M.J.L., Amadeo, N., Laborde, M., Apesteguia, C.R., Activity and structure-sensitivity of the water-gas shift reaction over Cu-Zn-Al mixed-oxide catalysts. *Appl. Catal., A* **1995**, 131 (2), 283-296.

Golunski, S., Rajaram, R., Hodge, N., Hutchings, G.J., Kiely, C.J., Low-temperature redox activity in co-precipitated catalysts: a comparison between gold and platinum-group metals. *Catal. Today* **2002**, 72 (1-2), 107-113.

Grenoble, D.C., Estadt, M.M., Ollis, D.F., The chemistry and catalysis of the water gas shift reaction: 1. The kinetics over supported metal-catalysts. *J. Catal.* **1981**, 67 (1), 90-102.

Idakiev, V., Tabakova, T., Yuan, Z.Y., Su, B.L., Gold catalysts supported on mesoporous titania for low-temperature water-gas shift reaction. *Appl. Catal., A* **2004**, 270 (1-2), 135-141.

Jacobs, G., Graham, U.M., Chenu, E., Patterson, P.M., Dozier, A., Davis, B.H., Low-temperature water-gas shift: impact of Pt promoter loading on the partial reduction of ceria and consequences for catalyst design. *J. Catal.* **2005**, 229 (2), 499-512.

Jacobs, G., Williams, L., Graham, U., Thomas, G.A., Sparks, D.E., Davis, B.H., Low temperature water-gas shift: in situ DRIFTS-reaction study of ceria surface area on the evolution of formates on Pt/CeO_2 fuel processing catalysts for fuel cell applications. *Appl. Catal., A* **2003**, 252 (1), 107-118.

Karpenko, A., Leppelt, R., Cai, J., Plzak, V., Chuvilin, A., Kaiser, U., Behm, R.J., Deactivation of a Au/CeO_2 catalyst during the low-temperature water-gas shift reaction and its reactivation: A combined TEM, XRD, XPS, DRIFTS, and activity study. *J. Catal.* **2007**, 250 (1), 139-150.

Kim, C.H., Thompson, L.T., Deactivation of Au/CeO_x water gas shift catalysts. *J. Catal.* **2005**, 230 (1), 66-74.

Koryabkina, N.A., Phatak, A.A., Ruettinger, W.F., Farrauto, R.J., Ribeiro, F.H., Determination of kinetic parameters for the water-gas shift reaction on copper catalysts under realistic conditions for fuel cell applications. *J. Catal.* **2003**, 217 (1), 233-239.

Leppelt, R., Schumacher, B., Plzak, V., Kinne, M., Behm, R.J., Kinetics and mechanism of the low-temperature water-gas shift reaction on Au/CeO_2 catalysts in an idealized reaction atmosphere. *J. Catal.* **2006**, 244 (2), 137-152.

Luengnaruemitchai, A., Osuwan, S., Gulari, E., Comparative studies of low-temperature water-gas shift reaction over Pt/CeO_2, Au/CeO_2, and Au/Fe_2O_3 catalysts. *Catal. Commun.* **2003**, 4 (5), 215-221.

Moe, J.M., Design of water-gas shift reactors. *Chem. Eng. Prog.* **1962**, 58 (3), 33-36.

Ovesen, C.V., Stoltze, P., Norskov, J.K., Campbell, C.T., A kinetic model of the water gas shift reaction. *J. Catal.* **1992**, 134 (2), 445-468.

Panagiotopoulou, P., Christodoulakis, A., Kondarides, D.I., Boghosian, S., Particle size effects n the reducibility of titanium dioxide and its relation to the water-gas shift activity of Pt/TiO_2 catalysts. *J. Catal.* **2006**, 240 (2), 114-125.

Rhodes, C., Hutchings, G.J., Ward, A.M., Water-Gas Shift reaction - Finding the mechanistic boundary. *Catal. Today* **1995**, 23 (1), 43-58.

Rodriguez, J.A., Liu, P., Hrbek, J., Evans, J., Perez, M., Water gas shift reaction on Cu and Au nanoparticles supported on $CeO_2(111)$ and $ZnO(000_1)$: Intrinsic activity and importance of support interactions. *Angew. Chem.-Int. Edit.* **2007**, 46 (8), 1329-1332.

Salmi, T., Hakkarainen, R., Kinetic study of the low-temperature water-gas shift reaction over a Cu-ZnO catalyst. *Appl. Catal.* **1989**, 49 (2), 285-306.

Shido, T., Iwasawa, Y., Reactant promoted reaction mechanism for water-gas shift reaction on ZnO, as the genesis of surface catalysis. *J. Catal.* **1991**, 129 (2), 343-355.

Shishido, T., Yamamoto, M., Atake, I., Li, D.L., Tian, Y., Morioka, H., Honda, M., Sano, T., Takehira, K., Cu/Zn-based catalysts improved by adding magnesium for water-gas shift reaction. *J. Mol. Catal. A* **2006**, 253 (1-2), 270-278.

Tabakova, T., Boccuzzi, F.B., Manzoli, M., Andreeva, D., FTIR study of low-temperature water-gas shift reaction on gold/ceria catalyst. *Appl. Catal., A* **2003**, 252 (2), 385-397.

Twigg, M.V., Spencer, M.S., Deactivation of supported copper metal catalysts for hydrogenation reactions. *Appl. Catal., A* **2001**, 212 (1-2), 161-174.

Wang, X., Gorte, R.J., Wagner, J.P., Deactivation mechanisms for Pd/ceria during the water-gas-shift reaction. *J. Catal.* **2002**, 212 (2), 225-230.

Yurieva, T.M., Plyasova, L.M., Kriger, T.A., Zaikovskii, V.I., Makarova, O.V., Minyukova, T.P., State of copper-containing catalyst for methanol synthesis in the reaction medium. *React. Kinet. Catal. Lett.* **1993**, 51 (2), 495-500.

Chapter 4

Determination of the Low-Temperature Water-Gas Shift Reaction Kinetics using a Cu-based Catalyst

In this chapter, an integral packed-bed reactor was used to determine the kinetics of the water-gas shift (WGS) reaction over a $CuO/ZnO/Al_2O_3$ catalyst, at no film or intra-particle resistance operating conditions. Experiments were carried out over a wide range of temperatures as well as space times using a simulated reformate gas mixture (4.70 % CO, 34.78 % H_2O, 28.70 % H_2, 10.16 % CO_2 balanced in N_2). In the first part of the work, three different mechanistic rate equations and two empirical kinetic models were proposed to describe the WGS reaction in the entire range of temperatures. For improving the independence between parameters in using the Arrhenius and van´t Hoff equations the temperature was centered. A good agreement was obtained between the Langmuir-Hinshelwood (LH) rate equations and the experimental results.

Further analysis using two different temperature regimes for parameter's estimation revealed distinct rate-controlling mechanisms for each range. For temperatures from $180-200\ ^oC$, the associative (LH) mechanism was predominant while the redox pathway showed the best fit to the experimental reaction rates in the range of $230-300\ ^oC$.

Finally, an isothermal plug-flow reactor model was used to simulate the packed-bed tubular reactor for the WGS reaction using the composed kinetics. The reactor model was assessed against the experimental CO conversion and satisfactory agreement was found between model predictions and experimental results.

The contents of this chapter were adapted from: Mendes, D., Chibante, V, Mendes, A., Madeira, L. M., Determination of the low-temperature water-gas shift reaction kinetics using a Cu-based catalyst. Submitted to publication, 2010.

4.1 Introduction

In the literature, two main distinct reaction mechanisms for the WGS reaction (equation 1.1) have been proposed. A regenerative (oxidation-reduction cycle) mechanism of the Eley-Rideal type in which the surface is oxidized by adsorbed H_2O and subsequently reduced by gas-phase CO to form CO_2, completing the catalytic cycle (Newsome, 1980). The other mechanism normally considered is the associative one, of the Langmuir-Hinsheldwood (LH) type, which is based on the interaction of adsorbed carbon monoxide and water to form an intermediate species that subsequently decomposes into CO_2 and H_2 (Rhodes et al., 1995).

Most of the kinetic studies taken so far have been carried out using only water and carbon monoxide in the feed, in a narrow range of temperatures and/or space time values. The objective of this study is therefore to determine the best kinetics (and inherently the mechanism) for the WGS reaction carried out on a commercial $CuO/ZnO/Al_2O_3$ catalyst under conditions (pressure, temperature and feed composition) close to the ones likely to be encountered in fuel processors for polymer electrolyte membrane fuel cell (PEMFC) applications. This catalyst was selected because, among other promising samples, it showed the best relation activity/stability in the temperature range of $150-300\ ^{o}C$, as mentioned in the previous chapter. It is also aim of this work that the kinetic expression found allows the obtained experimental data to be fit with a high statistical significance and be used to simulate a low-temperature WGS converter. This way, it can also be useful for other purposes/applications, for instance when the catalyst is used in membrane reactors, as shown later on (chapters 5-6).

4.2 Kinetic Modeling

4.2.1 Proposed mechanisms and mechanistic-derived models

The proposed mechanisms were based on the work by Ayastuy et al. (Ayastuy et al., 2005). These authors analyzed a total of 16 mechanistic models and 70 rate equations for the

low temperature (LT) WGS reaction over a commercial Cu-based catalyst. We have selected three rate equations (two Langmuir-Hinsheldwood (LH) mechanisms and a redox one), taking into account the good fitting obtained to the experimental results of Ayastuy et al.. The first LH model suggests that both reactants are adsorbed over similar active sites on the catalyst surface (equations 4.1 and 4.2) forming the reaction products that are further desorbed (equations 4.4 and 4.5). The formation of the intermediate formate/carbonate species via adsorbed CO and H_2O can be considered fast enough and so is not shown in equation 4.3. This pathway can be described by the following equations:

$$CO + S \leftrightarrow CO{\bullet}S \tag{4.1}$$

$$H_2O + S \leftrightarrow H_2O{\bullet}S \tag{4.2}$$

$$CO{\bullet}S + H_2O{\bullet}S \leftrightarrow CO_2{\bullet}S + H_2{\bullet}S \tag{4.3}$$

$$H_2{\bullet}S \leftrightarrow H_2 + S \tag{4.4}$$

$$CO_2{\bullet}S \leftrightarrow CO_2 + S \tag{4.5}$$

A rate equation was then derived assuming the surface reaction between molecularly adsorbed reactants as the rate determining step (RDS – equation 4.3):

$$\text{Model 1: } \left(-r_{CO}\right) = \frac{k\left(p_{CO}p_{H_2O} - \frac{p_{CO_2}p_{H_2}}{K_e}\right)}{\left(1 + K_{CO}p_{CO} + K_{H_2O}p_{H_2O} + K_{CO_2}p_{CO_2} + K_{H_2}p_{H_2}\right)^2} \tag{4.6}$$

where $\left(-r_{CO}\right)$ is the reaction rate, k is the rate constant for the WGS reaction, K_e is the equilibrium constant, K_i is the equilibrium adsorption constant of species i and p_i is the corresponding partial pressure. The temperature dependence of K_e is given in chapter 2 (equation 1.2).

A second LH mechanism was proposed by Ayastuy et al. suggesting that the adsorbed reactants produce an intermediate species (equation 4.7), which subsequently gives rise to carbon dioxide and hydrogen:

$CO + S \leftrightarrow CO{\bullet}S$ (4.1a)

$H_2O + S \leftrightarrow H_2O{\bullet}S$ (4.2a)

$CO{\bullet}S + H_2O{\bullet}S \leftrightarrow COOH{\bullet}S + S$ (4.7)

$COOH{\bullet}S \leftrightarrow CO_2 + H{\bullet}S$ (4.8)

$2H{\bullet}S \leftrightarrow H_2 + 2S$ (4.9)

The corresponding model rate equation (equation 4.10) was derived assuming that the RDS was the surface reaction between molecularly adsorbed carbon monoxide and water to give the formate intermediate.

$$\text{Model 2: } \left(-r_{CO}\right) = \frac{k\left(p_{CO}p_{H_2O} - \frac{p_{CO_2}p_{H_2}}{K_e}\right)}{\left(1 + K_{CO}p_{CO} + K_{H_2O}p_{H_2O} + K_{CO_2}p_{CO_2}p_{H_2}^{0.5} + K_{H_2}^{0.5}p_{H_2}^{0.5}\right)^2} \quad (4.10)$$

The regenerative or surface redox mechanism, on the other hand, considers two cyclic steps. In the first one (equation 4.11), water adsorbs and dissociates on reduced sites of the $CuO/ZnO/Al_2O_3$ surface to produce hydrogen and oxidizes the vacant site. In the second step, CO is oxidized to CO_2 thus reducing and regenerating the active site (equation 4.12).

$H_2O + S \leftrightarrow H_2 + O{\bullet}S$ (4.11)

$CO + O{\bullet}S \leftrightarrow CO_2 + S$ (4.12)

The rate equation derived from this model was obtained assuming equation 4.11 as the rate-determining step:

$$\text{Model 3: } \left(-r_{CO}\right) = \frac{k\left(p_{H_2O} - \frac{p_{CO_2}p_{H_2}}{K_e p_{CO}}\right)}{1 + K_{CO_2}\frac{p_{CO_2}}{p_{CO}}} \quad (4.13)$$

4.2.2 Empirical reaction-rate models

In contrast to the rate expressions obtained from detailed reaction mechanisms, there are simple empirical rate expressions that do not consider any mechanism, which are also helpful

in reactors design and optimization. However, they are of more limited use, since the parameters obtained are in principle valid only for concentration and temperature ranges in which the kinetic studies have been carried out (Salmi and Hakkarainen, 1989). In this work, the experimental data were also fitted to the following equations:

Model 4 (Moe rate equation (Moe, 1962)):

$$-r_{CO} = k\, p_{CO}\, p_{H_2O}\,(1-\beta) \tag{4.14}$$

and

Model 5 (Power-law rate equation (Koryabkina et al., 2003)):

$$-r_{CO} = k\, p_{CO}^{a}\, p_{H_2O}^{b}\, p_{H_2}^{c}\, p_{CO_2}^{d}\,(1-\beta) \tag{4.15}$$

where *a*, *b*, *c*, and *d* are the apparent reaction orders of the component CO, H_2O, H_2 and CO_2, respectively. As referred in chapter 2, β is the term to account for the backward reaction or approach to equilibrium and is defined as:

$$\beta = \frac{p_{H_2}\, p_{CO_2}}{p_{CO}\, p_{H_2O}} \frac{1}{K_e} \tag{4.16}$$

The power law model seems to be adequate in many cases and has been extensively studied by several groups in kinetic studies for the high and low temperature WGS reaction (Koryabkina et al., 2003; Qi and Flytzani-Stephanopoulos, 2004; Rhodes and Hutchings, 2003).

4.2.3 Modeling

A model was used for simulating the performance of the packed-bed tubular reactor. This model comprises the steady-state mass balance equation, as well as the respective boundary conditions. It considers the following main assumptions, which are mentioned and validated below (namely in sections 4.3 and 4.4.1):

1. Fixed bed with negligible axial and radial dispersion;

2. Isothermal operation;

3. Negligible mass and heat-transfer resistances between catalyst and bulk gas phase (external limitations);

4. Negligible mass and heat-transfer resistances within the catalyst particle (internal limitations);

5. Reaction takes place on the surface of the catalyst;

6. Negligible pressure drop across the bed;

7. Ideal gas behavior.

The mass balance for the limiting reagent is, then, expressed by:

$$\frac{\mathrm{d}}{\mathrm{dz}}\left(u\, p_i\right) - \rho_b \Re T \left(\nu_i R_i\right) = 0 \qquad (4.17)$$

with the following boundary condition:

$$p_i\left(0\right) = P_t\, y_i^f \qquad (4.18)$$

where *i* refers to the *i*th component, *z* is axial coordinate, *u* is the superficial velocity, P_t is the total pressure, $\Re$ is the ideal gas constant, *T* is the absolute temperature, y_i^f is the feed molar fraction of component *i* and ρ_b is the catalyst bulk density (ρ_b = 1173.1 kg·m^{-3}). R_i stands for the rate of consumption or formation of the individual species and ν_i is the corresponding stoichiometric coefficient (negative for reagents and positive for products).

To simulate the WGS reactor, equation 4.17 with the respective boundary condition was solved numerically via a 4th order Runga-Kutta algorithm using the Matlab software package.

4.3 Experimental Section

A commercial CuO/ZnO/Al_2O_3 (50/40/10 wt.%) catalyst, furnished by REB Research & Consulting, was used for this study.

The kinetic measurements were performed on the apparatus shown in Figure 3.1 and described in chapter 3. In these experiments, a 7.75 mm i.d. stainless steel reactor was used

and the WGS reaction conducted isothermally and at 1.2 bar. A typical run for the WGS reaction was performed as follows: $0.072-2.40$ g of the Cu-based catalyst, previously crushed and sieved to a range of particles size of $250-355$ μm, was diluted with glass spheres of the same particle size (to avoid temperature gradients in the bed, which otherwise could be caused by the exothermic reaction) and loaded into the reactor. The total catalyst bed height was around 5 cm. The bed temperature was measured by introducing a thermocouple from the top of the reactor, placing it at the axial center of the catalyst bed; its displacement along the axial coordinate revealed negligible temperature profiles (± 1 ºC).

The gases were fed to the system by mass flow controllers and a Controller Evaporator Mixer (CEM, Bronkorst) system, as detailed in chapter 3. Prior to each experimental run the WGS catalyst was activated *in situ* with a mixed gas flow of H_2/N_2 (see chapter 3). Without catalyst, CO conversion was not detected. The gas phase products were then analyzed in an on-line gas chromatograph (Dani 1000 GC). Further details concerning the analysis method can be found in chapter 3 and in Appendix A.

Experimental runs to collect intrinsic kinetic data were conducted at reaction temperatures in the range of $180-300$ ºC and space time (W_{cat} / F_{CO}^{feed}) ratios in the range of 2.120 to 70.668 $g_{cat}\cdot h\cdot mol^{-1}$. Under these operating conditions and taking into account the characteristic dimensions (particle size, reactor length, etc.), criteria based on Froment and Bischoff (Froment and Bischoff, 1990), Rodrigues (Rodrigues, 1980) and Perez-Ramirez et al. (Perez-Ramirez et al., 2000) were applied in order to guarantee the applicability of the plug-flow model (neglecting axial dispersion and wall effects in gas-solid operation) and neglect pressure drop. For these preliminary calculations, simplified power law equations were used to describe the kinetic data. These criteria are as follows:

$$1.\ \frac{L_b}{d_p} > \frac{20n}{Pe_p}\ln\left(\frac{1}{1-X_{CO}}\right) \qquad (4.19)$$

where L_b is the catalyst bed height, d_p is the catalyst particle diameter, n is the reaction order, and X_{CO} is the carbon monoxide conversion. The particle *Péclet number* (Pe_p) is expressed by:

$$Pe_p = \frac{u\, d_p}{\varepsilon_b D_{ax}} \tag{4.20}$$

where ε_b is the void bed fraction (assuming the ratio of the volume occupied by the voids to the total bed volume = 0.36). The fluid dispersion in the axial direction, D_{ax}, is calculated by the following expression:

$$D_{ax} = 0.73 D_{CO,\,mix} + \frac{0.5 u\, d_p}{1 + 9.49 \dfrac{D_{CO,\,mix}}{u\, d_p}} \tag{4.21}$$

where $D_{CO,\,mix}$ is the bulk diffusivity of CO in the gas mixture, which, in turn, is estimated using the *Wilke method* (Perry and Green, 1999) (see Appendix B for more details about the calculation of $D_{CO,\,mix}$). The value for $D_{CO,\,mix}$ was found at the maximum temperature of 300 ºC and feed composition to be 7.290×10^{-5} $m^2 \cdot s^{-1}$. In these conditions, the axial dispersion coefficient was estimated to be 5.451×10^{-5} $m^2 \cdot s^{-1}$ (volumetric feed flow rate was kept constant at 270 $mL_N \cdot min^{-1}$ as explained below). For these conditions and W_{cat} / F_{CO}^{feed} = 70.67 $g_{cat} \cdot h \cdot mol^{-1}$ (higher conversions), the minimum inequality computed through equation 4.19 was 140.9 > 106.9; this establishes that for all conditions employed axial dispersion can be assumed negligible and that flow pattern can be well described by the plug-flow hypothesis.

2. $$\frac{D_t}{d_p} > 10 \tag{4.22}$$

where D_t is the internal diameter of the reactor. In this work, we used $D_t / d_p \geq 21.8$, which fulfills this criterion (so wall effects in the gas-solid operation can be neglected).

3. *Ergun equation*: $\frac{\Delta P_b}{L_b} = \frac{150\mu_g}{d_p^2}\frac{(1-\varepsilon_b)^2}{\varepsilon_b^3}u + \frac{1.75\rho_g}{d_p}\frac{(1-\varepsilon_b)}{\varepsilon_b^3}u^2 < 0.05\frac{P_t}{L_b}$ (4.23)

where ΔP_b is the pressure drop in the catalyst bed, L_b is the catalyst bed height, μ_g is the gas mixture viscosity, and ρ_g is the gas density. It was considered that the specific pressure drop should be smaller than 5 % of the total operation pressure in the reactor. This was clearly guaranteed in our work because the minimum inequality obtained was 2.9×10^4 Pa·m^{-1} < 1.2×10^5 Pa·m^{-1}. The properties of the gases were calculated using the correlations presented in Appendix B.

4.4 Results and Discussion

4.4.1 Film and particle resistances

4.4.1.1 Mass transport limitations – Preliminary tests

Preliminary experiments were carried out in order to determine suitable conditions for which external and internal mass transfer resistances are not predominant. The importance of the intraparticle diffusion was evaluated by performing the WGS reaction on catalyst samples with different average particles sizes $180-500\,\mu m$. It was observed that, in the range of the particle sizes tested, no intraparticle diffusion limitation occurred for the experimental conditions used (rate data were independent of d_p). Considering the effect of external mass transfer, the total gas feed flow rate (Q_{feed}) was varied between 167 mL$_N$·min^{-1} and 285 mL$_N$·min^{-1} under a constant space time of $32.04\ g_{cat}\cdot h^{-1}\cdot mol_{CO}^{-1}$ at 300 ºC. As shown in Figure 4.1, the conversion of CO was found to be independent of the gas velocity when the total gas flow rate was equal to or higher than 235 mL$_N$·min^{-1}. The following experiments were performed at 270 mL$_N$·min^{-1}, thus assuring the absence of external mass transfer limitations.

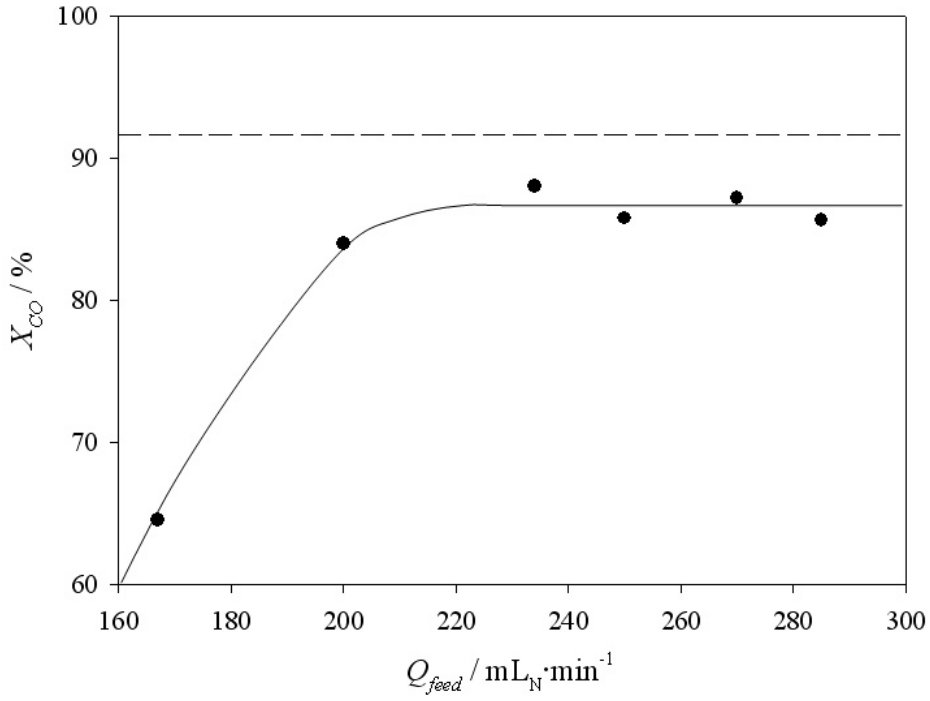

Figure 4.1 – Effect of total volumetric feed flow rate on the CO conversion for the WGS reaction at a constant space time of $32.04\ g_{cat} \cdot h^{-1} \cdot mol_{CO}^{-1}$ and 300 ºC. Dashed line represents the thermodynamic equilibrium conversion; the continuous line is for improving the readability.

4.4.1.2. Heat transport effects

The intraparticle heat transport limitation was analysed using the *Mears analysis* (Dekker et al., 1995; Mears, 1971; Perez-Ramirez et al., 2000) criterion:

$$\gamma_i \beta_i \left(\eta \phi^2\right) = \left(\frac{E_a}{\Re T_s}\right)\left|\frac{\left(-\Delta H_r\right) D_{eff} C_{CO}^s}{\lambda_{eff} T_s}\right|\left(\frac{\left(-r_{CO}^{obs}\right)\rho_b L^2}{D_{eff} C_{CO}^s}\left(\frac{n+1}{2}\right)\right) < 5\times10^{-2} \qquad (4.24)$$

where γ_i is the internal *Arrhenius number* (evaluated at particle surface conditions), β_i represents the maximum temperature difference that can exist in the particle relative to the surface temperature (also called *Prater thermicity factor* in the surface conditions (Rodrigues, 1980)), η is the internal effectiveness factor, ϕ is the *Thiele modulus*, E_a is the activation energy, T_s is the surface particle temperature, $\left(-\Delta H_r\right)$ is the heat of reaction, C_{CO}^s is the CO concentration at the surface of the catalyst particle and D_{eff} is the effective mass

diffusivity, obtained from $D_{eff} = \left(\frac{D_{\mathrm{CO},\,mix} \cdot \varepsilon_p}{\tau} \right)$ (Fogler, 2006). The effective diffusivity D_{eff} was estimated to be 5.375×10^{-6} $m^2 \cdot s^{-1}$ (assuming an average catalyst volume void fraction $\varepsilon_p = 0.4$ and for feed conditions of composition and temperature $T = 300$ ºC). The thermodynamic and transport properties were calculated using the correlations presented in Appendix B. Here, τ is the catalyst tortuosity factor, taken as 5.5 (Chen and Jheng, 2007). Still in equation 4.24, L is the characteristic dimension of the particle (for spheres $L = d_p / 6$) and λ_{eff} is the effective thermal conductivity of the catalyst, obtained using the following correlation (Malek and Farooq, 1997; Yagi et al., 1960):

$$\frac{\lambda_{eff}}{\lambda_g} = \left(\varepsilon_p + \frac{1-\varepsilon_p}{0.139\varepsilon_p - 0.0339 + 6.667\lambda_g} \right) + 0.75\varepsilon_p \left(Pr\right)\left(Re_p\right) \qquad (4.25)$$

where *Pr* is the *Prandtl number* $\left(Pr = \frac{C_p \mu_g}{\lambda_g} \right)$ and Re_p is the particle *Reynolds number* $\left(Re_p = \frac{\rho_g \, u \, d_p}{\mu_g} \right)$. The term λ_g is the molecular thermal conductivity of the gas mixture, which was calculated using the *Wassiljewa correlation* (Perry and Green, 1999) to be 6.089×10^{-5} $kJ \cdot m^{-1} \cdot s^{-1} \cdot K^{-1}$ (see Appendix B for more details). The effective thermal conductivity $\left(\lambda_{eff}\right)$ was found to be 1.684×10^{-3} $kJ \cdot m^{-1} \cdot s^{-1} \cdot K^{-1}$. Both parameters were computed at the above mentioned conditions. Substituting these values in the inequality, equation 4.24, one obtains $3.8\times10^{-4} < 5.0\times10^{-2}$. This indicates that the temperature profile inside the particle is, for steady-state conditions, negligible. The same result was also obtained whatever the conditions of the catalytic runs used.

The internal heat transfer resistance was also estimated using the *Prater analysis* (Fogler, 2006; Kumar et al., 2008; Rodrigues, 1980), given by:

$$\Delta T_{max,\,particle} = \frac{\left(-\Delta H_r\right) D_{eff} C_{\mathrm{CO}}^{s}}{\lambda_{eff}} \qquad (4.26)$$

where $\Delta T_{max,\,particle}$ is the upper limit of temperature variation between the pellet center and its surface. A value of 0.15 K was obtained for $\Delta T_{max,\,particle}$, which shows that the particle has an approximately uniform temperature profile. This increment of temperature corresponds to a maximum increase of 0.42 % (at 300 ºC) on the kinetic constant.

Further, the inexistence of temperature gradients between the bulk fluid and the surface of the catalyst particle was determined using the following criterion (Dekker et al., 1995; Mears, 1971):

$$\gamma_e \beta_e Ca = \left(\frac{E_a}{\Re T_b}\right)\left|\frac{(-\Delta H_r)k_f C_{CO}^b}{hT_b}\right|\left(\frac{(-r_{CO}^{obs})\rho_b}{a' k_f C_{CO}^b}\right) < 5\times10^{-2} \qquad (4.27)$$

where γ_e is the external Arrhenius number, β_e represents the maximum temperature difference that can exist in the film relative to the bulk phase temperature, Ca is the *Carberry number* which represents the extent of external mass-transfer limitation and ranges from 0 to 1, a' is the specific external surface area of the catalyst particle ($a' = 6/d_p$ for spherical particles), h and k_f are the heat and mass transfer coefficients between the gas and the particle, respectively. Both parameters (h and k_f) were estimated from a correlation expressed in terms of the *Colburn J* factor analogy, equations 4.28–4.30:

$$J_D = \frac{k_f}{u} Sc^{2/3} \qquad (4.28)$$

$$J_H = \frac{h}{C_p u \rho_g} Pr^{2/3} \qquad (4.29)$$

$$J_D = J_H = \frac{0.4548}{\varepsilon_p} Re_p^{-0.4069} \qquad (4.30)$$

where J_D and J_H are the mass and heat transfer *J* factors, respectively, and Sc is the *Schmidt number* $\left(Sc = \frac{\mu_g}{\rho_g D_{CO,\,mix}}\right)$. A mass transfer coefficient of 0.187 $m \cdot s^{-1}$ and a heat

transfer coefficient of 0.156 $kJ \cdot m^{-2} \cdot s^{-1} \cdot K^{-1}$ were calculated at a temperature of 300 ºC and feed composition conditions. The estimated value for the $\gamma_e \beta_e Ca$ product was 6.2×10^{-5}, which is much lower than the criterion value of 5.0×10^{-2}, indicating the inexistence of extraparticle heat transfer limitations. This was also checked for other conditions.

The heat transfer limitation across the gas film was also determined using the following expression (Kumar et al., 2008; Levenspiel, 1999):

$$\Delta T_{max,\,film} = \frac{\left(-\Delta H_r\right)\left(-r_{CO}^{obs}\right)\rho_b L}{h} \tag{4.31}$$

where $\Delta T_{max,\,film}$ is the upper limit of temperature difference between the gas bulk and the particle surface. A negligible value of 1.8×10^{-3} K was obtained, confirming the absence of external heat transfer limitations.

4.4.1.3 Mass transport effects

The absence of mass transfer resistances was evaluated experimentally, as mentioned above, but also theoretically. The intraparticle difusional resistance was evaluated by the so-called *Wheeler-Weisz modulus* (Φ) criterion, which is given by (Dekker et al., 1995):

$$\Phi = \frac{\left(-r_{CO}^{obs}\right)\rho_b L^2}{D_{eff} C_{CO}^{s}}\left(\frac{n+1}{2}\right) < 0.10 \tag{4.32}$$

The maximum estimated value for Φ was 0.090, confirming the inexistence of pore diffusion limitations.

For the exclusion of extraparticle mass transfer resistances the *Carberry number* (Ca) must satisfy the following condition:

$$Ca = \frac{\left(-r_{CO}^{obs}\right)\rho_b}{a' k_f C_{CO}^{b}} < 5.0 \times 10^{-2} \tag{4.33}$$

The maximum estimated value for *Ca* was 3.2×10^{-2}. A *Carberry number* smaller than 5.0×10^{-2} indicates that observed reaction rate retardation by external mass transfer may be neglected.

4.4.2 Determination of the reaction kinetics and parameters estimation

Figure 4.2 shows the CO conversion as a function of the ratio of weight of catalyst to CO feed flow rate ($W_{cat} / F_{\mathrm{CO}}^{feed}$) at reaction temperatures ranging from 180 ºC to 300 ºC.

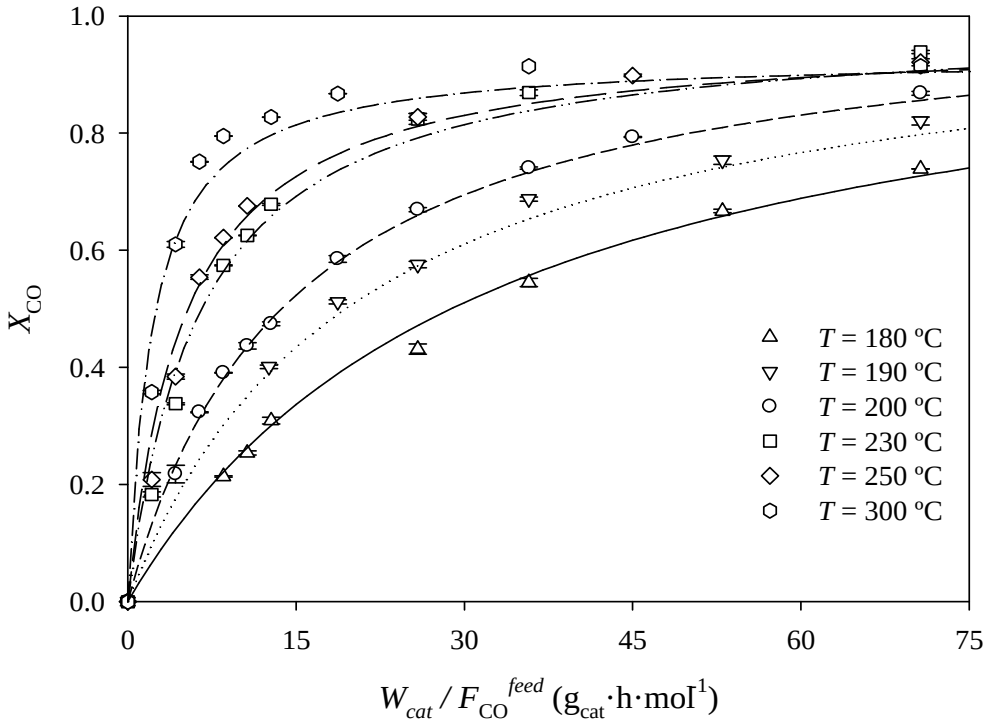

Figure 4.2 – Carbon monoxide conversion in the WGS reaction as a function of the contact time at various temperatures.

The experimental rates of reaction were obtained by taking the slopes at various points from the conversion versus $W_{cat} / F_{\mathrm{CO}}^{feed}$ plot using the differential method (Fogler, 2006; Froment and Bischoff, 1990):

$$\left(-r_{\mathrm{CO}}\right) = \frac{\mathrm{d}X_{CO}}{\mathrm{d}\left(W_{cat} / F_{\mathrm{CO}}^{feed}\right)} \tag{4.34}$$

The experimental reaction rates were then fitted to the above-mentioned models (cf. sections 4.2.1 and 4.2.2). In all of them, the *Arrhenius equation* was used to describe the variation of the rate constant with temperature:

$$k = k_0 \exp\left(-\frac{E_a}{\Re T}\right) \tag{4.35}$$

To improve the independence (smaller correlation coefficient) between the pre-exponential factor (k_0) and the activation energy (E_a), the rate constants may be obtained by temperature centering, choosing an appropriate temperature near the middle of the range of temperatures studied (T_m) (equation 4.36). This scaling procedure has consequences of providing more robust parameters and reduces non-linearity of correlation (Patel and Pant, 2007; Wojciechowski and Rice, 2003). In the present study T_m = 503 K was used for the parameter estimation, and the *Arrhenius equation* can be rewritten as follows:

$$k = k_m \exp\left[-\frac{E_a}{\Re}\left(\frac{1}{T}-\frac{1}{T_m}\right)\right] \tag{4.36}$$

where k_m is the rate constant evaluated at the mean temperature. Similarly, the equilibrium constants of the adsorbed species as a function of temperature were estimated using the *van't Hoff* expression with temperature centering (equation 4.37):

$$K_i = K_{i,m} \exp\left[-\frac{\Delta H_i}{\Re}\left(\frac{1}{T}-\frac{1}{T_m}\right)\right] \tag{4.37}$$

where $K_{i,m}$ is the adsorption equilibrium constant evaluated at the mean temperature.

All the possible rate expressions we have considered have been tested to reach the best possible fit for the kinetic data. The parameters estimation is based on the adaptive random-search algorithm – MSGA (Salcedo, 1992). The optimum parameters were obtained by minimizing the sum of residual squares. The comparison between models was done by

applying the *Se* test (also called variance) (Froment and Bischoff, 1990; Patel and Pant, 2007), because the number of fitting parameters changes from model to model:

$$Se = \frac{\sum_{j=1}^{n_{exp}} \left(\left(-r_{CO}\right)_{exp,j} - \left(-r_{CO}\right)_{pred,j} \right)^2}{\left(n_{exp} - p\right)} \tag{4.38}$$

where $\left(-r_{CO}\right)_{exp,j}$ is the measured rate of CO consumption in experiment *j*, $\left(-r_{CO}\right)_{pred,j}$ is the corresponding model predicted rate, n_{exp} is the total number of experimental points and *p* stands for the number of parameters in the model.

The average values obtained for the reaction-rate equations parameters are presented in Table 4.1. It is also given the fitting error associated to each parameter, assuming t-student and for 95 % confidence level, and computed using the 10 best fittings. In the temperature range of $180-300$ ºC among the empirical equations it can be seen that the power-law (model 5) shows the best fit for the kinetic data (lowest *Se* value). Concerning the mechanistic-derived equations, the lowest *Se* value was obtained for model 1. However, due to the very similar values of *Se* for models 1 and 2, both can be considered almost indistinguishable and therefore as good models to describe the experimental rates. Then, for the experimental conditions employed and in particular for the wide range of temperatures used for the parameters estimation, the associative (LH) mechanism seems to be the predominant pathway for the WGS reaction. A comparison of the measured rates of CO consumption and the model predictions is shown in Figure 4.3.

A closer look on the data reported in literature revealed similar results to the ones presented in this work. Ayastuy et al. (Ayastuy et al., 2005) conducted kinetic experiments

Table 4.1 – Calculated parameters for empirical (models 4 and 5) and mechanistic-derived (models 1-3) rate equations in the temperature range of 180 – 300 ºC. Fitting errors associated to each parameter are for 95 % confidence level.

Parameter	Empirical models		Mechanistic-derived models		
	Moe equation (model 4)	**Power Law (model 5)**	**LH (model 1)**	**LH (model 2)**	**Redox (model 3)**
k_0	$8.689\times10^{-7} \pm 0.004\times10^{-7}$	4.785 ± 2.187	$2.215\times10^{-4} \pm 0.253\times10^{-4}$	$3.191\times10^{-2} \pm 0.054\times10^{-2}$	$3.101\times10^{-4} \pm 0.176\times10^{-4}$
E_a	32.839 ± 0.002	34.983 ± 0.014	3.783 ± 0.683	6.227 ± 0.233	0.537 ± 0.152
$K_{CO,0}$			$1.756\times10^{-27} \pm 0.382\times10^{-27}$	$8.562\times10^{-2} \pm 0.215\times10^{-2}$	
$K_{H_2O,0}$			$9.321\times10^{-4} \pm 2.984\times10^{-4}$	$2.663\times10^{-12} \pm 0.457\times10^{-12}$	
$K_{CO_2,0}$			$2.280\times10^{-3} \pm 0.120\times10^{-3}$	$1.706\times10^{-4} \pm 0.013\times10^{-4}$	$1.882\times10^{-2} \pm 0.107\times10^{-2}$
$K_{H_2,0}$			$2.739\times10^{-12} \pm 0.554\times10^{-12}$	$1.331\times10^{-15} \pm 0.017\times10^{-15}$	
ΔH_{CO}			-80.410 ± 4.431	-0.095 ± 0.000	
ΔH_{H_2O}			-4.109 ± 0.820	-91.214 ± 1.119	
ΔH_{CO_2}			-9.795 ± 0.316	-8.693 ± 0.035	-33.522 ± 0.152
ΔH_{H_2}			-83.608 ± 1.925	-125.901 ± 0.304	
a		0.854 ± 0.005			
b		1.990 ± 0.058			
c		-1.926 ± 0.005			
d		-0.573 ± 0.035			
Se	2.509×10^{-5}	1.603×10^{-5}	3.218×10^{-6}	3.370×10^{-6}	1.844×10^{-5}

over a commercial $CuO/ZnO/Al_2O_3$ catalyst in a narrow range of temperatures $(180-217\ ^{o}C)$, founding that models 1 and 2 provided also the best rate equations for the WGS reaction.

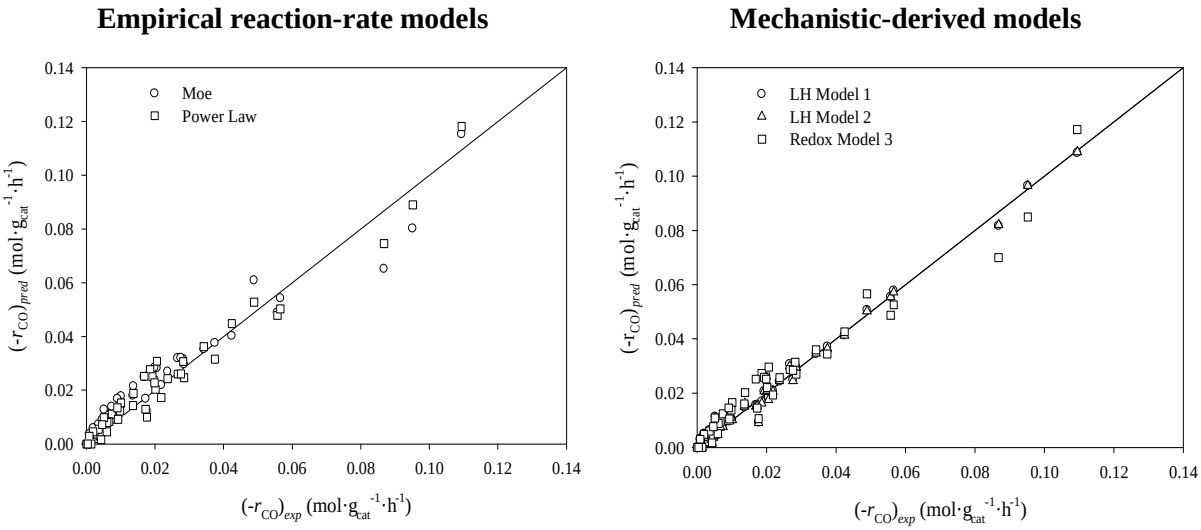

Figure 4.3 – Parity plots of the CO conversion rates obtained for the tested reaction rate models.

Amadeo and Laborde (Amadeo and Laborde, 1995) observed that model 1 was the best mechanistic equation to describe their experimental WGS reaction rates, conducted in the range of temperatures of $180-230\ ^{o}C$. More recently, several authors have been reporting detailed studies based on periodic density functional calculations, proposing the associative route with the formation of an intermediate species (carboxyl) on Cu surfaces (Fajin et al., 2009; Gokhale et al., 2008). Combining it with a microkinetic analysis, Gokhale et al. (Gokhale et al., 2008) found very good agreement between the modelling rates and the experimental values, at 200 ºC. The authors suggested that the dominant reaction mechanism involves CO oxidation by an adsorbed $HO^{\bullet}$ (hydroxyl radical) to form an intermediate species, followed by its decomposition through a disproportionation reaction (model 2, equation 4.8).

Analysing Table 4.1, it is clear that similar apparent activation energies were obtained for the empirical model equations (32.84 kJ·mol^{-1} and 34.98 kJ·mol^{-1} for models 4 and 5,

Table 4.2 – Comparison of apparent activation energies and reaction orders for the forward power law reaction model (model 5).

Catalyst	Operating Conditions *	E_a ($kJ \cdot mol^{-1}$)	Reaction orders **				Reference
			CO	H_2O	CO_2	H_2	
50 wt.% $CuO/ZnO/Al_2O_3$	1 bar, 180 – 300 ºC	35.0	0.85 (4.7 %)	2.0 (35 %)	-1.9 (10 %)	-0.57 (28 %)	This work
50 wt.% $CuO/ZnO/Al_2O_3$	1 bar, 180 – 200 ºC	67.4	0.76 (4.7 %)	1.7 (35 %)	-1.9 (10 %)	-0.54 (28 %)	This work
25 wt.% $CuO/ZnO/Al_2O_3$	3 bar, 180 – 217 ºC	79.7	0.47 (6.5 – 36 %)	0.72 (4.3 – 27 %)	-0.38 (0 – 53 %)	-0.65 (0 – 27 %)	(Ayastuy et al., 2005)
40 wt.% $CuO/ZnO/Al_2O_3$	1 bar, 190 ºC	79	0.8 (5.0 – 25 %)	0.8 (10 – 46 %)	-0.9 (5.0 – 30 %)	-0.9 (25 – 60 %)	(Koryabkina et al., 2003)
8 wt.% CuO/Al_2O_3	1 bar, 200 ºC	62	0.9 (5.0 – 25 %)	0.8 (10 – 46 %)	-0.7 (5.0 – 30 %)	-0.8 (25 – 60 %)	(Koryabkina et al., 2003)
40 wt.% $CuO/ZnO/Al_2O_3$	5 bar, 180 – 220 ºC	86.5	1	1.4	-0.7	-0.9	(Ovesen et al., 1996)
40 wt.% $CuO/ZnO/Al_2O_3$	20 bar, 180 – 220 ºC	78.2	1	1.5	-0.7	-0.7	(Ovesen et al., 1996)
8 wt.% CuO/Al_2O_3	20 bar, 180 – 220 ºC	59.3	1	1.9	-1.4	-0.9	(Ovesen et al., 1996)
CuO/ZnO	1 bar, 200 and 250 ºC	–	0.55 and 1.08	0.07 and 0.45	–	–	(Salmi and Hakkarainen, 1989)
Cu (1 1 1)	1 bar, 190 ºC	78	0.9 (7 %)	0.85 (21 %)	0 (8.5 %)	-0.7 (38 %)	(Gokhale et al., 2008)

* Temperature and total pressure at which the reaction order measurements/predictions were carried out;
** Values between brackets represent the ranges of concentrations for each species in the feed.

respectively). Those values are lower than the ones reported in the literature, which range between ca. 60 $kJ \cdot mol^{-1}$ and 85 $kJ \cdot mol^{-1}$ (see Table 4.2). However, this might be explained by the range of temperatures used in the parameters estimation and by the fact that most of the data reported in literature were obtained at lower temperatures. To show that, the parameters were estimated for the power law equation for a narrower range of temperatures, $180-200\ ^{o}C$, Table 4.2. A value of 67.43 $kJ \cdot mol^{-1}$ was then obtained, which is closer to the literature reported values. Nevertheless, the catalyst formulation should be also taken into account.

In what concerns the mechanistic-rate equations, much lower values were obtained for the activation energy (cf. Table 4.1). A similar value of 4.08 $kJ \cdot mol^{-1}$, taking into consideration the LH model 1 in the temperature range of $180-230\ ^{o}C$, was reported by Amadeo and Laborde (Amadeo and Laborde, 1995). A decrease of the activation energy was also justified by the high water partial pressure in the reactant mixture that is responsible for a increase of the rate of formate decomposition (Shido and Iwasawa, 1993).

Still for the power law reaction model, the reaction orders found for most of the reaction species are in the range of values reported in literature (see Table 4.2). The only exception is the reaction order with respect to CO_2. Our results revealed that the sensitivity of the reaction rate to the water partial pressure is higher than that towards CO, as it was also reported by Ayastuy et al. (Ayastuy et al., 2005), Ovesen et al. (Ovesen et al., 1996) and Fishtik and Datta (Fishtik and Datta, 2002). In the case of the reaction products, our data revealed that the reaction rate is more sensitive to the CO_2 partial pressure than to the hydrogen one. The CO and H_2O reaction kinetics dependence decreases for lower temperatures $(180-200\ ^{o}C)$ – Table 4.2. This was also verified by Salmi and Hakkarainen (Salmi and Hakkarainen, 1989).

As referred above, much discussion exists around the predominance of either associative or redox mechanisms in the low temperature WGS reaction. Up to now, this study points out to an associative pathway in the temperatures range of $180-300\ ^{o}C$ (models 1 and 2).

However, we have also considered the possibility of having a change in the WGS mechanism with temperature. Therefore, it is also studied, in a macrokinetic point of view, the possibility of existing two different reaction routes for temperatures ranging from 180 ºC up to 300 ºC. To perform this analysis, the mechanistic models proposed (1, 2 and 3) were tested to reach the best possible fit for the kinetic data at two different temperatures regimes: $180-200$ ºC (lower-temperature), and $230-300$ ºC (higher temperature). This temperature range division was the one that originated the best fittings to the selected models. Table 4.3 shows the mean values of the estimated parameters (obtained at a 95 % confidence level), for the best fittings.

Table 4.3 – Calculated parameters for mechanistic-derived rate equations (models 1 and 3) for low- and high-temperature regimes, respectively. Fitting errors associated to each parameter are for 95 % confidence level, and computed using the 10 best fittings.

Parameter	$T = 180-200$ ºC	$T = 230-300$ ºC
	LH (model 1)	**Redox (model 3)**
k_0	1.188 ± 0.000	$1.841\times10^{-3} \pm 0.210\times10^{-3}$
E_a	36.658 ± 0.000	6.710 ± 0.399
$K_{CO,0}$	$2.283\times10^{-24} \pm 0.000\times10^{-24}$	
$K_{H_2O,0}$	$1.957\times10^{-28} \pm 0.000\times10^{-28}$	
$K_{CO_2,0}$	$5.419\times10^{-4} \pm 0.002\times10^{-4}$	$6.343\times10^{-1} \pm 0.727\times10^{-1}$
$K_{H_2,0}$	$2.349\times10^{-4} \pm 0.000\times10^{-4}$	
ΔH_{CO}	-45.996 ± 0.158	
ΔH_{H_2O}	-79.963 ± 0.172	
ΔH_{CO_2}	-16.474 ± 0.009	-19.459 ± 0.402
ΔH_{H_2}	-13.279 ± 0.192	
Se	1.025×10^{-6}	5.817×10^{-6}

As it can be seen in Table 4.3, the best fit for the kinetic data was obtained with models 1 and 3 for low- and high-temperature regimes, respectively; model 2 proved to produce worse fittings in each temperature range. This indicates that the rate-controlling mechanism for each temperature interval should be distinct: associative (low-temperature) and redox (high-temperature). Similar conclusions were also reported by Fishtik and Datta (Fishtik and

Datta, 2002) on a Cu (1 1 1) catalyst in a wide range of temperatures (100 – 450 ºC), although these conclusions were reached through a microkinetic model (based on the transition state theory).

It is also noteworthy that the goodness-of-fit for each model is much better in this narrower range of temperatures as compared to that reached from 180 ºC up to 300 ºC (*Se* value of both models decreased to 1/3 of the previous value, cf. Tables 4.1 and 4.3). A comparison between experimental rates and those predicted by the mechanistic rate equations for low- and high-temperature regimes is shown in Figure 4.4.

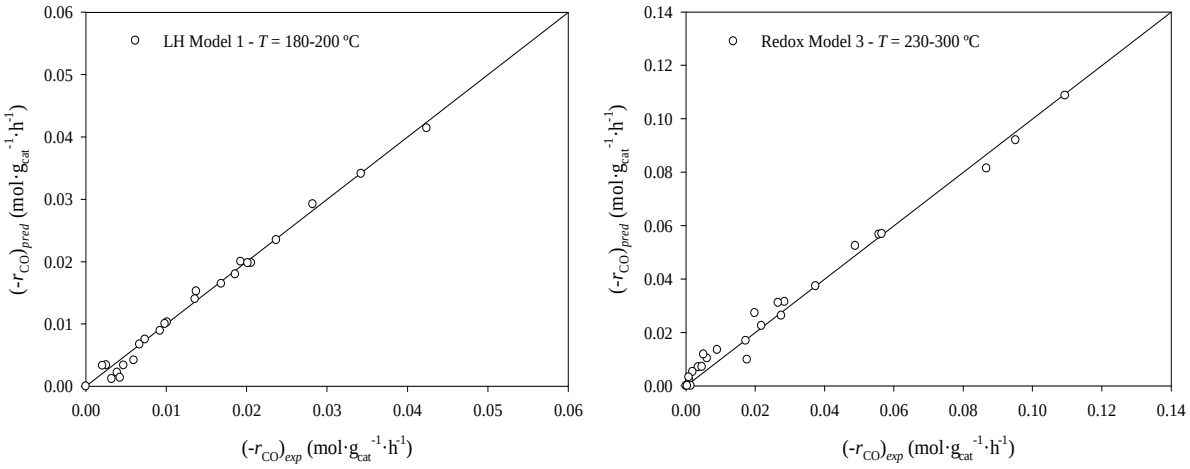

Figure 4.4 – Parity plots of the CO conversion rates obtained for models 1 and 3 in different temperature ranges.

Despite the good agreement between calculated and measured rates, the LH model tends to underestimate the reaction rates obtained at the high space time values. Contrarily, for the same range of space time values, the Redox model tends to overestimate the experimental data.

Finally, to validate the models (LH 1 and Redox), a comparison was carried out between the results predicted by both models and those obtained experimentally at 215 ºC (values not used for the parameters estimation). From Figure 4.5, it can be seen that both mechanistic

models fit adequately the experimental reaction rates obtained at this transition temperature. This indicates the good quality of the parameters estimation.

From this work, it can be proposed that the ternary copper-based catalyst can accommodate the dissociative adsorption of water required for a redox mechanism but also the reactions needed to precede the associative mechanism. Indeed, the WGS reaction can proceed via either of the reaction mechanisms, the relative rates of the two pathways being probably influenced by the experimental conditions (Rhodes et al., 1995), particularly the temperature.

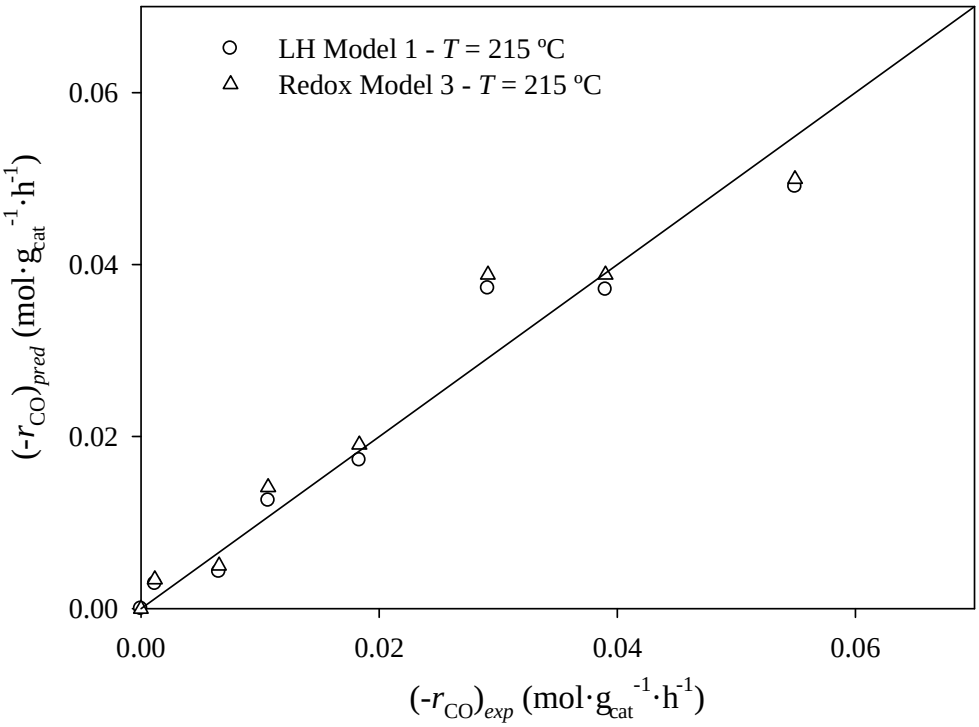

Figure 4.5 – Parity plot of the CO conversion rates obtained for models 1 and 3 at 215 ºC.

4.4.3. Validation of the kinetic model and simulation study

The kinetic model proposed was used for simulating a packed-bed tubular reactor carrying out the WGS reaction for the entire range of experimental conditions. This was used for validating the composed kinetic model. The reactor model assumes plug-flow behaviour, as described in section 4.2.3 (equation 4.17 with the respective boundary condition).

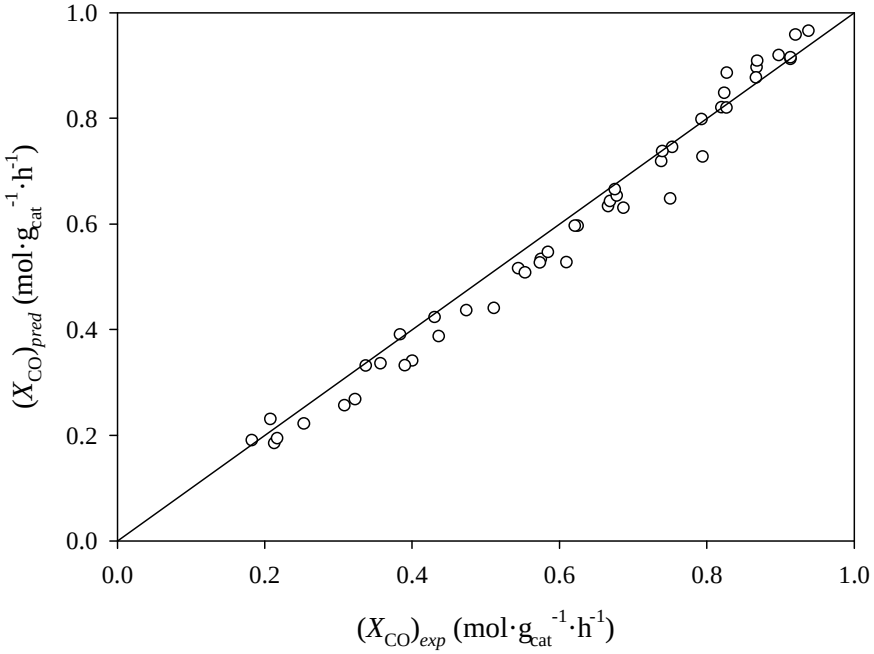

Figure 4.6 – Parity plot of the predicted and measured CO conversion.

As can be inferred from Figure 4.6, the packed-bed reactor model using the composed kinetics predicts quite well the experimental conversion values in the range of 20 % to 100 %.

4.5 Conclusions

The kinetics of the WGS reaction over a commercial $CuO/ZnO/Al_2O_3$ catalyst was investigated using a typical reformate gas mixture in the temperature range of $180-300\ ^{o}C$. Three different mechanistic-rate equations were considered to describe the WGS rate data in the entire range of temperatures. The LH kinetic models based on surface reaction of molecularly adsorbed reactants and on the formation of a formate intermediate as rate-determining steps showed good fit to experimental data. Empirical kinetic rate equations were also proposed and evaluated for the WGS reaction. Among these, and for the operating conditions, the best fit was obtained for a power law equation.

Further investigations using two different temperature regimes for parameters estimation, $180-200$ ºC (lower-temperature), and $230-300$ ºC (higher temperature), revealed a better goodness of fit and thus support the existence of distinct rate-controlling mechanisms for these two temperature ranges: associative/LH (model 1 – lower-temperature) and redox (model 3 – higher-temperature). A good quality of the parameters estimative for each mechanistic model was also shown by fitting the models to experimental data not initially used in the numerical optimisation (i.e. at an intermediate temperature of 215 ºC).

Finally, an isothermal plug-flow reactor model was used to simulate the packed bed tubular reactor for the WGS reaction for validating the combined kinetic model. The reactor model was assessed against the measured CO conversion and satisfactory agreement was found between model predictions and experimental results (average absolute deviation of ca. 3.5 %).

4.6 Nomenclature and Acronyms

a'	specific external surface area of the catalyst particle ($a' = 6/d_p$ for spheres) [m^{-1}]
a, *b*, *c*, *d*	apparent reaction orders for CO, H_2O, H_2 and CO_2, respectively
C_{CO}^{s}	CO concentration at the surface of the catalyst particle [$mol \cdot m^{-3}$]
C_{CO}^{b}	CO concentration in the bulk phase [$mol \cdot m^{-3}$]
c_p	specific heat capacity of the gas mixture [$kJ \cdot kg^{-1} \cdot K^{-1}$]
d_p	catalyst particle diameter [m]
D_{ax}	dispersion coefficient in the axial direction [$m^2 \cdot s^{-1}$]
$D_{CO,\,mix}$	diffusivity of CO in the gas mixture [$m^2 \cdot s^{-1}$]
D_t	internal diameter of the reactor [m]
D_{eff}	effective mass diffusivity in the catalyst particle [$m^2 \cdot s^{-1}$]
E_a	activation energy for the WGS reaction [$J \cdot mol^{-1}$]

h	heat transfer coefficient between gas and particle [$J \cdot m^{-2} \cdot s^{-1} \cdot K^{-1}$]
HT	high temperature
i	species involved in the reaction (CO, H_2O, CO_2 or H_2)
k	rate constant for the WGS reaction [$mol \cdot g_{cat}^{-1} \cdot h^{-1} \cdot Pa^{-n}$]
k_0	pre-exponential factor of the rate constant [$mol \cdot g_{cat}^{-1} \cdot h^{-1} \cdot Pa^{-n}$]
k_f	mass transfer coefficient [$m \cdot s^{-1}$]
k_m	rate constant evaluated at the mean temperature, T_m [$mol \cdot g_{cat}^{-1} \cdot h^{-1} \cdot Pa^{-n}$]
K_e	equilibrium constant for the WGS reaction
K_i	adsorption equilibrium constant of species i [Pa^{-1} or $Pa^{-1.5}$]
$K_{i,0}$	pre-exponential adsorption equilibrium constant of species i [Pa^{-1} or $Pa^{-1.5}$]
$K_{i,m}$	adsorption equilibrium constant of species i evaluated at T_m [Pa^{-1} or $Pa^{-1.5}$]
L	characteristic catalyst dimension (for spherical particles $L = d_p / 6$) [m]
L_b	catalyst bed height [m]
LH	Langmuir-Hinshelwood
LT	low temperature
n	reaction order
n_{exp}	total number of experimental values
p	number of parameters in the model according to the *Se* test
p_i	partial pressure of component *i* [Pa or bar]
PEMFC	polymer electrolyte membrane fuel cell
P_t	total pressure [Pa or bar]
Q_{feed}	feed volumetric flow rate [$mL_N \cdot min^{-1}$]
$\Re$	ideal gas constant [$J \cdot mol^{-1} \cdot K^{-1}$]
R_i	rate of consumption or formation of species *i* [$mol \cdot g_{cat}^{-1} \cdot h^{-1}$]
$(-r_{CO})_{exp}$	observed reaction rate [$mol \cdot g_{cat}^{-1} \cdot h^{-1}$]

$(-r_{CO})_{pred}$ predicted reaction rate [$mol \cdot g_{cat}^{-1} \cdot h^{-1}$]

RDS rate determining step

S catalyst active site

Se criteria for comparing goodness-of-fit of the different models

T absolute temperature [K]

T_b bulk phase temperature [K]

T_m temperature adopted in the centering of the Arrhenius and van´t Hoff equations [K]

T_s surface particle temperature [K]

u superficial velocity [$m \cdot s^{-1}$]

W_{cat} / F_{CO}^{feed} space time [$g_{cat} \cdot h \cdot mol^{-1}$]

WGS water-gas shift

X_{CO} carbon monoxide conversion

y_i^f feed molar fraction of component *i*

z axial coordinate of the reactor [m]

Dimensionless numbers

Ca Carberry number $\left(Ca = \frac{(-r_{CO}^{obs})\rho_b}{a' k_f C_{CO}^b} \right)$

Pe_p particle Peclet number $\left(Pe_p = \frac{u d_p}{\varepsilon_b D_{ax}} \right)$

Pr Prandtl number $\left(Pr = \frac{C_p \mu_g}{\lambda_g} \right)$

Re_p catalyst/particle Reynolds number $\left(Re_p = \frac{\rho_g u d_p}{\mu_g} \right)$

Sc Schmidt number $\left(Sc = \frac{\mu_g}{\rho_g D_{CO,\,mix}} \right)$

J_D, J_H mass transfer and heat transfer J factor, respectively $\left(J_D = \frac{k_f}{u} Sc^{2/3} \text{ and } J_H = \frac{h}{C_p u \rho_g} Pr^{2/3} \right)$

Greek Letters

β term for the backward reaction or approach to equilibrium $\left(\beta = \frac{p_{H_2} p_{CO_2}}{p_{CO} p_{H_2O}} \frac{1}{K_e} \right)$

β_e adimensional number for extraparticle heat transport $\left(\beta_e = \left| \frac{(-\Delta H_r) k_f C_{CO}^b}{h T_b} \right| \right)$

β_i adimensional number for intraparticle heat transport $\left(\beta_i = \left| \frac{(-\Delta H_r) D_{eff} C_{CO}^s}{\lambda_{eff} T_s} \right| \right)$

γ_e external Arrhenius number $\left(\gamma_e = \frac{E_a}{\Re T_b} \right)$

γ_i internal Arrhenius number $\left(\gamma_i = \frac{E_a}{\Re T_s} \right)$

ΔH_i heat of adsorption of component *i* [J·mol^{-1}]

ΔH_r^o standard heat of reaction [J·mol^{-1}]

ΔP_b pressure drop in the catalyst bed [Pa]

$\Delta T_{max,\ film}$ maximum temperature difference between the bulk gas phase and the particle surface [K]

$\Delta T_{max,\ particle}$ maximum temperature variation between pellet center and its surface [K]

ε_b void bed fraction

ε_p catalyst volume void fraction

η internal effectiveness factor

ϕ generalised Thiele modulus $\left(\phi = L \sqrt{\left(\frac{n+1}{2} \right) \frac{k\left(C^s\right)^{n-1}}{D_{eff}}} \right)$ (k = rate constant per unit volume [$\left(\text{mol}\cdot\text{m}^{-3}\right)^{n-1} \cdot \text{s}^{-1}$])

λ_{eff} effective thermal conductivity of the catalyst [$J \cdot m^{-1} \cdot s^{-1} \cdot K^{-1}$]

λ_g gas mixture thermal conductivity [$J \cdot m^{-1} \cdot s^{-1} \cdot K^{-1}$]

μ_g (dynamic) gas mixture viscosity [$kg \cdot m^{-1} \cdot s^{-1}$]

ρ_b catalyst bulk density [$kg \cdot m^{-3}$]

ρ_g gas mixture density [$kg \cdot m^{-3}$]

τ catalyst tortuosity factor

Φ Wheeler-Weisz modulus $\left(\Phi = \eta\phi^2\right)$

ν_i stoichiometric coefficient of species *i*

4.7 References

Amadeo, N.E., Laborde, M.A., Hydrogen-production from the low-temperature water-gas shift reaction - kinetics and simulation of the industrial reactor. *Int. J. Hydrogen Energy* **1995**, 20 (12), 949-956.

Ayastuy, J.L., Gutierrez-Ortiz, M.A., Gonzalez-Marcos, J.A., Aranzabal, A., Gonzalez-Velasco, J.R., Kinetics of the low-temperature WGS reaction over a $CuO/ZnO/Al_2O_3$ catalyst. *Ind. Eng. Chem. Res.* **2005**, 44 (1), 41-50.

Chen, W.H., Jheng, J.G., Characterization of water gas shift reaction in association with carbon dioxide sequestration. *J. Power Sources* **2007**, 172 (1), 368-375.

Dekker, F.H.M., Bliek, A., Kapteijn, F., Moulijn, J.A., Analysis of mass and heat-transfer in transient experiments over heterogeneous catalysts. *Chem. Eng. Sci.* **1995**, 50 (22), 3573-3580.

Fajin, J.L.C., Cordeiro, M.N.D.S., Illas, F., Gomes, J.R.B., Influence of step sites in the molecular mechanism of the water gas shift reaction catalyzed by copper. *J. Catal.* **2009**, 268 (1), 131-141.

Fishtik, I., Datta, R., A UBI-QEP microkinetic model for the water-gas shift reaction on Cu(111). *Surf. Sci.* **2002**, 512 (3), 229-254.

Fogler, H.S., *Elements of chemical reaction engineering*. Prentice Hall: 2006.

Froment, G.F., Bischoff, K.B., *Chemical reactor analysis and design.* Wiley: New York, 1990.

Gokhale, A.A., Dumesic, J.A., Mavrikakis, M., On the mechanism of low-temperature water gas shift reaction on copper. *J. Am. Chem. Soc.* **2008**, 130 (4), 1402-1414.

Koryabkina, N.A., Phatak, A.A., Ruettinger, W.F., Farrauto, R.J., Ribeiro, F.H., Determination of kinetic parameters for the water-gas shift reaction on copper catalysts under realistic conditions for fuel cell applications. *J. Catal.* **2003**, 217 (1), 233-239.

Kumar, P., Akpan, E., Ibrahim, H., Aboudheir, A., Idem, R., Kinetics and reactor modeling of a high temperature water-gas shift reaction (WGSR) for hydrogen production in a packed bed tubular reactor (PBTR). *Ind. Eng. Chem. Res.* **2008**, 47 (12), 4086-4097.

Levenspiel, O., *Chemical reaction engineering*. 3 ed.; John Wiley & Sons: New York, 1999.

Malek, A., Farooq, S., Study of a six-bed pressure swing adsorption process. *AIChE J.* **1997**, 43 (10), 2509-2523.

Mears, D.E., Tests for transport limitations in experimental catalytic reactors. *Ind. Eng. Chem. Process Des. Dev.* **1971**, 10 (4), 541-547.

Moe, J.M., Design of water-gas shift reactors *Chem. Eng. Prog.* **1962**, 58 (3), 33-36

Newsome, D.S., The water-gas shift reaction. *Catal. Rev.-Sci. Eng* **1980**, 21 (2), 275-318.

Ovesen, C.V., Clausen, B.S., Hammershoi, B.S., Steffensen, G., Askgaard, T., Chorkendorff, I., Norskov, J.K., Rasmussen, P.B., Stoltze, P., Taylor, P., Microkinetic analysis of the water-gas shift reaction under industrial conditions. *J. Catal.* **1996**, 158 (1), 170-180.

Patel, S., Pant, K.K., Experimental study and mechanistic kinetic modeling for selective production of hydrogen via catalytic steam reforming of methanol. *Chem. Eng. Sci.* **2007**, 62 (18-20), 5425-5435.

Perez-Ramirez, J., Berger, R.J., Mul, G., Kapteijn, F., Moulijn, J.A., The six-flow reactor technology - A review on fast catalyst screening and kinetic studies. *Catal. Today* **2000**, 60 (1-2), 93-109.

Perry, R.H., Green, D.W., *Perry's chemical engineers' handbook*. McGraw-Hill 1999.

Qi, X.M., Flytzani-Stephanopoulos, M., Activity and stability of Cu-CeO_2 catalysts in high-temperature water-gas shift for fuel-cell applications. *Ind. Eng. Chem. Res.* **2004**, 43 (12), 3055-3062.

Rhodes, C., Hutchings, G.J., Studies of the role of the copper promoter in the iron oxide/chromia high temperature water gas shift catalyst. *Phys. Chem. Chem. Phys.* **2003**, 5 (12), 2719-2723.

Rhodes, C., Hutchings, G.J., Ward, A.M., Water-Gas Shift reaction - finding the mechanistic boundary. *Catal. Today* **1995**, 23 (1), 43-58.

Rodrigues, A.E. In *Scientific basis for the design of two phase catalytic reactors*, NATO advanced study institute on multiphase chemical reactors, 1980; Rodrigues, A.E., Calo, J.M., Sweed, N.H., Eds. 1980.

Salcedo, R.L., Solving nonconvex nonlinear-programming and mixed-integer nonlinear-programming problems with adaptive random search. *Ind. Eng. Chem. Res.* **1992**, 31 (1), 262-273.

Salmi, T., Hakkarainen, R., Kinetic-study of the low-temperature water-gas shift reaction over a Cu-ZnO catalyst. *Appl. Catal.* **1989**, 49 (2), 285-306.

Shido, T., Iwasawa, Y., The effect of coadsorbates in reverse water gas shift reaction on ZnO, in relation to reactant-promoted reaction-mechanism. *J. Catal.* **1993**, 140 (2), 575-584.

Wojciechowski, B., Rice, N., *Experimental methods in kinetic studies*. Elsevier Science BV.: Amsterdam, 2003.

Yagi, S., Kunii, D., Wakao, N., Studies on axial effective thermal conductivities in packed beds. *AIChE J.* **1960**, 6 (4), 543-546.

Chapter 5

Enhancing the Production of Hydrogen via WGS reaction using Pd-based Membrane Reactors

In this chapter, it is described an experimental study regarding the performance of a Pd-Ag membrane reactor recently proposed and suitable for the production of ultra-pure hydrogen. A dense metallic permeator tube was assembled by an innovative annealing and diffusion welding technique from a commercial flat sheet membrane of Pd-Ag. A "finger-like" configuration of the self-supported membrane has been designed and used as a packed-bed membrane reactor (MR) for producing ultra-pure hydrogen via water-gas shift reaction (WGS).

A $CuO/ZnO/Al_2O_3$ catalyst, from REB Research & Consulting, was used for packing the WGS membrane reactor. The performance of the reactor was evaluated in terms of CO conversion and H_2 recovery in a wide range of conditions: temperature from 200 ºC to 300 ºC, feed pressure from 1.0 bar to 4.0 bar, vacuum and sweep gas modes and with a simulated reformate feed (4.70 % CO, 34.78 % H_2O, 28.70 % H_2, 10.16 % CO_2 balanced in N_2). Also, the effect of the reactants feed composition was investigated and discussed. CO conversions remained in most conditions above the thermodynamic equilibrium based on feed conditions. In particular, it is worth mentioning that around 100 % of CO conversion and almost complete H_2 recovery was achieved when operating the MR at 300 ºC with a feed space velocity of 1200 $L_N \cdot kg_{cat}^{-1} \cdot h^{-1}$, a retentate pressure of 4 bar, a permeate pressure of 3 bar and using 1 $L_N \cdot min^{-1}$ of sweep gas.

The contents of this chapter were adapted from: Mendes, D., Chibante, V., Zheng, J.-M., Tosti, S., Borgognoni, F., Mendes, A., Madeira, L. M., Enhancing the production of hydrogen via water-gas shift reaction using Pd-based membrane reactors. *Int. J. Hydrogen Energy* **2010**, accepted for publication.

5.1 Introduction

In recent years, many researchers have focused their attention in the use of Pd-Ag membrane reactors for the WGS reaction. A review covering the application of Pd-based MRs is presented in Chapter 2. Among the works reported so far, it is worth mentioning the Pd-based membranes that are made of self-supporting metal foils with thickness of $25-100\ \mu m$ due to their full permselectivity towards hydrogen. Nevertheless, some issues related to membrane lifetime remain to be solved. With this concern in mind, Tosti et al. (Tosti et al., 2006) developed a new Pd-based permeator tube, in a "finger-like" configuration, which reduces the restrictions between the membrane tube and the module and avoids the presence of any mechanical (cyclic) stresses, assuring a long lifetime and no change in the H_2 separation ability.

Most of the experimental and modeling studies concerning Pd or Pd-Ag based WGS reactors and reported so far devoted their attention to the reaction conversion enhancement (Adrover et al., 2009; Basile et al., 2001; Hwang et al., 2010). In fact, a detailed experimental study on the effect of all operational parameters (temperature, reaction pressure, feed flow rate and reactants feed composition) in terms of H_2 recovery has been hardly addressed, with the exception of very few works (Bi et al., 2009; Brunetti et al., 2009). Moreover, most of the simulation studies consider reaction rate models taken from the literature, where the effect of CO_2 inhibition on the reactor performance (Ma and Lund, 2003) is not properly accounted.

Ideal feeds (CO and H_2O balanced in an inert gas) and/or very specific operating conditions are typically tested in MRs, in particular in the Pd-Ag "finger-like" self-supported membranes, conceived specially for the ultra-pure hydrogen production. Indeed, only very few works studied this type of MR for the WGS reaction and the operating conditions reported are limited and very different from those in the present work. Therefore, the objective of this study was to assess the performance (both in terms of conversion

enhancement and H_2 recovery) of such MR employing a $CuO/ZnO/Al_2O_3$ catalyst using simulated reformate gas mixture. In particular, it was addressed the effect of the reaction temperature (from 200 ºC to 300 ºC), reaction pressure (in the range of $1-4$ bar), feed gas hourly space velocity ($1200-10\,800\ L_N \cdot kg_{cat}^{-1} \cdot h^{-1}$), reactants gas feed composition, and different MR operation modes (vacuum and sweep gas modes). For improving the hydrogen permeation and the reaction rate it is desirable to use high feed pressures. In this work, a new strategy was employed to operate this MR at (relatively) high feed pressures (up to 4 bar, clearly above the ranges tested so far with this system). This was made possible feeding the sweep gas at a higher pressure so that the maximum pressure difference that the Pd-Ag membrane can withstand was assured.

The conversions attained in this work were also compared with the thermodynamic one based on the inlet conditions (temperature and feed composition) – maximum limit attainable in a conventional packed-bed reactor. The results were compared, whenever possible, with literature data.

5.2 Experimental Section

5.2.1 Membrane tube preparation and module assembly

The thin wall permeator tube was prepared starting from a commercial 50-μm Pd-Ag sheet (with 25 wt.% Ag). To reduce the metal hardness, it was carried out the annealing of the metal alloy foil (Tosti et al., 2000a). The heat treatment was performed in a high-vacuum (< 10^{-4} mbar) oven, to avoid oxidation, with a heating ratio of 5 °C·min^{-1} up to 900 ºC, staying at this temperature for 1 h. This thin metal foil has been cut to measure, providing however a sufficient side margin to allow the edges to be overlapped in the area of welding. Subsequently, the metal alloy thin foil has been wrapped around an alumina bar in order to obtain permeating tubes of length 50 mm and internal diameter 10 mm and proceed with the

joining of the limbs by a diffusion bounding welding. This welding technique consists in a thermal treatment (under the same operating conditions of the annealing process) where the limbs of the metal foil, overlapped and compressed in a special device, are joined mainly because of the silver atoms diffusion in the metal alloy. To apply a controlled pressure over the overlapped limbs of the Pd-Ag tube, a thermo-mechanical press consisting of Inconel® plates and Invar screws is used. During this step, a foil of mica (flogopite) with thickness $25-40$ μm comes arranged between the press and the limbs of the Pd-Ag tube to avoid the diffusion of the Pd and Ag atoms to the press during the heat treatment. A dynamometric key is finally used to allow a controlled and precise tightening over the welding area. Finally, the Pd-Ag tube with 50 mm of length has been joined to a stainless steel VCR connection and a steel plug by brazing. In this way, the permeator has the stiffness needed to assure a tight assembly into the membrane module. Figure 5.1 shows a scheme (a) and a picture (b) of the thin wall permeator tube, which has been inserted into a stainless steel module.

a) b)

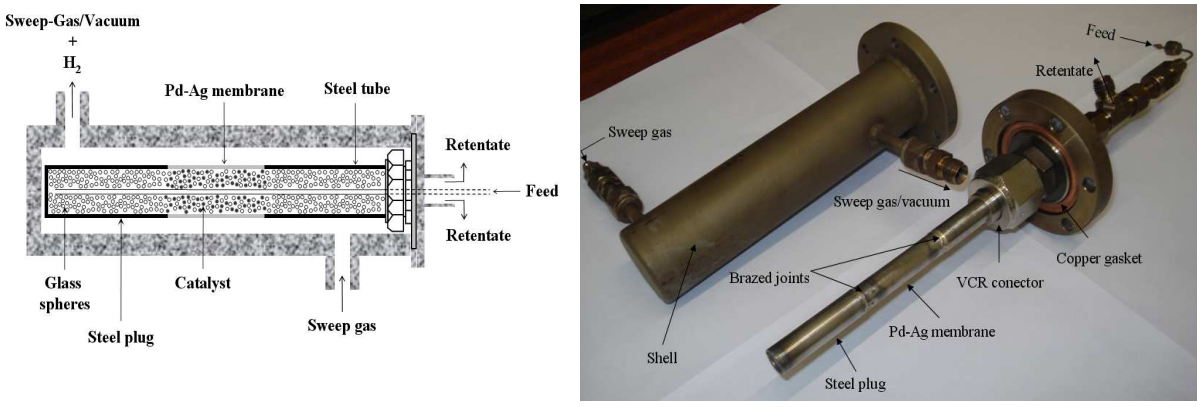

Figure 5.1 - Scheme (a) and picture (b) of the Pd-Ag "finger-like" configuration membrane reactor.

The assembly of the Pd-Ag membrane has a "finger-like" configuration in order to allow the membrane elongation and contraction due to the hydrogenation and thermal cycles. Long-term tests (1 year) already demonstrated the complete hydrogen selectivity and durability of these permeators, showing no formation of defects (holes and cracks) (Tosti et

al., 2006). As can be seen in Figure 5.1, a stainless steel tube (O.D. 1/16 inch) is inserted inside the Pd-Ag membrane in order to feed the gas stream; the retentate chamber is in the annular section.

5.2.2 Experimental setup

Mass flow controllers (Bronkhorst Hi-Tec, model F201) were used to feed pure hydrogen or gas mixtures to the MR (cf. Figure 5.2). For experiments involving humidified gas streams, deionized water was metered, vaporized and mixed in a Controller Evaporator Mixer (CEM, Bronkhorst) system with the other gases before entering the reactor. The MR was encased in an electrical oven (Memmert, type UNE200), controlled by a programmable temperature controller. A thermocouple was inserted through the top of the reactor for reading the membrane surface temperature (permeation side), approximately at the axial center. The pressure in the lumen/feed side was measured using a pressure transducer (Druck, ref. 4010, 7 bar) and adjusted using a back-pressure regulator (Swagelok); a second pressure transducer (Druck, ref. 4010, 5 bar) and a back-pressure regulator (Swagelok) were used to read and regulate the shell side pressure. Different operation modes were used to produce a pressure gradient between lumen and shell side: (i) permeate chamber was open to the atmosphere, (ii) nitrogen was used as sweep gas, and (iii) the shell side was continuously evacuated using a diaphragm vacuum pump (Thomas Instruments, ref.: 7011-0069). In this case, the permeate feed was closed using an on/off valve - Figure 5.2.

The reactor outlet stream (retentate) was passed through a condenser at room temperature to remove the condensable water. The dried gaseous stream flow rate was measured using a mass flow meter (Bronkhorst Hi-Tec, model F201) (cf. Figure 5.2); the permeating hydrogen stream was also read using a second mass flow meter (Bronkhorst Hi-Tec, model F201). The gas phase products, N_2, CO and CO_2, were analyzed in a gas chromatograph (Dani 1000

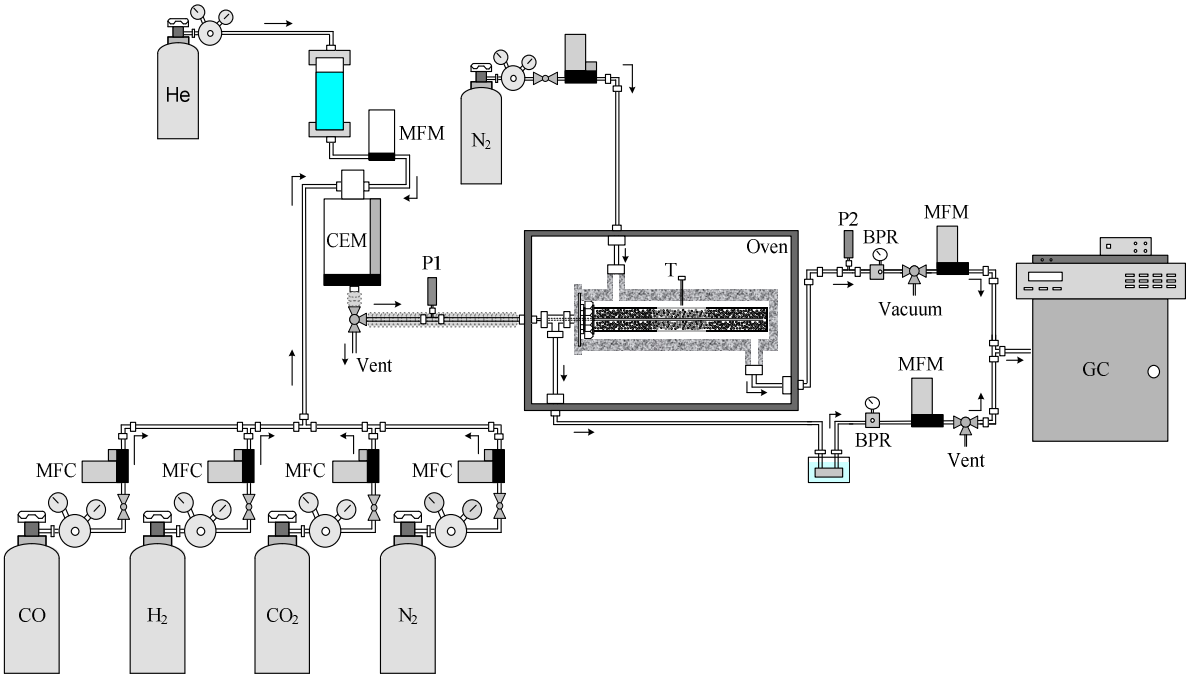

Figure 5.2 – Scheme of the experimental set-up (BPR: back-pressure regulator; CEM: controller-evaporator-mixer; GC: gas chromatograph; MFC: mass flow controller; MFM: mass flow meter; P1 and P2: pressure transducers; T: thermocouple).

GC), equipped with a chromatographic column Supelco Carboxen 1010 Plot, 30 m x 0.32 mm I.D., and a TCD (Valco thermal conductivity detector); helium was used as carrier. The relative errors of carbon and nitrogen molar balances were typically lower than 5 %. Regarding hydrogen, it is difficult to analyze it by GC-TCD since the thermal conductivity of hydrogen is close to that of helium, used as carrier gas. Therefore, the H_2 composition in the retentate stream was calculated from the mass balance (difference from 100 %, dry basis). Further details concerning the analysis method can be found in chapter 3 and Appendix A.

5.2.2.1 Permeation experiments

Pure hydrogen was fed to lumen side (cf. Figures 5.1 and 5.2) with pressure ranging from 1.1 bar to 2.5 bar, temperature ranging from 200 ºC to 300 ºC and flow rate ranging from $50-190\ mL_N \cdot min^{-1}$. Permeance was measured using the stainless steel permeator sketched

in Figure 5.1. Upon heating the module, the membrane was kept in a N_2 atmosphere until the desired temperature was reached, then H_2 was introduced. The H_2 feed gas flowed along the inner side of the membrane and the permeating stream flow rate was measured on the shell side at atmospheric pressure with a mass flow meter after steady state (approximately 1 h) had been achieved, at the operating temperature. Pressure differences between retentate and permeate sides were obtained by varying the pressure on the upstream side and keeping the downstream pressure constant at 1 bar. Neither sweep gas nor vacuum was used. Pressures in the two sides of the membrane tube were monitored via pressure transducers. Frequently, the selectivity of the membrane was obtained against nitrogen. When nitrogen was introduced pressurized in the retentate chamber and the unit closed, no decline in the pressure was noticed after 8 hours, confirming the full hydrogen permeation selectivity of the Pd-Ag membrane.

5.2.2.2 WGS reaction tests

In chapter 3, a commercial $CuO/ZnO/Al_2O_3$ catalyst, supplied by REB Research & Consulting, was evaluated (among other promising samples) to catalyze the WGS reaction. The copper-based catalyst showed the best relation activity/stability for the entire range of temperatures tested ($150-300$ ºC) using a simulated reformate feed composition. In this chapter, the WGS reaction was performed in the temperature range $200-300$ ºC by packing a certain amount of the same catalyst into the lumen side of the MR (cf. Figure 5.1a). Prior to the reaction runs, the WGS catalyst was activated *in situ* with a mixed gas flow of H_2/N_2. The pre-reduction protocol considered heating the catalyst, in nitrogen, from room temperature up to 230 ºC, at 5 ºC·min^{-1}; then, a reduction mixture (5 vol.% of H_2/N_2, total flow rate of 100 $mL_N \cdot min^{-1}$) was admitted and the sample maintained at 230 ºC for 5 hours. After reduction, the catalyst was cooled or heated to the reaction temperature (analyzed in the range $200-300$ ºC) and the reactor flushed with N_2 prior to feeding the reaction

mixture. Overheating of the catalyst bed and subsequent metal particles sintering during the reduction was avoided controlling closely the hydrogen feed flow rate. The $CuO/ZnO/Al_2O_3$ catalyst (1.5 g) was diluted with glass spheres of the same particle size ($250-355$ μm) to avoid temperature gradients in the bed (checked previously in a packed-bed reactor), caused by the exothermic reaction. During the experimental campaign, in the absence of the reaction mixture, the system was kept under N_2 atmosphere to avoid re-oxidation.

The reaction tests were carried out using the following feed gas composition: 4.70 % CO, 34.78 % H_2O, 28.70 % H_2, and 10.16 % CO_2 balanced in N_2, which simulates a reformate feed. The reaction pressure (that is, the pressure in the lumen side of the membrane) and the feed flow rate were varied in the range $1-4$ bar and $30-270$ $mL_N \cdot min^{-1}$, respectively. In the first set of experiments, hydrogen has been recovered in the shell side of the membrane cell by vacuum pumping (shell side pressure ~ 30 mbar). Then, nitrogen was fed to the shell side (sweep gas), at a flow rate ranging from 100 to 1500 $mL_N \cdot min^{-1}$, counter-currently, to decrease further the hydrogen partial pressure. During this procedure, the total pressure gradient between lumen and shell side was maintained at 1 bar (for mechanical reasons). Additionally, to simulate the performance of a packed bed reactor (PBR from now on) for posterior comparison with the MR operation, the permeate chamber was closed and data taken after steady-state was achieved.

The influence of the most important operating variables (i.e. reaction pressure, temperature, steam-to-CO ratio, feed space velocity and sweeping gas flow rate) on the reaction conversion and H_2 recovery were studied.

5.3 Results and Discussion

The catalytic performance and separation ability of the Pd-Ag membrane reactor for conducting the WGS reaction have been evaluated in terms of the steady-state carbon

monoxide conversion (X_{CO}) and hydrogen recovery (Re_{H_2}). Both parameters were calculated according to equations 5.1 and 5.2, respectively:

$$X_{CO} = 1 - \frac{F_{CO}^{R,\,out}}{F_{CO}^{R,\,in}} \tag{5.1}$$

$$Re_{H_2} = \frac{F_{H_2}^{P,\,out}}{F_{H_2}^{R,\,out} + F_{H_2}^{P,\,out}} \tag{5.2}$$

where F is the molar flow rate. The superscripts *R* and *P* stand for retentate and permeate chambers, respectively; *in* and *out* means inlet and exit of the reactor, respectively.

5.3.1 Permeation tests

The H_2 mass transfer through thick palladium-based membranes at high temperatures (> 150 ºC) is usually rate-limited by the diffusion of hydrogen through the metal lattice (Paglieri and Way, 2002) and is described by the *Fick's law*:

$$J = -D_H \frac{\mathrm{d}C_H}{\mathrm{d}x} \tag{5.3}$$

where J is the hydrogen diffusion flux through the metal lattice, D_H is the effective diffusion coefficient of atomic hydrogen, and C_H is the atomic hydrogen concentration at the spatial position x along the membrane thickness.

C_H is related to the hydrogen partial pressure, p_{H_2} , by *Sieverts' law* (equilibrium conditions) (Paglieri and Way, 2002):

$$C_H = S\, p_{H_2}^{0.5} \tag{5.4}$$

where S is the sorption coefficient of hydrogen in the lattice. If the sorbed hydrogen is in equilibrium with gas phase at both membrane surfaces, combining equations (5.3) and (5.4), and integrating for the membrane thickness, δ, one obtains:

$$J_{H_2} = \frac{L_{H_2}}{\delta}\left(\sqrt{p_{H_2}^{R}} - \sqrt{p_{H_2}^{P}}\right) \tag{5.5}$$

where L_{H_2} is the hydrogen permeability.

Equation (5.5) is valid for defect free membranes. To account also for the mass transport through defects the previous equation is normally written as:

$$J_{H_2} = \frac{L_{H_2}}{\delta}\left(p_{H_2}^{R\ n} - p_{H_2}^{P\ n} \right) \tag{5.6}$$

where *n* stands for the power dependency of the hydrogen concentration on its partial pressure; *n* ranges from 0.5 to 1 and should be obtained experimentally (Dittmeyer et al., 2001).

Assuming that the mass transport is controlled by the diffusion of atomic hydrogen (*n* = 0.5) within the temperature range considered, the relationship between the hydrogen permeability and the temperature can be described by an *Arrhenius-type equation* (Dittmeyer et al., 2001):

$$L_{H_2} = L_{H_2}^0 \, exp\left(-\frac{E^p}{\Re T} \right) \tag{5.7}$$

Combining expressions (5.5) and (5.7) the *Richardson's equation* is obtained:

$$J_{H_2} = \frac{L_{H_2}^0 \, exp\left(-\frac{E^p}{\Re T} \right)}{\delta}\left(\sqrt{p_{H_2}^R} - \sqrt{p_{H_2}^P} \right) \tag{5.8}$$

The permeation tests carried out at different transmembrane pressure differences and temperatures were used for obtaining the parameters of equation 5.6 (L_{H_2} and *n*) and further its permeation activation energy, E^p. In Figure 5.3, the results presented indicate that the permeation rate of H_2 is directly proportional to the difference between the square roots of the H_2 partial pressure in the retentate and permeate sides (*n* = ½ in equation 5.6, determined by regression – data not shown). This shows that the mass transport is controlled by the diffusion of atomic hydrogen through the Pd-Ag membrane – *Sieverts' law*.

The experimental permeability values towards H_2 (L_{H_2}) at different temperatures (T) were then used to estimate the activation energy for H_2 permeation. Table 5.1 reports a comparison of the permeation parameters for Pd-based membranes typically found in the literature with the ones from this work.

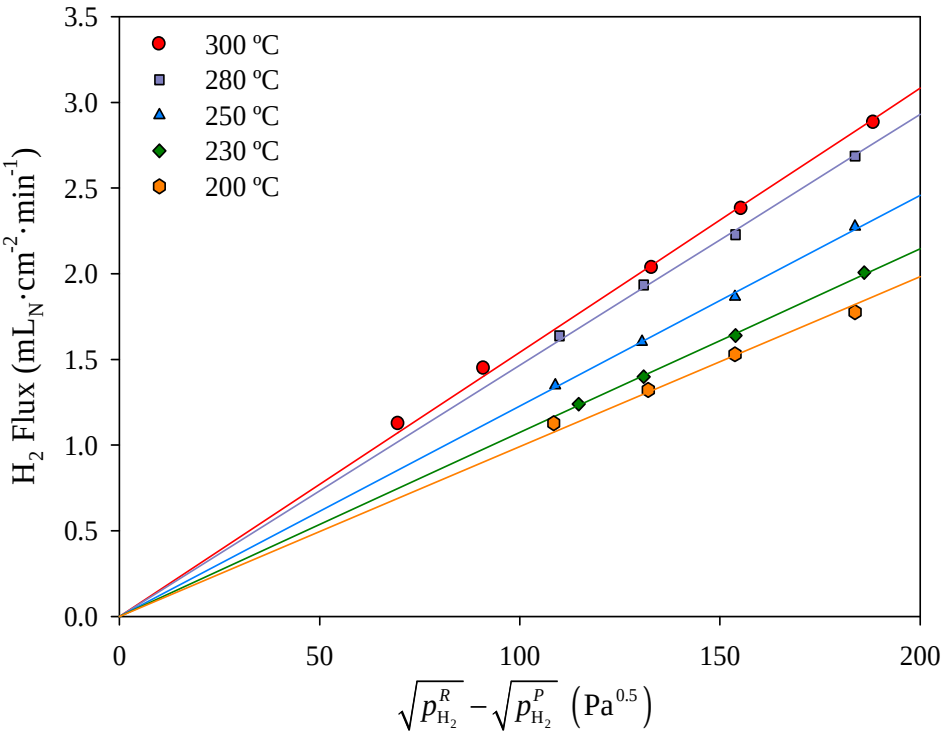

Figure 5.3 – Hydrogen flux through the 50 μm thick Pd-Ag membrane as a function of the difference between the square root of hydrogen partial pressure in the retentate and permeate sides.

Table 5.1 – Apparent activation energy and pre-exponential factor for hydrogen permeation through dense Pd-Ag membranes determined in this work and taken from the literature.

E^P / kJ·mol^{-1}	$L^o_{H_2}$ / mol·m·m^{-2}·s^{-1}·Pa$^{-0.5}$	Reference
10.72	5.44×10^{-8}	This work
11.24	6.64×10^{-8}	(Tosti et al., 2006)
17.60	2.06×10^{-7}	(Iulianelli et al., 2008)
18.45	3.23×10^{-7}	(Uemiya et al., 1991a)
18.56	3.85×10^{-7}	(Davis, 1954)

The calculated values for the permeation activation energy and pre-exponential factor ($L^{o}_{H_2}$) are in good agreement to other experimental data, as also shown in Figure 5.4.

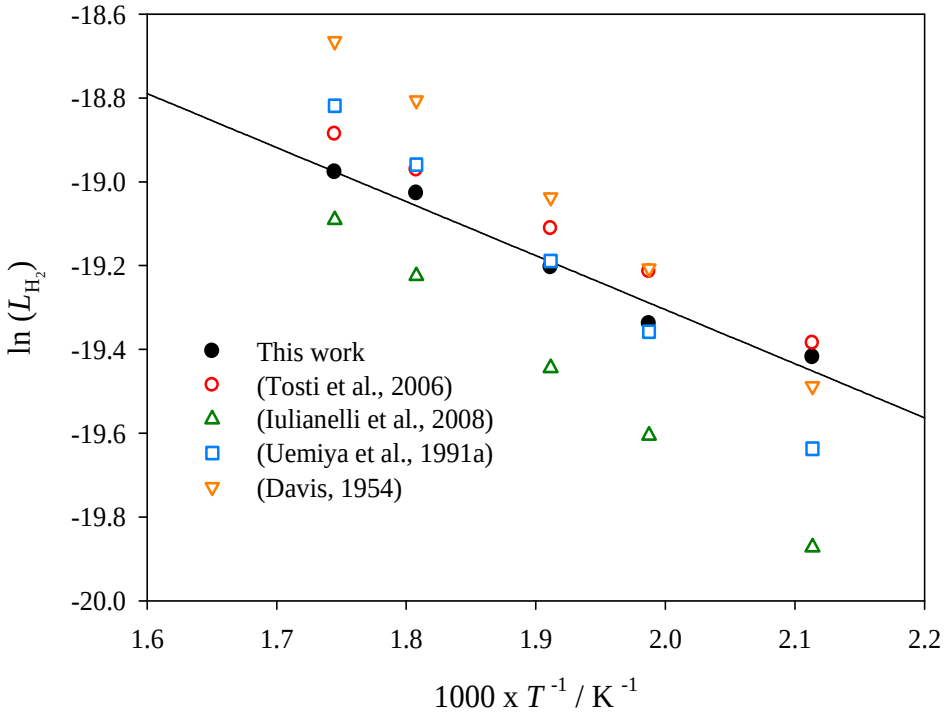

Figure 5.4 – Hydrogen permeability versus temperature for the Pd-based membrane of this work and others reported in the literature. The line represents the regression of data from this work with equation 5.7.

5.3.2 WGS reaction in the Pd-Ag MR

In this section the performance of the Pd-Ag MR using a copper-based catalyst for the WGS reaction is analyzed. Such evaluation (performed in terms of catalyst activity - X_{CO} - and separation ability - Re_{H_2}) takes into account the effect of the most important operating variables. Each data point in the graphs results from the average of at least three experiments.

5.3.2.1 Influence of the reaction temperature

Figure 5.5 illustrates the CO conversion in the WGS reaction and the H_2 recovery obtained in the Pd-Ag MR as a function of the temperature. In this section, hydrogen was collected in the permeate side of the membrane module by vacuum pumping ($P^P \sim 30$ mbar, vacuum mode). A feed pressure of 1.1 bar and a GHSV (gas hourly space velocity) = 3200 $L_N \cdot kg_{cat}^{-1} \cdot h^{-1}$ were used. The dotted curve shows the WGS thermodynamic equilibrium conversion (X_{CO}^{eq}) calculated based on the inlet reformate gas composition – see chapter 2.

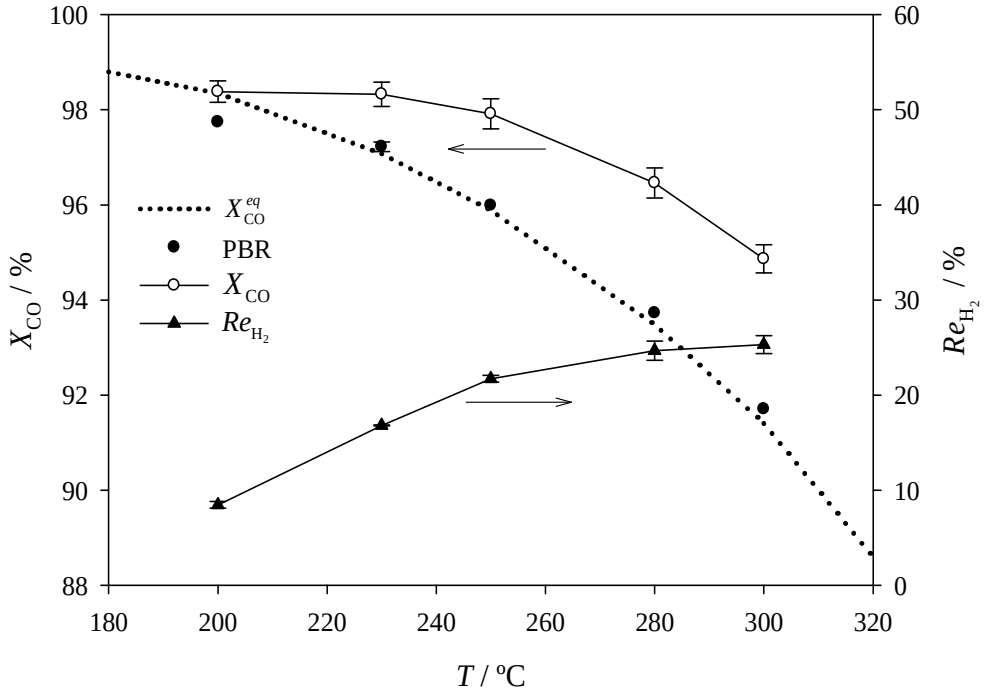

Figure 5.5 – Influence of the reaction temperature on the CO conversion and H_2 recovery for the WGS reaction over a Cu-based catalyst in packed-bed reactor and in Pd-Ag MR (P^F = 1.1 bar, $P^P \sim 30$ mbar (vacuum mode), GHSV = 3200 $L_N \cdot kg_{cat}^{-1} \cdot h^{-1}$, and feed composition: 4.70 % CO, 34.78 % H_2O, 28.70 % H_2, 10.16 % CO_2 balanced in N_2).

At conditions close of a packed-bed reactor, the CO conversion for 200 ºC is below the equilibrium conversion due to kinetic limitations (cf. Figure 5.5). With the increase of the temperature the kinetics is favored, and thus the WGS conversion in the PBR approaches the thermodynamic limit, which is not favored by the exothermic nature of the reaction (and is

thus smaller than at 200 ºC). Operating with the Pd-Ag MR, X_{CO} is enhanced in the entire range of temperatures used. In particular, the shift on the conversion is more noticeable at higher temperatures because of the larger H_2 extraction from the reaction zone despite the lower H_2 partial pressure in the retentate side (lower carbon monoxide conversion). Even though the H_2 recovery and kinetic rate are both improved by temperature (especially up to 250 ºC), CO conversion in the MR is penalized by thermodynamic constraints of the exothermic WGS reaction.

For the MR properties and operating conditions used in this work, higher CO conversions $(98.0-98.5\ \%)$ can be reached at lower temperatures (< 230 ºC) where the equilibrium conversion is favored (cf. Figure 5.5). This observation highlights the fact that Pd-Ag MRs can be advantageously used also in terms of energy savings when compared with the conventional reactors.

The optimum performance of a Pd-Ag MR conducting the WGS reaction should balance a high CO conversion and a high H_2 recovery. Despite the equilibrium conversion being favored for low temperatures, this is a very limiting condition in terms of H_2 recovery. As it can be seen in Figure 5.5, the lowest recovery ($Re_{H_2} \sim 8.5\ \%$) was obtained at 200 ºC. As mentioned previously, H_2 permeation through dense Pd-Ag membranes is an activated process; therefore, Re_{H_2} is not favored when operating at lower temperatures. In addition, it is well-known the blocking effect of the Pd membrane surface sites caused by CO for T < 350 ºC (Mejdell et al., 2009); this inhibitory effect decreases with temperature because less CO is adsorbed on the membrane surface. The increments of the H_2 recovery were more evident at temperatures < 250 °C (specifically, by moving from 200 °C to 250 °C) where the H_2 permeation kinetics are rate limiting. Above 250 ºC, Re_{H_2} did not increase significantly due to the compromise between the kinetic rate of the WGS reaction, hydrogen permeation

through the membrane and the thermodynamic constraints of the WGS reaction. This fact was also recently observed by other authors (Bi et al., 2009).

In order to improve the performance of the MR described in this work, in particular hydrogen recovery, other relevant operation parameters were studied as described in the following sections.

5.3.2.2 Influence of the feed space velocity

The space velocity was varied by changing the feed flow rate while keeping the amount of catalyst constant. The effect of feed space velocity on CO conversion and H_2 recovery was investigated by performing the WGS in the Pd-Ag MR operating in vacuum mode (simulated PBR performance is also included for comparison). The results are indicated in Figure 5.6.

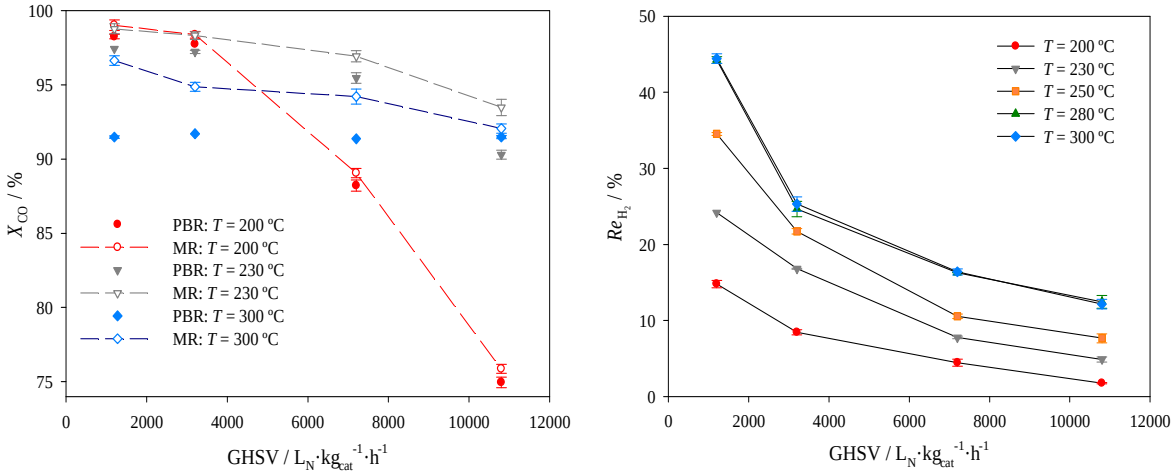

Figure 5.6 - CO conversion and H_2 recovery as a function of the gas hourly space velocity (GHSV) for the WGS reaction over a Cu-based catalyst in packed-bed reactor and in Pd-Ag MR (P^F = 1.1 bar, P^P ~ 30 mbar (vacuum mode) and feed composition: 4.70 % CO, 34.78 % H_2O, 28.70 % H_2, 10.16 % CO_2 balanced in N_2).

The results show a CO conversion enhancement with the Pd-Ag MR as compared to the PBR for the entire range of space velocities. Moreover, CO conversions at 300 ºC remained above the thermodynamic equilibrium value (curve not shown for simplicity) for the entire range of feed space velocities tested. The shift on the conversion (MR vs. PBR) becomes higher at

elevated temperatures, where the H_2 recovery is also favored, in line with the results shown in the previous section. From Figure 5.6, it is clear that lower levels of CO conversions and H_2 recoveries are obtained as GHSV increases (except for X_{CO} in the PBR at 300 ºC because conversions close to the thermodynamic limit are always reached). In fact, higher feed space velocities lead to lower residence times, which are disadvantageous in terms of H_2 generation as well as in terms of H_2 permeation through the Pd membrane. Particularly, at 200 ºC X_{CO} decreases from ca. 99.0 % to ca. 75.9 % – cf. Figure 5.6. For higher temperatures such decrease is less noticeable, due to the fact that under such conditions conversion is already close/above the thermodynamic one and the membrane permeation is higher (see also Figure 5.5).

The effects of the GHSV obtained in this work are in line with the trends reported in other works (e.g. (Bi et al., 2009; Criscuoli et al., 2000; Uemiya et al., 1991b)). In particular, Uemiya et al. (Uemiya et al., 1991b) studied the WGS reaction in a 20-µm thick palladium composite membrane obtaining a conversion enhancement from 75 % to 94 % when the GHSV was decreased from 2150 to 250 $L_S \cdot kg_{cat}^{-1} \cdot h^{-1}$ (12 g of a ferrochrome catalyst; ideal feed mixture – $H_2O/CO = 1$; 400 ºC; feed at atmospheric pressure and sweeping the permeate with Ar).

As shown in Figure 5.6, the MR operating at 300 ºC and GHSV = 1200 $L_N \cdot kg_{cat}^{-1} \cdot h^{-1}$ produces a maximum H_2 recovery of 44.3 %. In this work, the H_2 recovery dependence with the space velocity follows an exponential decay trend, whatever the temperature used. Bi et al. (Bi et al., 2009) observed a quick and linear decay on the H_2 recovery (from 84.8 % to 48.7 %) with an increase of the space velocity (from 4050 to 9100 $L_N \cdot kg_{cat}^{-1} \cdot h^{-1}$).

From Figure 5.6, it can be seen that very similar H_2 recoveries were obtained for all range of GHSV tested at 280 ºC and 300 ºC. This can be explained by the above mentioned compromise between the hydrogen permeation and the equilibrium constraints of the WGS reaction.

5.3.2.3 Influence of the feed pressure

For a successful application of Pd-Ag MRs in the WGS reaction it is important to achieve high hydrogen permeation rates. This can be achieved by increasing the hydrogen partial pressure difference between retentate and permeate sides and hence maximizing the driving force for hydrogen permeation (see equation 5.5). One method to accomplish this is to increase the feed pressure despite it does not influence the WGS reaction from a thermodynamic point of view. Other options are decreasing the permeate chamber pressure by applying vacuum to the permeate side, or by applying a sweep gas.

In the next sections, the effect of the feed pressure in the MR performance was studied for different operation modes (at a GHSV = 1200 $L_N \cdot kg_{cat}^{-1} \cdot h^{-1}$): (i) vacuum mode – the permeate chamber was continuously evacuated by vacuum pumping (the vacuum pressure was limited to ~ 30 mbar), and (ii) sweep-gas mode – nitrogen was supplied to the permeate side in a counter-current manner to sweep the permeated hydrogen. From the mechanical point of view, it is worth noting that the difference between the lumen and external (total) pressure cannot overcome 2 bar. Moreover, the total pressure gradient ($\Delta P = P^F - P^P$) must be always positive in order to avoid the collapse of the membrane. Having these issues in mind, a new strategy, at least never tested for this kind of membranes, allowed us to achieve (relatively) high pressures by using a pressurized sweep gas, as shown below.

a) Vacuum and sweep gas mode

Figure 5.7 illustrates the influence of feed pressure on CO conversion for the WGS and H_2 recovery obtained in the Pd-Ag MR. For the same permeate pressure (~ 30 mbar), the results show that CO conversion and H_2 recovery increased substantially with the feed pressure. Particularly, at 300 ºC the increase of feed pressure from 1.1 bar to 2.0 bar promoted notably the H_2 recovery, from 44.4 % to 84.2 %, driving up CO conversion from

96.6 % to 99.1 %. The effect of the feed pressure is ascribed to a higher permeation driving force, as mentioned above. However, it has also a positive effect on the WGS reaction rate.

The CO conversion and H_2 recovery obtained with the Pd-Ag MR operating on sweep gas mode as a function of the feed pressure, keeping constant the overall pressure difference $\Delta P = P^F - P^P = 1$ bar, is shown in Figure 5.8.

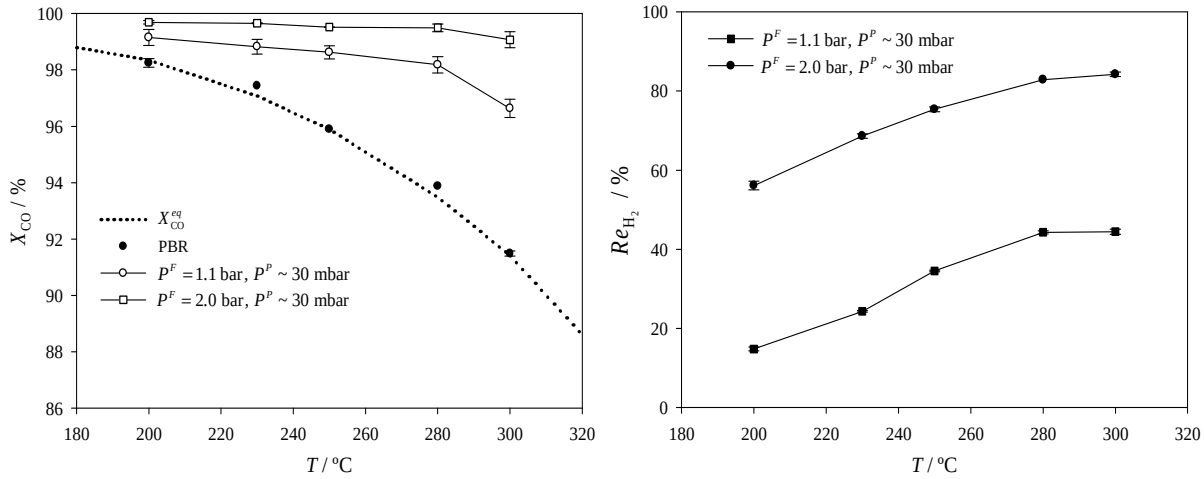

Figure 5.7 - CO conversion and H_2 recovery as a function of the feed pressure for the WGS reaction in the Pd-Ag MR operating in vacuum mode (GHSV = 1200 $L_N \cdot kg_{cat}^{-1} \cdot h^{-1}$, feed composition: 4.70 % CO, 34.78 % H_2O, 28.70 % H_2, 10.16 % CO_2 balanced in N_2).

The use of sweep gas acts positively on the hydrogen permeation, thus allowing a higher H_2 recovery and enhanced CO conversion – cf. Figures 5.7 and 5.8. Comparing the MR operating modes (for the same feed pressure), higher conversions and H_2 recoveries are achieved when the permeated hydrogen is swept by nitrogen. This is a consequence of the vacuum pump limitations.

From Figure 5.8, one can see that the increase of feed pressure from 2.0 bar to 4.0 bar raised the H_2 recovery from 90.8 % to 99.2 %, enhancing the CO conversion from 99.6 % to 100 %, at 300 ºC. The decay on CO conversion in the temperature range studied is almost unnoticeable when N_2 sweeps the permeated H_2. On the other hand, the improvement on the H_2 recovery is more evident. It is thus remarkable that under moderate conditions of

temperature and pressure, almost complete CO conversion and total H_2 recovery have been achieved.

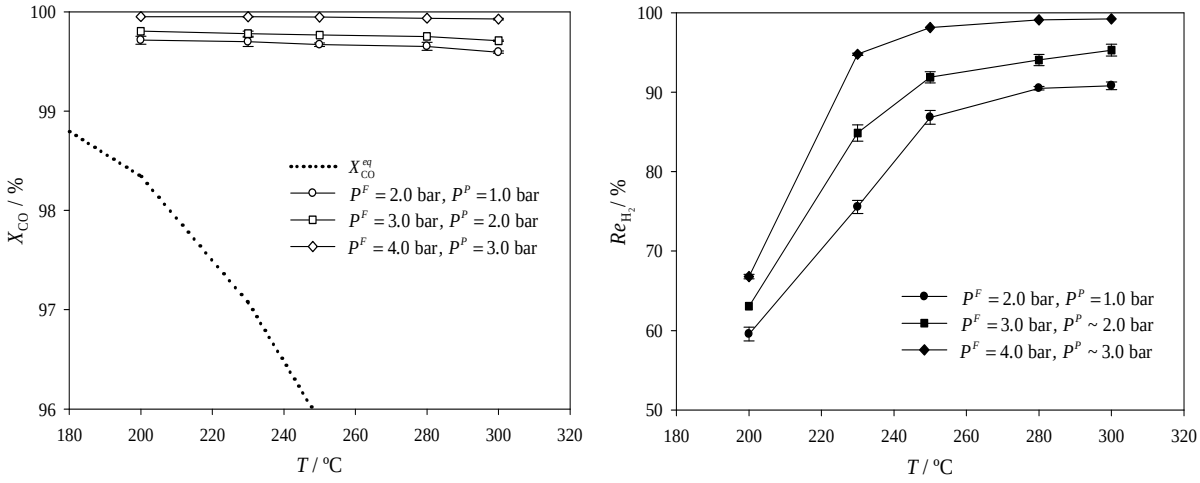

Figure 5.8 – CO conversion and H_2 recovery as a function of the feed pressure for the WGS reaction in the Pd-Ag MR operating on sweep gas mode (N_2 sweep gas flowrate = 1 $L_N \cdot min^{-1}$, GHSV = 1200 $L_N \cdot kg_{cat}^{-1} \cdot h^{-1}$, feed composition: 4.70 % CO, 34.78 % H_2O, 28.70 % H_2, 10.16 % CO_2 balanced in N_2).

To the best of our knowledge, only a few experimental studies concerning the evaluation of the feed pressure effect on the WGS reaction were carried out on Pd-based MRs (e.g. (Basile et al., 1996; Pinacci et al., 2009)). Also, Bi et al. (Bi et al., 2009) obtained a H_2 recovery enhancement, from 40.5 % to 89.2 %, and a CO conversion improvement, from 86.0 % to 95.5 %, but by increasing the feed pressure from 4 bar to 12 bar (at 350 ºC and GHSV = 4050 $L_N \cdot kg_{cat}^{-1} \cdot h^{-1}$ with no sweep gas).

It is important mentioning that, for real applications, a balance should be done between the positive effects due to a pressure increase on the MR performance (higher CO conversion and hydrogen recovery) and the consequent disadvantages in terms of operating costs linked to the feed compression.

b) The effect of sweep gas flow rate

As mentioned above, a sweep gas stream can be used to maintain a high H_2 partial pressure gradient across the membrane, promoting CO conversion and H_2 recovery. The influence of the sweep gas flow rate on X_{CO} and Re_{H_2} was studied and the results are indicated in Figure 5.9. The reaction was carried out in the P^F range of 2.0 bar to 4.0 bar at temperatures of 200 ºC and 300 ºC.

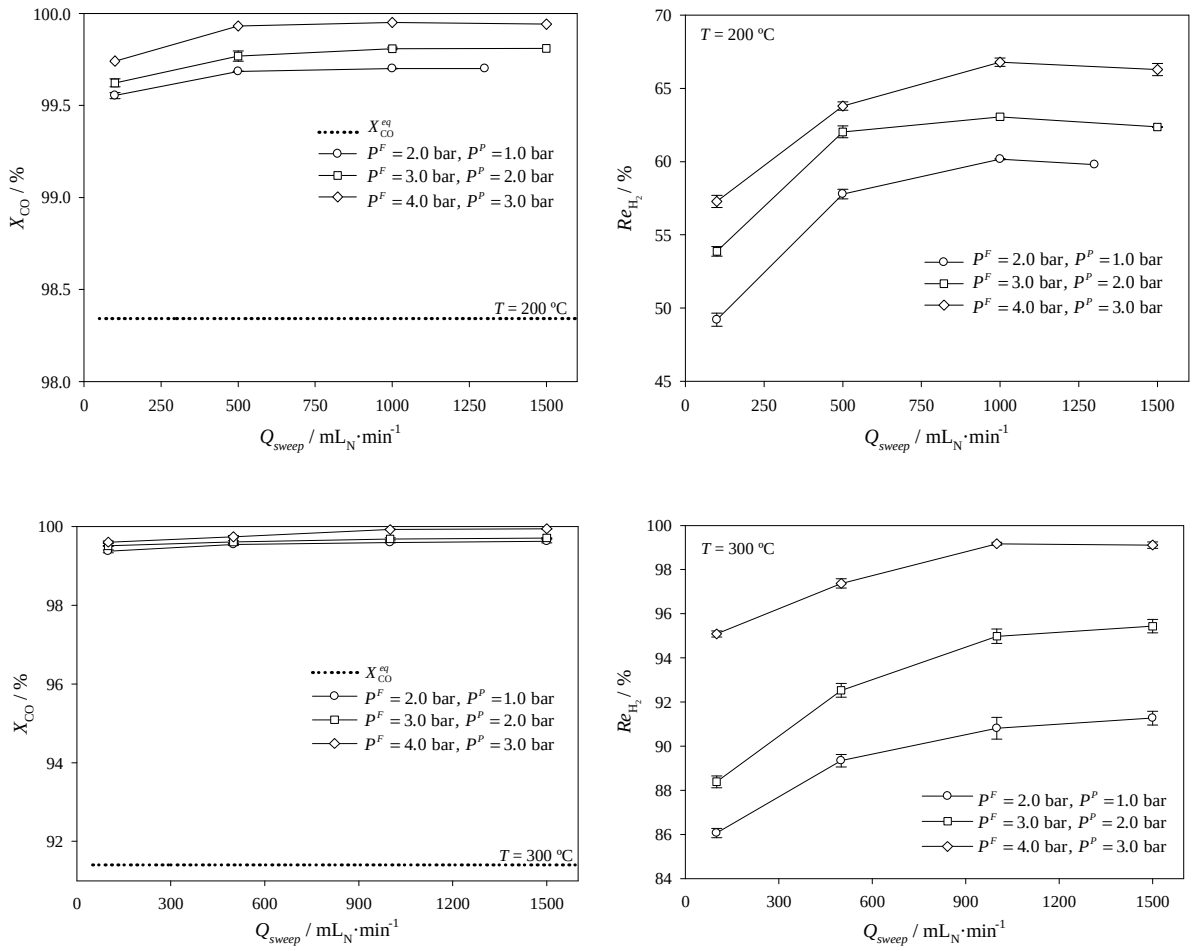

Figure 5.9 - CO conversion and H_2 recovery as a function of the sweep-gas flow rate for the WGS reaction in the Pd-Ag MR (GHSV = 1200 $L_N \cdot kg_{cat}^{-1} \cdot h^{-1}$, feed composition: 4.70 % CO, 34.78 % H_2O, 28.70 % H_2, 10.16 % CO_2 balanced in N_2).

From Figure 5.9, it can be seen that CO conversion and H_2 recovery are generally favored when the sweep gas flow rate is increased. The positive effect of the sweep gas flow rate is related to equation 5.5. In other words, by increasing the sweep gas flow rate the

hydrogen partial pressure in the shell side decreases, resulting in a higher driving force for the hydrogen permeation. So, the H_2 recovery is promoted, favoring the CO shift.

Due to the high conversions achieved, improvements are more clearly visible when the system operates with sweep-gas in the range of low flow rates. Particularly, at 200 ºC, $P^F = 4.0$ bar and $P^P = 3.0$ bar, the H_2 recovery increases from 57.3 % to 66.8 % when the sweep flow rate increases from 100 to 1000 $mL_N \cdot min^{-1}$. Operating at 300 ºC and at the same pressure conditions, the recovery increased from 95.1 % to 99.2 %.

Slight decreases on CO conversion and H_2 recovery are observed when using sweep gas flow rates higher than 1000 $mL_N \cdot min^{-1}$, particularly at 200 ºC. The use of a very high sweep gas flow rate can lead to a small temperature decrease on the outer surface of membrane, decreasing the H_2 permeability (*Arrhenius law* – equation 5.7).

The positive effects of the sweep-gas flow rate are again in accordance with literature data. In particular, Tosti el al. (Tosti et al., 2000b) report CO conversion enhancement from 84 % to total conversion when the sweep gas flow rate was increased from 230 to 470 $mL_N \cdot min^{-1}$. The authors used a MR containing a membrane selective only to hydrogen (60-μm Pd layer on a ceramic support) operating at 330 ºC and using the stoichiometric feed ratio ($H_2O/CO = 1$) containing only CO plus H_2O.

It is interesting to highlight the fact that the use of a sweep gas plays a more important role in the improvement of the CO conversion when the MR utilizes a membrane 100 % selective to H_2. This occurs because otherwise there is permeation of other reactants through the membrane to some extend. Criscuoli et al. (Criscuoli et al., 2000) performed the WGS reaction on a mesoporous MR at T = 322 ºC, H_2O/CO = 0.73 with both retentate and permeate pressures at 1 bar. A decrease in the CO conversion was observed for sweep gas flow rates higher than 100 $mL_N \cdot min^{-1}$ due to the counter-diffusion effect of N_2 (sweep gas) from the shell to the reaction side.

5.3.2.4 Influence of the steam-to-CO ratio

Commercial processes involving the WGS reaction are operated in the presence of excess of steam (i.e. high steam-to-carbon monoxide ratios) to favor the equilibrium shift. However, from an economic point of view, the large amount of water vapor required is disadvantageous because it increases the energy consumption (in its vaporization). On the other hand, Pd-Ag MRs must possess versatility to operate with WGS feeds from different reforming processes and hydrocarbon feedstocks. Therefore, the study of the reactant's molar fraction effect on the WGS MR performance gains an important relevance.

The studies concerning the influence of the CO and H_2O content in the feed were performed in vacuum mode for a better qualitative evaluation of the Pd-Ag MR performance. The WGS reaction was conducted at GHSV = 1200 $L_N \cdot kg_{cat}^{-1} \cdot h^{-1}$, $P^F = 1.1$ bar and in the $200 - 300$ ºC temperature range.

a) Influence of the CO content in the feed

From the *Le Chatelier's principle*, an increase of the CO concentration in the gas feed (lower H_2O/CO ratios) favors the CO equilibrium conversion, as illustrated in Figure 5.10 (dotted line). However, and as reported previously, in a conventional packed-bed reactor operating at conditions far from equilibrium (kinetic regime) the CO content in the feed has a negative effect over the activity of the copper-based WGS catalyst (see chapter 3). Despite the importance of studying the performance of the WGS MR for various reactants molar ratios, it is also interesting to observe the influence of the CO feed content. The results are indicated in Figure 5.10, where the CO concentration was varied from 2.0 % to 10.0 %.

The experimental results obtained for the Pd-Ag MR show that H_2 recovery is favored by the reactants molar ratio, driving up the CO conversion, overcoming the equilibrium restrictions for all the tested conditions (Figure 5.10). Particularly, at 300 ºC and H_2O/CO ratio = 17.39 (2.0 % CO in the feed), a shift of 11 % beyond the equilibrium value of X_{CO}

was reached – cf. Figure 5.10. A marginal improvement on the conversion (< 1 %) was obtained at 200 ºC and H_2O/CO ratio = 3.48; also only 8.9 % H_2 recovery was obtained. At these conditions H_2 permeability is highly affected by temperature and simultaneously by the stronger co-adsorption of other species at the Pd surface, such as carbon monoxide. For each temperature, it is important to outline that the MR performance in terms of CO conversion follows the opposite trend as the indicated by the thermodynamic equilibrium. Consequently, the enhancement of the CO conversion (experimental vs. equilibrium one) increases with the reactants molar ratio (lower CO concentration in the feed gas stream). This can be explained not only because the catalyst becomes more active for lower CO contents (cf. chapter 3), but also because the effective membrane permeability towards hydrogen increases as the CO concentration decreases. Indeed, the strong covalent interaction of CO with the membrane surface affects H_2 permeation.

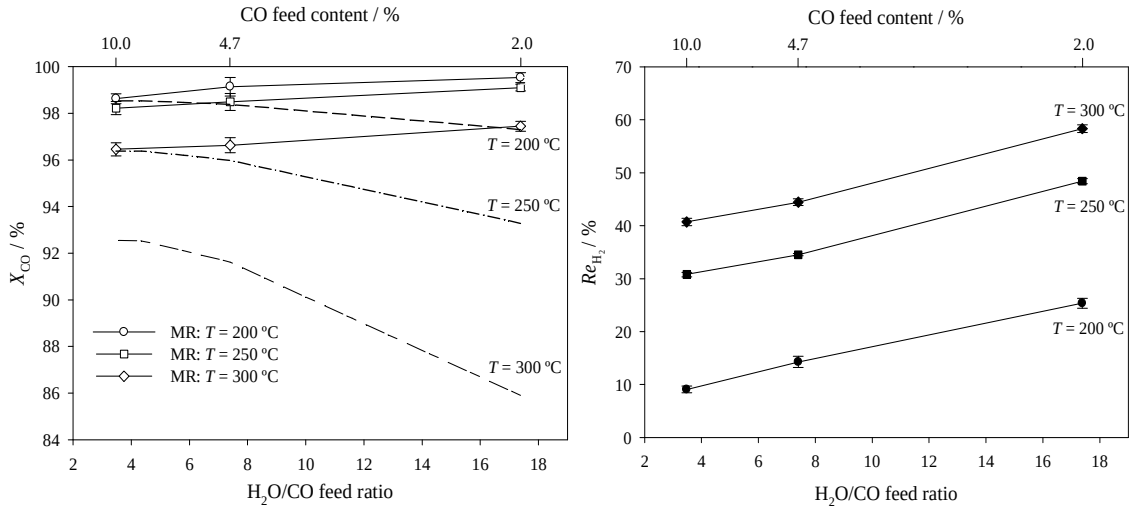

Figure 5.10 - CO conversion and H_2 recovery as a function of the CO feed content for the WGS reaction in the Pd-Ag MR (GHSV = 1200 $L_N \cdot kg_{cat}^{-1} \cdot h^{-1}$ and feed composition: 2.0 – 10.0 % CO, 34.78 % H_2O, 28.70 % H_2, 10.16 % CO_2 balanced in N_2). Dotted lines represent the CO equilibrium conversions for the specified inlet conditions.

It is therefore possible to conclude that the Pd-Ag MR conducts the WGS reaction on the kinetic regime. Therefore, it is also possible to infer that the non-equilibrium MR

conversions obtained depend not only on the operating conditions but also on the WGS reaction path, as generally referred by Barbieri et al. (Barbieri et al., 2008).

b) Influence of the H_2O content in the feed

In principle, a MR gives the same level of conversion at a lower ratio of steam-to-carbon monoxide as compared with that achieved in a conventional reactor operating at a higher ratio. It is obvious, therefore, that a membrane reactor serves to reduce the amount of steam needed to achieve reasonable levels of conversion. A set of experiments was then performed where the H_2O concentration was varied from 20.0 % to 40.0 %.

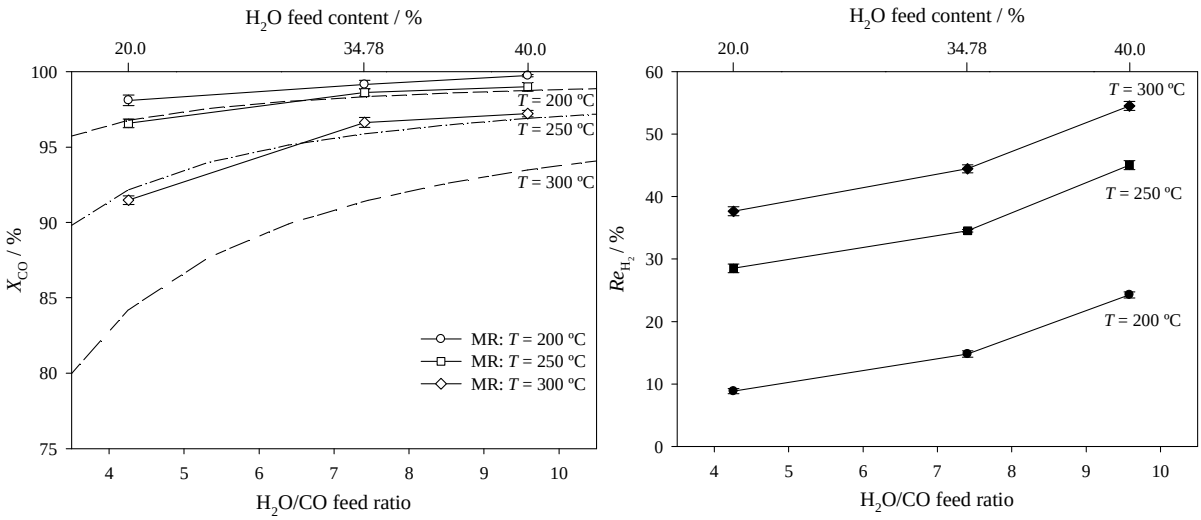

Figure 5.11 - CO conversion and H_2 recovery as a function of the H_2O feed content for the WGS reaction in the Pd-Ag MR (GHSV = 1200 $L_N \cdot kg_{cat}^{-1} \cdot h^{-1}$ and feed composition: 4.70 % CO, $20-40$ % H_2O, 28.70 % H_2, 10.16 % CO_2 balanced in N_2). Dotted lines represent the CO equilibrium conversions for the specified inlet conditions.

It is clear from Figure 5.11 that, in general, the water vapor content enhances the Pd-Ag MR performance in the temperature range of $200-300$ ºC. In the literature it is reported that the water content is crucial for the performance of a commercial CuO/ZnO catalyst (Ginés et al., 1995). Operating at conversions beyond the thermodynamic equilibrium, the MR system behaves in accordance with *Le Chatelier's* principle (see dotted lines in Figure 5.11). This

fact indicates that the variation of each reactant concentration (CO or H_2O) has different effects on the WGS MR performance. Once again, the experimental results show that H_2 recovery is favored by increasing the reactants molar ratio, driving up the CO conversion – cf. Figure 5.11. At 300 ºC, where the H_2 recovery is higher, CO conversion was promoted from 91.5 % to 97.2 % by increasing the H_2O/CO ratio from 4.26 to 9.58. Even operating the MR in vacuum mode and at lower temperatures, the results obtained follow the same trend as reported elsewhere (Basile et al., 1996; Uemiya et al., 1991b).

5.4 Conclusions

In this chapter, Pd-Ag membranes were successfully prepared by an innovative annealing and diffusion welding technique in order to separate and produce ultra-pure hydrogen. The combination of an active low-temperature $CuO/ZnO/Al_2O_3$ catalyst with a high H_2 permeable and selective Pd-Ag self-supported membrane resulted in a WGS membrane reactor that exhibited significant improvements in comparison to analogous systems reported in literature. The influence of various parameters, such as temperature, pressure, sweep-gas mode, reactants feed composition, and feed space velocity, was investigated in a detailed parametric study.

For this effective H_2 separation/production system, higher CO conversions can generally be achieved at lower temperatures where the equilibrium conversion is favored. On the other hand, H_2 recovery can be improved increasing the operating temperature and/or applying a higher H_2 partial pressure difference between the retentate and permeate sides of the dense Pd-Ag membrane. The performance of the WGS MR can also be improved operating the system at lower feed space velocities. Such conditions promote a higher residence time in the catalytic bed as well as permit that more H_2 permeates the Pd membrane interface.

The best operating mode to achieve higher MR performance is using a sweep stream for increasing the hydrogen permeation driving force (due to limitations in the vacuum pump

and membrane mechanical resistance). It is noteworthy that around 100 % of CO conversion and almost complete H_2 recovery can be achieved operating the MR at 300 ºC with a GSHV = 1200 $L_N \cdot kg_{cat}^{-1} \cdot h^{-1}$, $P^F = 4.0$ bar, $P^P = 3.0$ bar and using 1 $L_N \cdot min^{-1}$ of sweep gas. Since the Pd-Ag membrane prepared cannot withstand high-pressure differences between retentate and permeate sides (above 2 bar), for improving the hydrogen permeation it was increased the feed pressure as well as the sweep gas pressure. This operating mode resulted in improved reaction rate and hydrogen recovery.

Higher purge gas flow rates could increase the removal of hydrogen, promoting the CO conversion, due to the large driving force for hydrogen permeation. However, the CO conversion was essentially constant for sweep gas flow rates above 1000 $mL_N \cdot min^{-1}$, indicating that such flow rate was large enough for the removal of the hydrogen produced.

It was also found that changing the reactants concentration in the feed has opposite effects on the MR performance. While carbon monoxide conversion (and also hydrogen recovery) is improved by a higher water content, following the thermodynamic trend, the reverse effects are noticed for higher CO concentrations in the feed (following the opposite trend as the thermodynamic limit). It was concluded that the Pd-Ag MR operates in kinetic regime, where the non-equilibrium conversions obtained depend not only on the operating conditions but also on the WGS reaction path.

Finally, it is important to remark that the ultra-pure hydrogen stream produced (permeate stream) is suitable to directly feed a PEMFC. On-going studies concerning the thickness reduction of the membrane (< 1 μm) are being carried out in order to reduce the membrane costs, increasing the permeance while keeping the selectivity towards H_2.

5.5 Nomenclature and Acronyms

C_H hydrogen concentration in the lattice of the metallic membrane [$mol \cdot m^{-3}$]

D_H	diffusion coefficient of hydrogen atoms [$m^2 \cdot s^{-1}$]
E^p	activation energy for hydrogen permeation [$kJ \cdot mol^{-1}$]
FC	fuel cell
F_i	molar flow rate of species *i* [$mol \cdot h^{-1}$]
GHSV	gas hourly space velocity [$L_N \cdot kg_{cat}^{-1} \cdot h^{-1}$]
J_{H_2}	flux of hydrogen through the Pd-Ag membrane [$mol \cdot m^{-2} \cdot s^{-1}$]
L_{H_2}	hydrogen permeability [$mol \cdot m \cdot m^{-2} \cdot s^{-1} \cdot Pa^{-n}$]
$L^0_{H_2}$	pre-exponential factor for hydrogen permeation [$mol \cdot m \cdot m^{-2} \cdot s^{-1} \cdot Pa^{-n}$]
MR	membrane reactor
n	hydrogen partial pressure exponent constant
P	total pressure [bar or Pa]
p_i	partial pressure of component *i* [bar or Pa]
PBR	packed-bed reactor
PEM	polymer electrolyte membrane
Q	volumetric flow rate at normal conditions [$mL_N \cdot min^{-1}$]
$\Re$	ideal gas constant [= 8.314 $J \cdot mol^{-1} \cdot K^{-1}$]
Re_{H_2}	hydrogen recovery
S	sorption coefficient of hydrogen in the lattice [$mol \cdot m^{-3} \cdot Pa^{-n}$]
T	temperature [K or ºC]
WGS	water-gas shift
x	spatial position along the membrane thickness [m]
X_{CO}	carbon monoxide conversion
X^{eq}_{CO}	thermodynamic equilibrium conversion for the WGS reaction

Subscripts

i	species involved in the reaction experiments (CO, H_2O, CO_2, H_2 or N_2)

Superscripts

in	inlet of the reactor
out	outlet of the reactor
p	relative to the H_2 permeation
F	feed-side
P	permeate-side
R	retentate-side
sweep	sweep gas

Greek Letters

δ	Pd-Ag membrane thickness [m]

5.6 References

Adrover, M.E., Lopez, E., Borio, D.O., Pedernera, M.N., Simulation of a membrane reactor for the WGS reaction: Pressure and thermal effects. *Chem. Eng. J.* **2009**, 154 (1-3), 196-202.

Barbieri, G., Scura, F., Brunetti, A., *Mathematical modeling of Pd-alloy membrane reactors.* Elsevier: Amsterdam, The Netherlands, 2008; Vol. 9.

Basile, A., Chiappetta, G., Tosti, S., Violante, V., Experimental and simulation of both Pd and Pd/Ag for a water gas shift membrane reactor. *Sep. Purif. Technol.* **2001**, 25 (1-3), 549-571.

Basile, A., Criscuoli, A., Santella, F., Drioli, E., Membrane reactor for water gas shift reaction. *Gas Sep. Purif.* **1996**, 10 (4), 243-254.

Bi, Y.D., Xu, H.Y., Li, W.Z., Goldbach, A., Water-gas shift reaction in a Pd membrane reactor over Pt/Ce0.6Zr0.4O2 catalyst. *Int. J. Hydrogen Energy* **2009**, 34 (7), 2965-2971.

Brunetti, A., Barbieri, G., Drioli, E., Upgrading of a syngas mixture for pure hydrogen production in a Pd-Ag membrane reactor. *Chem. Eng. Sci.* **2009**, 64 (15), 3448-3454.

Criscuoli, A., Basile, A., Drioli, E., An analysis of the performance of membrane reactors for the water-gas shift reaction using gas feed mixtures. *Catal. Today* **2000**, 56 (1-3), 53-64.

Davis, W.D., 1954. Diffusion of gases through metals: I. Diffusion of gases through palladium. US Atomic Energy Commission Report No. KAPL-1227.

Dittmeyer, R., Hollein, V., Daub, K., Membrane reactors for hydrogenation and dehydrogenation processes based on supported palladium. *J. Mol. Catal. A: Chem.* **2001**, 173 (1-2), 135-184.

Ginés, M.L., Amadeo, N., Laborde, M., Apesteguía, C.R., Activity and structure-sensitivity of the Water-Gas shift reaction over Cu-Zn-Al mixed-oxide catalysts. *Appl. Catal., A* **1995**, 131 (2), 283-296.

Hwang, K.R., Ihm, S.K., Park, J.S., A catalytic membrane reactor for water-gas shift reaction. *Korean J. Chem. Eng.* **2010**, 27 (3), 816-821.

Iulianelli, A., Longo, T., Basile, A., Methanol steam reforming reaction in a Pd-Ag membrane reactor for CO-free hydrogen production. *Int. J. Hydrogen Energy* **2008**, 33 (20), 5583-5588.

Ma, D.H., Lund, C.R.F., Assessing high-temperature water-gas shift membrane reactors. *Ind. Eng. Chem. Res.* **2003**, 42 (4), 711-717.

Mejdell, A.L., Jondahl, M., Peters, T.A., Bredesen, R., Venvik, H.J., Effects of CO and CO2 on hydrogen permeation through a similar to 3 μm Pd/Ag 23 wt.% membrane employed in a microchannel membrane configuration. *Sep. Purif. Technol.* **2009**, 68 (2), 178-184.

Mendes, D., Garcia, H., Silva, V.B., Mendes, A., Madeira, L.M., Comparison of nanosized gold-based and copper-based catalysts for the low-temperature water-gas shift reaction. *Ind. Eng. Chem. Res.* **2009**, 48 (1), 430-439.

Paglieri, S.N., Way, J.D., Innovations in palladium membrane research. *Sep. Purif. Methods* **2002**, 31 (1), 1-169.

Pinacci, P., Broglia, M., Valli, C. In *Evaluation of the water gas shift in a palladium membrane reactor*, 9th International Conference on Catalysis in Membrane Reactors (ICCMR9), Lyon - France, 2009; Lyon - France, 2009; pp. 77-78.

Tosti, S., Basile, A., Bettinali, L., Borgognoni, F., Chiaravalloti, F., Gallucci, F., Long-term tests of Pd-Ag thin wall permeator tube. *J. Membr. Sci.* **2006**, 284 (1-2), 393-397.

Tosti, S., Bettinali, L., Violante, V., Rolled thin Pd and Pd-Ag membranes for hydrogen separation and production. *Int. J. Hydrogen Energy* **2000a**, 25 (4), 319-325.

Tosti, S., Violante, V., Basile, A., Chiappetta, G., Castelli, S., De Francesco, M., Scaglione, S., Sarto, F., Catalytic membrane reactors for tritium recovery from tritiated water in the ITER fuel cycle. *Fusion Eng. Des.* **2000b**, 49, 953-958.

Uemiya, S., Matsuda, T., Kikuchi, E., Hydrogen permeable palladium silver alloy membrane supported on porous ceramics. *J. Membr. Sci.* **1991a**, 56 (3), 315-325.

Uemiya, S., Sato, N., Ando, H., Kikuchi, E., The water gas shift reaction assisted by a palladium membrane reactor. *Ind. Eng. Chem. Res.* **1991b**, 30 (3), 585-589.

Chapter 6

Experimental and Modeling Studies on the Water-Gas Shift Reaction in a Dense Pd-Ag Packed-Bed Membrane Reactor

In this chapter, it was investigated the water-gas shift (WGS) reaction in a Pd-Ag membrane reactor (MR), using a simulated reformate feed. The experiments were performed under a broad range of operating conditions of temperature ($200-300\ ^{o}C$) and space velocity ($1200-10800\ L_N \cdot kg_{cat}^{-1} \cdot h^{-1}$); the effect of feed pressure ($1-2\ bar$) was also analyzed as well as the operating mode at the permeate side, vacuum (30 mbar) or sweep gas (nitrogen at $1\ L_N \cdot min^{-1}$). It is proposed a one-dimensional, isothermal and steady-state model that assumes axially dispersed plug-flow pattern in retentate side and no axial dispersion behavior for the permeate side. Moreover, it is considered pressure drop in the retentate chamber, but constant pressure for the permeate one. In general, the simulation results showed a good adherence to the experimental data, either in terms of carbon monoxide conversion and retentate outlet compositions, using only two fitting parameters related to the decline of H_2 permeability due to the presence of CO.

Both simulation and experimental runs showed that the MR achieves high performances, for some operating conditions clearly above the maximum limit for conventional packed bed reactors. The performance reached is particularly relevant when hydrogen is recovered via sweep gas mode (a high sweep flow rate was employed), because a lower partial pressure could be reached than using vacuum pumping. In the first case, almost complete CO conversion and H_2 recovery could be reached.

The contents of this chapter were adapted from: Mendes, D., Sá, S., Tosti, S., Sousa, J.M., Madeira, L. M., Mendes, A., Experimental and modeling studies on the water-gas shift reaction in a dense Pd-Ag packed-bed membrane reactor. Submitted for publication, 2010.

6.1 Introduction

Several authors have developed mathematical models with various level of complexity reporting the advantages of using Pd-alloy membrane reactors (MRs) for the WGS reaction. Most of them are steady-state and one-dimensional (Adrover et al., 2009; Basile et al., 2001; Brunetti et al., 2007; Criscuoli et al., 2000; Gosiewski et al., 2010), but two-dimensional including axial and radial gradients are also being reported (Markatos et al., 2005). Isothermal MR operation is generally assumed, but a few other works include also energy balances, allowing to simulate non-isothermal operation, adiabatic or non-adiabatic (Adrover et al., 2009; Brunetti et al., 2007). However, very few studies critically compare the proposed models with experimental results. Moreover, such comparisons are mostly based only in terms of conversion (or conversion enhancement) and takes into account data reported in the open literature respecting membrane properties and kinetic reaction rates, most of the times obtained for very specific conditions, sometimes different from those employed in the simulations.

One of the first works that combined experimental results with mathematical modeling was performed by Uemiya et al. (Uemiya et al., 1991). These authors have conducted the WGS reaction at 1 bar and 400 ºC using a commercial iron-chromium oxide catalyst on a 20 μm-thick Pd membrane supported on porous glass tube. An ideal stream ($CO + H_2O$) was fed into the MR and argon supplied to the permeation side, counter-currently, to sweep the permeated hydrogen. To validate the experimental results, the authors developed a model based on simple assumptions, namely isobaric and isothermal operation conditions and a plug-flow pattern for both retentate and permeate streams, but whose results agreed well with the experimental data. A similar mathematical model was also developed by Criscuoli et al. (Criscuoli et al., 2000) for a Pd-supported membrane reactor using a typical reformate gas mixture for the WGS reaction and kinetic data taken from literature. Also here the model fitted well the experimental results.

The main objective of the present study was to develop a comprehensive model and critically compare it with the experimental results obtained for a broad range of operation conditions. Experiments were carried out in a compact Pd-Ag membrane reactor, which arrangement was recently proposed by S. Tosti (Tosti et al., 2006, Mendes et al., 2010), packed with a $CuO/ZnO/Al_2O_3$ catalyst. This Pd alloy membrane has both high permeability and selectivity for hydrogen (Tosti et al., 2006), showing to be suitable to carry out the WGS reaction. The kinetic equation used in the model was dependent on the temperature operation range, according to the results obtained in chapter 4. The model was validated in terms of CO conversion and retentate composition, for the temperature, feed space velocity and feed pressure ranges considered. Additionally, the model was used to simulate the performance of the Pd-Ag WGS MR in terms of CO conversion and H_2 recovery in a wide range of the parametric space, described by the *Damköhler's number* (*Da*) and contact time (Γ). These two parameters describe generally the possible operation conditions to be used in the reactor, allowing thus to define the optimal operating regions in terms of CO conversion and H_2 recovery.

6.2 Experimental

6.2.1 Palladium-silver membrane tube

The Pd-Ag permeator tube has been produced by diffusion welding of an annealed commercial metal foil (25 wt.% of Ag, from Johnson-Matthey) according to a previously described technique (see chapter 5). In order to give the required mechanical stiffness and to guarantee the tightness with the membrane module, a stainless steel VCR® connection and a steel plug were brazed at the ends of the membrane tube, as shown in Figure 6.1.

The permeator tube was assembled inside the membrane module in a "finger-like" configuration that allows the elongation/contraction of the membrane, following thermal and hydrogen permeation cycles. In this way, mechanical stress is avoided and a long lifetime for

the membrane is expected (Tosti et al., 2006). The WGS catalyst was packed in the bore side and the permeated hydrogen was collected in the shell side. The configuration of the single-tube MR used is schematically illustrated in Figure 6.2.

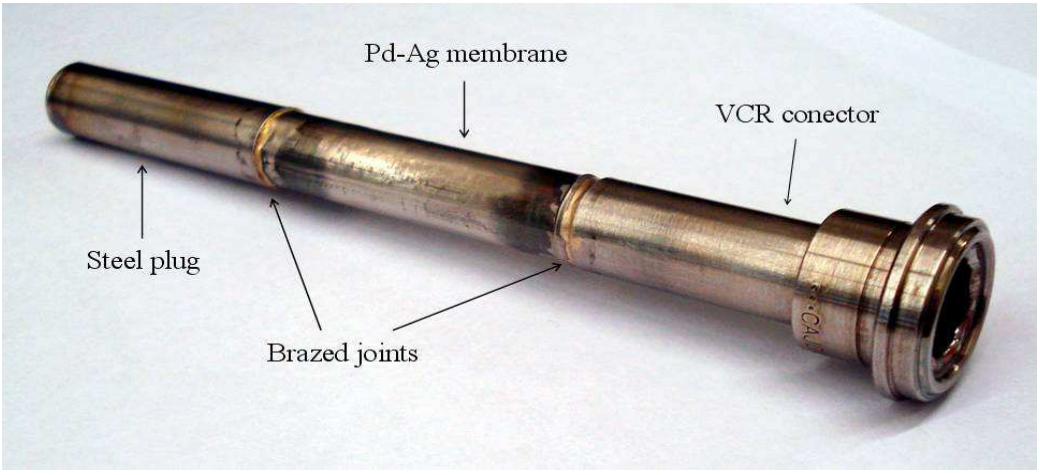

Figure 6.1 – View of the Pd-Ag membrane tube (geometrical characteristics of the membrane section: 10 mm I.D., 50 μm thick and 50 mm of length).

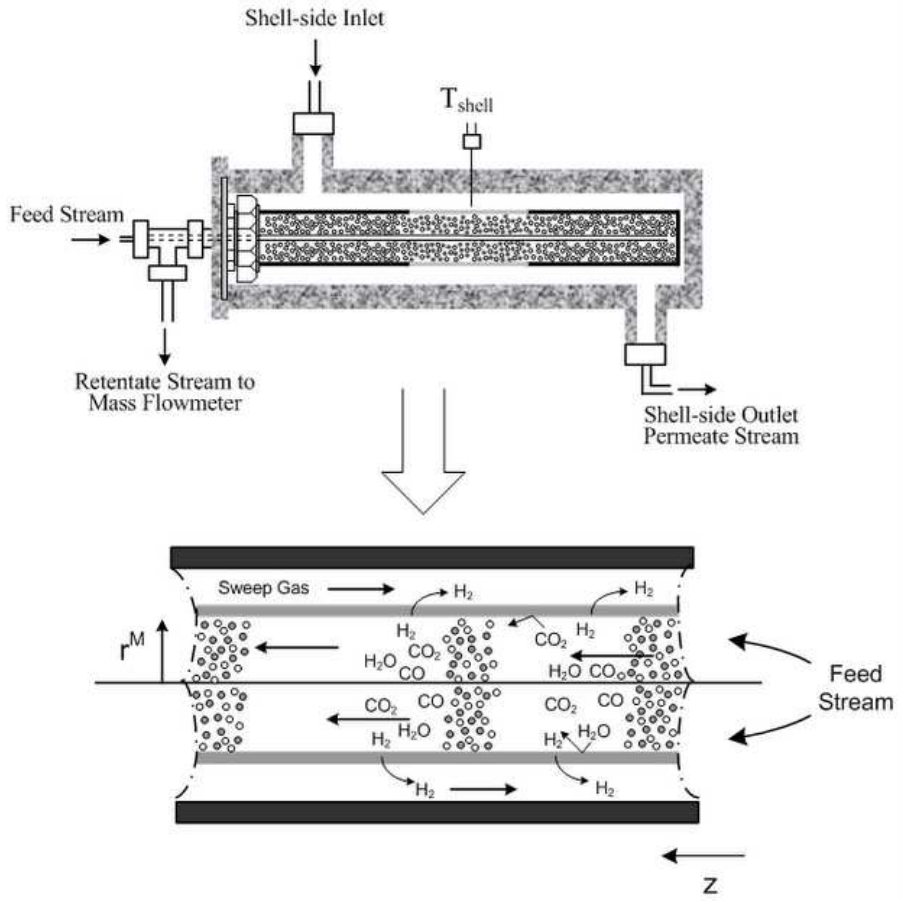

Figure 6.2 – Scheme of the Pd-Ag MR (sweep gas flowing counter-currently).

6.2.2 Experimental setup

The experimental apparatus used for carrying out the WGS reaction, as well as the evaluation of the membrane separation properties, is divided into three sections, namely: (i) the feed section, consisting of gas cylinders and pressure regulators, mass flow controllers (Bronkhorst Hi-Tec, model F201) and a Controller Evaporator Mixer (CEM, Bronkhorst) unit to provide the desired water vapor flow rate; (ii) the reactor section, consisting of the membrane reactor and an oven (Memmert, type UNE200) for heating it, two pressure gauges (Druck, ref. 4010, 7 and 5 bar respectively), two back-pressure regulators (Swagelok) for controlling the pressure, a condenser and a diaphragm vacuum pump (Thomas Instruments, ref.: 7011-0069) and (iii) the analysis section, which consists of two flow-meters (Bronkhorst Hi-Tec, model F201) to measure separately the retentate and permeate streams and a gas chromatograph (Dani 1000 GC) to analyze the retentate dry gas composition. Further details concerning the analysis method can be found in chapter 3 and appendix A.

6.2.2.1 Hydrogen permeation and WGS reaction tests

As mentioned in chapter 5, pure hydrogen permeation tests were performed at temperatures ranging from 200 ºC to 300 ºC, in the range of pressures from 1.1 bar to 2.5 bar, and flow rates ranging from $50-190\ mL_N \cdot min^{-1}$. The H_2 feed gas flowed along the inner side of the membrane and the permeating stream flow rate was measured on the shell side at atmospheric pressure with a mass flow meter after steady state (approximately 1 h) had been achieved, at the desired temperature. Neither sweep gas nor vacuum was used. Pressures in the two sides of the membrane tube were monitored via pressure transducers.

As sketched in Figure 6.2, the MR considered in this work is a tube-and-shell configuration system. The WGS reaction was performed in the temperature range $200-300\ ºC$ by packing a certain amount of a commercial $CuO/ZnO/Al_2O_3$ catalyst, supplied by REB Research & Consulting, into the lumen side of the MR. Prior to the reaction

runs, the WGS catalyst was activated *in situ* with a mixed gas flow of H_2/N_2. Details about the catalyst pre-treatment (reduction) can be found in chapter 5.

The reaction tests, previously described in chapter 5, were carried out using the following feed gas composition: 4.70 % CO, 34.78 % H_2O, 28.70 % H_2, and 10.16 % CO_2 balanced in N_2, which simulates a reformate feed. The reaction pressure (that is, the pressure in the lumen side of the membrane) and the feed flow rate were varied in the range $1-2$ bar and $30-270\ mL_N \cdot min^{-1}$, respectively. As the driving force for H_2 permeation through the membrane is the difference between the partial pressures on both sides of the Pd-Ag membrane, the permeation flux increases by reducing the hydrogen permeate pressure. This can be achieved by decreasing the total permeate pressure (pure hydrogen) or using sweep gas. Two operating modes were then studied: (i) hydrogen was recovered in the shell side by vacuum pumping (shell side pressure ~ 30 mbar), and (ii) an inert gas (N_2, $1\ L_N \cdot min^{-1}$) was fed into the shell side flowing counter-currently (cf. Figure 6.2). Additionally, to simulate the performance of a packed-bed reactor (PBR from now on) for posterior comparison with the MR operation, the permeate chamber was closed and data taken after steady-state was achieved.

Different parameters affecting the catalytic reaction and the membrane operation have been studied, namely the feed flow rate, the reaction temperature, feed pressure and operation mode (permeate side under vacuum or with sweep gas flowing counter-currently). Such effects have been evaluated in terms of the carbon monoxide conversion (X_{CO}) and hydrogen recovery (Re_{H_2}) at steady-state conditions. Both parameters were calculated according to equations 6.1 and 6.2, respectively:

$$X_{CO} = 1 - \frac{u^{R,out} p_{CO}^{R,out}}{u^{R,in} p_{CO}^{R,in}} \tag{6.1}$$

$$Re_{H_2} = \frac{u^{P,out} p_{H_2}^{P,out}}{u^{R,out} p_{H_2}^{R,out} + u^{P,out} p_{H_2}^{P,out}} \tag{6.2}$$

where u is the interstitial velocity and p is the partial pressure. The superscripts R and P stand for retentate and permeate chambers, respectively. *in* and *out* means inlet and exit of the reactor, respectively.

6.2.2.2 WGS reaction kinetics

Experimental runs to collect intrinsic kinetic data with a commercial $CuO/ZnO/Al_2O_3$ catalyst, supplied by REB Research & Consulting, were carried out in a packed-bed reactor for the temperature range $180-300\ ^oC$. According to the results obtained in chapter 4, two different kinetics models were proposed. For temperatures between 180 ºC and 200 ºC, the associative mechanism showed the best fitting while the redox pathway showed the best agreement in the range of $215-300\ ^oC$. These two kinetic models, described by equations 6.3 and 6.4 below, were used in the present work to describe the catalytic activity of the catalyst for the WGS reaction carried out in the Pd-Ag membrane reactor.

For temperatures in the range $180-200\ ^oC$ (lower temperatures – LT):

$$R^{LT} = \frac{k^{LT}\left(p_{CO}p_{H_2O} - \frac{p_{CO_2}p_{H_2}}{K_e}\right)}{\left(1+\sum_i K_i^{a,LT}p_i\right)^2} \tag{6.3}$$

For temperatures in the range $215-300\ ^oC$ (higher temperatures – HT):

$$R^{HT} = \frac{k^{HT}\left(p_{CO}p_{H_2O} - \frac{p_{CO_2}p_{H_2}}{K_e}\right)}{p_{CO}\left(1+K_{CO_2}^{a,HT}\frac{p_{CO_2}}{p_{CO}}\right)} \tag{6.4}$$

where i refers to the i^{th} component, R stands for the local reaction rate, k is the forward rate constant, K_e is the thermodynamic equilibrium constant and K^a is the equilibrium adsorption constant of each species. In the membrane reactor, the pressure of each species is the one at the retentate side.

The temperature dependence of the reaction rate and of the adsorption equilibrium constants are described by the *Arrhenius* and *van't Hoff* laws, equations 6.5 and 6.6, respectively:

$$k = k^0 \, exp\left(-\frac{E^k}{\Re T}\right) \tag{6.5}$$

$$K_i^a = K_i^{a,0} \, exp\left(-\frac{\Delta H_i^a}{\Re T}\right) \tag{6.6}$$

where k^0 is the pre-exponential factor of the reaction rate constant, E^k is the activation energy for the WGS reaction, $\Re$ is the gas constant, T is the absolute temperature, $K^{a,0}$ refers to the pre-exponential equilibrium adsorption constant, and H^a stands for the enthalpy of adsorption. The temperature dependence of the thermodynamic equilibrium constant is described by equation 2.1.

Depending on the temperature regime, the variables of equations 6.5 and 6.6 have different values. The mean values of the estimated parameters, for the best fittings, are presented in Table 6.1. It is also given the fitting error associate to each parameter, assuming t-student distribution and for 95 % confidence level, and computed using the 10 best fittings.

Analyzing the parameters for the LT regime, it can be inferred that, under the operating condition used in this work, the adsorption of CO and H_2O at the catalyst surface is much lower than the adsorption of CO_2 and H_2. In this way, the kinetic equation considered in the simulation calculations performed along this study was simplified to:

$$R^{LT} = \frac{k^{LT}\left(p_{CO}\,p_{H_2O} - \frac{p_{CO_2}\,p_{H_2}}{K_e}\right)}{\left(1 + K_{CO_2}^{a,LT}\,p_{CO_2} + K_{H_2}^{a,LT}\,p_{H_2}\right)^2} \tag{6.3a}$$

Table 6.1 – Calculated parameters for mechanistic-derived rate equations. Fitting errors of parameters are for 95 % confidence level (chapter 4).

Parameter	$T = 180 - 200$ °C (LT)	$T = 215 - 300$ °C (HT)
k^0 $(\text{mol}\cdot\text{g}_{\text{cat}}^{-1}\cdot\text{h}^{-1}\cdot\text{Pa}^{-2})$	1.188 ± 0.000	$1.841\times10^{-3} \pm 0.210\times10^{-3}$
E^k $(\text{kJ}\cdot\text{mol}^{-1})$	36.658 ± 0.000	6.710 ± 0.399
$K_{\text{CO}}^{a,0}$ (Pa^{-1})	$2.283\times10^{-24} \pm 0.000\times10^{-24}$	
$K_{\text{H}_2\text{O}}^{a,0}$ (Pa^{-1})	$1.957\times10^{-28} \pm 0.000\times10^{-28}$	
$K_{\text{CO}_2}^{a,0}$ (Pa^{-1})	$5.419\times10^{-4} \pm 0.002\times10^{-4}$	$6.343\times10^{-1} \pm 0.727\times10^{-1}$*
$K_{\text{H}_2}^{a,0}$ (Pa^{-1})	$2.349\times10^{-4} \pm 0.000\times10^{-4}$	
ΔH_{CO}^{a} $(\text{kJ}\cdot\text{mol}^{-1})$	-45.996 ± 0.158	
$\Delta H_{\text{H}_2\text{O}}^{a}$ $(\text{kJ}\cdot\text{mol}^{-1})$	-79.963 ± 0.172	
$\Delta H_{\text{CO}_2}^{a}$ $(\text{kJ}\cdot\text{mol}^{-1})$	-16.474 ± 0.009	-19.459 ± 0.402
$\Delta H_{\text{H}_2}^{a}$ $(\text{kJ}\cdot\text{mol}^{-1})$	-13.279 ± 0.192	

* This value is dimensionless.

6.3 Membrane reactor model

6.3.1 Development of the model

The catalytic membrane reactor considered in this study has the general features described above. The pseudo-homogeneous 1-D model proposed for describing this reactor is based on the following main assumptions:

- Steady-state and isothermal operation;
- Axially dispersed plug-flow pattern in the retentate side with pressure drop described by Ergun equation;
- Negligible mass and heat-transfer resistances;
- Ideal plug-flow pattern in the permeate side with no pressure drop;
- Ideal gas behavior.

It has been found that axial and radial dispersion inside the reactor can have a large effect on the predicted conversion (Koukou et al., 1996). However, radial concentration gradients

should be negligible when the permeation flux is comparatively lower than the convective flux (Tiemersma et al., 2006). So, only axial dispersion was considered.

The assumption of isothermal operation in a reactor depends on the extent of the reaction heat compared to the heat loss/gain through the reactor walls. This hypothesis is acceptable in low-scale (laboratory) reactors due to the high ratio between heat transfer area and the reaction volume or when the consumption or release of heat is low, but this condition may not be true when higher process scales are used (Adrover et al., 2009).

Permeation of hydrogen through a dense palladium membrane occurs via a solution-diffusion mechanism (Dittmeyer et al., 2001). The *Richardson's equation* (based on *Sieverts' law*) is typically used to describe the overall permeation rate of hydrogen through the membrane (Basile, 2008).

Due to the high ratio membrane radius/membrane thickness, the Pd-Ag membrane is approached to a flat shape, despite its cylindrical geometry.

The governing equations for the retentate (reaction) and permeation sides are:

Retentate side:

Partial mass balance

$$\frac{\mathrm{d}}{\mathrm{d}z}\left(u^R p_i^R\right)-\frac{\mathrm{d}}{\mathrm{d}z}\left(D_{ax}P^R\frac{\mathrm{d}}{\mathrm{d}z}\left(\frac{p_i^R}{P^R}\right)\right)+\frac{2\pi r^m}{\varepsilon_b A^R}\Re T J_i-\frac{W_{cat}}{\varepsilon_b V^R}\Re T\nu_i R=0 \qquad (6.7)$$

Total mass balance

$$\frac{\mathrm{d}}{\mathrm{d}z}\left(u^R P^R\right)+\frac{2\pi r^m}{\varepsilon_b A^R}\Re T\sum_i J_i-\frac{W_{cat}}{\varepsilon_b V^R}\Re T\sum_i \nu_i R=0 \qquad (6.8)$$

Pressure drop

$$\frac{\mathrm{d}P^R}{\mathrm{d}z}+150\frac{\mu_g\left(1-\varepsilon_b\right)^2}{\left(\varepsilon_b\right)^3\left(d_p\right)^2}u^R+1.75\frac{\rho_g\left(1-\varepsilon_b\right)}{d_p\left(\varepsilon_b\right)^3}u^R\left|u^R\right|=0 \qquad (6.9)$$

Boundary conditions

Danckwerts boundary conditions for retentate side (Froment and Bischoff, 1990):

$$z=0:\quad \frac{\mathrm{d}}{\mathrm{d}z}\left(\frac{p_i^R}{P^R}\right)=-\frac{u^R}{\varepsilon_b D_{ax}}\frac{\left(p_i^{R,in}-p_i^R\right)}{P^R},\quad u^R\equiv u^{R,in}=\frac{u^F}{\varepsilon_b}\ \text{ and }\ P^R=P^{R,in}=P^F \qquad (6.10)$$

$$z = \ell: \quad \frac{\mathrm{d}}{\mathrm{d}z}\left(\frac{p_i^R}{P^R}\right) = 0 \tag{6.11}$$

where z is the axial coordinate, ℓ is the reactor length, u is the interstitial velocity, P is the total pressure, D_{ax} is the effective axial dispersion coefficient , r^m is the internal radius of the membrane, A^R is the cross-sectional area of the retentate chamber, V^R is the volume of the retentate chamber, ε_b is the void fraction of the catalyst bed, J is the flux through the membrane, W_{cat} is the mass of catalyst bed and d_p is the catalyst particle diameter. ν_i is the stoichiometric coefficient of species *i*, taken negative for the reactants, positive for the reaction products, and null for components that do not take part in the reaction. The viscosity of the gas mixture, μ_g, was obtained by the *Wilke method* (Poling et al., 2004). The respective density, ρ_g, was calculated by the virial equation, with the coefficients taken from Smith et al. (Smith et al., 1996). The variation of the effective axial dispersion coefficient, D_{ax}, for the range of conditions tested was negligible (Perry and Green, 1999); so, the average value of 5.40×10^{-5} $m^2 \cdot s^{-1}$ was used.

Permeate side:

Partial mass balance

$$\frac{\mathrm{d}}{\mathrm{d}z}\left(u^P p_i^P\right) + f\,\frac{2\pi r^m}{A^P}\Re T J_i = 0 \tag{6.12}$$

Total mass balance

$$P^P \frac{\mathrm{d}u^P}{\mathrm{d}z} + f\,\frac{2\pi r^m}{A^P}\Re T \sum_i J_i = 0 \tag{6.13}$$

Boundary conditions

Vacuum mode:

$$z = 0: \quad u^P = 0 \ \text{ and } \ p_i^P = P^P \tag{6.14}$$

Sweep gas mode (*counter-current operation*)*:*

$$z = \ell: \quad p_i^P = p_i^{P,in} \ \text{ and } \ u^P = u^{P,in} \tag{6.15}$$

where A^P is the cross-sectional area of the permeate chamber and f is defined as -1 or +1 according to the flow (either in co- or counter-current, respectively).

Membrane permeation equation

The transport properties of the Pd-Ag membrane used in this investigation were previously studied based on single permeation measurements (for details, see chapter 5). The Pd-Ag membrane showed *ideal* selectivity towards H_2, therefore $N_i = 0$ except for $i \equiv H_2$, equations 6.7-6.8 and 6.12-6.13.

The H_2 permeating flux through the Pd-Ag membrane is expressed in terms of the *Richardson's equation* (equation 6.16) and corrected for the temperature using the *Arrhenius equation* (equation 6.17):

$$J_{H_2}(z) = \frac{L_{H_2}}{\delta}\left(\sqrt{p^R_{H_2}(z)} - \sqrt{p^P_{H_2}(z)}\right) \tag{6.16}$$

$$L_{H_2} = L^0_{H_2}\, exp\left(-\frac{E^p}{\Re T}\right) \tag{6.17}$$

where L_{H_2} is the membrane permeability towards hydrogen, δ is the membrane thickness, E^p is the permeation activation energy and $L^0_{H_2}$ is the pre-exponential factor.

Gaseous species such as H_2O, CO, CO_2 and N_2 inevitably co-exist in the WGS reaction process, affecting the hydrogen permeance of the Pd-based membranes, though without affecting the H_2 selectivity (Barbieri et al., 2008; Unemoto et al., 2007). In the present MR model, the hindrance effect due to the presence of CO was taken into account using an extended equation, previously proposed by Barbieri et al. (Barbieri et al., 2008). By including a correction factor, the authors arrived to a modified equation, named *Sieverts'-Langmuir formulation*:

$$J_{H_2}(z) = \left[\left(1 - \psi\frac{K^p_{CO}\, p_{CO}}{1 + K^p_{CO}\, p_{CO}}\right) L_{H_2}\right]\left(\sqrt{p^R_{H_2}(z)} - \sqrt{p^P_{H_2}(z)}\right) \tag{6.18}$$

ψ and K_{CO}^{p} are adjustable parameters and were obtained by fitting the H_2 recovery from the theoretical model to the respective experimental results, as described below (section 6.4.1). In this equation, the term $K_{CO}^{p} p_{CO} / \left(1 + K_{CO}^{p} p_{CO}\right)$ defines the fraction of the membrane surface covered by adsorbed CO. The proportionality coefficient, ψ, accounts for the dimensionless reduction of the permeable area hindered by CO molecules. This parameter depends only on the temperature, while K_{CO}^{p} depends on the temperature and CO pressure. The previous equation accounts not only for the CO hindering effect, but also affects the hydrogen adsorption and dissociation (Barbieri et al., 2008; Mejdell et al., 2009).

6.3.2 Dimensionless equations

The model variables were made dimensionless with respect to the feed conditions, u^F, to hydrogen species, L_{H_2}, to the reactor length, ℓ, to a reference pressure, 100 kPa, and to a reference temperature, 273 K. Changing for dimensionless variables and introducing suitable dimensionless parameters, equations 6.3a-6.15 and 6.18 become as follows:

$$R^{LT^*} = \frac{exp\left(\gamma^{k,LT}\left(1-\frac{1}{T^*}\right)\right)\left(p_{CO}^{*} p_{H_2O}^{*} - \frac{p_{CO_2}^{*} p_{H_2}^{*}}{K_e}\right)}{\left(1 + K_{CO_2}^{a,0,LT}\, exp\left(-\frac{\Delta H_{CO_2}^{a,LT}}{\Re T}\right) P_{ref}\, p_{CO_2}^{*} + K_{H_2}^{a,0,LT}\, exp\left(-\frac{\Delta H_{H_2}^{a,LT}}{\Re T}\right) P_{ref}\, p_{H_2}^{*}\right)^2} \quad (6.19)$$

$$R^{HT^*} = \frac{exp\left(\gamma^{k,HT}\left(1-\frac{1}{T^*}\right)\right)\left(p_{CO}^{*} p_{H_2O}^{*} - \frac{p_{CO_2}^{*} p_{H_2}^{*}}{K_e}\right)}{p_{CO}^{*}\left(1 + K_{CO_2}^{a,0,LT}\, exp\left(-\frac{\Delta H_{CO_2}^{a,LT}}{\Re T}\right)\frac{p_{CO_2}^{*}}{p_{CO}^{*}}\right)} \quad (6.20)$$

$$\frac{d}{dx}\left(u^{R^*} p_i^{R^*}\right) - \frac{1}{Pe}\frac{d}{dx}\left(P^{R^*}\frac{d}{dx}\left(\frac{p_i^{R^*}}{P^{R^*}}\right)\right) + \Gamma T^* J_i^* - DaT^* \nu_i R^* = 0 \quad (6.21)$$

$$\frac{d}{dx}\left(u^{R^*} P^{R^*}\right) + \Gamma T^* \sum_i J_i^* - DaT^* \sum_i \nu_i R^* = 0 \quad (6.22)$$

$$\frac{\mathrm{d}P^{R*}}{\mathrm{d}x}+\alpha\mu_g^* u^{R*}+\beta\rho_g^* u^{R*}\left|u^{R*}\right|=0 \tag{6.23}$$

$$x=0:\quad \frac{1}{Pe}\frac{\mathrm{d}}{\mathrm{d}x}\left(\frac{p_i^{R*}}{P^{R*}}\right)=u^{R,in*}\frac{\left(p_i^{R*}-p_i^{R,in*}\right)}{P^{R*}},\quad u^{R*}=u^{R,in*}\ \text{ and }\ P^{R*}=P^{R,in*} \tag{6.24}$$

$$x=1:\quad \frac{\mathrm{d}}{\mathrm{d}x}\left(\frac{p_i^{R*}}{P^{R*}}\right)=0 \tag{6.25}$$

$$\frac{d}{dx}\left(u^{P*}p_i^{P*}\right)+f\Gamma\sigma T^* J_i^*=0 \tag{6.26}$$

$$\frac{d}{dx}\left(u^{P*}P^{P*}\right)+f\sigma T^*\sum_i J_i^*=0 \tag{6.27}$$

Vacuum mode:

$$x=0:\quad p_i^{P*}=P^{P*}\ \text{ and }\ u^{P*}=0 \tag{6.28}$$

Counter-current mode:

$$x=1:\quad p_i^{P*}=p_i^{P,in*}\ \text{ and }\ u^{P*}=u^{P,in*} \tag{6.29}$$

$$J_{\mathrm{H_2}}^*(x)=\left[\left(1-\psi\frac{K_{\mathrm{CO}}^p P_{\mathrm{ref}}\,p_{\mathrm{CO}}^{R*}}{1+K_{\mathrm{CO}}^p P_{\mathrm{ref}}\,p_{\mathrm{CO}}^{R*}}\right)exp\left(\gamma^p\left(1-\frac{1}{T^*}\right)\right)\right]\left(\sqrt{p_{\mathrm{H_2}}^{R*}(x)}-\sqrt{p_{\mathrm{H_2}}^{P*}(x)}\right) \tag{6.30}$$

where $\gamma^{k,LT}=E^{k,LT}/\Re T_{\mathrm{ref}}$, $\gamma^{k,HT}=E^{k,HT}/\Re T_{\mathrm{ref}}$, $\gamma^p=E^p/\Re T_{\mathrm{ref}}$, $p_i^*=p_i/P_{\mathrm{ref}}$, $P^*=P/P_{\mathrm{ref}}$, $u^*=u/u_{\mathrm{ref}}$, $L_{\mathrm{H_2}}^*=1$, $x=z/\ell$, $\alpha=150\left(1-\varepsilon_b\right)^2\mu_{\mathrm{ref}}u_{\mathrm{ref}}\ell/\left(\varepsilon_b\right)^3\left(d_p\right)^2P_{\mathrm{ref}}$, $\beta=1.75\left(1-\varepsilon_b\right)M_{\mathrm{ref}}\left(u_{\mathrm{ref}}\right)^2\ell/d_p\left(\varepsilon_b\right)^3\Re T_{\mathrm{ref}}$, $\sigma=\varepsilon_b A^R/A^P$, $Pe=\ell u_{\mathrm{ref}}/D_{ax}$ and $\Gamma=A^m\Re T_{\mathrm{ref}}\sqrt{P_{\mathrm{ref}}}L_{\mathrm{ref}}(T_{\mathrm{ref}})/\varepsilon_b u_{\mathrm{ref}}A^R$. The superscript * stands for dimensionless variables, and the subscript *ref* stands for reference component or conditions. Pe is the *Péclet number* for mass transfer, Γ is the contact time (ratio between the characteristic feed flow time and the characteristic permeance time of the reference component). The *Damköhler number* (ratio between the reaction rate at the reference temperature and the feed flow rate to the reactor) was defined independently for each of the kinetic models, depending on the

temperature range. For the lower temperature range, $Da = W_{cat}\Re T_{\text{ref}} k^{LT}(T_{\text{ref}})(P_{\text{ref}})^2 / \varepsilon_b u_{\text{ref}} A^R$, while $Da = W_{cat}\Re T_{\text{ref}} k^{HT}(T_{\text{ref}}) P_{\text{ref}} / \varepsilon_b u_{\text{ref}} A^R$ for the higher temperature range. The remaining symbols are reported in the nomenclature.

6.3.3 Numerical solution strategy

To simulate the WGS membrane reactor, it is necessary to solve equations 6.21-6.23, and 6.26-6.27 with the respective boundary conditions. These equations were transformed into pseudo-transient ones, by adding a time derivative term to their right-hand side, avoiding so numerical instability problems (Sá et al., 2009). The partial differential equations were spatially discretized using the finite volumes method (Sá et al., 2009) and the resulting ODE's were integrated in time by LSODA, a package written by Alan Hindmarsh and Linda Petzold (Hindmarsh, 2006), until an error criterion was achieved (time derivative of each dependent variable and for each of the spatial coordinate smaller than 1×10^{-12}). All physical properties of the gas mixture (μ_g and ρ_g) were evaluated at local conditions.

6.4 Results and Discussion

6.4.1 Dimensional analysis: model validation

In this section, the effect of temperature, feed space velocity and reaction pressure on the performance of the MR operating in vacuum and sweep gas modes was studied. Moreover, for all the operating conditions considered, the catalyst activity (evaluated based on CO conversion) and the membrane separation ability (evaluated in terms of H_2 recovery) were quantified and the results compared with the ones from the proposed model. The experimental conditions and the simulation variables are summarized in Table 6.2.

As described in section 6.3.1, ψ and K_{CO}^{p} are adjustable parameters, obtained by fitting the H_2 recovery from the theoretical model to the respective experimental results. The

adjusted values of ψ and K_{CO}^{p} were in the ranges 0.6-1.0 and (0.5-1.5)×10^{-4} Pa^{-1}, respectively, considering the values for all temperatures and flow rates. Similar results were reported by Mejdell et al. (Mejdell et al., 2009). As can be realized from Figure 6.3-A the adherence of the simulated hydrogen recovery to the experimental results is very good. The comparison between the experimental and the calculated results for the CO conversion is illustrated in Figure 6.3-B. Again, the model shows a good agreement with the experimental data, with a few exceptions at the lowest carbon monoxide conversions, obtained for temperatures of 200 ºC.

Table 6.2 – Experimental conditions for the Pd-Ag MR runs.

Variable	Value/Range	Variable	Value/Range
T	200-300 ºC	r^{m}	0.50 cm
P^{F}	1-2 bar	r^{shell}	1.75 cm
P^{P}	0.030-1 bar	E^{p}	10.72 kJ·mol^{-1}
W_{cat}	1.5 g	$L_{H_2}^{0}$	5.445×10^{-8} mol·m·m^{-2}·s^{-1}·$Pa^{-0.5}$
GHSV	1200-10 800 L_N·kg_{cat}^{-1}·h^{-1}	δ	50 μm
Q_{sweep}	1 L_N·min^{-1}	d_p	300 μm
ℓ	5 cm	ε_b	0.40

Figures 6.4 and 6.5 show the influence of reaction temperature and feed space velocity (feed flow rate) on the MR performance, both theoretical and experimental. The thermodynamic equilibrium conversion of CO, X_e, based on the inlet reformate gas composition, is also included to show the conversion enhancement that is possible to attain with the membrane reactor comparatively to the maximum value possible to be obtained in a packed bed reactor. Each figure refers to a different operation mode of collecting the permeated hydrogen: sweep gas mode in Figure 6.4 ($Q_{sweep(N_2)}$ = 1.0 $L_N \cdot min^{-1}$, P^{P} = 1.0 bar, P^{F} = 2.0 bar) and vacuum mode in Figure 6.5 (P^{P} ~ 30 mbar, P^{F} = 1.1 bar).

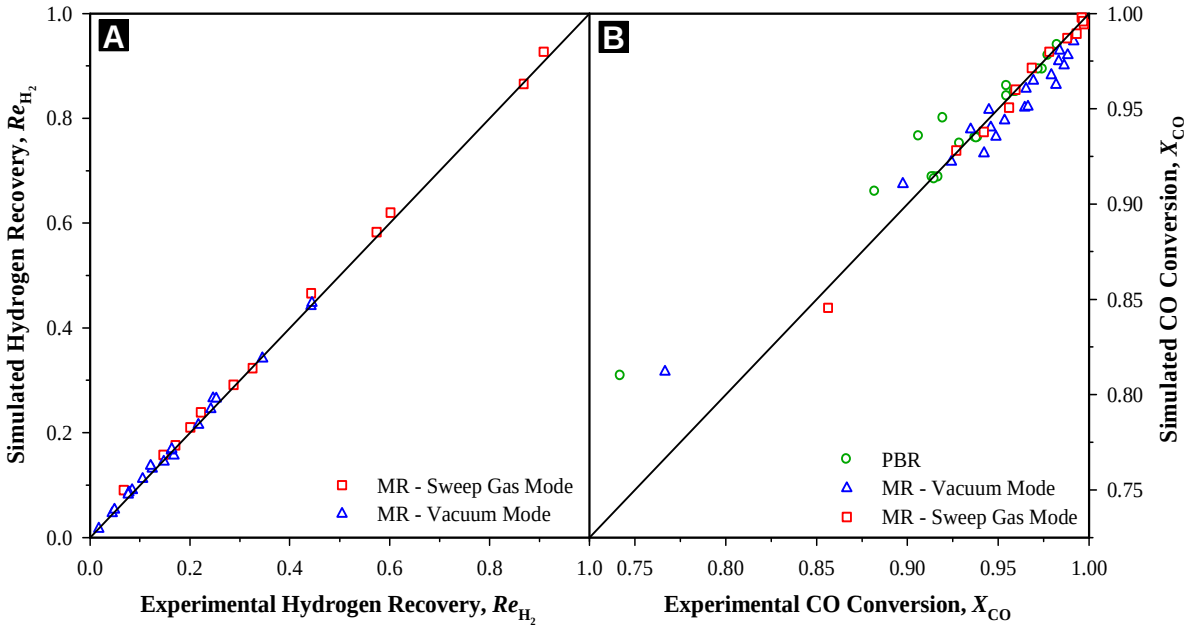

Figure 6.3 – Parity plots of calculated and experimental results for H_2 recovery (A) and CO conversion (B).

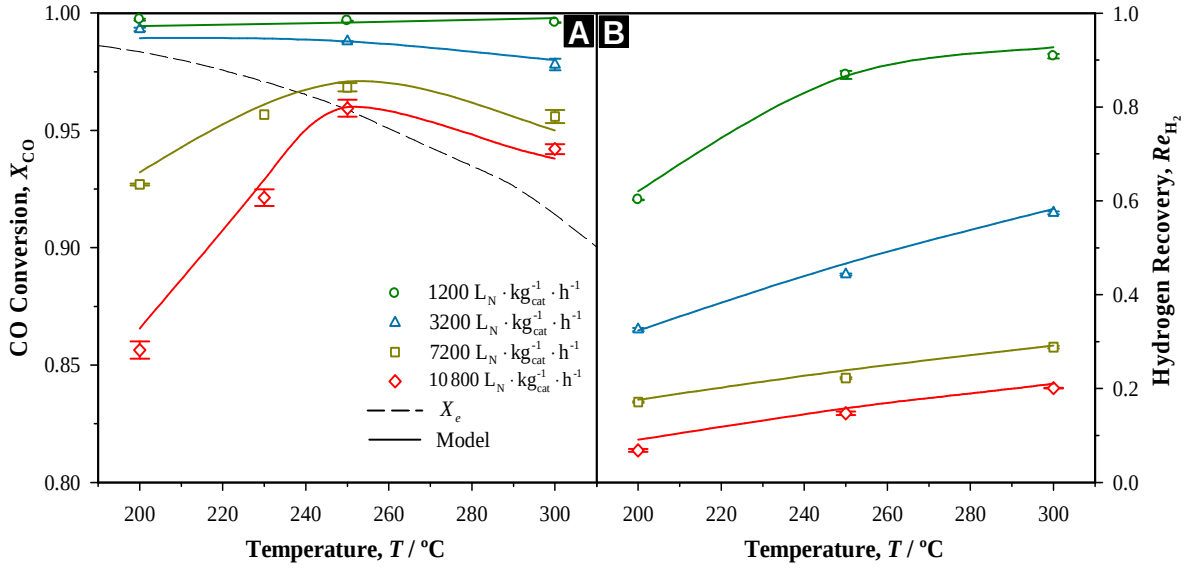

Figure 6.4 – The effect of feed gas space velocity on the CO conversion (A) and H_2 recovery (B) as a function of the reaction temperature in the MR, operating in counter-current mode. $Q_{sweep} = 1.0\ L_N \cdot min^{-1}$, $P^F = 2.0$ bar, and $P^P = 1.0$ bar.

Figure 6.4 shows that the model describes quite well the trend of the CO conversion and H_2 recovery as a function of the temperature, for each feed flow rate. For any of the

operating temperatures, both CO conversion and H_2 recovery increase with the residence time, that is, they decrease with the gas hourly space velocity – GHSV.

Figure 6.4-A also shows that the CO conversion attained in the MR may surpass the thermodynamic equilibrium conversion. This conversion enhancement is achieved for the lower temperatures at the lower feed flow rates. With the temperature increase, such conversion enhancement is attained for higher and higher feed flow rates. For low temperatures, the reaction rate is relatively slow, so only a limited amount of CO is converted. Besides, the permeation of H_2 is also limited, so the equilibrium shifts due to the hydrogen removal from the reaction medium is limited; in this sense, only for low feed flow rates such enhancement is achieved. As the temperature increases, two effects must be taken into account. On one hand, the increase of the reaction rate with the temperature leads to an increase of CO conversion (though penalized by the decrease of the equilibrium constant – exothermal reaction) and, consequently, to an increase of the H_2 concentration. On the other hand, the same increase of the temperature leads to an increase of the permeation rate, so to a greater capacity of removing H_2 from the reaction medium. From this “synergistic” effect results that a conversion enhancement is attained for increasingly higher feed flow rate.

Figure 6.4-B shows also that H_2 recovery may tend to a plateau, for certain operating conditions. This behavior can be inferred from Figure 6.4-B for low feed flow rates and it is clear in Figure 6.5-B. This level off (or even decrease, see Figure 6.5-B) of the H_2 recovery is attained for a temperature relatively high and is the result of the conjoint effect of reaction and permeation rates. From one hand, the driving force for the permeation tends to vanish. Due to a depletion of H_2 from the reaction side, its partial pressure tends to equal the one in the permeate side, unless the sweep gas flow rate is so high that the concentration of H_2 in the permeate side approaches zero. In this case, the plateau is attained for 100 % of recovery. On the other hand, the backward reaction becomes faster with the temperature (notice that the WGS is an equilibrium-limited reaction), decreasing the H_2 partial pressure and

canceling the effect of its removal from the reaction medium. Additionally, the decreasing of the thermodynamic equilibrium constant with the temperature should be taken into account, which conducts to a decrease of the CO conversion as a function of the temperature (Figures 6.4-A and 6.4-B). As shown in the previous chapter, the usage of sweep gas revealed to be an effective way to decrease the hydrogen partial pressure in the permeate chamber.

Figure 6.5 shows the CO conversion and H_2 recovery results, both experimental and predicted by the model, as a function of temperature and for different feed space velocities in the same MR. In this case, the permeated hydrogen was collected by vacuum pumping. Again, a good adhesion between model and experimental results was obtained in what concerns the H_2 recovery (Figure 6.5-B), but not concerning CO conversion (Figure 6.5-A), though only for some of the operating conditions. Anyway, the model still describes the trend of the experimental results (CO conversion and H_2 recovery) as a function of the temperature and feed space velocity.

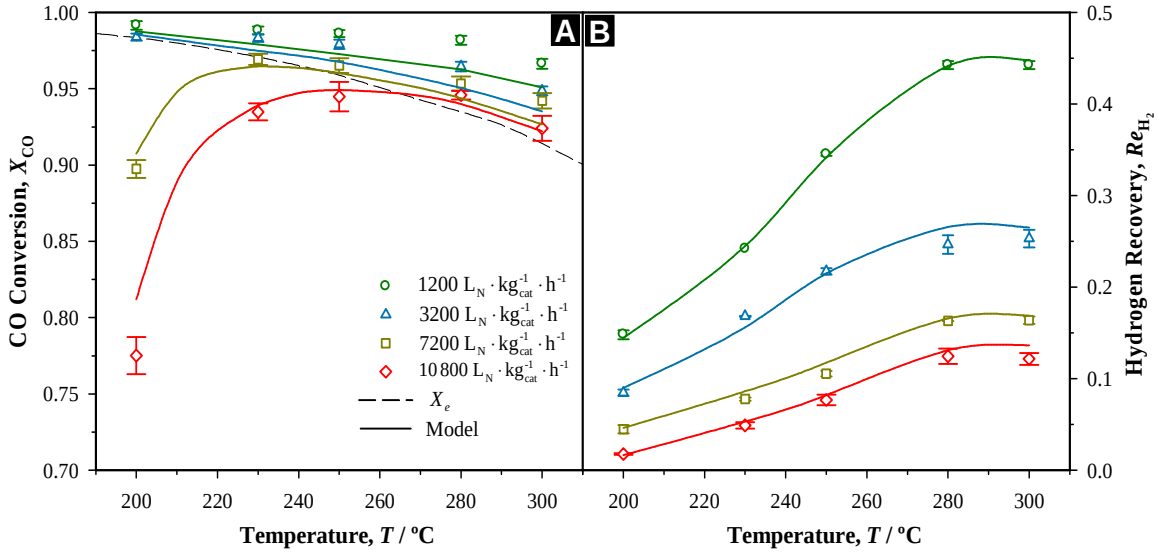

Figure 6.5 – Effect of the reaction temperature and feed gas space velocity on the CO conversion (A) and H_2 recovery (B) in the MR, operating in vacuum mode. $P^F = 1.1$ bar and $P^P \sim 30$ mbar.

Figure 6.6 shows the simulated axial composition profiles in the retentate side for each species (dry basis) in terms of the concerning molar fraction, for the GHSV =

1200 $L_N \cdot kg_{cat}^{-1} \cdot h^{-1}$ and for the two operating modes of the MR, vacuum and sweep gas, both with 2 bar in the feed. The experimental compositions obtained at the exit of the reactor are also included.

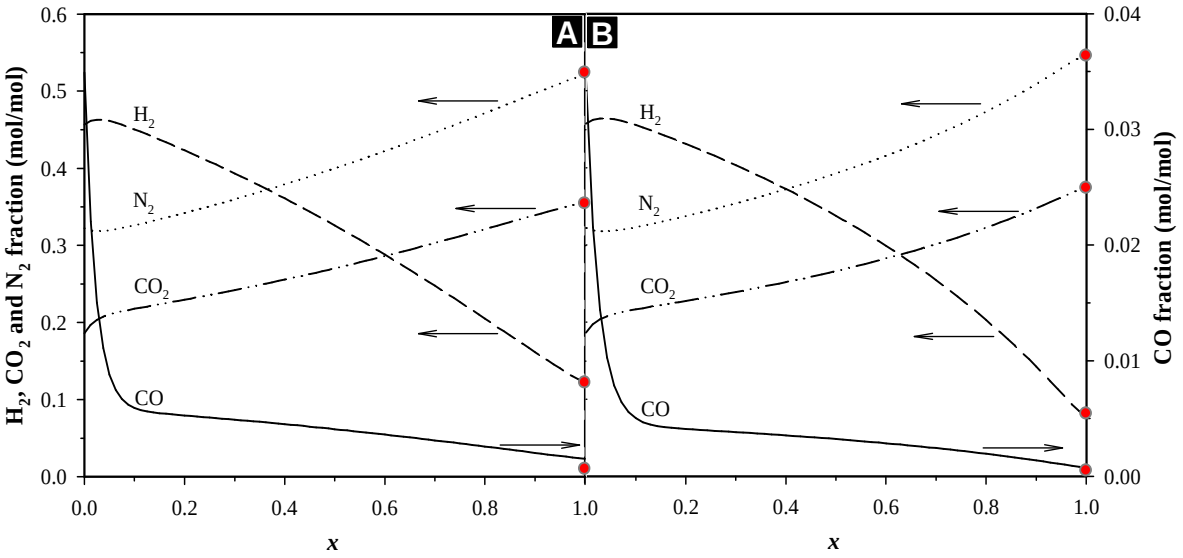

Figure 6.6 – Simulated profiles on the reaction side as a function of the dimensionless reactor length: Vacuum mode, P^F = 2.0 bar and P^P ~ 30 mbar (A) and sweep gas mode, P^F = 2.0 bar, P^P = 1.0 bar and Q_{sweep} = 1.0 $L_N \cdot min^{-1}$ (B). Other experimental conditions: T = 300 ºC, GHSV = 1200 $L_N \cdot kg_{cat}^{-1} \cdot h^{-1}$. Symbols ● represent the experimental molar fraction (dry basis) of each species measured at the exit of the reactor.

The comparison between the predicted compositions and the experimental results at the exit of the reactor shows also the goodness of the model fitting (cf. Figure 6.6). As it can be realized from Figure 6.6, there are clearly two different regions inside the reaction medium. In the first one, for about 10 % of the initial length of the reactor, the molar fraction of CO decreases rapidly, while the molar fraction of H_2 increases slightly. Since the reaction temperature is high in both cases (T = 300 ºC), the reaction kinetics and H_2 permeation are favored. As the reaction condition for the feed mixture is far away from the thermodynamic equilibrium condition, the chemical reaction shifts quickly towards the reaction products, decreasing rapidly the CO concentration. However, the rate of H_2 permeation does not

follow the rate of production from the WGS reaction, and thus the concentration of H_2 increases. After this point, the shift of the reaction condition towards the reaction products depends only on the H_2 removal due to permeation. As a consequence, the concentrations for both reactants decrease slowly and in a more or less linear way. The concentration profiles of CO_2 and N_2 exhibit an increasing trend along the reactor axis, because the mixture becomes richer in the non-permeating species and, moreover, CO_2 is a reaction product. The reactor can then be divided into a region of chemical control and a region of permeation control, this accounting for the last 90 % of the reactor length.

The membrane reactor can only withstand to ca. two bar pressure difference. Higher feed pressures can only be applied if using a sweep gas at a pressure such as the pressure threshold difference is not overcome. High feed pressure coupled with high sweep flow rates results in a high H_2 partial pressure difference between the two chambers of the membrane reactor. On the other hand, operating at a higher feed pressure results in an enhancement on CO conversion besides improving H_2 recovery. Following, lower contents of CO and H_2 were obtained at the exit of the retentate chamber when the sweep mode was used (c.f. Figures 6.6-A and 6.6-B).

6.4.2 Influence of Damköhler number and contact time

From the results presented above, it is clear that there are regions where the CO conversion is almost complete, as well as the H_2 recovery is maximum. However, it would be of interest to define the parametric regions where such variables could be optimized. In order to do so, it is presented a simulation result of the CO conversion and H_2 recovery as a function of the two model dimensionless parameters, *Damköhler number* (*Da*) and contact time (Γ) - Figures 6.7 and 6.8.

The analysis of the MR operating with vacuum pumping and sweep gas mode is briefly accessed in terms of dimensionless parameters. The values for ψ and K_{CO}^{p} were assumed to be 0.93 and 9.53×10^{-5} Pa^{-1}, respectively, as reported by Mejdell et al. (Mejdell et al., 2009).

Figure 6.7-A shows that there is a region in the parametric space contact time/Damköhler number where an almost complete conversion of CO can be achieved. This happens for *Da* > ≈7 and Γ > ≈0.25. For lower values of Γ, the CO conversion decreases slightly, but for lower values of *Da*, the decrease is abrupt. Figure 6.7-B, on it turns, shows that the H_2 recovery is maximized in the same parametric region. The maximum value attained for vacuum operation was about 0.93, which is related to the hydrogen partial pressure at the permeate side ~30 mbar. For lower values of Γ and in the same region of *Da*, the H_2 recovery decreases quickly, with a still high CO conversion. This is a consequence of the quick decrease of the stage cut, that is, the fraction of H_2 in the retentate increases. Figure 6.8-B shows again that the H_2 recovery is much more sensitive to the contact time than CO conversion.

These results show that, for a given membrane reactor (with a fixed amount of catalyst – fixed *Damköhler*) and operating in vacuum mode, the CO conversion is mostly controlled by feed flow rate, while the H_2 recovery depends also strongly on the hydrogen permeation (which depends on the hydrogen partial pressure at the permeate side and total pressure at feed side). If the membrane reactor operates in sweep mode and with 2 bar in the feed, it is possible to achieve almost 100 % of CO conversion with almost 100 % of H_2 recovery (as shown below – Figure 6.8).

The experimental results obtained for vacuum mode are presented in Figure 6.7 (white line). As it can be inferred, either CO conversion and H_2 recovery can be “improved” increasing essentially the contact time parameter (that is, decreasing GHSV/feed flow rate).

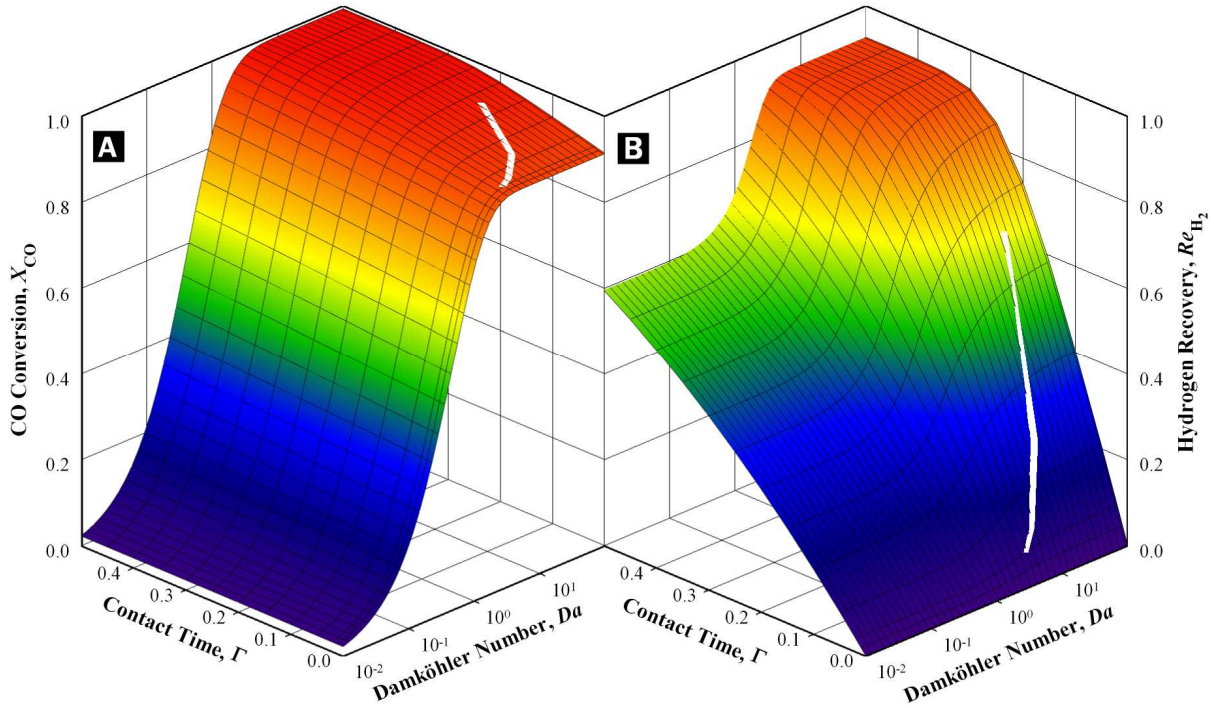

Figure 6.7 – Effect of *Da* and Γ on the CO conversion (A) and H_2 recovery (B) in the MR operating in vacuum mode. T = 300 ºC, P^F = 1.1 bar and P^P ~ 30 mbar. The white lines describe the parametric region based on the operating conditions used in this work.

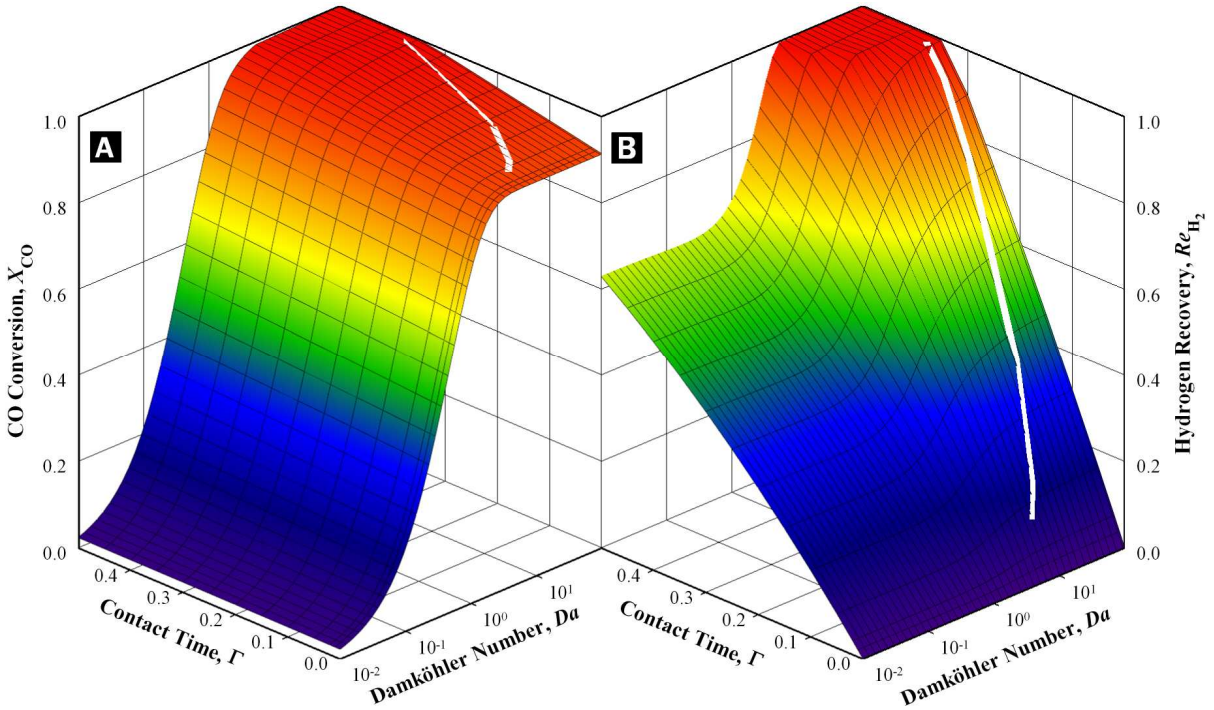

Figure 6.8 – Effect of *Da* and Γ on the CO conversion (A) and H_2 recovery (B) in the MR operating in sweep gas mode (operating counter-currently). T = 300 ºC, P^F = 2.0 bar, P^P = 1.0 bar and Q_{sweep} = 1 $L_N \cdot min^{-1}$. The white line describes the parametric region based on the operating conditions used in this work.

From Figure 6.8-A, it can be seen that CO conversion dependence on *Da* and Γ shows the same trend as in Figure 6.7-A. However, using sweep gas to collect the permeated hydrogen at P^F = 2.0 bar, total CO conversion can be achieved in the parametric space contact time/Damköhler number of *Da* > ≈7 and Γ > ≈0.4 – cf. Figure 6.8-A.

6.5 Conclusions

The present study deals with model analysis and experimental assessment of carbon monoxide conversion and hydrogen recovery of water-gas shift reaction conducted in a membrane reactor. Experimental tests on a Pd-Ag MR were performed under a broad range of operating conditions such as temperature $(200-300\ ^{o}\mathrm{C})$ and gas hourly space velocity $(1200-10800\ \mathrm{L_N \cdot kg_{cat}^{-1} \cdot h^{-1}})$, using different operating modes (vacuum and sweep gas). The simulation and experimental results showed a suitable agreement for the MR working in both sweep gas and vacuum operating modes. The comparison between the predicted compositions and the experimental results, at the exit of the reactor, confirm also the goodness of the proposed MR model. Apart from two fitting parameters (related with the decline of permeability due to the presence of CO in the reaction mixture), all other model parameters were determined from independent studies, namely reaction kinetics and membrane permeability towards hydrogen.

The model was also used to simulate the performance of the MR in a wide range of the parametric space, described by the *Damköhler's number* and contact time. This allowed us to define the optimal operating regions in terms of CO conversion and H_2 recovery.

6.6 Nomenclature

A	cross-sectional area [m^2]
d_p	catalyst particle diameter [m]

D_{ax} axial dispersion coefficient [$m^2 \cdot s^{-1}$]

Da Damköhler number

E^k activation energy for the WGS reaction [$kJ \cdot mol^{-1}$]

E^p activation energy for hydrogen permeation [$kJ \cdot mol^{-1}$]

f variable related with the operation mode (f = -1 for co-current; f = 1 for counter-current)

H^a enthalpy of adsorption [$J \cdot mol^{-1}$]

J flux through the membrane [$mol \cdot m^{-2} \cdot s^{-1}$]

k rate constant for the WGS reaction [$mol \cdot g_{cat}^{-1} \cdot h^{-1} \cdot Pa^{-2}$]

k^0 pre-exponential factor of the rate constant [$mol \cdot g_{cat}^{-1} \cdot h^{-1} \cdot Pa^{-2}$]

K_e equilibrium constant for the WGS reaction

K_{CO}^p equilibrium adsorption constant of CO for the Sieverts'-Langmuir formulation, adjustable parameter (equation 6.18) [Pa^{-1}]

K_i^a equilibrium adsorption constant of species i for the reaction rate equation [Pa^{-1}]

$K_i^{a,0}$ pre-exponential equilibrium adsorption constant of species i [Pa^{-1}]

ℓ reactor's length [m]

L_{H_2} hydrogen permeability [$mol \cdot m \cdot m^{-2} \cdot s^{-1} \cdot Pa^{-0.5}$]

$L_{H_2}^0$ pre-exponential factor for hydrogen permeation [$mol \cdot m \cdot m^{-2} \cdot s^{-1} \cdot Pa^{-0.5}$]

M molar mass [$g \cdot mol^{-1}$]

J flux through the membrane [$mol \cdot m^{-2} \cdot s^{-1}$]

p partial pressure [Pa or bar]

P total pressure [Pa or bar]

Pe Péclet number for mass transfer

r internal radius [m]

$\Re$ ideal gas constant [= 8.314 $J \cdot mol^{-1} \cdot K^{-1}$]

R rate of consumption or formation [$mol \cdot g_{cat}^{-1} \cdot h^{-1}$]

Re_{H_2} hydrogen recovery

T	temperature [K or ºC]
u	interstitial velocity [$m \cdot s^{-1}$]
V^R	volume of the retentate chamber [m^3]
W_{cat}	mass of catalyst [g]
x	dimensionless axial coordinate
X_{CO}	conversion of carbon monoxide
X_e	thermodynamic equilibrium conversion
z	axial coordinate [m]

Subscripts

i	species involved in the reaction experiments (CO, H_2O, CO_2, H_2 or N_2)
ref	reference component (H_2) or conditions

Superscripts

*	dimensionless variable
in	inlet of the reactor
k	relative to the reaction kinetics
m	membrane
out	outlet of the reactor
p	relative to the H_2 permeation
F	feed-side
P	permeate-side
R	retentate-side

Greek Letters

α	Ergun equation coefficient (equation 6.23)
β	Ergun equation coefficient (equation 6.23)
δ	Pd-Ag membrane thickness [m]

ε_b	void bed fraction
γ	Arrhenius' number
Γ	dimensionless contact time
μ_g	(dynamic) gas mixture viscosity [$kg \cdot m^{-1} \cdot s^{-1}$]
ρ_g	gas mixture density [$kg \cdot m^{-3}$]
σ	dimensionless parameter: ratio between the cross-sectional areas of the retentate and the permeate chambers
ν_i	stoichiometric coefficient of species *i* in the WGS reaction
Ψ	adjustable parameter (equation 6.18)

Acronyms

GHSV	gas hourly space velocity [$L_N \cdot kg_{cat}^{-1} \cdot h^{-1}$]
HT	higher temperature regime
LT	lower temperature regime
MR	membrane reactor
PBR	packed-bed reactor
PEMFC	polymer electrolyte membrane fuel cell
WGS	water-gas shift

6.7 References

Adrover, M.E., Lopez, E., Borio, D.O., Pedernera, M.N., Theoretical study of a membrane reactor for the water gas shift reaction under nonisothermal conditions. *AIChE J.* **2009,** 55 (12), 3206-3213.

Aresta, M., Dibenedetto, A., Utilisation of CO_2 as a chemical feedstock: opportunities and challenges. *Dalton Trans.* **2007** (28), 2975-2992.

Ayastuy, J.L., Gutierrez-Ortiz, M.A., Gonzalez-Marcos, J.A., Aranzabal, A., Gonzalez-Velasco, J.R., Kinetics of the low-temperature WGS reaction over a $CuO/ZnO/Al_2O_3$ catalyst. *Ind. Eng. Chem. Res.* **2005,** 44 (1), 41-50.

Barbieri, G., Scura, F., Lentini, F., De Luca, G., Drioli, E., A novel model equation for the permeation of hydrogen in mixture with carbon monoxide through Pd-Ag membranes. *Sep. Purif. Technol.* **2008,** 61 (2), 217-224.

Barbir, F., *PEM Fuel Cells: Theory and Practice*. Elsevier Academic Press: New York, 2005.

Basile, A., Hydrogen production using Pd-based membrane reactors for fuel cells. *Top. Catal.* **2008,** 51 (1-4), 107-122.

Basile, A., Chiappetta, G., Tosti, S., Violante, V., Experimental and simulation of both Pd and Pd/Ag for a water gas shift membrane reactor. *Sep. Purif. Technol.* **2001,** 25 (1-3), 549-571.

Brunetti, A., Caravella, A., Barbieri, G., Drioli, E., Simulation study of water gas shift reaction in a membrane reactor. *J. Membr. Sci.* **2007,** 306 (1-2), 329-340.

Criscuoli, A., Basile, A., Drioli, E., An analysis of the performance of membrane reactors for the water-gas shift reaction using gas feed mixtures. *Catal. Today* **2000,** 56 (1-3), 53-64.

Dittmeyer, R., Hollein, V., Daub, K., Membrane reactors for hydrogenation and dehydrogenation processes based on supported palladium. *J. Mol. Catal. A: Chem.* **2001,** 173 (1-2), 135-184.

Froment, G.F., Bischoff, K.B., *Chemical Reactor Analysis and Design*. 2 ed.; John Wiley & Sons: New York, 1990.

Gosiewski, K., Warmuzinskia, K., Tanczyka, M., Mathematical simulation of WGS membrane reactor for gas from coal gasification. *Catal. Today* **2010,** doi:10.1016/j.cattod.2010.02.031.

Hindmarsh, A.C., 2006. Serial fortran solvers for ODE initial value problems, https://computation.llnl.gov/casc/odepack (Accessed July 2010) Livermore, CA, U.S.A.

ISO, 2008. Hydrogen fuel - product specification - Part 2: proton exchange membrane (PEM) fuel cell applications for road vehicles, ISO/TS 14687-2. International organization for standardization.

Koryabkina, N.A., Phatak, A.A., Ruettinger, W.F., Farrauto, R.J., Ribeiro, F.H., Determination of kinetic parameters for the water-gas shift reaction on copper catalysts under realistic conditions for fuel cell applications. *J. Catal.* **2003**, 217 (1), 233-239.

Koukou, M.K., Papayannakos, N., Markatos, N.C., Dispersion effects on membrane reactor performance. *AlChE J.* **1996**, 42 (9), 2607-2615.

Markatos, N.C., Vogiatzis, E., Koukou, M.K., Papayannakos, N., Membrane reactor modelling - A comparative study to evaluate the role of combined mass and heat dispersion in large-scale adiabatic membrane modules. *Chem. Eng. Res. Des.* **2005,** 83 (A10), 1171-1178.

Mejdell, A.L., Jondahl, M., Peters, T.A., Bredesen, R., Venvik, H.J., Effects of CO and CO_2 on hydrogen permeation through a similar to 3 µm Pd/Ag 23 wt.% membrane employed in a microchannel membrane configuration. *Sep. Purif. Technol.* **2009,** 68 (2), 178-184.

Mendes, D., Chibante, V., Zheng, J.-M., Tosti, S., Borgognoni, F., Mendes, A., Madeira, L.M., Enhancing the production of hydrogen via water-gas shift reaction using Pd-based membrane reactors. *Int. J. Hydrogen Energy* **2010**, accepted for publication.

Moe, J.M., Design of water-gas shift reactors. *Chem. Eng. Prog.* **1962,** 58 (3), 33-36.

Olah, G.A., Goeppert, A., Prakash, G.K.S., *Beyond oil and gas: the methanol economy*. Wiley-VCH: Germany, 2006.

Perinline, H.W., Luebke, D.R., Jones, K.L., Myers, C.R., Morsi, B.I., Heintz, Y.J., Ilconich, J.B., Progress in carbon dioxide capture and separation research for gasification-based power generation point sources. *Fuel Process. Technol.* **2008,** 89 (9), 897-907.

Perry, R.H., Green, D.W., *Perry's chemical engineer's handbook*. 7 ed.; McGraw Hill: New York, USA, 1999.

Poling, B.E., Prausnitz, J.M., O'Connell, J.P., *The properties of gases and liquids*. 5 ed.; McGraw-Hill: New York, 2004.

Ratnasamy, C., Wagner, J., Water gas shift catalysis *Catal. Rev.-Sci. Eng.* **2009,** 51 (3), 325-440.

Sá, S., Silva, H., Sousa, J.M., Mendes, A., Hydrogen production by methanol steam reforming in a membrane reactor: Palladium vs carbon molecular sieve membranes. *J. Membr. Sci.* **2009,** 339 (1-2), 160-170.

Smith, J.M., Ness, H.C.V., Abbott, M., *Introduction to chemical engineering thermodynamics*. McGraw-Hill: Singapore, 1996.

Tiemersma, T.P., Patil, C.S., Annaland, M.V., Kuipers, J.A.M., Modelling of packed bed membrane reactors for autothermal production of ultrapure hydrogen. *Chem. Eng. Sci.* **2006,** 61 (5), 1602-1616.

Tosti, S., Basile, A., Bettinali, L., Borgognoni, F., Chiaravalloti, F., Gallucci, F., Long-term tests of Pd-Ag thin wall permeator tube. *J. Membr. Sci.* **2006,** 284 (1-2), 393-397.

Uemiya, S., Sato, N., Ando, H., Kikuchi, E., The Water Gas Shift reaction sssisted by a palladium membrane reactor. *Ind. Eng. Chem. Res.* **1991,** 30 (3), 585-589.

Unemoto, A., Kaimai, A., Sato, K., Otake, T., Yashiro, K., Mizusaki, J., Kawada, T., Tsuneki, T., Shirasaki, Y., Yasuda, I., The effect of co-existing gases from the process of steam reforming

reaction on hydrogen permeability of palladium alloy membrane at high temperatures. *Int. J. Hydrogen Energy* **2007,** 32 (14), 2881-2887.

Chapter 7

Integrated Analysis of a Membrane-based Process for Hydrogen Production

The aim of this chapter is to investigate the performance and energy efficiency achieved by an integrated system based on two different ethanol fuel processor configurations: a Conventional Reactor (CR) and a Membrane Reactor (MR). The CR-based configuration system consists of an ethanol reformer followed by two water-gas shift reactors operating at high and low temperatures. The final hydrogen purification was carried out by a preferential oxidizer in order to reduce the CO concentration before feeding the polymer electrolyte membrane fuel cell (PEMFC). A multi-tubular MR process using thin Pd-Ag tubes has also been considered, where the water-gas shift reaction and the hydrogen separation take place simultaneously.

The analysis showed that the MR process configuration possesses a simpler system design with a minor advantage in terms of energy efficiency (30 %) compared with the conventional system (27 %). Moreover, a detailed parametric analysis concerning the effects of water-to-ethanol molar ratio, reaction pressure, reformer and MR temperature, sweep-gas molar ratio and MR configuration on the achieved performance (hydrogen yield) and energy efficiency of the system has also been done.

The importance of optimizing integrated systems is shown since the optimal operating conditions from a global efficiency analysis point of view are in general distinct when compared with those obtained when focusing on the reformer reactor or individual process units alone.

The contents of this chapter were adapted from: Mendes, D., Tosti, S., Borgognoni, F., Mendes, A., Madeira, L. M., Integrated analysis of a membrane-based process for hydrogen production from ethanol steam reforming. *Catal. Today* **2010**, doi:10.1016/j.cattod.2010.02.029.

7.1 Introduction

It is being consensual the fact that the full environmental benefit of a society transition to hydrogen is achieved only when the hydrogen needs can be derived from renewable resources, such as water photovoltaic hydrolysis or biomass gasification (Deluga et al., 2004). In this perspective, the interest of processes for producing hydrogen from reforming of ethanol, obtained by the fermentation of biomass, is growing (Deluga et al., 2004; Liguras et al., 2003; Ni et al., 2007).

An experimental apparatus for producing pure hydrogen, that feeds a 500 W polymeric exchange membrane fuel cell (PEMFC), has been built at ENEA facilities, in Frascati – Italy. The experimental set-up consists of a conventional ethanol reformer followed by a Pd-Ag multi-tube membrane reactor (MR) performing both the water-gas shift (WGS) reaction and the separation of the hydrogen produced (Tosti et al., 2008). However, the preliminary studies and experiments have been putting into evidence the need of considering the simulation and optimization of these innovative membrane processes, both in terms of hydrogen yield and energy efficiency integration.

The system integration of such membrane-based processes is rarely addressed in the literature despite its importance under the process intensification strategy point of view (Bernardo et al., 2006). In fact, for stationary applications the PEMFCs should be highly integrated systems, including a fuel processor, the fuel cell itself and a post-combustion unit that fulfils the energetic demands of the system. Therefore, the integration should not only be expressed in terms of material flows but also in terms of energy balance (Godat and Marechal, 2003).

In this chapter, a membrane-based process is proposed and then compared with a heat integrated conventional process configuration. This design study starts from the analyses carried out on a hypothetical conventional process for producing hydrogen via ethanol steam reforming (SR), WGS reactors, a preferential oxidation (PrOx) unit, followed by a PEMFC

stack. Following the same system design approach, a membrane-based ethanol fuel processor was implemented replacing the WGS and PrOx reactors by a unique multi-tubular Pd-Ag MR where the WGS reaction is conducted with simultaneous hydrogen purification. Commercial process simulation software (HYSYS) was used to solve the mass and energy balances, and to compute the operating conditions for each process unit (HYSYS, 2003). The effect of key variables such as the reformer temperature, the reactants molar ratio, the reaction pressure, the temperature of the membrane reactor and the effect of sweep gas on the fuel cell system efficiency is also discussed.

7.2 Description of the Ethanol Reformer Systems

Both systems described below, CR standing for Conventional Reactor and MR standing for Membrane Reactor, have in common the following characteristics:

- a fuel processor, which chemically converts the ethanol into hydrogen, and hydrogen clean-up equipment(s);
- a fuel cell stack, which electrochemically converts the hydrogen into electric power;
- associated equipment for heat, oxygen and water management; and
- auxiliary equipment such as pumps, compressors and expanders.

Two different configurations were studied: (i) the conventional-based approach – CR (Figure 7.1) and (ii) the membrane-based approach – MR (Figure 7.2).

In terms of system design, the main difference between conventional- and membrane-based configurations is related with the hydrogen clean-up equipment(s) used and inherently on the process complexity. In the conventional configuration, three units were used to allow reaching a high H_2 content in the PEMFC feed stream: high- (HT-WGS) and low- (LT-WGS) temperature WGS reactors, and finally the PrOx unit. On other hand, in the membrane-based configuration only one unit was used – a WGS MR.

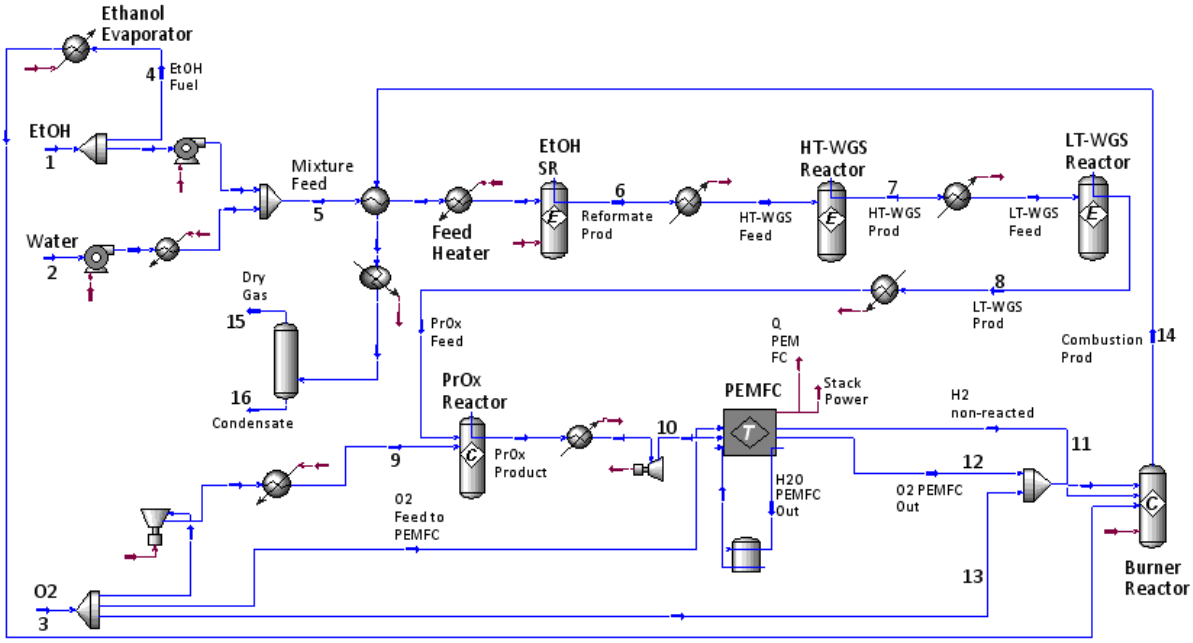

Figure 7.1 – Flowsheet of an integrated PEMFC unit with an ethanol steam reforming system – conventional configuration.

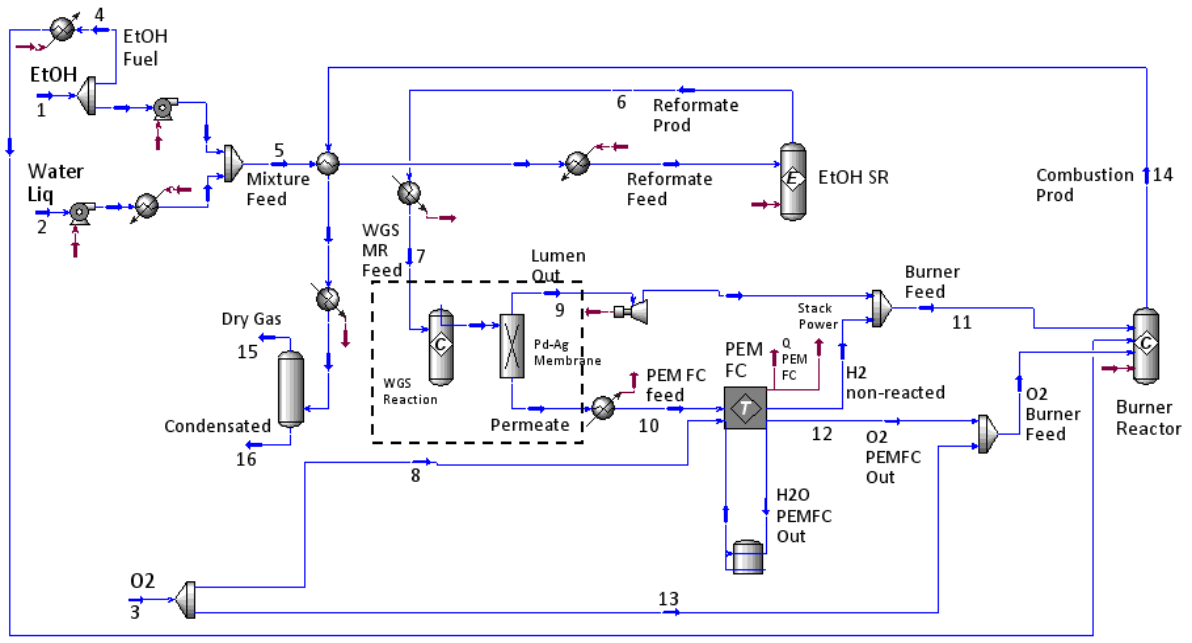

Figure 7.2 – Flowsheet of a PEMFC unit integrated with an ethanol steam reforming system – membrane-based configuration (dotted box represents the WGS MR).

In the simulated systems, both ethanol and water streams are provided at 20 ºC and 0.1 MPa (streams 1 and 2 in Figures 7.1 and 7.2), then were pumped to a mixer and finally fed at 250 $g \cdot h^{-1}$ to the ethanol reformer unit. The water flow rate required for the steam reformer is controlled by the water-to-ethanol molar ratio. The process design considers a burner reactor used for combusting the vent streams from the fuel processor, which is used to balance the heat demands of the system, namely for heating/vaporizing the steam reforming feed and to heat the reformer itself. The oxygen required for the combustor, fuel cell and PrOx unit in the conventional configuration system is also supplied at 0.1 MPa and 20 ºC (cf. stream 3 in Figure 7.1 and Table 7.1). A compressor is subsequently used to pressurize this stream to achieve the specified pressure and perform the CO oxidation reaction.

For simplicity, compressor, expander and pumps adiabatic efficiencies were assumed to be 75 %. No pressure drops were accounted. These process systems were designed taking into account that CO_2 is separated from H_2 and dehydrated in a condenser after the burner reactor for subsequent release or capture (e.g. compression) – cf. Figures 7.1 and 7.2.

The MR operation was simulated by an in house-designed program, as explained below, outside the simulator environment. For simplicity, this unit was represented by a "conversion reactor" (the reaction medium according to HYSYS terminology) and a splitter (the Pd-Ag membrane) – cf. Figure 7.2. The operating conditions of both systems are summarized in Tables 7.1 and 7.2.

7.2.1 Ethanol reforming unit

The reaction pathway and thermodynamics of the ethanol steam reforming have received a significant attention in the published literature (Ioannides, 2001; Mas et al., 2006; Ni et al., 2007; Vaidya and Rodrigues, 2006). Moreover, the types of catalysts employed play a crucial role in the reactivity towards complete conversion of ethanol, hydrogen selectivity, and inhibition of coke formation. Non-noble metal, such as Ni-based catalysts, are promising

Table 7.1 – Operating conditions of the main streams in the CR-based system illustrated in Figure 7.1 ($T_{reformer}$ = 700 ºC, $P_{reaction}$ = 2 MPa and H_2O/EtOH = 3).

Stream	T / K	P / MPa	F_m / g·h^{-1}	x_{EtOH}	x_{H_2O}	x_{CO}	x_{H_2}	x_{CO_2}	x_{O_2}
1	293.2	0.10	141.7	1.0	–	–	–	–	–
2	293.2	0.10	134.9	–	1.0	–	–	–	–
3	293.2	0.10	604.7	–	–	–	–	–	1.0
4	293.2	0.10	26.77	1.0	–	–	–	–	–
6	973.2	2.0	250.0	3.86×10^{-3}	1.80×10^{-1}	1.69×10^{-1}	5.70×10^{-1}	7.74×10^{-2}	–
8	483.2	2.0	250.0	3.86×10^{-3}	3.56×10^{-2}	2.43×10^{-2}	7.14×10^{-1}	2.22×10^{-1}	–
10	343.2	0.10	280.6	3.86×10^{-3}	1.08×10^{-1}	9.90×10^{-7}	6.41×10^{-1}	2.46×10^{-1}	–
14	1273.2	0.10	374.7	–	4.84×10^{-1}	1.63×10^{-6}	–	5.16×10^{-1}	–
15	293.2	0.10	273.6	–	2.43×10^{-2}	–	–	9.76×10^{-1}	–
16	293.2	0.10	101.1	–	1.0	–	–	–	–

Table 7.2 – Operating conditions of the main streams in the MR-based system illustrated in Figure 7.2 ($T_{reformer}$ = 700 ºC, $P_{reaction}$ = 2 MPa, T_{MR} = 360 ºC and H_2O/EtOH = 3).

Stream	T / K	P / MPa	F_m / g·h^{-1}	x_{EtOH}	x_{H_2O}	x_{CO}	x_{H_2}	x_{CO_2}	x_{O_2}
1	293.2	0.10	132.7	1.0	–	–	–	–	–
2	293.2	0.10	134.9	–	1.0	–	–	–	–
3	293.2	0.10	555.0	–	–	–	–	–	1.0
4	293.2	0.10	17.65	1.0	–	–	–	–	–
6	973.2	2.0	250.0	3.86×10^{-3}	1.80×10^{-1}	1.69×10^{-1}	5.70×10^{-1}	7.74×10^{-2}	–
9	633.2	2.0	221.7	1.36×10^{-2}	6.67×10^{-2}	2.66×10^{-2}	4.99×10^{-2}	8.43×10^{-1}	–
10	633.2	0.10	28.44	–	–	–	1.0	–	–
14	1273.2	0.10	364.2	–	5.18×10^{-1}	1.24×10^{-2}	–	4.70×10^{-1}	–
15	293.2	0.10	253.4	–	1.28×10^{-2}	2.53×10^{-2}	–	9.62×10^{-1}	–
16	293.2	0.10	110.7	–	1.0	–	–	–	–

materials to conduct the reaction due to their relative low-cost, high activity, selectivity to H_2 and stability (Ni et al., 2007). In the present study, the steam reforming of ethanol is considered as an ideal case, where no intermediate compounds are formed, as previously suggested by Song et al. (Song et al., 2005). Furthermore, each reaction step described by reactions 7.1 and 7.2 is considered to be at equilibrium conditions at the reactor outlet.

Ethanol decomposition reaction:

$$C_2H_5OH + 3H_2O \leftrightarrow 2CO_2 + 6H_2, \quad \Delta H^o_{298K} = 170.41\ kJ \cdot mol^{-1} \tag{7.1}$$

Reverse water-gas shift (WGS) reaction:

$$CO_2 + H_2 \leftrightarrow CO + H_2O, \quad \Delta H^o_{298K} = 41.1\ kJ \cdot mol^{-1} \tag{7.2}$$

The dependence of the equilibrium constants with temperature for reactions (7.1) and (7.2) have been provided by Semelsberger et al. (Semelsberger et al., 2004) and Moe (Moe, 1962), respectively. The equilibrium constants for each reaction (K_e) were then interpolated by HYSYS, obtaining for each reaction a linear equation of the type:

$$\ln(K_e) = A + BT^{-1} + C\ln(T) + DT \tag{7.3}$$

The values of the parameters are described in Table 7.3.

The reactor is assumed to be isothermal, meaning that heat has to be supplied from an external energy source to maintain the temperature. In conventional tubular steam reforming adopted for both the CR and the MR configuration, the energy required to drive the endothermic reforming reactions is assumed to be supplied by the combustion of a portion of fuel outside the reactor, cf. Figures 7.1 and 7.2.

Table 7.3 – Values of the estimated parameters in equation 7.3 for reactions 7.1 and 7.2.

Reaction	***A***	***B* / K**	***C***	***D* / K^{-1}**
$C_2H_5OH + 3H_2O \leftrightarrow 2CO_2 + 6H_2$	4.740×10^{1}	-2.276×10^{4}	–	2.359×10^{-3}
$CO_2 + H_2 \leftrightarrow CO + H_2O$	5.268×10^{-1}	-4.380×10^{3}	5.809×10^{-1}	-4.066×10^{-4}

7.2.2 Water-gas shift reaction unit

Typically, gas can emerge from the reformer with a CO level of $1-10$ vol.%, which gets adsorbed on the noble catalyst of the PEMFC, poisoning it. Therefore, the fuel processor must be designed to convert the CO content in the fuel stream to levels that are tolerated by the Pt catalyst of the PEMFC; moreover, the high conversion of CO increases the hydrogen yield. This task is partially accomplished by the water-gas shift reactors, where reaction 1.1 takes place.

The performance of these units depends on the input concentration of CO and H_2O/CO ratio. Such variables are in turn related to the reformer reaction pathway as well as to the water-to-ethanol feed molar ratio (H_2O/EtOH), reformer unit temperature ($T_{reformer}$), and reaction pressure ($P_{reaction}$), which parametric analysis is done below. Besides, the temperature of the WGS reaction unit affects its performance because it modifies the CO conversion.

7.2.2.1 Conventional configuration

In the conventional configuration (Figure 7.1), the WGS reaction was assumed to be carried out, as usual, in two adiabatic shift reactors in series with an inter-cooler in between. This allows a smaller adiabatic temperature rise and a better steam management, therefore making the process more economical (Thomas and Thomas, 1997). These units perform the exothermal WGS reaction that is considered to be at equilibrium conditions at the reactor outlet. The HYSYS library was used to obtain the equilibrium data for the reaction. The first WGS stage is characterized by working at higher temperatures, favoring a fast CO consumption and minimizing the catalyst bed volume, and it is called the high-temperature shift (HT-WGS) reactor. A chromium-promoted iron oxide catalyst is assumed to be used in the HT-WGS reactor. In the next stage the reaction takes place at a lower temperature for obtaining a higher CO conversion, which is limited by the thermodynamic equilibrium of the

exothermal WGS reaction. An inter-stage cooling system was thus used to operate the second WGS reactor at a lower temperature. A copper-zinc-alumina catalyst is usually employed in the LT stage. In this study it was assumed that the HT- and the LT-WGS reactors operate at 360 ºC and 210 ºC, respectively (chapter 2).

7.2.2.2 Membrane-based configuration

In the membrane-based configuration (Figure 7.2) the WGS reaction was supposed to be carried out in an adiabatic multi-tube membrane reactor. A membrane reactor consisting of 19 Pd-Ag thin wall tubes has been considered for the simulation work. These permeator tubes of 10 mm of internal diameter, wall thickness of 0.050 mm and 250 mm of length can be produced by cold rolling and diffusion welding of metal foils made of a Pd alloy with $20-25$ wt.% of Ag. Such a multi-tube membrane module has been built at ENEA laboratories (in Italy) and should be coupled with a 500 W PEM fuel cell. The catalyst bed is assumed to be inserted in the membrane lumen and the permeated hydrogen is collected in the shell side at 0.1 MPa. The permeate stream formed by pure H_2 is then fed to the PEMFC stack. The retentate stream, i.e. essentially the produced CO_2, the CO not eliminated and the H_2 not permeated (stream number 9 in Figure 7.2), is conducted to the combustion unit to fulfill the energetic needs of the system. The energy released by the expander unit, when the WGS MR is operated at pressures higher than 0.1 MPa, was not taken into consideration in the energy balance.

A computer code developed for simulating a WGS-MR of one membrane tube has been used (Tosti et al., 2009). The model accounts for the kinetics of the WGS reaction over an iron-based catalyst and the hydrogen transport (permeation) through the Pd-Ag membrane. A Langmuir-Hinshelwood kinetic model was used based on the surface reaction of molecularly adsorbed reactants as the rate determining step, which leads to the following expression of the reaction rate:

$$-r_{CO} = \frac{k K_{CO_2} K_{H_2O} (p_{CO} p_{H_2O} - (p_{CO_2} p_{H_2} / K_e))}{(1 + K_{CO} p_{CO} + K_{H_2O} p_{H_2O} + K_{CO_2} p_{CO_2})^2} \quad (7.4)$$

where $-r_{CO}$ is the rate of carbon monoxide consumption ($mol \cdot min^{-1} \cdot g_{cat}^{-1}$), k is the rate constant, p_i is the partial pressure of the component i (i = CO, H_2O, H_2 and CO_2), K_e is the equilibrium constant and K_i is the adsorption constant for species i. The kinetic constants have been evaluated by Podolski and Kim (Podolski and Kim, 1974) with a 93 % iron and 7 % chromium catalyst:

$$k = \exp\left(-\frac{2456}{T} + 20.292\right) \ mol \cdot min^{-1} \cdot g_{cat}^{-1} \quad (7.5)$$

$$K_{CO} = \exp\left(\frac{1542}{T} - 3.392\right) \ atm^{-1} \quad (7.6)$$

$$K_{H_2O} = \exp\left(\frac{3128}{T} + 6.426\right) \ atm^{-1} \quad (7.7)$$

$$K_{CO_2} = \exp\left(\frac{6312}{T} - 9.285\right) \ atm^{-1} \quad (7.8)$$

The MR model is based on the following main assumptions: steady-state conditions, plug-flow, isothermal operation, ideal gas behavior, negligible pressure drops, negligible radial temperature and concentration profiles (one dimensional model – negligible concentration polarization).

Pressure drop is not of concern as it is typically negligible in the range of flow rates that are usual for the application of the reactor (Tosti et al., 2008). Besides, all other hypotheses are in principle valid for the dimensions of the set-up considered (i.e. for coupling to a 500 W PEM fuel cell).

The tubular membrane reactor is divided into finite volume elements where the composition of the gas, reaction rate and permeability towards hydrogen can be considered constant. Assuming as inlet boundary conditions for each volume the outlet values of the previous one, the mass balance for each component of the mixture is performed. The

computation of mass balances, both at the retentate and at the permeate side of the reactor, requires the evaluation of reaction rate and permeation rate. These, in turn, depend on the partial pressures of the gases in the reactor. Moreover, the permeation rate depends on the partial pressure of hydrogen at the permeate side of the reactor. Therefore, an iterative method of computation has been set up, as described elsewhere (Tosti et al., 2009). The calculation is iterated up to convergence (error $<1\times10^{-10}$ mol·s^{-1}).

Using the code, the molar flow rates of the gaseous species inside each permeator tube of the membrane reactor have been evaluated.

7.2.3 Preferential oxidation reactor

In the CR configuration, due to the WGS reaction equilibrium limitations, the LT-WGS reactor typically achieves a residual CO concentration in the order of $0.5-1.5$ dry vol.%. Thus, the preferential oxidation (PrOx) unit is used to bring down to ppm levels the CO concentration (cf. Figure 7.1). Supported noble metal catalysts are typically used to promote the reaction, in particular, platinum/alumina (Farrauto et al., 2003). The precious metals used are efficient, but only start to be active at about 170 ºC. Additionally, they are not active at low O_2/CO ratios because O_2 and CO compete for the same sites. Therefore, air is added in slight excess, and so is normal that a small amount of hydrogen is oxidized. In this reactor, the oxidation of CO using oxygen proceeds according with the following reaction:

$$CO + \frac{1}{2}O_2 \rightarrow CO_2, \quad \Delta H^{o}_{298K} = -283.2 \text{ kJ}\cdot\text{mol}^{-1} \tag{7.9}$$

As mentioned previously, the selectivity of the catalyst will typically not avoid the combustion of some hydrogen that is present in the gas stream through the following reaction:

$$H_2 + \frac{1}{2}O_2 \rightarrow H_2O, \quad \Delta H^{o}_{298K} = -241.0 \text{ kJ}\cdot\text{mol}^{-1} \tag{7.10}$$

In this study, the O_2 inlet flow is computed as a function of the CO flow rate assuming the requirement of two moles of O_2 per mole of CO (Francesconi et al., 2007). In the model, the CO oxidation is considered completed after reaching 10 ppm at the reactor's outlet. Since this combination of specifications cannot be solved directly, the Adjust operation of HYSYS was used to automatically conduct the trial-and-error iterations. The remaining O_2 reacts totally with hydrogen, which represents a selectivity (mol H_2 consumed per mol CO consumed) of nearly 3 (Francesconi et al., 2007). An adiabatic operation at a temperature of 200 ºC has been considered for the PrOx reactor (Ghenciu, 2002; Trimm and Onsan, 2001).

7.2.4 Polymer electrolyte membrane fuel cell stack

To investigate the performance of a PEMFC system, an equilibrium-based electrochemical model has been employed (Francesconi et al., 2007; Godat and Marechal, 2003). The basic expression for the voltage of a single cell is:

$$V_{\text{cell}} = E_{\text{Nernst}} + \eta_{\text{act, an}} + \eta_{\text{act, cat}} + \eta_{\text{ohmic}} \tag{7.11}$$

where E_{Nernst} is the thermodynamic potential, $\eta_{\text{act, an}}$ is the anode overvoltage, a measure of the voltage loss associated with the anode, $\eta_{\text{act, cat}}$ is the cathode overvoltage, a measure of the voltage loss associated with the cathode, and η_{ohmic} is the ohmic overvoltage, i.e. the internal losses associated with the proton conductivity of the electrolyte and electronic internal resistances. The three overvoltage terms are all negative in the above expression and represent reductions from E_{Nernst} to give the real cell voltage, V_{cell}. For simplification, the operating voltage was set at 0.5 V (Francesconi et al., 2007; Giunta et al., 2007; Song et al., 2005).

The current, I_{cell}, is related with the hydrogen molar flow rate that is consumed at the anode:

$$I_{\text{cell}} = 2F(f^{\text{in}}_{\text{H}_2,\text{ an}} - f^{\text{out}}_{\text{H}_2,\text{ an}}) \tag{7.12}$$

where F is the Faraday constant (96,500 C).

The actual electrical power generated by the cell (P_{cell}) can then be calculated from:

$$P_{cell} = V_{cell} I_{cell} \tag{7.13}$$

It is assumed that the cell operates with the inlet oxidant fed to the cathode humidified at a relative humidity of 80 %. The PEMFC is considered to be isothermal and isobaric. A pressure of 0.1 MPa and a fuel cell temperature of 70 ºC are assumed. The fuel utilization is considered to be 80 % (Francesconi et al., 2007) and the oxygen fed to the PEMFC is supplied with 30 % of excess concerning the inlet H_2.

7.2.5 Post-combustion unit

The addition of a burner reactor for converting the vented fuel from the PEMFC (cf. Figures 7.1 and 7.2) can improve the energy efficiency of the system by providing most of the heat needs (Benito et al., 2007). Therefore, in this study, the generated heat obtained in the post-combustion unit (operating at 1000 ºC and 0.1 MPa) is used to balance the energy requirement of the overall fuel processing system. Supplementary firing of ethanol is considered if the energy content of the vented fuel is not sufficient to close the energetic balance. Some assumptions were made:

– the combustion is complete and

– stoichiometric combustion has been considered according with the following reaction:

$$C_2H_5OH + 3O_2 \rightarrow 2CO_2 + 3H_2O, \quad \Delta H^o_{298K} = -1275.56\ kJ \cdot mol^{-1} \tag{7.14}$$

Finally, concerning the heat exchange, the steam reforming unit is the only reactor which consumes energy due to the endothermic characteristic of the reaction set. There is also energy consumption for heating the feed and the evaporation of the additional ethanol that is fired, prior to entering the reactors, and for auxiliary equipment such as pumps and compressors (cf. Figures 7.1 and 7.2).

7.2.6 Definition of the fuel cell system efficiency

Concerning the evaluation of the overall efficiency of the integrated systems, an expression was formulated where the energy output obtained by the PEMFC is divided by the heating value (HV) of the ethanol consumed in the fuel processor for reforming ($n_{EtOH}^{reformer}$) and burning unit (n_{EtOH}^{burner}):

$$\eta_{PEMFC\ system} = \frac{P_{cell}}{(n_{EtOH}^{reformer} + n_{EtOH}^{burner})\,HV} \tag{7.15}$$

The higher heating value (HHV) was used as the HV factor, representing the amount of heat produced by the complete combustion of the fuel (initial and final states at standard conditions). The value of 1300 $kJ \cdot mol^{-1}$ was then considered.

7.3 Results and Discussion

The two integrated process models have been used to determine the effect of the most relevant operating conditions. The influence of the water-to-ethanol molar ratio, reforming and membrane reactor temperature, reaction pressure and sweep-gas were studied in terms of ethanol fuel processor performance as well as in terms of overall energy efficiency.

7.3.1 Influence of the water-to-ethanol molar ratio and reaction pressure

In this section, the effects of the water-to-ethanol feed molar ratio (H_2O/EtOH) and reaction pressure ($P_{reaction}$) are investigated. Figure 7.3 presents the reactors' yields and the total yield of the integrated ethanol fuel processor for the conventional and membrane-based configuration systems. These yields are computed as the ratio of moles of hydrogen produced per mole of ethanol incoming to the reformer (Y_{H_2}).

In this study, the performance in terms of the total H_2 yield for both ethanol fuel processor configurations is favored for higher H_2O/EtOH ratios (Figure 7.3). Due to the

water excess, the thermodynamic equilibrium conversion of the ethanol reforming reaction enhances the H_2 production and penalizes the CO concentration at the outlet stream of the unit (cf. Equations 7.1 and 7.2); therefore, in both processors, the WGS step produces less hydrogen. Moreover, in the WGS membrane reactor the hydrogen yield significantly decreases with the feed molar ratio. In fact, an excess of water reduces the hydrogen partial pressure and inherently the H_2 recovery, decreasing the CO shift effect. In a conventional ethanol fuel processor, due to the lower CO formation at the reformer section, the performance of the PrOx reactor improves, consuming less H_2.

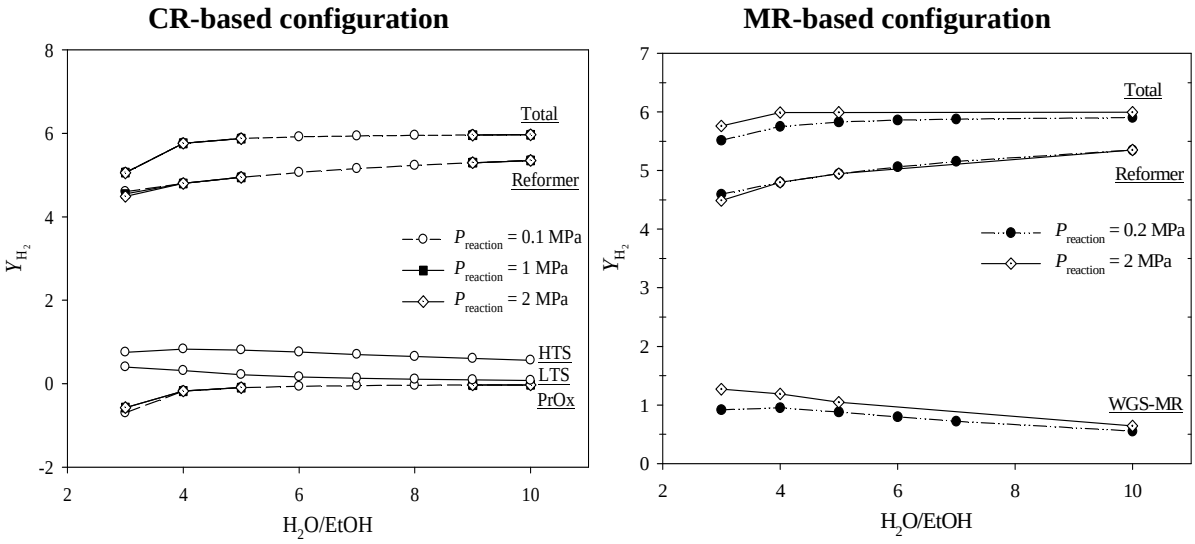

Figure 7.3 – Reactors yields vs. water-to-ethanol molar ratio at different reaction pressures ($T_{reformer}$ = 700 ºC and T_{MR} = 360 ºC).

The total H_2 yields attained in both fuel processor configurations are very similar at high H_2O/EtOH values (Figure 7.3). However, a slight difference is noted in the conventional processor, particularly at the lowest H_2O/EtOH value, where a higher amount of H_2 is consumed during the oxidation of CO at the PrOx unit.

In both configurations, the largest contribution to the H_2 yield is, as expected, due to the reformer. Nevertheless, the WGS reactor(s) contribution cannot be neglected, accounting up

to 28 % (for $H_2O/EtOH = 3$ and $P_{reaction} = 0.1$ MPa) in the conventional unit and up to 22 % (for $H_2O/EtOH = 3$ and $P_{reaction} = 2$ MPa) in the MR-based one.

The reaction pressure has distinct effects in both fuel processors, as shown also in Figure 7.3. In the case of the conventional one, the total H_2 yield is almost insensitive to the pressure variation in the range studied $(0.1-2$ MPa$)$. This is related with the fact that the ethanol decomposition achieves 100% conversion for $H_2O/EtOH > 4$, whatever is the reaction pressure. For $H_2O/EtOH < 4$ there is an increasing slight negative influence of the pressure, as predicted from the *Le Chatelier's principle* (because there is an increase in the total number of moles – cf. Equation 7.1). On the other hand, the overall performance of the membrane-based fuel processor increases with the reaction pressure. Since the pressure gradient across the membrane increases, the H_2 permeation through the membrane is favored, shifting the WGS reaction equilibrium towards additional formation of H_2.

Figure 7.4 presents the energy demand of the reforming reactor, feed heater and ethanol evaporator of each integrated system versus the water-to-ethanol molar ratio at a constant reforming temperature and reaction pressure ($T_{reformer} = 700$ ºC and $P_{reaction} = 2$ MPa). The energy demand evaluation of a MR-based system should be performed at conditions of high hydrogen recovery.

Despite the high H_2 yields obtained for both fuel processors for $H_2O/EtOH > 4$ – Figure 7.3, the higher water feed flow rate demands extra energy for feed heating and vaporizing, Figure 7.4. Therefore, additional ethanol should be furnished to the system, decreasing the energy efficiency, as described later on. The maximum energy demand is, however, located at the minimum water-to-ethanol molar ratio due to the high energy consumptions in the reformer unit. In opposition, at these conditions the energy efficiency is maximized since the amount of H_2 supplied to the PEMFC becomes higher.

Comparing both system configurations, it is worth mentioning that when increasing the reactants molar ratio the MR-based configuration system shows a lower overall energy

demand (cf. Figure 7.4). This fact is justified by the lower H_2 recovery in the MR that follows the increase on the H_2O/EtOH; by increasing the water-to-ethanol molar ratio the enthalpy content of the stream exiting the burner is therefore higher, favoring this way the heat exchanger performance.

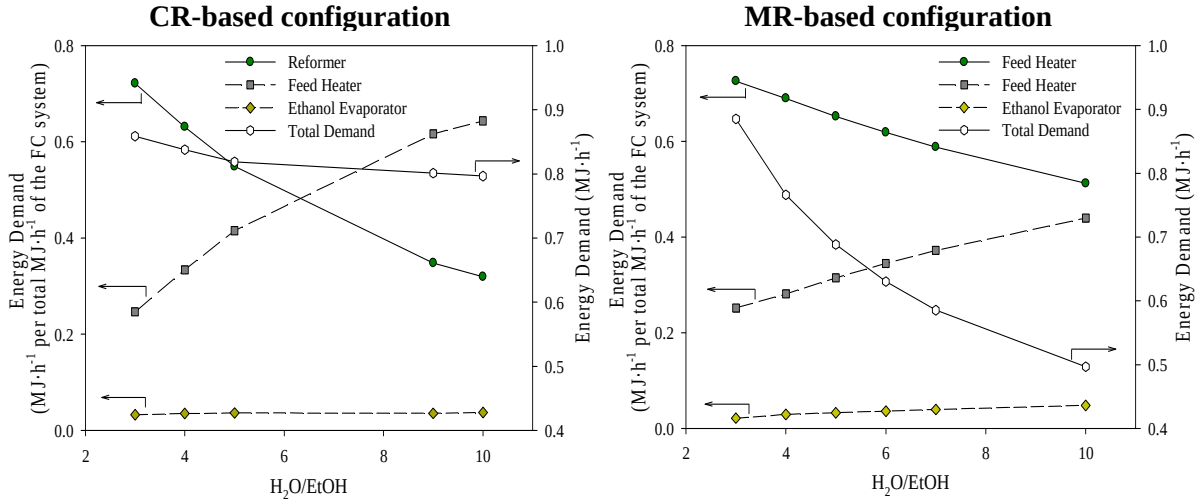

Figure 7.4 – The effect of the water-to-ethanol feed molar ratio (H_2O/EtOH) on the energy demand of the system ($P_{reaction}$ = 2 MPa, $T_{reformer}$ = 700 ºC and T_{MR} = 360 ºC).

In Figure 7.5, a 3D surface is presented where the global efficiency of the system based on the HHV is shown. The energy efficiency is presented as a function of the water-to-ethanol molar ratio and reaction pressure. Comparing both configurations, it can be seen that only a minor increase on the energy efficiencies can be obtained in the membrane-based configuration system. Particularly, at a reformer temperature of 700 ºC, a maximum efficiency of 29.1 % is achieved at H_2O/EtOH = 3 and $P_{reaction}$ = 2 MPa and of 27.3 % at H_2O/EtOH = 4 and $P_{reaction}$ = 0.1 MPa for the MR- and CR-based configurations, respectively (cf. Figure 7.5).

In the work by Benito et al. (Benito et al., 2007), a conventional bio-ethanol processor-PEMFC system, with heat integration, was proposed and evaluated. A similar theoretical energy efficiency to the one reported here was obtained by those authors. Higher energy efficiency values for CR configurations can be, however, found in the literature. For

example, Francesconi et al. (Francesconi et al., 2007), Godat and Marechal (Godat and Marechal, 2003) and Perna (Perna, 2007) obtained maximum energy efficiencies of around 36 %, 46 % and 43 %, respectively. The difference of such values compared with the ones obtained here, for the CR system, is related with the different operating conditions and fuel cell system modeled (e.g. fuel utilization factor, fuel cell temperature and pressure and real cell voltage). Moreover, also different heat exchange networks were considered, which leads to different efficiencies of the FC systems configuration.

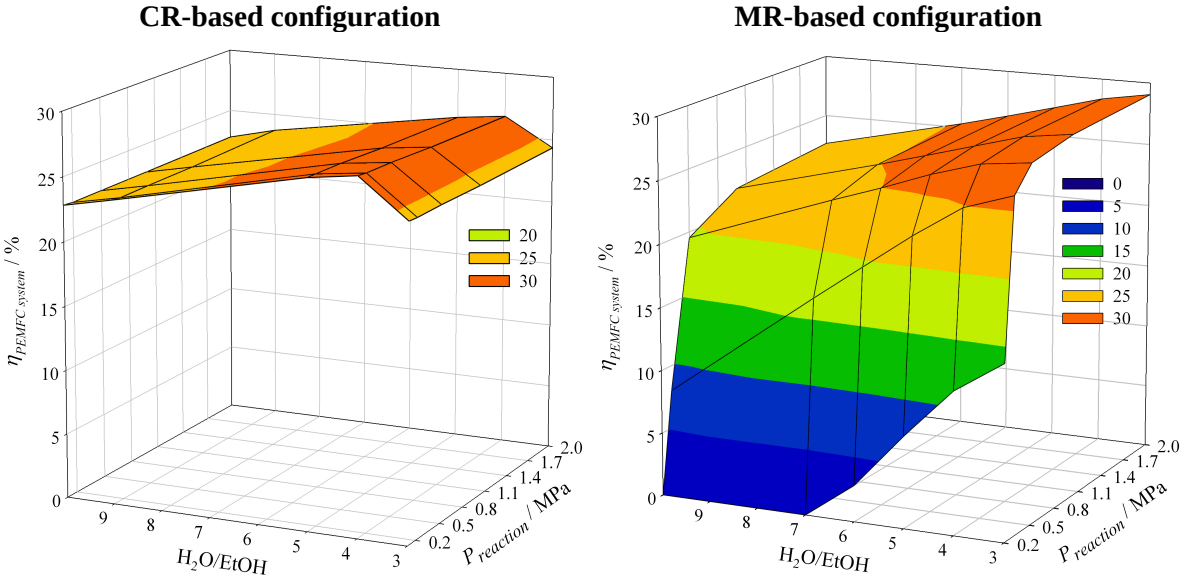

Figure 7.5 – Effect of the water-to-ethanol molar ratio and reaction pressure on the overall energy efficiency ($T_{reformer}$ = 700 ºC and T_{MR} = 360 ºC).

From Figure 7.5 it is also possible to conclude that the membrane-based configuration is more affected by the operating conditions used than the conventional one. In fact, H_2O/EtOH = 3 favors the MR-based system where a higher H_2 partial pressure is obtained at the outlet stream of the reformer. Therefore, a higher H_2 recovery is obtained at the permeate stream of the MR, which leads to an increase of the power output. However, when changing the other parameter, i.e. the reaction pressure, one can see that it might have a tremendous effect on the energy efficiency of the MR-based unit (cf. Figure 7.5). In the MR-based system, since the H_2 permeation flux depends on the H_2 partial pressure gradient across the membrane, it is

expected that the increase of the reaction pressure favors the fuel cell output power and synergistically the energy efficiency of the system. In limiting cases, i.e., when the reaction pressure tends to be very low but the water-to-ethanol molar ratio is simultaneously high ($H_2O/EtOH \geq 7$), null efficiencies are obtained. On the other hand, the effect of the reaction pressure on the CR-based system is almost negligible, while the influence of $H_2O/EtOH$ is a bit more notorious. The optimum in the energy efficiency for $H_2O/EtOH \approx 4$ results from the combination of two facts: by decreasing $H_2O/EtOH$, higher amounts of hydrogen are obtained (because the equilibrium conversion effect is almost negligible), however for low $H_2O/EtOH$ values a more significant consumption of hydrogen occurs in the PrOx unit.

At lower water-to-ethanol molar ratio values, especially for $H_2O/EtOH < 3$, there is the formation of coke over the steam reforming catalyst. Coke can "destroy" the catalyst structure and occupy the catalyst surface, reducing the catalyst activity; besides, the H_2 yield of the process becomes severely reduced due to the formation of by-products. So, higher water-to-ethanol molar ratios are frequently employed in practice to reduce the rate of carbon deposition and favor the H_2 production. Even at a H_2O/C_2H_5OH molar ratio of 5, the MR-based system shows an energy efficiency that is very close to the CR configuration, when operated at a relatively high reaction pressure – Figure 7.5. The reaction pressure is certainly an important design variable of the MR-based system, although above 0.5 MPa the energy efficiency increases only marginally.

It is worth noting that the optimal water-to-ethanol molar ratio and reaction pressure, considering the reformer alone and the total H_2 yields achieved for each fuel processor configuration (Figure 7.3), does not agree with the best operating conditions from the point of view of a global efficiency analysis (cf. Figures 7.4 and 7.5). This fact indicates the importance of optimizing integrated systems rather than optimizing process units separately for different objective functions, as also indicated by Francesconi et al. (Francesconi et al., 2007).

Up to now, the MR-based system configuration revealed to be promising in terms of both performance and efficiency for the range of conditions studied when compared with the conventional process. Despite the advantages of using the MR-based process, a decisive selection between both systems should be made on the basis of an economic balance considering the investment, capital and operation costs involved in each one. The membrane reactor is probably the most expensive piece of equipment because it uses 50-μm thick palladium-based membranes. However, much thinner membranes are being developed and it is expected that a composite palladium membrane 1 μm tick costs only $50-100$ % more than the corresponding ceramic support.

In the following sections, the MR-based system will be studied in more detail in order to investigate the effects of some other operating conditions.

7.3.2 Influence of the reformer temperature

To reduce the operating costs and increase the energy efficiency of the FC system, a compromise should be made between the temperature and pressure at the reformer unit; this should take into account the H_2 yields obtained by the fuel processor and the temperature limit at which coke formation is negligible.

The effect of the reforming temperature on the MR-based configuration is analyzed in this section considering $H_2O/EtOH = 3$. The plot of the H_2 yield in the fuel processor (Figure 7.6) shows that increasing the temperature, the total hydrogen production is favored, which is in opposition to the performance behavior of the reformer unit. The ethanol steam reforming is an equilibrium-limited reaction. Due to its endothermicity, temperature has a positive effect on the ethanol conversion. In the range of temperatures considered, the H_2 yield in the reformer unit is, however, negatively affected. This happens because the equilibrium conversion of reaction 7.1 (which is close to completion) is less affected by this variable than the equilibrium conversion of reaction 7.2. In particular, the equilibrium conversion for the

ethanol decomposition increases from 98.39 % (H_2O/EtOH = 3, $P_{reaction}$ = 0.2 MPa and $T_{reformer}$ = 500 ºC) to 99.85 % (H_2O/EtOH = 3, $P_{reaction}$ = 0.2 MPa and $T_{reformer}$ = 900 ºC). For the RWGS reaction, the conversion increases from 49.58 % to 80.56 %, in the same temperature range (and equal conditions). This way, the effect on the RWGS overcomes the 6 mol of H_2 produced for each mol of ethanol consumed through reaction 7.1. Since the CO content is increased by the effect of $T_{reformer}$, the H_2 production of the fuel processor is then mainly favored via the WGS reaction (cf. Figure 7.6).

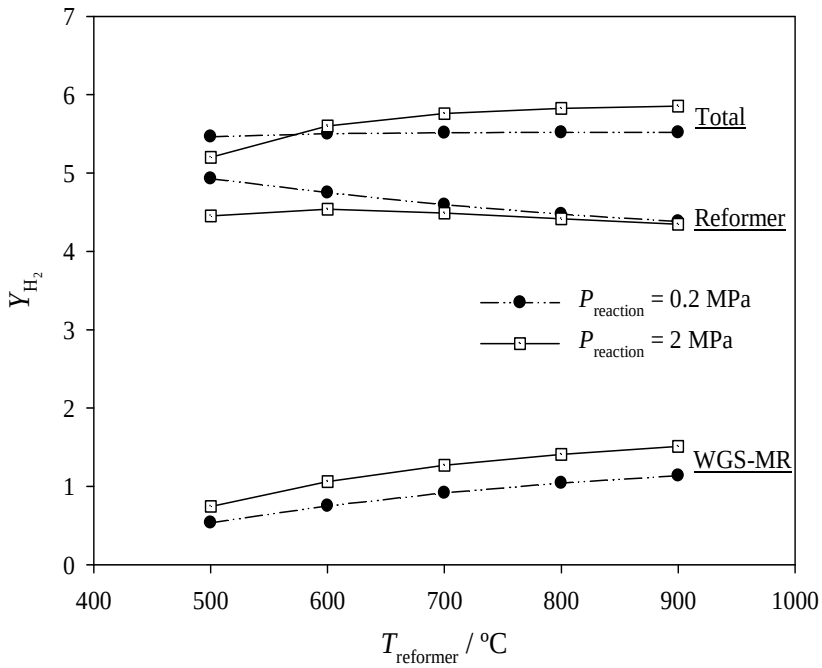

Figure 7.6 – Reactors yields vs. temperature of the reformer at different reaction pressures for the MR-based process (H_2O/EtOH = 3 and T_{MR} = 360 ºC).

Globally, the H_2 production of the fuel processor is favored by the reformer temperature. This fact is more evident at higher reaction pressures, where the H_2 recovery and CO shift is higher. At lower pressures (e.g. 0.2 MPa in Figure 7.6), the positive effect reached in the WGS-MR is offset by the negative effect in the reformer, being the overall H_2 yield nearly independent of the reformer temperature.

In Figure 7.7, the energy efficiency of the MR system is shown as a function of the water-to-ethanol ratio and reforming temperature at 2.0 MPa (high H_2 recovery conditions).

Higher energy efficiencies are obtained at lower reformer temperatures because of the smaller energy requirements in the reactor and evaporation. A maximum efficiency of $\eta_{PEMFC\ system}$ = 30.2 % occurs at the minimum temperature (500 ºC) of the reformer considered in this study. Additionally, at these conditions, no supplementary firing of ethanol is necessary.

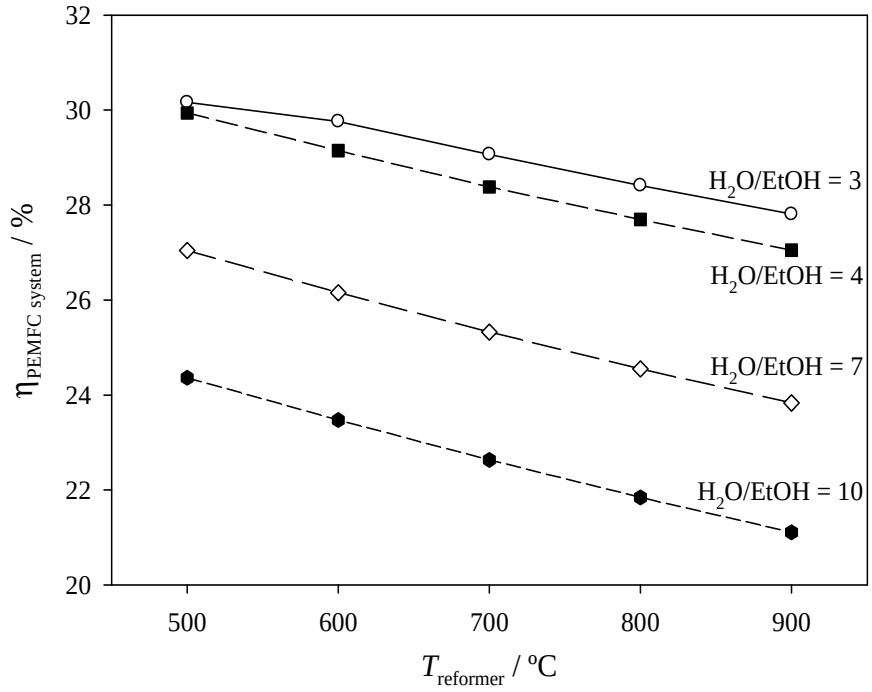

Figure 7.7 – The effect of the water-to-ethanol feed molar ratio and reformer temperature on the energy efficiency of the fuel cell system for the MR-based configuration ($P_{reaction}$ = 2 MPa and T_{MR} = 360 ºC).

Ethanol steam reforming operation at 500 ºC or below is experimentally described in the literature as a promising choice for fuel cell applications. The effect of H_2O/EtOH in the energetic efficiency is similar to that reported in Figure 7.5 (i.e. the smaller the water-to-methanol ratio, the higher the efficiency because more H_2 is produced).

7.3.3 Influence of the WGS MR temperature

In this section, the reactor's performance and the global energy efficiency of the system are studied as a function of the WGS MR temperature.

The hydrogen diffusion through palladium occurs via a solution/diffusion mechanism, which is frequently described as follows (Dittmeyer et al., 2001):

$$J = \frac{\Phi}{\delta}(p_1^n - p_2^n) \tag{7.16}$$

where J is the hydrogen permeation flux ($mol \cdot m^{-2} \cdot s^{-1}$), Φ is the hydrogen permeability ($mol \cdot m \cdot m^{-2} \cdot s^{-1} \cdot Pa^{-n}$), δ is the metal wall thickness (m), n is a model constant (n = 0.5 assuming *Sieverts' law*), and p_1 and p_2 (Pa) are the hydrogen partial pressures upstream and downstream, respectively (i.e. in the lumen and permeate sides, respectively). Moreover, the hydrogen transport through the dense palladium-based membrane is an activated process. Assuming that the permeability follows the *Arrhenius' law*, it can be written:

$$\Phi = \Phi_o \exp(-E/\Re T) \tag{7.17}$$

where Φ_o is the pre-exponential factor ($mol \cdot m \cdot m^{-2} \cdot s^{-1} \cdot Pa^{-0.5}$), E is the activation energy ($J \cdot mol^{-1}$), $\Re$ is the gas constant and T (K) is the absolute temperature. The hydrogen permeability parameters of the Pd-Ag (23 wt.% Ag) alloy have been obtained from the literature (Tosti et al., 2009):

$\Phi_o = 7.730 \times 10^{-8}$ $mol \cdot m \cdot m^{-2} \cdot s^{-1} \cdot Pa^{-0.5}$;

$E = 6.601 \times 10^{3}$ $J \cdot mol^{-1}$.

The hydrogen permeation is then expected to increase with the temperature and transmembrane hydrogen partial pressure difference. Therefore, it is important to evaluate the influence of these variables on the global performance of the MR-based system.

In Figures 7.8 and 7.9, the effect of the WGS MR temperature and reaction pressure on the global H_2 yield, CO conversion, H_2 recovery and energy efficiency are shown; a H_2O/EtOH = 3 and a $T_{reformer}$ = 700 ºC were considered.

Figure 7.8a shows that increasing the temperature of the WGS-MR, the hydrogen total yield of the fuel processor has a maximum value at 360 ºC, within the pressure range presented in this study (although more easily noticed in the figure at $P_{reaction}$ = 0.2 MPa). This result is explained by the combined effect that the CO conversion and the H_2 recovery attained in the WGS-MR have with the temperature (see Figure 7.8b). In other words, due to the exothermicity of the WGS reaction, temperature negatively affects the thermodynamic CO conversion level based in the feed conditions. However, the shift effect is enhanced by the increase of the H_2 recovery, which is favored by the temperature (see equation 7.17). Therefore, an optimal temperature of the WGS MR can be obtained in order to achieve the maximum CO conversion and inherently the global H_2 yield.

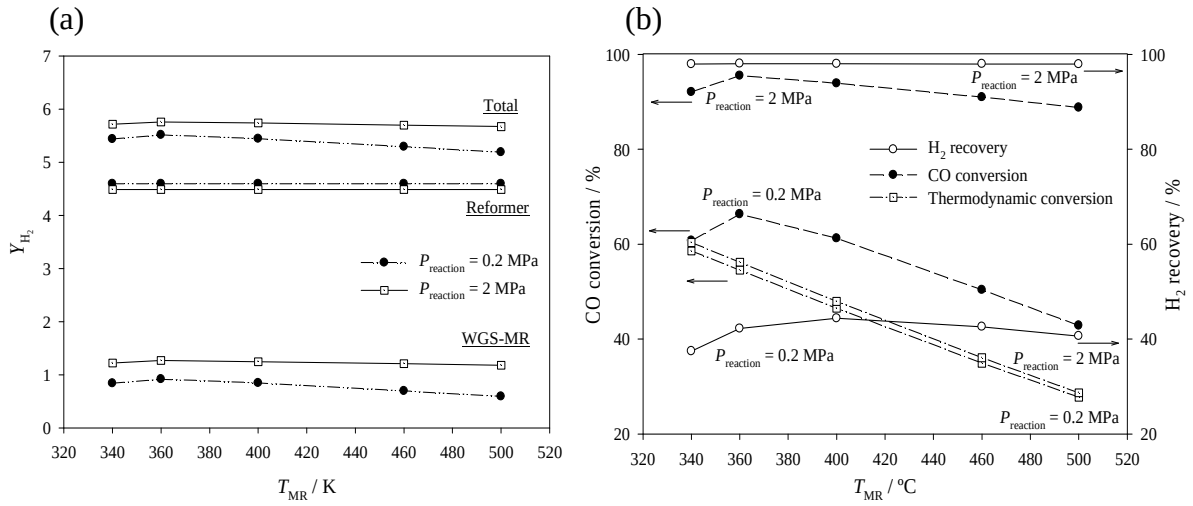

Figure 7.8 – The influence of the WGS-MR temperature on a) the H_2 yield and b) CO conversion and H_2 recovery at different pressures ($T_{reformer}$ = 700 ºC, H_2O/EtOH = 3).

The relationship between the catalyst activity and the membrane permeation is quite important on the optimization of the membrane reactor. Despite the work performed being related to a functional model under development at ENEA, the optimization of the reactor area/volume aspect ratio can be done using the *Damköler–Permeation (DaPe) numbe*r (Battersby et al., 2006). The membrane is needed to permeate hydrogen produced from CO conversion, which reaction takes place in the fixed bed delimited by the membrane walls.

Figure 7.8b plots CO conversion and recovered hydrogen as a function of the MR temperature. From this figure it can be seen that most of the produced hydrogen is recovered, indicating that the reactor aspect ratio is adequate.

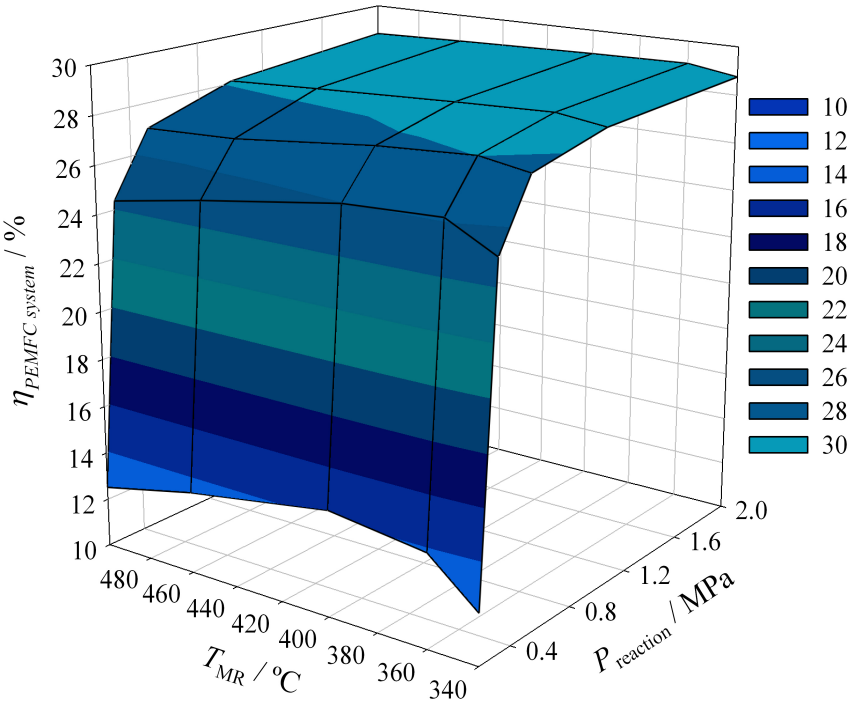

Figure 7.9 – The effect of the reaction pressure and temperature of the MR on the energy efficiency of the fuel cell system ($T_{reformer}$ = 700 ºC, H_2O/EtOH = 3).

From Figure 7.8b, it can be seen that the total CO conversion was not achieved for the WGS MR module and operating conditions simulated. In other words, a retentate stream containing mainly CO_2, some steam, non-recovered hydrogen and the non-converted CO (Table 7.2) is obtained. This indicates that improvements should be made in the membrane module (e.g. higher permeation area and/or lower membrane thickness) and/or in the process conditions (e.g. using a higher reaction pressure) to improve the H_2 recovery and the remaining CO consumption.

The WGS MR shows higher energy efficiencies for 360 ºC, where the H_2 production is favored, and for reaction pressures above 0.5 MPa (Figure 7.9). A compromise should then

exist between the WGS MR temperature and the lumen (retentate) side pressure, in order to achieve higher performances and global energy efficiencies.

7.3.4 Influence of the sweep gas and MR configuration

Up to this point, we assumed that the WGS MR operates without sweep gas in the permeate side, which was settled as ambient pressure. Despite the higher simplicity of the process in terms of final H_2 purification and cost, these are very limiting conditions for the H_2 recovery and yield. This limitation can be overcome by applying vacuum to the permeate side or by feeding a sweep gas to the permeate chamber (shell side) of the membrane module.

In a previous work by Tosti et al. (Tosti et al., 2009), the authors concluded that the permeating hydrogen should be collected in the shell side using a sweep gas stream in counter-current mode for increasing the permeation driving force.

Using steam as sweep gas has the advantage of being usually available on-site and being easily separated from the permeated hydrogen; alternatively, the hydrogen humidified stream could be directly fed to the fuel cell (Hughes, 2001). Often, the higher the sweep gas flow rate, the greater the permeation rate. However, the vaporization of water is one of the most energy intensive operations in industry. Therefore, the flow rate of water sweep gas should be studied not only in terms of the H_2 recovery achieved in the MR, but also in terms of the energy efficiency of the system.

Taking this into consideration, Figure 7.10 shows the effect of the sweep gas molar ratio (ratio of the steam sweep flow rate to the ethanol flow rate incoming into the reformer unit) over the energy efficiency of system, at different retentate pressures. The role of the steam sweep-gas molar ratio on the energy efficiency of the system clearly depends on the pressure of the WGS MR retentate/reaction side. At low reaction pressures, where the pressure gradient across the membrane is low and inherently the H_2 recovery, higher energy

efficiencies are in principle favored by the usage of a higher steam sweep molar ratio. However, once attained the maximum energy efficiency, the increase of the sweep molar ratio, despite the enhancement of the H_2 recovery, is no longer advantageous (cf. Figure 7.10). Extra energy is then necessary to vaporize the sweep gas water, decreasing the energy efficiency of the system. When operating at higher reaction pressures, a lower amount of sweep-gas is needed to achieve higher energy efficiency.

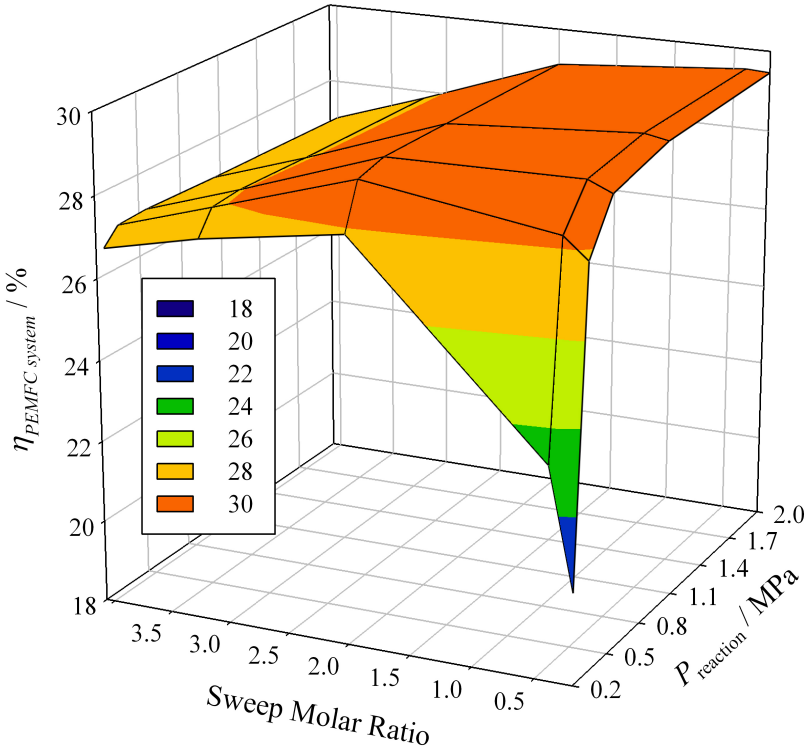

Figure 7.10 – The effect of the steam sweep gas molar ratio and reaction pressure on the global energy efficiency. Operating conditions are: the steam sweep gas is fed in counter-current mode and $T_{reformer}$ = 700 ºC, H_2O/EtOH = 3 and T_{MR} = 360 ºC.

At this point it is interesting to analyze the improvements obtained using the steam sweep gas compared with no sweep gas. In Figure 7.11 it is compared the performance of the WGS-based system operating with and without sweep gas, in terms of global H_2 yield and energy efficiency, both in a normalized way. Operating at low pressures, some improvements on the global performance are possible to obtain using a WGS MR operating with sweep gas. In particular, the energy efficiency can achieve twice as much the one with

no sweep gas. These differences vanish if higher reaction pressures are used. In fact, at $P_{reaction}$ = 2 MPa the H_2 yields in both systems are similar. On the other hand, at $P_{reaction}$ = 2 MPa the usage of sweep gas at relatively high sweep molar ratios results in a lower energy efficiency (cf. Figure 7.11).

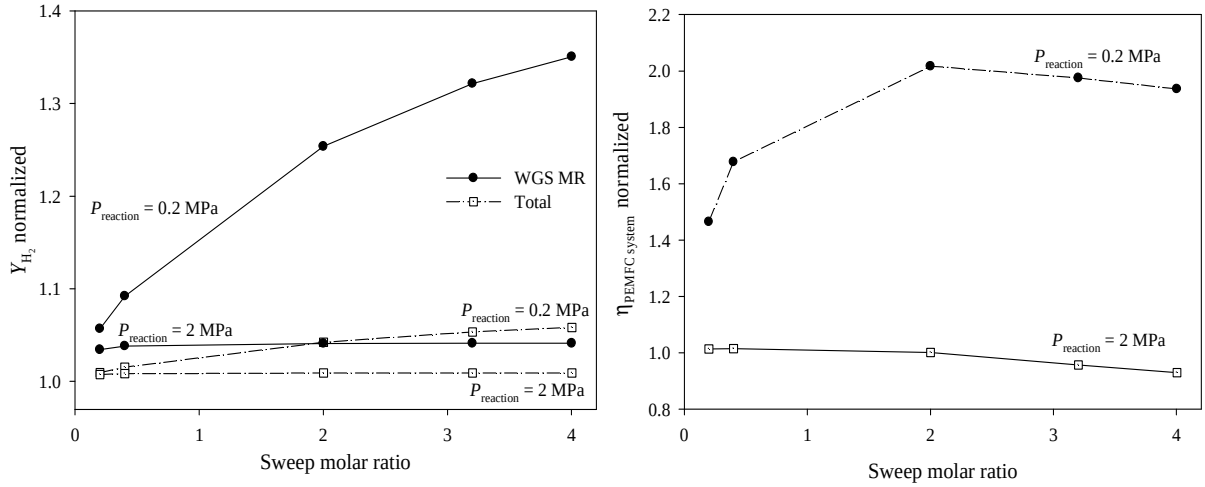

Figure 7.11 – Comparison of WGS-MR system performance operating with and without steam sweep gas in terms of the reactor's yield and global energy efficiency. Variables are normalized by the performance of the system without sweep gas. Other conditions are: $T_{reformer}$ = 700 ºC, H_2O/EtOH = 3 and T_{MR} = 360 ºC.

7.4 Conclusions

A PEMFC/fuel processor stationary system fed with ethanol has been simulated using HYSYS process simulator. The conventional configuration of a fuel processor was compared with a configuration using a WGS Pd-Ag membrane reactor, in terms of hydrogen yield and energy efficiency. The influence of several variables was simulated and discussed, showing the importance of analyzing the integrated systems.

Comparing both configurations, it was found that similar energy efficiencies can be obtained if the membrane-based system runs under conditions that favor high H_2 recovery. This can be achieved operating at elevated reaction pressure with no sweep gas or,

alternatively, with low lumen (retentate) pressure but with steam sweep in counter-current mode.

In the membrane reactor configuration, a maximum efficiency of 30.2 % is attained at the minimum temperature of the reformer considered in this study (500 ºC). The membrane reactor should operate at an optimum temperature of 360 ºC in order to attain a compromise between maximum CO conversion and H_2 recovery, thus improving the H_2 yield of the processor and the energy efficiency of the system.

The results obtained show that the usage of water vapor as sweep gas improves the H_2 yield of the processor in a large range of operating conditions. In terms of energy efficiency of the system, this still holds for low pressures ($P_{reaction} < 0.5$ MPa), but the improvements are marginal and restricted to a narrower range of conditions at high pressures.

Finally, it was shown that the MR-based fuel cell system is more suitable than the CR one for producing hydrogen under the operating conditions used in this study. The MR-based fuel cell system is simpler than the CR one and shows slightly higher energy efficiencies. Besides, with such a configuration the reduction in system complexity (along with synergetic effects) can be achieved, moving into the logic of the process intensification strategy.

7.5 Nomenclature and Acronyms

CR	conventional reactor
E	permeability activation energy [J·mol^{-1}]
E_{Nernst}	thermodynamic potential [V]
F	Faraday's constant [= 96 500 C]
FC	fuel cell
$f_{H_2,a}^{in}$	hydrogen molar flow rate entering the anode [mol·h]
$f_{H_2,a}^{out}$	hydrogen molar flow rate exiting the anode [mol·h]
F_m	total mass flow rate in a given stream [g·h^{-1}]

HHV	high heating value [$MJ \cdot kg^{-1}$]
HT-WGS	high temperature water gas shift
I_{cell}	current of the fuel cell stack [A]
J	hydrogen molar flux across the Pd-Ag membrane [$mol \cdot m^{-2} \cdot s^{-1}$]
k	rate constant ($mol \cdot min^{-1} \cdot g_{cat}^{-1}$)
K_e	equilibrium constant
K_i	adsorption constant for species i (i = CO, H_2O, H_2, CO_2) [atm^{-1}]
LT-WGS	low temperature water gas shift
MR	membrane reactor
n	pressure exponent constant
$n_{EtOH}^{reformer}$	ethanol molar flow rate consumed in the reformer [$mol \cdot h^{-1}$]
n_{EtOH}^{burner}	ethanol molar flow rate consumed in the burner [$mol \cdot h^{-1}$]
P_{cell}	power of the fuel cell stack [W]
p_i	partial pressure of component i (i = CO, H_2O, H_2 and CO_2)
PEMFC	polymer electrolyte membrane fuel cell
$P_{reaction}$	reaction pressure (in the MR it refers to the lumen pressure) [MPa]
PrOx	preferential oxidation
p_1	hydrogen partial pressure at the retentate side of the Pd-Ag membrane reactor [MPa]
p_2	hydrogen partial pressure at the permeate side of the Pd-Ag membrane reactor [MPa]
H_2O/EtOH	water-to-ethanol feed molar ratio
$\Re$	ideal gas constant [= 8.314 $J \cdot mol^{-1} \cdot K^{-1}$]
$-r_{CO}$	rate of reaction regarding carbon monoxide consumption ($mol \cdot min^{-1} \cdot g_{cat}^{-1}$)
SR	steam reformer
T	absolute temperature [K]
T_{MR}	temperature of the Membrane Reactor unit [K or ºC]

$T_{reformer}$	temperature of the Reformer unit [K or ºC]
WGS	water-gas shift
V_{cell}	fuel cell voltage [V]
$\eta_{act,an}$	anode overvoltage [V]
$\eta_{act,\ cat}$	cathode overvoltage [V]
η_{ohmic}	ohmic overvoltage [V]
x_i	molar fraction of component *i* (*i* = CO, H_2O, H_2 and CO_2)
Y_{H_2}	hydrogen yield (ratio of moles of hydrogen produced per mole of ethanol incoming to the reformer)
$\eta_{PEMFC\ system}$	energy efficiency of the integrated system
δ	Pd-Ag membrane thickness [m]
Φ	hydrogen permeability [$mol \cdot m \cdot m^{-2} \cdot s^{-1} \cdot Pa^{-0.5}$]
Φ_0	permeability pre-exponential factor [$mol \cdot m \cdot m^{-2} \cdot s^{-1} \cdot Pa^{-0.5}$]

7.6 References

Battersby, S., Teixeira, P.W., Beltramini, J., Duke, M.C., Rudolph, V., da Costa, J.C.D., An analysis of the Peclet and Damkohler numbers for dehydrogenation reactions using molecular sieve silica (MSS) membrane reactors. *Catal. Today* **2006**, 116 (1), 12-17.

Benito, M., Padilla, R., Sanz, J.L., Daza, L., Thermodynamic analysis and performance of a 1 kW bioethanol processor for a PEMFC operation. *J. Power Sources* **2007**, 169 (1), 123-130.

Bernardo, P., Barbieri, G., Drioli, E., An exergetic analysis of membrane unit operations integrated in the ethylene production cycle. *Chem. Eng. Res. Des.* **2006**, 84 (A5), 405-411.

Deluga, D.A., Salge, J.R., Schmidt, L.D., Verykios, X.E., Renewable hydrogen from ethanol by autothermal reforming. *Science* **2004**, 303 (5660), 993-997.

Dittmeyer, R., Hollein, V., Daub, K., Membrane reactors for hydrogenation and dehydrogenation processes based on supported palladium. *J. Mol. Catal. A: Chem.* **2001**, 173 (1-2), 135-184.

Farrauto, R., Hwang, S., Shore, L., Ruettinger, W., Lampert, J., Giroux, T., Liu, Y., Ilinich, O., New material needs for hydrocarbon fuel processing: Generating hydrogen for the PEM fuel cell. *Annu. Rev. Mater. Res.* **2003**, 33, 1-27.

Francesconi, J.A., Mussati, M.C., Mato, R.O., Aguirre, P.A., Analysis of the energy efficiency of an integrated ethanol processor for PEM fuel cell systems. *J. Power Sources* **2007**, 167 (1), 151-161.

Ghenciu, A.F., Review of fuel processing catalysts for hydrogen production in PEM fuel cell systems. *Curr. Opin. Solid State Mater. Sci.* **2002**, 6 (5), 389-399.

Giunta, P., Mosquera, C., Amadeo, N., Laborde, M., Simulation of a hydrogen production and purification system for a PEM fuel-cell using bioethanol as raw material. *J. Power Sources* **2007**, 164 (1), 336-343.

Godat, J., Marechal, F., Optimization of a fuel cell system using process integration techniques. *J. Power Sources* **2003**, 118 (1-2), 411-423.

Hughes, R., Composite palladium membranes for catalytic membrane reactors *Membr. Technol.* **2001**, (131), 9-13.

HYSYS, 2003. Process Simulator Version 3.2. Hyprotech Ltd., Calgary, Canada.

Ioannides, T., Thermodynamic analysis of ethanol processors for fuel cell applications. *J. Power Sources* **2001**, 92 (1-2), 17-25.

Liguras, D.K., Kondarides, D.I., Verykios, X.E., Production of hydrogen for fuel cells by steam reforming of ethanol over supported noble metal catalysts. *Appl. Catal., B* **2003**, 43 (4), 345-354.

Mas, V., Kipreos, R., Amadeo, N., Laborde, M., Thermodynamic analysis of ethanol/water system with the stoichiometric method. *Int. J. Hydrogen Energy* **2006**, 31 (1), 21-28.

Moe, J.M., Design of water-gas shift reactors. *Chem. Eng. Prog.* **1962**, 58 (3), 33-36

Ni, M., Leung, D.Y.C., Leung, M.K.H., A review on reforming bio-ethanol for hydrogen production. *Int. J. Hydrogen Energy* **2007**, 32 (15), 3238-3247.

Perna, A., Hydrogen from ethanol: Theoretical optimization of a PEMFC system integrated with a steam reforming processor. *Int. J. Hydrogen Energy* **2007**, 32 (12), 1811-1819.

Podolski, W.F., Kim, Y.G., Modeling water-gas shift reaction. *Ind. Eng. Chem. Proc. Des. Dev.* **1974**, 13 (4), 415-421.

Semelsberger, T.A., Brown, L.F., Borup, R.L., Inbody, M.A., Equilibrium products from autothermal processes for generating hydrogen-rich fuel-cell feeds. *Int. J. Hydrogen Energy* **2004**, 29 (10), 1047-1064.

Song, S.Q., Douvartzides, S., Tsiakaras, P., Exergy analysis of an ethanol fuelled proton exchange membrane (PEM) fuel cell system for automobile applications. *J. Power Sources* **2005**, 145 (2), 502-514.

Thomas, J.M., Thomas, W.J., *Principles and practice of heterogeneous catalysis.* Wiley - VCH: Weinheim, Germany, 1997.

Tosti, S., Basile, A., Bettinali, L., Borgognoni, F., Gallucci, F., Rizzello, C., Design and process study of Pd membrane reactors. *Int. J. Hydrogen Energy* **2008**, 33 (19), 5098-5105.

Tosti, S., Borgognoni, F., Rizzello, C., Violante, V., Water gas shift reaction via Pd-based membranes. *Asia-Pac. J. Chem. Eng.* **2009**, 4 (3), 369-379.

Trimm, D.L., Onsan, Z.I., Onboard fuel conversion for hydrogen-fuel-cell-driven vehicles. *Catal. Rev.-Sci. Eng.* **2001**, 43 (1-2), 31-84.

Vaidya, P.D., Rodrigues, A.E., Insight into steam reforming of ethanol to produce hydrogen for fuel cells. *Chem. Eng. J.* **2006**, 117 (1), 39-49.

Chapter 8

Conclusions and Suggestions for Future Work

8.1 Concluding remarks

The thesis focused on the study of an efficient unit to produce ultra-pure hydrogen via the water-gas shift (WGS) reaction using a hybrid technology (reaction/separation) based on a packed-bed membrane reactor. Since the WGS reaction conversion is thermodynamically limited, the use of a packed-bed membrane reactor should allow to overcome the conversion limitations imposed by the reaction equilibrium in conventional reactors. In this sense, several topics were addressed from the fundamentals (mechanism and kinetics of the reaction), to the process development (catalyst screening, modeling and simulation) and its intensification (integration of a packed-bed reactor and a H_2-selective membrane).

It was first evaluated the catalytic performance of promising materials to carry out the WGS reaction in the low-temperature range. For this purpose, an experimental set-up was built at LEPAE able to measure the catalyst's activity in terms of CO conversion at temperatures up to 300 ºC in the presence of a simulated reformate feed. The same unit, with slight modifications was also employed for measuring the reaction kinetics and to evaluate

the performance of the Pd-Ag membrane/membrane reactor (i.e., for measuring the hydrogen selectivity and permeability or for carrying out the WGS reaction).

The first challenge was to find a catalyst more adequate for "on-board" fuel processor operations than the conventional WGS samples. In this sense, a nano-sized gold-based catalyst (Au/CeO_2) was prepared and characterized at ITQ (in Valencia, Spain) in order to compare its catalytic activity and stability, for the low-temperature WGS reaction, with tree commercial samples ($CuO/ZnO/Al_2O_3$, CuO/Al_2O_3 and Au/TiO_2). The prepared sample revealed to be the most active, in particular, in the temperature range of $150-200$ ºC. A comparison between gold-based catalysts shows that ceria is a promising support due to its enhanced redox properties. Among the cupper-based samples, it was observed that the presence of ZnO seems to improve the catalyst activity. It was also found that the presence of reaction products in the feed stream has a higher negative effect on CO conversion for Cu-based catalysts when compared with the gold-based ones, namely, at 150 °C. In this sense, the use of gold-based catalytic systems to conduct the WGS reaction on CO_2- or H_2-selective membranes might be promising. Additionally, it was observed that the CO concentration present in the reactor feed greatly affects the activity of all catalysts tested. Depending on the reaction temperature and how far the system operates from equilibrium, this effect can be negative or positive in terms of the catalyst's performance.

Concerning the activity/stability properties, the commercial $CuO/ZnO/Al_2O_3$ catalyst showed to be the best sample. At temperatures ≥ 250 °C Au/CeO_2 is clearly a better option since it is mostly not to be affected by the deactivation mechanism and shows a higher CO conversion than $CuO/ZnO/Al_2O_3$. However, at lower temperatures, the stability is a negative factor for its selection and the latter material shows to be a better option. The results of this study indicate that the catalyst selection for the WGS reaction has to take into account the operation temperature range. Due to the difficulties found reproducing active and stable

Au/CeO_2 samples, the commercial $CuO/ZnO/Al_2O_3$ catalyst was used throughout the ensuing work.

It was then studied the type of kinetics (and inherently of mechanism) that controls the WGS reaction over copper-based catalysts. Therefore, the kinetics of the WGS reaction over a commercial $CuO/ZnO/Al_2O_3$ catalyst was investigated using a simulated reformate gas mixture in the temperature range of $180-300\ ^oC$. Several kinetic models were proposed, which were subjected to a rigorous parameter estimation and model discrimination in order to find the most appropriate one. The Langmuir-Hinshelwood (LH) kinetic model based on surface reaction of molecularly adsorbed reactants and on the formation of a formate intermediate as rate-determining step showed good fit to experimental data. Further investigations using two different temperature regimes for parameters estimation, $180-200\ ^oC$ (lower-temperature) and $230-300\ ^oC$ (higher-temperature), revealed a better goodness of fit and thus support the existence of distinct rate-controlling mechanisms for these two ranges: associative/LH (lower-temperature) and redox (higher-temperature).

Finally, an isothermal plug-flow reactor model was used to simulate the packed-bed tubular reactor for the WGS reaction for validating the composed kinetic model. The reactor model was assessed against the measured CO conversion and satisfactory agreement was found between model predictions and experimental results (average absolute deviation of ca. 3.5 %).

Pd-Ag membranes are seen as good materials to selectively separate hydrogen from a gas mixture obtaining an ultra-pure hydrogen stream. However, difficulties exist regarding membrane stability, durability and achievement of total selectivity towards hydrogen. In this sense, at ENEA laboratories (in Frascati, Italy), Pd-Ag membranes were prepared by an innovative annealing and diffusion welding technique in order to separate and produce ultra-pure hydrogen. The combination of an active low-temperature $CuO/ZnO/Al_2O_3$ catalyst with

a high H_2 permeable and selective Pd-Ag self-supported membrane resulted in a WGS membrane reactor (MR) that exhibited significant improvements in comparison to analogous systems reported in literature. With this effective H_2 separation/production system, higher CO conversions were generally achieved at lower temperatures where the equilibrium conversion is favored. On other hand, the H_2 recovery was improved by increasing the operating temperature and/or applying a higher H_2 partial pressure difference between the retentate and permeate sides of the dense Pd-Ag membrane.

It is noteworthy that around 100 % of CO conversion and almost complete H_2 recovery were achieved operating the MR at 300 ºC with a GSHV (gas hourly space velocity) = 1200 $L_N \cdot kg_{cat}^{-1} \cdot h^{-1}$, a feed pressure of 4 bar, a permeate pressure of 3 bar and using 1 $L_N \cdot min^{-1}$ of sweep gas. The best operating mode to achieve a higher MR performance was using a sweep stream because it permits to use high feed pressures and, for sufficiently high sweep flowrates, the permeate hydrogen partial pressure can be made as low as needed. Since the Pd-Ag membrane prepared could not withstand high-pressure differences between retentate and permeate sides (above 2 bar), for improving the hydrogen permeation it was increased the feed pressure as well as the sweep gas pressure. This operating mode resulted in improved reaction rate and hydrogen recovery.

It was also found that changing the reactants concentration in the feed has opposite effects on the MR performance. While carbon monoxide conversion (and also hydrogen recovery) was improved by a higher water content, following the thermodynamic trend, the reverse effects were observed for higher CO concentrations in the feed (following the opposite thermodynamic trend). It was concluded that the Pd-Ag MR operates in kinetic regime, where the non-equilibrium conversions obtained depend not only on the thermodynamic conditions but also on the WGS reaction path.

Very few studies on WGS membrane reactors critically compare the proposed theoretical models with experimental results. Moreover, such comparisons are mostly based in terms of conversion enhancement and take into account data reported in the open literature concerning membrane properties and kinetic reaction rates, most of the times obtained for specific conditions. In this sense, a comprehensive phenomenological model was developed and validated with experimental results for a broad range of operation conditions, obtained in the Pd-Ag membrane reactor, packed with a $CuO/ZnO/Al_2O_3$ catalyst, and described in chapter 5. It is noteworthy that, apart from two fitting parameters (related with the decline of permeability due to the presence of CO in the reaction mixture), all other model parameters were determined from independent studies, described along this thesis (catalyst properties, kinetic parameters, hydrogen permeation rate equation, etc.). The model was validated in terms of CO conversion and generally showed a good agreement with the experimental data. Additionally, the model was used to simulate the performance of the Pd-Ag WGS MR in terms of CO conversion and H_2 recovery in a wide parametric space, described by the *Damköhler's number* (*Da*) and contact time (Γ). The two parameters were used to describe the possible operation conditions to be used in the reactor, allowing thus to define the optimal operating region. Operating with vacuum, an almost complete conversion of CO can be achieved in the parametric region (contact time/*Damköhler number*) of $Da > \approx 7$ and $\Gamma > \approx 0.25$. However, in this case, the maximum H_2 recovery is limited by the performance of the vacuum pump. In case of operating the MR in sweep gas mode, total CO conversion and almost full H_2 recovery can be achieved in the region of $Da > \approx 7$ and $\Gamma > \approx 0.4$.

Finally it was evaluated the benefits resulting from the integration of a WGS packed-bed MR in a H_2-based plant. This study was based in a pilot ethanol reforming plant developed at ENEA laboratories. Then, a PEMFC/fuel processor stationary system fed with ethanol was simulated using HYSYS process simulator. The conventional configuration of a fuel

processor (which consists in an ethanol reformer followed by two WGS reactors operating at high and low temperatures) was compared with a configuration using a WGS multi-tubular Pd-Ag membrane reactor, in terms of hydrogen yield and energy efficiency. Comparing both configurations, it was found that similar energy efficiencies can be obtained if the membrane-based system runs under conditions that favor high H_2 recovery. This was achieved operating at elevated reaction pressure with no sweep gas or, alternatively, with low lumen (retentate) pressure but with steam sweep in counter-current mode.

The results obtained show that the usage of water vapor as sweep gas improves the H_2 yield of the processor in a large range of operating conditions. In terms of energy efficiency of the system, this still holds for low pressures (reaction pressure lower than 5 bar), but the improvements are marginal and restricted to a narrower range of conditions at high pressures.

Finally, it was shown that the MR-based fuel cell system is more suitable than the conventional reactor CR-based one for producing hydrogen under the operating conditions used in this study. The MR-based fuel cell system is simpler than the CR one and shows slightly higher energy efficiencies (30 % vs. 27 %). Besides, with such a configuration the reduction in system complexity (along with synergetic effects) can be achieved, moving into the logic of the process intensification strategy.

8.2 Suggestions for future work

Membrane reactor technology combines two distinct sciences dealt with in this work: catalysis and membranes. For many researchers, the difficulty is to evaluate which of them has more relevance in MR development. However, it is reasonable to understand that catalyst performance is certainly an important factor in the design of better MRs, in particular to improve H_2 production units, e.g. fulfilling the requirements for the integration of fuel processors with fuel cells. One of the issues that is rarely addressed in the open literature

concerns the problems related to poisoning/contaminants effects. It was reported that the lifetime of industrial Cu-based catalyst is dependent on the sulfur contamination (Lloyd et al., 1989). Specifically, only a few publications have reported the effects of H_2S poisoning (not completely removed in the HDS units) on the WGS catalysts under real fuel processing conditions (Xue et al., 1996). The lack of these studies is more evident over the promising precious metal catalysts, and is therefore an open topic of research in the WGS catalysis field.

Since WGS is such a well-studied process, it is often assumed that the catalysts used in present commercial processes will be equally effective when used in a Pd-based membrane reactor. It is known that CO_2 inhibits the reaction conversion and lowers the reaction rate over conventional WGS catalysts (namely Cu- and Fe-based). In a WGS Pd-based membrane reactor the concentration of CO_2 increases with the conversion of the reaction and because hydrogen is removed through the membrane. Hence, while current WGS catalysts are quite effective and sufficiently active when used in traditional WGS processes, they may not be as suitable for being used in Pd-based membrane reactors. Therefore, future research on catalysis should cover this topic. The development of promising materials, such as those based on precious metals (namely gold) and Cu-ceria, appears to be a great opportunity to overcome this difficulty. Indeed, these catalysts are less sensitive to the presence of carbon dioxide (see Table 2.2).

Pt-based catalysts have been widely used in the automotive industry and have been reported as being high-performance materials to catalyze many reactions in the fuel cell field. However, much more attention has been given to Au-based catalysts, which have gained higher academic and industrial recognition (Cameron et al., 2003) (although to the best of the author's knowledge, no industrial applications exist using Au-ceria materials for WGS). Despite the technical performance of the latter compared with the Pt catalysts, which are really promising in terms of catalytic activity, the greater availability of Au justifies the

possibility of future developments on these materials. The challenge is significant, however, since it is expected that the catalytic activity of both of these precious-metal-based catalysts has to be increased $10-100$ times over the conventional materials for becoming competitive on a cost basis for WGS (Ladebeck and Wang, 2003).

Particular attention should also be given to the feedstock used for H_2 production, because it affects the composition of the synthesis gas produced and the presence of contaminants in such streams. While natural gas is essentially used for stationary applications, it is expected that alcohols or other more exotic fuels such as ammonia will have a major role in the future portable applications. This affects not only the WGS catalyst selection (namely its tolerance toward impurities) but also the MR design (type of membrane, dimensions, etc.).

A problem that still exists in the area of the WGS reaction carried out in MRs is the inability to compare the performance data obtained in many scientific works, due to the different operating conditions used in the experimental tests. Moreover, although there are a considerable number of studies on the WGS reaction performed in MRs cited in the literature, only a small number of them concern cost analysis of these devices. This might be attributed to the fact that MR technology still presents some deficiencies to be overcome before implementation at larger scales. Future research should be devoted to the preparation of thin and defect-free membranes able to work for long periods at high temperatures and pressures.

Traditionally, these membranes have a thickness of at least $50\,\mu m$, which limits the hydrogen flux and inherently the membrane size and cost. For this reasons, synthesis of new thin Pd-alloy membranes is crucial. Several deposition methods have been employed to prepare thin Pd-Ag composite membranes including sputtering (Jayaraman and Lin, 1995; Tucho et al., 2009), metal-organic chemical vapor deposition – MOCVD (Xomeritakis and Lin, 1997), electroless plating (She et al., 2001; Tanaka et al., 2006) and electro-plating (Tong et al., 2005). However, the electroless and electrodeposition techniques require less

expensive equipments and have the potential for the cost-effective production of the membranes on an industrial scale (Bunshah, 1994).

Minimizing the palladium loading has been the main driving force behind the development of Pd-based membranes. In this sense, coating of thin Pd films onto appropriate supports (porous ceramics and metallic materials) is preferred rather than to use free standing thick foils, achieving in the first case a higher hydrogen permeance, lower costs and higher mechanical resistance for severe conditions (high pressures and temperatures).

Another issue worth of noting is the effect of gas-phase impurities on metallic membranes permeability. Generally, when using MRs allocating membranes completely hydrogen permselective (dense Pd and Pd-alloy based membranes), hydrogen permeation can present deviations from *Sieverts' law* due to contaminants acting on the membrane surface. For example, using thick palladium-based membranes, the deviation from *Sieverts' law* can be related to a decrease of the surface reaction rate as a consequence of the adsorption of such contaminants on the membrane surface such as C, S, CO, CO_2, etc. In particular, the presence of CO can decrease the hydrogen permeation acting as blockage of the Pd-Ag membrane surface. This effect is more pronounced for lower temperatures (Amandusson et al., 2001). On the contrary, working at temperatures higher than 350 ºC, no effects of contamination due to CO are noticed. Therefore, taking into account Pd-Ag membranes, oxidizing with air at $300-450$ ºC can favor the contaminant removal (Basile et al., 2008). Understanding these phenomena is of great importance in WGS MRs operation, particularly because different feed compositions can be used from process to process, but also from the modeling point of view; for instance, in chapter 6 all model parameters were determined in independent studies along this thesis, except those related with the decline of permeability due to the presence of CO, which were obtained by fitting to H_2 recovery data using literature information.

Still in the modelling field, more elaborated models should be developed (and validated against experimental data), for conditions closer to real practice operation. For instance, taking into account mass (and eventually heat) transfer resistances, either internal or external, radial profiles, and for higher operation pressures.

Once these problems can be solved (i.e. synthesis of defect-free, stable and impurity resistant membranes), the benefits resulting from the use of MRs instead of traditional reactors for carrying out the WGS reaction at industrial scale could become more realistic. On the other hand, better economic analyses are needed for stimulating improvements in this area.

8.3 References

Amandusson, H., Ekedahl, L.G., Dannetun, H., Hydrogen permeation through surface modified Pd and Pd-Ag membranes. *J. Memb. Sci.* **2001**, 193 (1), 35-47.

Basile, A., Tosti, S., Gallucci, F., Synthesis, characterization and applications of palladium membranes. In *Membrane Science and Technology - Inorganic membranes: synthesis, characterization and applications*, Mallada, R., Menéndez, M., Eds. Elsevier: Amsterdam, 2008.

Bunshah, R.F., *HandBook of deposition technologies for films and coatings - science, technology and applications*. Noyes publications: Park Ridge, NJ, 1994.

Cameron, D., Holliday, R., Thompson, D., Gold's future role in fuel cell systems. *J. Power Sources* **2003**, 118 (1-2), 298-303.

Jayaraman, V., Lin, Y.S., Synthesis and hydrogen permeation properties of ultrathin palladium-silver alloy membranes. *J. Membr. Sci.* **1995**, 104 (3), 251-262.

Ladebeck, J.R., Wang, J.P., Catalyst development for water-gas shift. In *Handbook of fuel cells, fuel cell technology and applications*, John Wiley & Sons, England, 2003; Vol. 3, pp. 190-201.

Lloyd, L., Ridler, D.E., Twigg, M.V., The water-gas shift reaction. In *Catalyst handbook*, 2nd ed.; Twigg, M.V., Ed. Wolfe Publishing Ltd.: London, 1989.

She, Y., Han, J., Ma, Y.H., Palladium membrane reactor for the dehydrogenation of ethylbenzene to styrene. *Catal. Today* **2001**, 67 (1-3), 43-53.

Tanaka, D.A.P., Tanco, M.A.L., Nagase, T., Okazaki, J., Wakui, Y., Mizukami, F., Suzuki, T.M., Fabrication of hydrogen-permeable composite membranes packed with palladium nanoparticles. *Adv. Mater*. **2006**, 18 (5), 630-632.

Tong, J.H., Shirai, R., Kashima, Y., Matsumura, Y., Preparation of a pinhole-free Pd-Ag membrane on a porous metal support for pure hydrogen separation. *J. Memb. Sci*. **2005**, 260 (1-2), 84-89.

Tucho, W.M., Venvik, H.J., Stange, M., Walmsley, J.C., Holmestad, R., Bredesen, R., Effects of thermal activation on hydrogen permeation properties of thin, self-supported Pd/Ag membranes. *Sep. Purif. Technol*. **2009**, 68 (3), 403-410.

Xomeritakis, G., Lin, Y.S., Fabrication of thin metallic membranes by MOCVD and sputtering. *J. Membr. Sci*. **1997**, 133 (2), 217-230.

Xue, E., OKeeffe, M., Ross, J.R.H., Water-gas shift conversion using a feed with a low steam to carbon monoxide ratio and containing sulphur. *Catal. Today* **1996**, 30 (1-3), 107-118.

Appendix A

Gas Chromatograph Calibration

A.1 The Gas Chromatograph

A Dani gas chromatograph (GC) model 1000 equipped with a VICI Microvolume thermal conductivity detector (TCD) was used to analyze the gas composition of the dry streams. The GC was fitted with one column, a Supelco Carboxen 1010 plot (from Sigma-Aldrich) of dimensions 30 m × 0.32 mm i.d., for separating H_2, O_2, N_2, CO and CO_2.

The GC was equipped with a Valco valve to automatically control the switching of sample introduction. It was also equipped with a sample loop to provide precise and repeatable sample injections to the GC.

A.2 GC Parameter Calibration

Before preparing calibration standards, which relate the peak areas obtained in a chromatogram with the composition of the mixture being analyzed, it is necessary to determine which operating parameters are the most adequate for the GC analyses. These parameters include the volumetric flow of the gases (carrier and reference gas - He), the

temperature of the GC oven and the temperature of the TCD (filaments and detector heater block).

The volumetric flow rates were controlled in the GC software by setting the appropriated pressure and further verified at the outlet of the filaments by means of a mass flow meter Humonics ADM 2000. The current settings for gas flow rates are presented in Table A.1. The flow rates were adjusted based on a compromise between signal stability/resolution and analysis duration.

Table A.1 – Gas flow rate specifications

Type	**Gas (He), $mL_N \cdot min^{-1}$**
Carrier	1.15
Reference	1.20

Generally, the detector sensitivity increases as the temperature differential between the detector and the filaments increases, but filament life decreases as its temperature increases. Typically, the filament temperatures should be at least 50 °C and as much as 100 °C higher than the detector temperature. In this sense, the detector and the filaments temperatures were set as 210 ºC and 270 ºC, respectively.

Finally, the last parameter that needs to be set is the temperature of the oven. This value is limited upwards by the specification of the column and downwards by the speed of analysis. Usually, higher temperatures result in faster analysis but also in poorer separations. In this work, has been decided not to use a fixed temperature for analysis, but rather a temperature program, as follows:

- isothermal operation at 35 ºC for 7.5 min;
- heating from 35 ºC to 80 ºC with a rate of 10 $ºC \cdot min^{-1}$;
- keeping the oven at 80 ºC for 8 min.

Using this protocol, temperature is maintained constant for a certain period and further increased in order to separate better and speed up the analysis. A typical chromatogram is presented in Figure A.1.

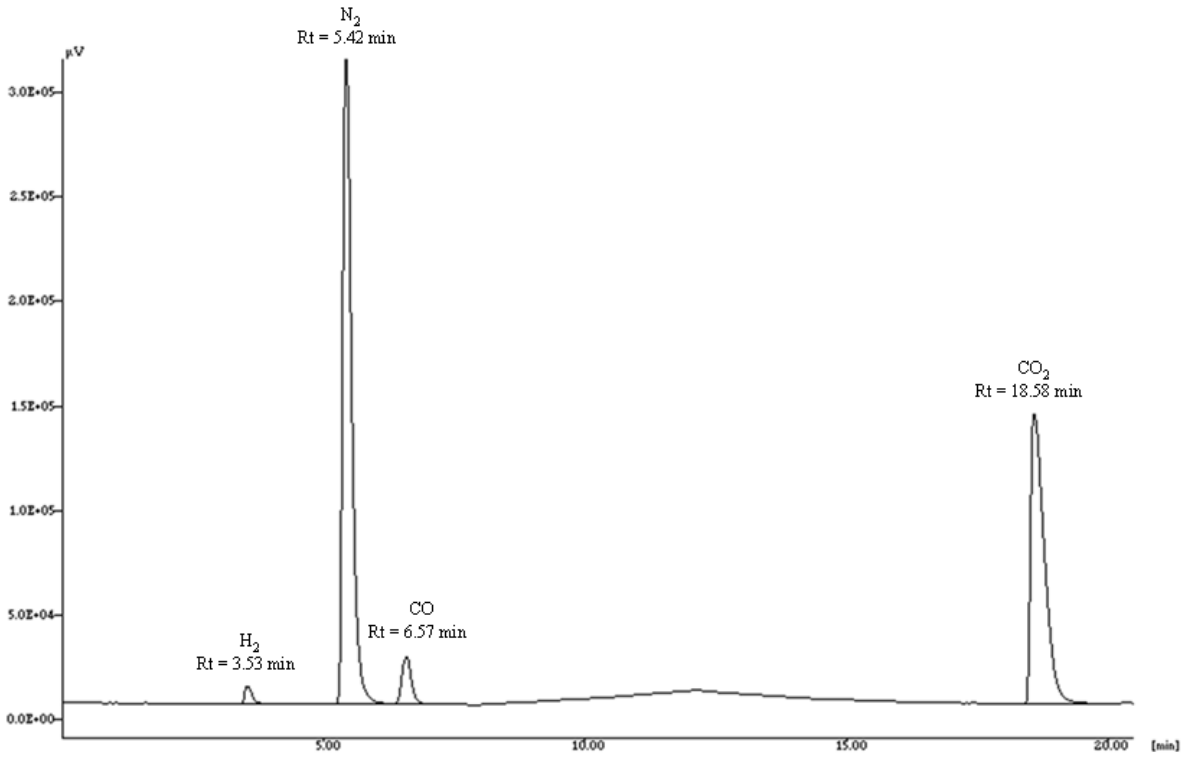

Figure A.1 – Typical chromatogram from a gas mixture containing H_2, N_2, CO and CO_2 (Rt means retentation time).

A.3 GC Calibration

The calibration of the gas chromatograph (GC) to analyze and quantify the CO, CO_2 and N_2 species was performed by injecting different mixtures of known compositions and registering the respective peak area values (see examples of Table A.2 and A.3). The compositions were chosen to cover a wide range of values, in particular, to emulate real concentrations that are expected to exist at any given time inside the reactor.

Multi-component mixtures were prepared on a cylindrical vessel ($V = 0.55\times10^{-3}$ m^3; i.d. = 8.2 cm; h = 10.5 cm) connected to a pressure gauge (Druck-PMP 4000 Series - 10 bara).

After the introduction of all gases, the mixture was homogenized using a magnetic stirrer (Falc – F30).

Table A.2 – Experimental data for mixture 1.

Component	**Partial pressure (bara)**	**Molar composition (%)**	**Average area** * **(μV·min)**
CO	0.009	0.105	1.015×10^{4}
CO_2	1.206	14.089	1.591×10^{6}
N_2	5.930	69.276	6.751×10^{6}
H_2	1.415	16.530	–

* This value is an average of at least three measurements.

Table A.3 – Experimental data for mixture 2.

Component	**Partial pressure (bara)**	**Molar composition (%)**	**Average area** * **(μV·min)**
CO	0.092	1.158	1.002×10^{5}
CO_2	4.244	53.417	6.233×10^{6}
N_2	2.125	26.746	2.716×10^{6}
H_2	1.484	18.678	–

* This value is an average of at least three measurements.

The GC was calibrated periodically to ensure the permanent good quality of the analysis. Examples of calibration plots for CO, CO_2 and N_2 species are shown in the Figures below:

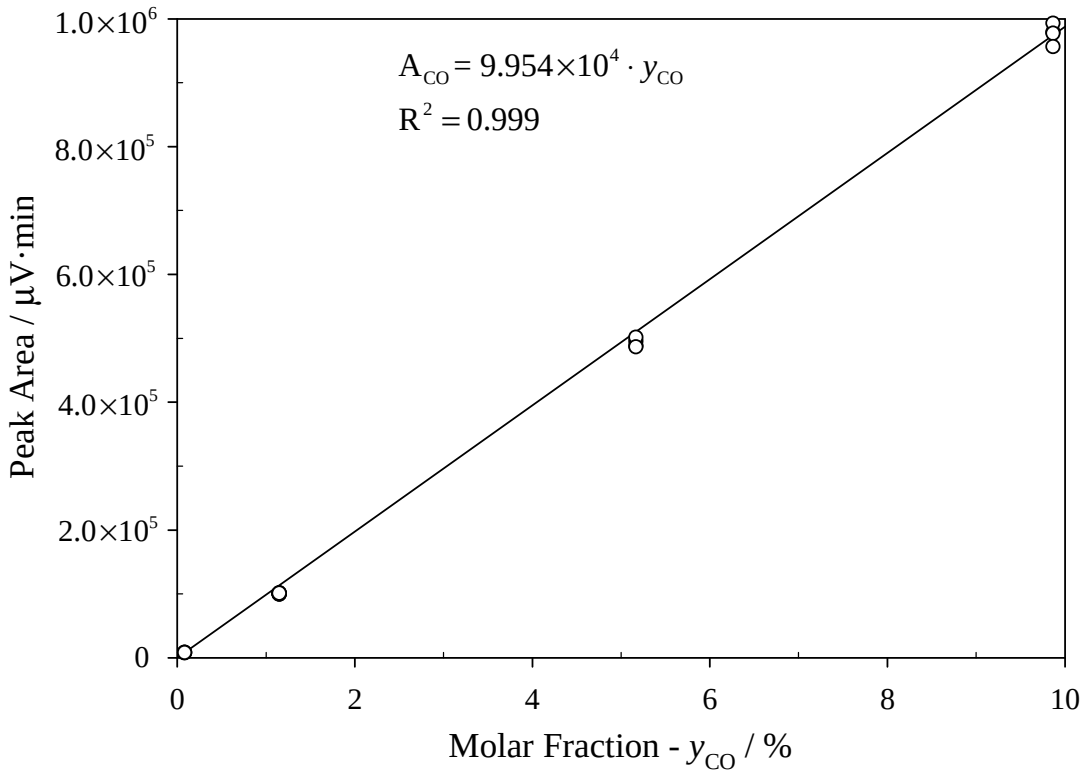

Figure A.2 – Peak area of CO as a function of the CO molar composition in the mixture

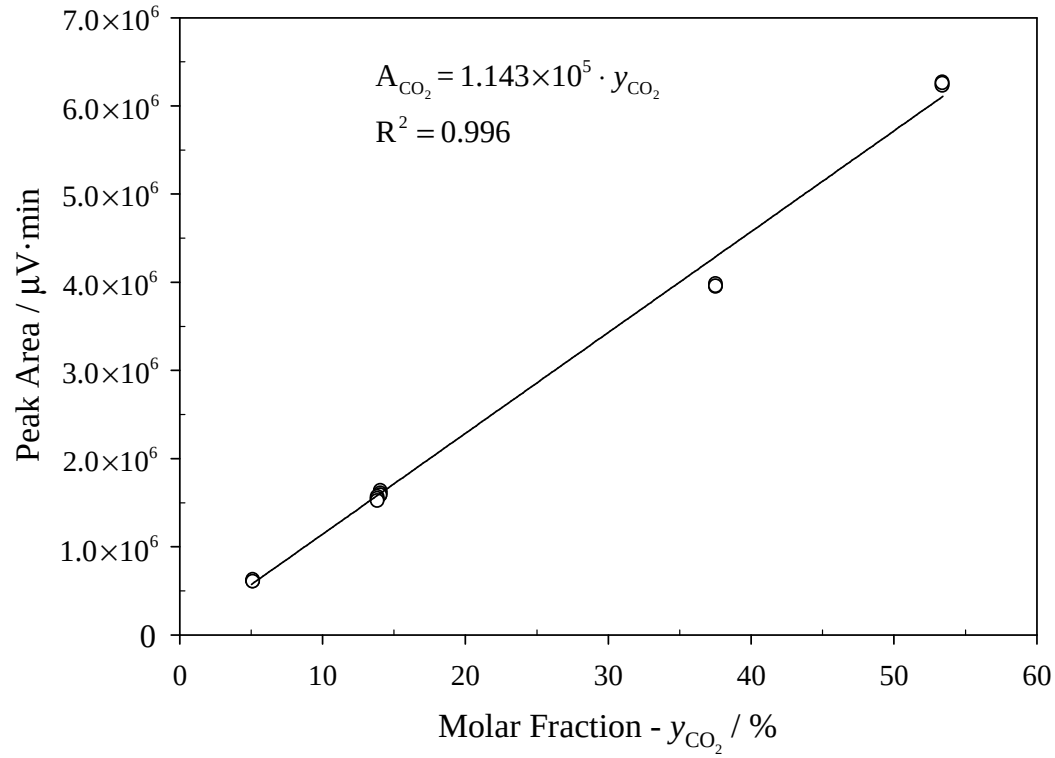

Figure A.3 – Peak area of CO_2 as a function of the CO_2 molar composition in the mixture.

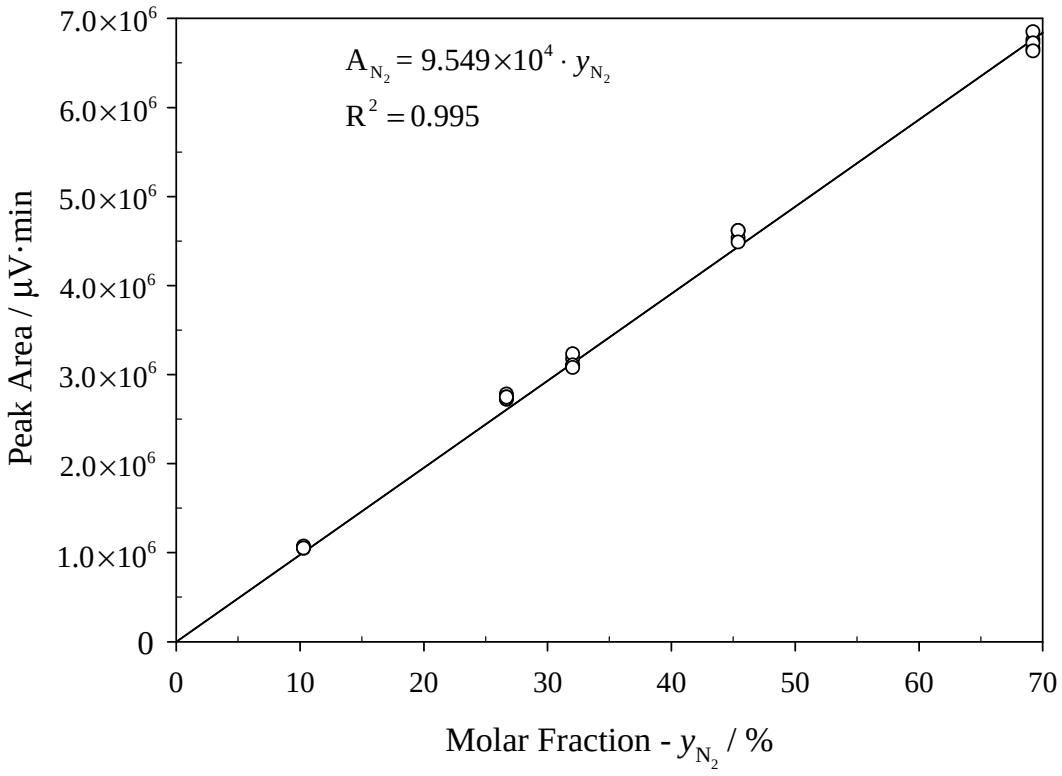

Figure A.4 – Peak area of N_2 as a function of the N_2 molar composition in the mixture.

Appendix B

Calculation of Thermodynamic and Transport Properties

Available Literature Data

In Chapters 4 and 6, several criteria and mathematical models were developed. In order to solve each one, various transport parameters are required. This Appendix reports the correlations used to calculate the different transport parameters.

In Table B.1 some physical and thermodynamic properties of the species involved in the reaction experiments are presented.

Table B.1 – Basic properties of CO, H_2O, CO_2, H_2 and N_2 (Perry and Green, 1999; Smith et al., 1996).

Molecule	CO	H_2O	CO_2	H_2	N_2
Molecular weight, M ($g \cdot mol^{-1}$)	28.01	18.02	44.01	2.02	28.01
Normal boiling temperature, T_b (K)	81.6	373.2	194.7	20.4	77.3
Critical temperature, T_c (K)	132.9	647.1	304.2	33.19	126.2
Critical pressure, P_c (bar)	34.99	220.55	73.83	13.13	34.00
Compressibility factor, Z_c	0.299	0.229	0.274	0.305	0.289

Heat of Reaction

The heat of the water-gas shift (WGS) reaction, ΔH_r (kJ·mol^{-1}), at a given temperature T (K), is expressed by the following expression (Smith et al., 1996):

$$\Delta H_r(T) = \Delta H_r^{298\,\mathrm{K}} + \Re \int_{298\,\mathrm{K}}^{T} \frac{\Delta C_p^{\circ}}{\Re} dT \qquad \text{(B.1)}$$

where $\Delta H_r^{298\,\mathrm{K}}$ (= 41.1 kJ $\cdot$ mol^{-1}) is the standard heat of the WGS reaction, $\Re$ is the ideal gas constant (= 8.314 J·mol^{-1}·K^{-1}), and ΔC_p°(J $\cdot$ mol^{-1} $\cdot$ K^{-1}) is the standard heat-capacity change of the reaction (the individual heat capacities were determined by equation B.17).

Molecular Diffusivity of the gas mixture

The molecular diffusivity of component *i* in the gas mixture, $D_{\mathrm{i,\,mix}}$(m^2 $\cdot$ s^{-1}), was estimated using the *Wilke method* (Bird et al., 2002):

$$D_{\mathrm{i,\,mix}} = \frac{1 - y_{\mathrm{i}}}{\sum_{\substack{\mathrm{j} \\ \mathrm{j} \neq 1}}^{n} \frac{y_{\mathrm{j}}}{D_{\mathrm{i,j}}}} \qquad \text{(B.2)}$$

where *n* is the number of components and $D_{\mathrm{i,j}}$ (m^2 $\cdot$ s^{-1}) is the binary diffusivity of species *i* when diffusing into a component *j*, present as y_{j} mole fraction. For prediction of the gas diffusivity $D_{\mathrm{i,j}}$, the method of *Fuller* was used, as reported in Perry and Green (Perry and Green, 1999):

$$D_{\mathrm{i,\,j}} = \frac{0.1013 T^{1.75} \left(\frac{1}{M_{\mathrm{i}}} + \frac{1}{M_{\mathrm{j}}} \right)^{0.5}}{P \left[\left(\sum \nu \right)_{\mathrm{i}}^{1/3} + \left(\sum \nu \right)_{\mathrm{j}}^{1/3} \right]^2} \qquad \text{(B.3)}$$

where M (g $\cdot$ mol^{-1}) is the molecular weight of components *i* and *j*, P (Pa) is the operation pressure and $\sum \nu$ is found for each component by summing the atomic diffusion volumes

(i.e., taking into account the atoms present in each species). The diffusion volumes for simple molecules can be found in Table B.2:

Table B.2 – Diffusion volumes for simple molecules (Perry and Green, 1999).

Molecule, *i*	**Diffusion volume,** $\left(\sum \nu\right)$
CO	18.9
H_2O	12.7
CO_2	26.9
H_2	7.07
N_2	17.9

Thermal Conductivity of the gas mixture

The thermal conductivity of the gas mixture, $\lambda_{g,\,mix}$ $(\mathrm{W \cdot m^{-1} \cdot K^{-1}})$, was calculated using a correlation proposed by *Wassiljewa* (Perry and Green, 1999):

$$\lambda_{g,\,mix} = \sum_{\mathrm{i}=1}^{n} \frac{y_{\mathrm{i}} \lambda_{g,\,\mathrm{i}}}{\sum_{\mathrm{j}-1}^{n} y_{\mathrm{j}} A_{\mathrm{ij}}} \tag{B.4}$$

where $\lambda_{g,\,\mathrm{i}}$ $(\mathrm{W \cdot m^{-1} \cdot K^{-1}})$ is the thermal conductivity of pure component *i* at the temperature of interest and calculated by equation B.8, as explained above. The A_{ij} term is the binary interaction parameter which is obtained by the method of *Lindsay and Bromley* (Perry and Green, 1999):

$$A_{\mathrm{ij}} = \frac{1}{4}\left\{1+\left[\frac{\mu_{\mathrm{i}}}{\mu_{\mathrm{j}}}\left(\frac{M_{\mathrm{j}}}{M_{\mathrm{i}}}\right)^{3/4}\left(\frac{T+S_{\mathrm{i}}}{T+S_{\mathrm{j}}}\right)\right]^{1/2}\right\}^{2}\left(\frac{T+S_{\mathrm{ij}}}{T+S_{\mathrm{i}}}\right) \tag{B.5}$$

where $\mu_{\mathrm{i,\,j}}$ (Pa·s) is the vapour viscosity of pure component *i* or *j* at the temperature *T* (K) of interest, calculated as explained in the following section. *S* (K) is a component temperature

based parameter which takes a value of 79 K for H_2, and is expressed by equation B.7 for components CO, H_2O, CO_2 and N_2; S_{ij} (K) is obtained from equation B.6.

$$S_{ij} = C\sqrt{S_i S_j} \tag{B.6}$$

$$S_{i,j} = 1.5T_{bi,j} \tag{B.7}$$

where C is a constant which takes the value of 1.0 except when either or both components i and j are very polar; then C = 0.73. $T_{bi,j}$(K) is the normal boiling temperature of pure component i or j – Table B.1.

The pure component thermal conductivity was calculated using the equation proposed by *Eucken* as shown below (Poling et al., 1987):

$$\lambda_{g,i} = \mu_{i,j}\left(\frac{5}{4}\frac{\Re}{M_i} + \frac{C_{p,i}}{M_i}\right) \tag{B.8}$$

where $C_{p,i}$ is the molar heat capacity at constant pressure of component i (more details for $C_{p,i}$ calculation are given below).

Viscosity of the gas mixture

The viscosity of the gas mixture, $\mu_{g,mix}(\mathrm{Pa\cdot s})$, was calculated using the method of *Wilke* (Rase, 1990), according to the following equation:

$$\mu_{g,mix} = \frac{\sum_{i=1}^{n} y_i \mu_{g,i} M_i^{0.5}}{\sum_{i=1}^{n} y_i M_i^{0.5}} \tag{B.9}$$

where $\mu_{g,i}$ is the viscosity of pure component i. Such parameters were calculated by the *Lucas method* (Poling et al., 1987), as described by the following equations:

$$\mu_{g,i}\xi_{g,i} = \begin{bmatrix} 0.807T_{r,i}^{0.618} - 0.357\,exp(-0.449T_{r,i}) \\ +0.340\,exp(-4.058T_{r,i}) + 0.018 \end{bmatrix} F_{P,i}^{o} F_{Q,i}^{o} \tag{B.10}$$

$$\xi_{g,\mathrm{i}} = 0.176\times10^{-7}\left(\frac{T_{c,\mathrm{i}}}{M_{\mathrm{i}}^{3}P_{c,\mathrm{i}}^{4}}\right)^{1/6} \tag{B.11}$$

where $\xi_{g,\mathrm{i}}$ $(\mathrm{Pa\cdot s})$ is the reduced inverse viscosity of pure component *i*, defined by equation B.11, $T_{r,\mathrm{i}}$(K) is the reduced temperature, $T_{c,\mathrm{i}}$(K) and $P_{c,\mathrm{i}}$(bar) are the critical temperature and pressure of component *i*, respectively (cf. Table B.1). $F_{P,\mathrm{i}}^{o}$ and $F_{Q,\mathrm{i}}^{o}$ are correction factors to account for polarity or quantum effects of species *i*. To obtain $F_{P,\mathrm{i}}^{o}$ and $F_{Q,\mathrm{i}}^{o}$ a reduced dipole moment, $\mu_{r,\mathrm{i}}$ (debyes), is required and it can be calculated by the following equation (Poling et al., 1987):

$$\mu_{r,\mathrm{i}} = 52.46\frac{\mu_{g,\mathrm{i}}^{2}P_{c,\mathrm{i}}}{T_{c,\mathrm{i}}^{2}} \tag{B.12}$$

Then, $F_{P,\mathrm{i}}^{o}$ values are found as follows:

$$F_{P,\mathrm{i}}^{o} = 1 \qquad 0 \le \mu_{r,\mathrm{i}} < 0.022 \tag{B.13}$$

$$F_{P,\mathrm{i}}^{o} = 1+30.55(0.292-Z_{c,\mathrm{i}})^{1.72} \qquad 0.022 \le \mu_{r,\mathrm{i}} < 0.075 \tag{B.14}$$

$$F_{P,\mathrm{i}}^{o} = 1+30.55(0.292-Z_{c,\mathrm{i}})^{1.72}\left|0.96+0.1(T_{r,\mathrm{i}}\text{-}0.7)\right| \qquad 0.075 \le \mu_{r,\mathrm{i}} \tag{B.15}$$

where $Z_{c,\mathrm{i}}$ is the compressibility factor of species *i* at $T_{c,\mathrm{i}}$ and $P_{c,\mathrm{i}}$ conditions (see Table B.1).

The factor $F_{Q,\mathrm{i}}^{o}$ is used only for the quantum gases He, H_2, and D_2 (Poling et al., 1987).

Molar heat capacity of the gas mixture

The molar heat capacity of the gas mixture, $C_{p,\mathrm{mix}}$ $(\mathrm{J\cdot mol^{-1}\cdot K^{-1}})$, was calculated as follows:

$$C_{p,\mathrm{mix}} = \sum_{\mathrm{i}=1}^{n} y_i C_{p,\mathrm{i}} \tag{B.16}$$

$C_{p,\mathrm{i}}$ is calculated using equation B.17 (Smith et al., 1996):

$$\frac{C_{p,\mathrm{i}}}{\Re} = A + BT + CT^2 + DT^{-2} \qquad \text{(B.17)}$$

where *A*, *B* and *D* are constants characteristic of the particular substance (Table B.3). For the species of concern, parameter *C* in equation B.17 is null (Smith et al., 1996).

Table B.3 – Heat capacities of gases in the ideal gas state (Smith et al., 1996).

Specie	*A*	10^3 *B*	10^{-5} *D*
CO	3.376	0.557	-0.031
H_2O	3.470	1.450	0.121
CO_2	5.457	1.045	-1.157
H_2	3.249	0.422	0.083
N_2	3.280	0.593	0.040

Density of the gas mixture

Assuming ideal gas behaviour, the density of the gas mixture ρ_g ($\mathrm{kg \cdot m^{-3}}$) was calculated according to the following equation:

$$\rho_g = \frac{P}{\Re T}\left(\sum_{\mathrm{i}=1}^{n} y_{\mathrm{i}} M_{\mathrm{i}}\right) \qquad \text{(B.18)}$$

B.1 References

Bird, R.B., Stewart, W.E., Lightfoot, E.N., *Transport phenomena*. 2 ed.; Wiley: New York, 2002.

Perry, R.H., Green, D.W., *Perry's chemical engineer's handbook*. 7 ed.; McGraw Hill: New York, USA, 1999.

Poling, B.E., Prausnitz, J.M., O'Connell, J.P., *The properties of gases and liquids*. 4 ed.; McGraw-Hill: New York, USA, 1987.

Rase, H.F., *Fixed bed reactor design and diagnostic*. Butterworths: Boston, MA, 1990.

Smith, J.M., van Ness, H.C., Abbott, M., *Introduction to chemical engineering thermodynamics*. 5 ed.; McGraw-Hill: New York, 1996.